Harnessing Epsilon-Near-Zero (ENZ) effect in Nanophotonic Metamaterials for Modulation of Optical Intensity and Polarization

A thesis submitted

in partial fulfilment of the requirements

for the Degree of

Doctor of Philosophy

by

Tanmay Bhowmik

Department of Electronics and Electrical Engineering

Indian Institute of Technology Guwahati

Guwahati - 781039, Assam, India.

August 2024

Dedicated to my beloved Father

Late Gobinda Bhowmik

(January 15, 1966 to August 24, 2023)

Certificate

This is to certify that the thesis entitled "***Harnessing Epsilon-Near-Zero (ENZ) effect in Nanophotonic Metamaterials for Modulation of Optical Intensity and Polarization***", submitted by **Tanmay Bhowmik** (186102016), a research scholar in the Department of Electronics and Electrical Engineering, Indian Institute of Technology Guwahati, for the award of the degree of ***Doctor of Philosophy***, is a record of an original research work carried out by him under my supervision and guidance. The thesis has fulfilled all requirements as per the regulations of the institute and in our opinion has reached the standard needed for submission. The results embodied in this thesis have not been submitted to any other University or Institute for the award of any degree or diploma.

Date: August 19, 2024

Place: Guwahati

Dr. Debabrata Sikdar

Associate Professor

Dept. of Electronics and Electrical Engineering,

Indian Institute of Technology Guwahati,

Guwahati, Assam, India - 781 039

Declaration

I certify that

- The work enclosed in this thesis is original and has been done by me under the guidance of my supervisor.
- This work has not been submitted to other Institute for any degree or diploma.
- I have followed the standard guidelines provided by the institute in preparing the thesis.
- I have conformed to the norms and guidelines given in the Ethical Code of Conduct of the Institute.
- Whenever I have used materials (data, theoretical analysis, figures, and text) from other sources, I have given due credit to them by citing them in the text of the thesis and giving them details in the references. Further, I have taken permission from the copyright owners of the sources, whenever necessary

Date: August 19, 2024
Place: Guwahati

Tanmay Bhowmik
PhD Student
Dept. of Electronics and Electrical Engineering,
Indian Institute of Technology Guwahati,
Guwahati, Assam, India - 781 039

Acknowledgements

Looking through the years and taking a trip down the memory trail, I can't help but feel many memories connected to this magnificent IIT Guwahati campus. I have a lot of amazing individuals to thank at this point in my PhD thesis writing process who have either directly or indirectly helped me navigate through the ups and downs of my four-year journey.

First and foremost, I would like to thank my thesis supervisor, Dr. Debabrata Sikdar, for his guidance and unwavering support during the course of my study. I am extremely grateful for the freedom he provided me to pursue my interests and for teaching me how to become more confident in myself. I admire him for his acute intelligence, boundless curiosity, and unwavering devotion to science. His enthusiasm and upbeat demeanor have been a huge source of motivation for me to keep going even during times of obstacles, both personally and scientifically. I will always be highly impressed by the virtually unattainable high standard he has set for me. I genuinely appreciate the effort he put into carefully reading through each manuscript I sent to him and providing insightful feedback.

I owe my doctorate committee members an amount of gratitude for taking the time out of their hectic schedules to assess my progress and provide vital comments and ideas that have improved this thesis work. I am grateful to Prof. Rakhesh Singh Kshetrimayum for his insightful advice and guidance as the head of my PhD committee. I would like to express my sincere gratitude to Dr. Ramesh Kumar Sonkar for his valuable guidance during my progress review. I am eternally grateful to Prof. Gagan Kumar for his guidance and unwavering assistance throughout my PhD journey, as well as for giving me the chance to gain experience in a collaborative work environment as part of a sponsored research project funded by Indian Space Research Organization.

I am grateful to the Head of the Department, EEE, other professors (special notes to Dr. Rishikesh Kulkarni and Dr. Mahima Arrawatia) and staff members of EEE Department, for their assistance at various periods of my academic career.

I do not have words to convey my gratitude to Dr. Ashish Kumar Chowdhary and Mr. Jegyasu Gupta, my colleagues cum friends, for their constant support and assistance throughout my doctoral journey, especially for those brainstorming sessions we have done. I am incredibly grateful to my seniors, Dr. Darpan Mishra and Dr. Manoranjan Minz for their insightful talks and recommendations regarding our subject of photonics. I would like to thank my friends from IIT Guwahati, Bhairov, Gangesh, Praveen, Vineet, Vikas, Anik, Dibaskar, Sourodipto, Sumit, and many more for creating a friendly and supportive environment during my PhD journey. I would like to thank my juniors, Bodhan and Aakash, for working with me on their M. Tech thesis. They have consistently offered helpful suggestions, creating an enjoyable research atmosphere.

Last but not the least, this PhD journey would not have been possible without the endless support and unconditional love from my beloved parents, father, Late Gobinda Bhowmik, and mother, Smt. Jhunu Bhowmik. I have no words to show gratitude and love towards my late father, who first motivated me to pursue my career in the scientific research field and unfortunately left us last year due to cancer. My loving wife Smt. Mandira Biswas, deserves particular recognition for being a wonderful life partner. She has always played an irreplaceable role in all aspects that I achieved so far. My sincere thanks to my sister, Smt.Tista Bhowmik, brother-in-law, Shri Sukanta Das, and my cute nephew, Master Satwik Das, for being such a support to me since I started my research work.

Tanmay Bhowmik

Abstract

Over several decades, the advancement of photonic technologies has led us to achieve active control of electromagnetic properties (*viz.* amplitude, phase, and polarization) of light. Active manipulation of reflected or transmitted light can be done under the influence of external stimuli such as electrical biasing (leading to electro-optic modulation) or optical pumping (all-optical modulation). Conventional free-space electro-optic modulators face the limitation posed by the small electro-optic coefficients of natural materials. The modulators are thus bulky and require very large voltage biasing. Hence, those are not suitable for nanophotonic applications. This motivated us to explore ultra-compact low-voltage alternative for nanophotonic modulators based on artificially-engineered materials or 'metamaterials'.

In the last few years, tunable metamaterials have emerged as a potential candidate to realize ultra-compact nanophotonic free-space optical modulators. By engineering their unit cells or meta-atoms, metamaterials have showcased capabilities of controlling light–matter interactions at a scale smaller than or comparable to the wavelength of light. Metamaterial based electro-optic modulators incorporating transparent conducting oxides (TCOs) have gained ample attention due to their exceptional electro-optic properties at the telecommunication wavelengths. By tuning the optical properties of TCOs, we can explore an exciting phenomenon named as 'epsilon-near-zero (ENZ) effect', where the real part of permittivity becomes vanishingly small at a certain wavelength.

The ENZ-effect can be exploited by controlling accumulation of the free-carriers of TCOs (using electrical biasing) while configured in a metal-oxide-semiconductor type structure. The variation of optical properties using electrical biasing opens the doors to designing electro-optic modulators for intensity and polarization modulation for nanophotonic applications. On the other hand, upon applying optical pumping, nonlinear-effects induced by intraband electronic transitions in ENZ-materials enable realization of all-optical modulators.

In this dissertation, the opportunities and challenges towards achieving efficient electro-optic and all-optical modulation are presented for various nanophotonic applications by leveraging the ENZ-phenomenon of TCOs integrated with several resonating metamaterials. First, two novel electro-tunable metamaterials are investigated and designed for enabling dual-band optical intensity modulation by harnessing the ENZ phenomenon of TCOs combined with guided-mode resonance (GMR) effect of grating waveguides and gap-plasmon resonance (GPR) of metal–insulator–metal (MIM) structure. The dual-band modulation is shown for both the primary telecommunication wavelength bands, *i.e.*, C-band and O-band, with high modulation depth. Although these metamaterials could be useful for attaining dual-band intensity modulation, the stringent dependency on polarization state of incident light imposes several limitations on reducing the footprint of a nanophotonic system. Hence, to mitigate the limitation, we further investigated polarization-insensitive metamaterial designs while leveraging the ENZ phenomenon. Then, two innovative designs of metamaterials are presented for polarization-insensitive free-space electro-optic intensity modulation that can be operated with a random variation of linearly polarized incident light.

Next, to enable ultra-fast free-space all-optical intensity modulation, a unique metamaterial design strategy is investigated by harnessing nonlinear phenomena in ENZ-materials integrated with a magnetic plasmon resonance based metamaterial. The designed metamaterial can operate with a high modulation depth at the telecom wavelength while maintaining ultrafast response time in sub-picosecond scale. Then, we further expanded our investigation on ENZ-materials in the domain of integrated photonic systems, where a polarization-insensitive directional-coupler based on-chip electro-optic intensity modulator is designed by leveraging hybrid integration of ENZ-material in a silicon waveguide. Finally, to enable free-space electro-optic polarization modulation or dynamic control of polarization states of light, a novel design strategy of metamaterial is investigated by utilizing the ENZ phenomenon. The proposed metasurface can dynamically switch among the three different linear polarization states of the reflected wave upon applying external electrical biasing, allowing a tri-state polarization modulation.

Contents

List of Figures

List of Tables

List of Acronyms

EOM	Electro-Optic Modulator
RF	Radio-Frequency
MOS	Metal-Oxide-Semiconductor
CMOS	Complementary-Metal-Oxide-Semiconductor
TCO	Transparent Conducting Oxides
ITO	Indium-Tin-Oxide
CdO	Cadmium Oxide
AZO	Aluminium-Doped Zinc Oxide
GZO	Gallium-Doped Zinc Oxide
ENZ	Epsilon-Near-Zero
ACL	**Ac**cumulation **L**ayer
NIR	Near-Infrared
FDTD	Finite-Difference Time-Domain
FEM	Finite Element Method
EMT	Effective Medium Theory
AOMs	All-Optical Modulators
LP	Linearly Polarized
CP	Circularly Polarized

EP	Elliptically Polarized
GPR	Gap-Plasmon Resonance
GMR	Guided-Mode Resonance
MIM	Metal–Insulator–Metal
EAM	Electro-Absorption Modulator
MZM	Mach–Zehnder Modulator
PML	Perfectly Matched Layer
MD	Modulation Depth
TTM	Two-Temperature Model
OPA	Optical Parametric Amplifier
TM	Transverse Magnetic
TE	Transverse Electric
PDM	Polarization-Division-Multiplexing
HPW	Hybrid Plasmonic Waveguide
ER	Extinction Ratio
IL	Insertion Loss

List of Publications

Patents Filed:

- **Tanmay Bhowmik,** Ashish Kumar Chowdhary, and Debabrata Sikdar, Frequency-scalable Polarization-insensitive Dual-mode Electro-Optic modulators, ***Indian Patent***, App. No.: 202231066529 (Filed on 19-11-2022). (Related to chapter 4)

Peer-Reviewed Journals:

1. **Tanmay Bhowmik,** Bhairov Kumar Bhowmik, Pranav Kumar Pandey, Gagan Kumar, and Debabrata Sikdar**,** "*Dual-band electro-optic modulator based on tunable broadband metamaterial absorber",* **Optics & Laser Technology**, vol. 161, Jan 2023. Publisher: Elsevier, **Q1**, IF: 5.0 (2022). (Related to chapter 3)

2. **Tanmay Bhowmik** and Debabrata Sikdar, "*Electrically tunable metasurface for dual-band spatial light modulation using the epsilon-near-zero effect*," **Optics Letters,** vol. 47, Aug. 2022**.** Publisher: OSA, **Q1**, IF: 3.6 (2022). (Related to chapter 3)

3. **Tanmay Bhowmik** and Debabrata Sikdar, "*Grating-assisted Polarization-insensitive Dual-Mode Spatial Light Modulators Design using Epsilon-Near-Zero Material*", **IEEE Journal of Quantum Electronics**, vol. 58, Aug. 2022. Publisher: IEEE, **Q1**, IF: 2. 43 (2022)**.** (Related to chapter 4)

4. **Tanmay Bhowmik**, Ashish Kumar Chowdhary, and Debabrata Sikdar, "*Polarization-and Angle-insensitive Tunable Metasurface for Electro-Optic Modulation*," **IEEE Photonics Technology Letters**, vol. 35, Aug. 2023**.** Publisher: IEEE, **Q1**, IF: 2.6 (2022). (Related to chapter 4)

5. **Tanmay Bhowmik,** Bodhan Chakraborty, and Debabrata Sikdar, "*All-Optical High-Contrast Femtosecond Switching using Nonlinearity from Epsilon-Near-Zero effect in Plasmonic Metamaterials*," **Optics Letters,** vol. 49, pp. 2397-2400, Apr. 2024**.** Publisher: OSA, **Q1**, IF: 3.6 (2022). (Related to chapter 5)

6. **Tanmay Bhowmik** and Debabrata Sikdar, "*Parallel Directional Coupler based Dual-Polarization Electro-Absorption Modulator using Epsilon Near-Zero Material*," **Journal of Physics D. Appl. Phys.**, vol. 55, 13, Dec. 2021. Publisher: IOP Science, **Q1,** IF: 3.4 (2022). (Related to chapter 6)

7. **Tanmay Bhowmik,** Jegyasu Gupta, and Debabrata Sikdar**, "***Electro-tunable Metasurface for Tri-State Dynamic Polarization Switching at Near-Infrared Wavelengths***", Journal of Physics: Condensed Matter,** vol. 35, Jun 2023**.** Publisher: IOP Science, **Q2**, IF: 2.68 (2022). (Related to chapter 7)

Research article not included in this thesis

8. Bhairov Kumar Bhowmik**, Tanmay Bhowmik,** Pranav Kumar Pandey**,** Makaraju Srinivasa Raju, Debabrata Sikdar, and Gagan Kumar**,** *"All-dielectric asymmetric planar metasurface based dual-parametric sensor,"* **Optics Communications,** vol. 550, Jan 2024. Publisher: Elsevier, Q2, IF: 2.6 (2022).

9. Ashish Kumar Chowdhary, **Tanmay Bhowmik**, and Debabrata Sikdar, "*Infrared-blocking Plasmonic Meta-glasses for Energy-saving Passive Windows*," **Optics Letters**, vol. 47, Apr. 2022. Publisher: OSA, **Q1**, IF: 3.6 (2022).

10. Bhairov Kumar Bhowmik**, Tanmay Bhowmik,** Pranav Kumar Pandey, Makaraju Srinivasa Raju, Debabrata Sikdar, and Gagan Kumar**,** *"All-dielectric metasurface based ultranarrow bandpass filter in optical C-band,"* **Journal of Optical Society of America B,** vol. 40**,** 2023. Publisher: OSA, Q2, IF: 2.0 (2022).

11. Ashish Kumar Chowdhary, **Tanmay Bhowmik**, and Debabrata Sikdar, "*Polarization- and angle-insensitive ultrabroadband metamaterial absorber for thermophotovoltaics*," **Journal of Optical Society of America B**, vol. 38, no. 2, 2021. Publisher: OSA, Q2, IF: 2.0 (2022).

12. Ashish Kumar Chowdhary, **Tanmay Bhowmik**, Jegyasu Gupta, and Debabrata Sikdar, "*Energy-saving all-weather window based on selective filtering of solar spectral radiation*," **Applied Optics**, vol. 60, Feb. 2021. Publisher: OSA, Q2, IF: 1.9 (2022).

13. Bodhan Chakraborty, **Tanmay Bhowmik,** and Debabrata Sikdar, "*Ultra-broadband polarization- and angle-insensitive perfect meta-absorber for energy harvesting and thermal infrared detection,"* **IEEE Transactions on Nanotechnology.** *Status – Submitted for review*

Conference Publications

1. **Tanmay Bhowmik**, Ashish Kumar Chowdhary, Jegyasu Gupta, and Debabrata Sikdar, "*Coupling-assisted Epsilon-Near-Zero Material based Energy-efficient Electro-Absorption Modulator*", **IEEE Workshop on Recent Advances in Photonics (IEEE WRAP) 2022**, Mumbai, India. (Related to chapter 6)

Conference articles not included in the thesis

2. **Tanmay Bhowmik**, Aakash Kumar, Ashish Kumar Chowdhary, and Debabrata Sikdar, "*Polarization-insensitive Electro-Tunable Broadband Plasmonic Metamaterial Absorber for Amplitude Modulation*", 15th International Congress on Artificial Materials for Novel Wave Phenomena – **IEEE Metamaterials, New York, USA, 2021**. (Related to chapter 4)

3. **Tanmay Bhowmik**, Ashish Kumar Chowdhary, Aakash Kumar, and Debabrata Sikdar, "*Guided-Mode Resonance based All-Dielectric Optical Intensity Modulator*", **IEEE Photonics Conference (IPC) 2021, Vancouver, Canada.** (Related to chapter 4)

4. **Tanmay Bhowmik,** Bodhan Chakraborty, Dibaskar Biswas, Jegyasu Gupta, Debabrata Sikdar, "*Guided-Mode Resonance Based Polarization-Insensitive Metasurface for Electro-Optic Modulation*", **Photonics 2023**, IISc Bangalore, India**.** (Related to chapter 4)

5. **Tanmay Bhowmik,** Jegyasu Gupta, Ashish Kumar Chowdhary, and Debabrata Sikdar, "*Tunable Metasurface based Polarization-insensitive Electro-Optic Amplitude Modulator for Nanophotonic Systems*", **IEEE Guwahati Subsection Conference (GCON) 2023**, Guwahati, India**.** (Related to chapter 4)

6. **Tanmay Bhowmik,** Bhairov Kumar Bhowmik, Pranav Kumar Pandey, Gagan Kumar, and Debabrata Sikdar, "*Epsilon-Near-Zero Material based Dual-Polarization On-Chip Electro-Optic Modulator*", **Frontiers in Optics + Laser Science** | **FiO+LS 2023**, Washington, USA.

7. **Tanmay Bhowmik,** Jegyasu Gupta, and Debabrata Sikdar**, "***Gap-plasmon Resonance based Energy-efficient Electro-tunable Metasurface for Polarization-independent Optical Intensity Modulation***",** Metamaterials, Photonic Crystals and Plasmonics Conference | **META 2023**, **Paris.**

8. **Tanmay Bhowmik**, Ashish Kumar Chowdhary, and Debabrata Sikdar, "*Energy-efficient Polarization-insensitive Electro-tunable Metasurface for Optical Intensity Modulation"*, 2022 International Conference on Optical MEMS and Nanophotonics (**IEEE OMN'22**), Israel, 2022**.**

9. Ashish Kumar Chowdhary, **Tanmay Bhowmik**, Jegyasu Gupta, and Debabrata Sikdar, "*Ultraviolet and Infrared Blocking Meta-glasses for Smart Electric Vehicles"*, 22nd International Conference on Numerical Simulation of Optoelectronic Devices (**IEEE NUSOD**), 2022**,** Italy.

10. Bhairov Kumar Bhowmik, **Tanmay Bhowmik,** Pranav Kumar Pandey, Debabrata Sikdar, and Gagan Kumar, "*Polarization-insensitive refractive index sensor based on high-Q resonance in all-dielectric metasurface*, **Frontiers in Optics + Laser Science 2022 (FIO, LS).** Rochester, USA, 2022.

11. Ashish Kumar Chowdhary, Veluri Anurag Reddy, **Tanmay Bhowmik,** and Debabrata Sikdar, "*Vanadium Dioxide Assisted Thermo-Optic Perfect Absorbers for Optical Switching*", IEEE Workshop on Recent Advances in Photonics **(IEEE WRAP)** 2022, Mumbai, India.

12. Ashish Kumar Chowdhary, Veluri Anurag Reddy, **Tanmay Bhowmik,** and Debabrata Sikdar, "*Spectrally Selective Nanophotonic Windows for Aiding Photosynthesis in Greenhouses",* **IEEE Photonics Conference (IPC) 2021**, Vancouver, Canada.

13. Bhairov Kumar Bhowmik, **Tanmay Bhowmik**, Pranav Kumar Pandey, Debabrata Sikdar and Gagan Kumar, "High-Q resonating all-dielectric metamaterial for refractive index sensing," **2023 IEEE GCON,** Guwahati, 2023.

14. Sourodipto Das, Jegyasu Gupta, **Tanmay Bhowmik**, Bodhan Chakraborty, and Debabrata Sikdar, "*Metasurface based Polarization-Insensitive Reflection mode Band-reject Filters for 6G* Applications," **IEEE GCON 2023,** Guwahati, India

15. Dibaskar Biswas, Sourodipto Das, **Tanmay Bhowmik**, Jegyasu Gupta and Debabrata Sikdar, "Epsilon-Near-Zero Material based C-Band Electro-absorption Modulator for Integrated Nanophotonic Systems," **IEEE GCON 2023**, Guwahati, India

16. Bodhan Chakraborty, **Tanmay Bhowmik**, Jegyasu Gupta, Dibaskar Biswas, and Debabrata Sikdar**, "***Plasmonic Metamaterial Perfect Absorber using Hybrid Split Cross-Ring Nanostructures***", IEEE GCON 2023**, Guwahati, India**.**

17. Dibaskar Biswas, Bodhan Chakraborty, **Tanmay Bhowmik,** Jegyasu Gupta, and Debabrata Sikdar, "*Wavelength Selective Metamaterials for Superior Thermal Camouflaging*," **Frontiers in Optics + Laser Science 2023**, Washington, USA.

Books and Chapters not included in the thesis

- **Tanmay Bhowmik**, Bhairov Kr Bhowmik, Bodhan Chakraborty, Dibaskar Biswas, Jegyasu Gupta, Pranav Kr Pandey, Gagan Kumar, Debabrata Sikdar, *Guided-Mode Resonance-Based Polarization-Insensitive Metasurface for Electro-Optic Modulation*. Springer Nature, **Advances in Nano-Photonics and Quantum Optics**, *pp. 87–93, Dec 2024, isbn: 978-981-97-4760-3*.

1

Introduction

Contents

The study of light–matter interactions has been a constant driving force in the last several decades for the growth of the photonic technologies. When light interacts with the molecules or atoms, several optical effects may evolve, such as scattering, refraction, absorption, emission, and so on. The capability to precisely control the light–matter interactions serves as the key factor in realizing the photonic devices for many applications starting from telecommunication and information processing to military technology. However, in the era of the nanotechnology, the diffraction limit of light imposes several restrictions to achieve precise control of light–matter interactions at the nanoscale. This leads the researchers to find the solution from the emerging area of research known as 'Nanophotonics'.

1.1. Brief Introduction to Nanophotonic Metamaterials

What is a metamaterial? "A metamaterial is an artificially structured material which attains its properties from the unit structure rather than the constituent materials. A metamaterial has an inhomogeneity scale that is much smaller than the wavelength of interest, and its electromagnetic response is expressed in terms of homogenized material parameters".

— V. Shalaev, Optical Metamaterials, 2010

Nanophotonics, a fast-growing multidisciplinary field of optics and engineering, has the capability of not only controlling light–matter interactions at the nanoscale but also could provide high operating speed, overcoming the limitations of electronics [1]. Figure 1.1 presents a comparison of dielectric photonics, semiconductor electronics, and nanophotonics [2]. The operating speed limit of electronic components is restricted by Resistive–Capacitive delay, or RC delay. In comparison to their electronic counterparts,

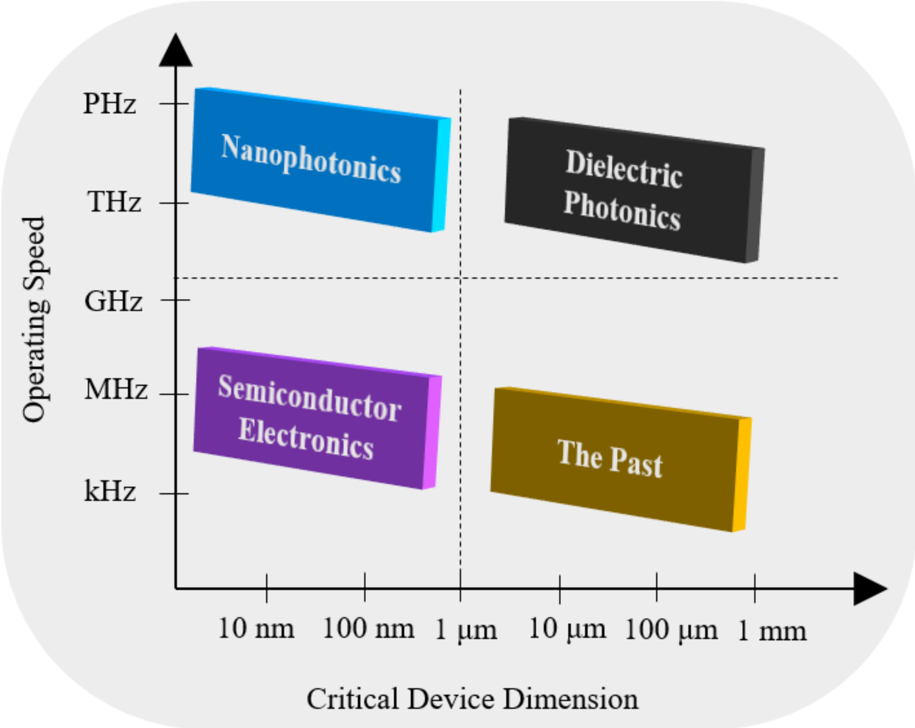

Figure 1.1: A comparative analysis among electronics, photonics, and nanophotonics in terms of device dimensions and operating speeds [2].

the photonic components provide higher operating speeds and wider operating bandwidths. On the contrary, nanophotonics has the potential to lead us towards the sub-wavelength components by availing the benefits from both electronics and photonics. Hence, investigating light–matter interactions at the nanoscale, nanophotonics offers novel physical phenomena that might lead to the development of technologies much beyond what is conceivable with traditional photonics and electronics.

In the same line, metamaterials, or artificially engineered materials, have emerged as a potential solution to overcome the limitations in optical properties of the naturally existing materials [3]. As the name suggests, metamaterials can be defined as crafted materials that can exhibit unusual optical properties, depending upon their constituent structural units, which cannot be observed in naturally available materials [4]. The optical properties of metamaterials and their two-dimensional counterparts, known as metasurfaces, are decided by their unit cells or ‘meta-atoms’, which are sub-wavelength in scale. This gives a lot of freedom to the engineers to customize the optical transmittance, reflectance, and absorption from the metasurfaces [5], [6]. Metamaterials allow us to modify the light spectrally, temporally, or spatially at sub-wavelength precision. The capability of the metamaterials has propelled them to the forefront of nanophotonics research during the last decade. Due to their exceptional abilities to control light–matter interactions at sub-wavelength scale, metamaterials have accelerated the development of flat optical components such as multifunctional meta-lens [7], hyperspectral imaging [8], spatial light modulators [9], optical sensors, filters [10], and so on. Thus, metamaterials have paved the way towards the realization of next-generation optical components for nanophotonic system.

1.2. Research Motivation

Over several decades, the advancement of photonic technologies has led us to achieve active control of electromagnetic properties of light (such as amplitude, phase, and polarization) [4]. The active manipulation of reflected or transmitted light can be done under the influence of external stimuli such as electrical biasing or optical pumping. The electro-optic modulators (EOMs) are such kind of active photonic devices, where the electrical biasing can be used as an external stimulus for tailoring the electromagnetic properties of light [11]–[13]. An all-optical modulator is another example of active photonic device, where we can use an external optical pump-signal to manipulate the amplitude or phase of the incoming optical probe-signal.

1.2.1. Electro-Optic Modulation — Challenges in Nanophotonics

The typical optical communication system requires an EOM for encoding electrical or radio-frequency (RF) data to the optical carrier, as depicted in [11]. To determine the

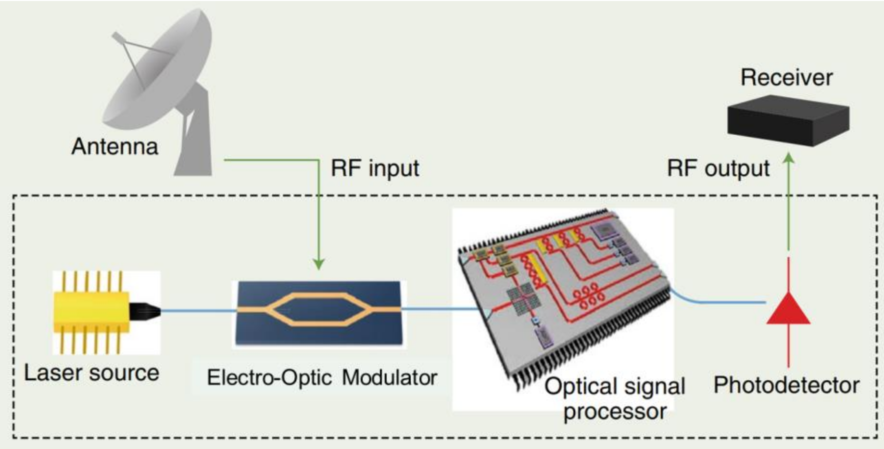

Figure 1.2: The typical optical communication system depicting the process of encoding the electrical data to optical carrier by electro-optical modulator. Adapted with permission from: [11] Copyright © 2019 Springer Nature Ltd.

overall performance of any photonic system, an EOM is a crucial component. The global EOM-market has been estimated as $21.8 Billion in 2022 and is projected to reach over $39 Billion by the year of 2031 due to the ever-increasing demand for EOMs in the telecom industries, military and defence sectors, space and satellite communications, and so on [14].

To realize electro-optic modulation, an active material is required, whose optical properties can be altered by using an external electric field. Finding active electro-optic materials featuring a large tuning of refractive index upon applying external electric field as low as possible has been a constant motivation for the researchers over the years. Various electro-optic material platforms have been exploited whose optical properties can be modified when subjected to an external electrical field. Lithium-niobate, barium-titanate, doped-silicon, gallium arsenide, graphene [15], *etc.* are a few such well-explored active material platforms for demonstrating the electro-optic modulation.

Based on the application scenario, EOMs can be classified as integrated waveguide-based modulators (such as in-line waveguide-type and ring resonator-type) and free-space modulators (such as transmission- and reflection-type), as represented in

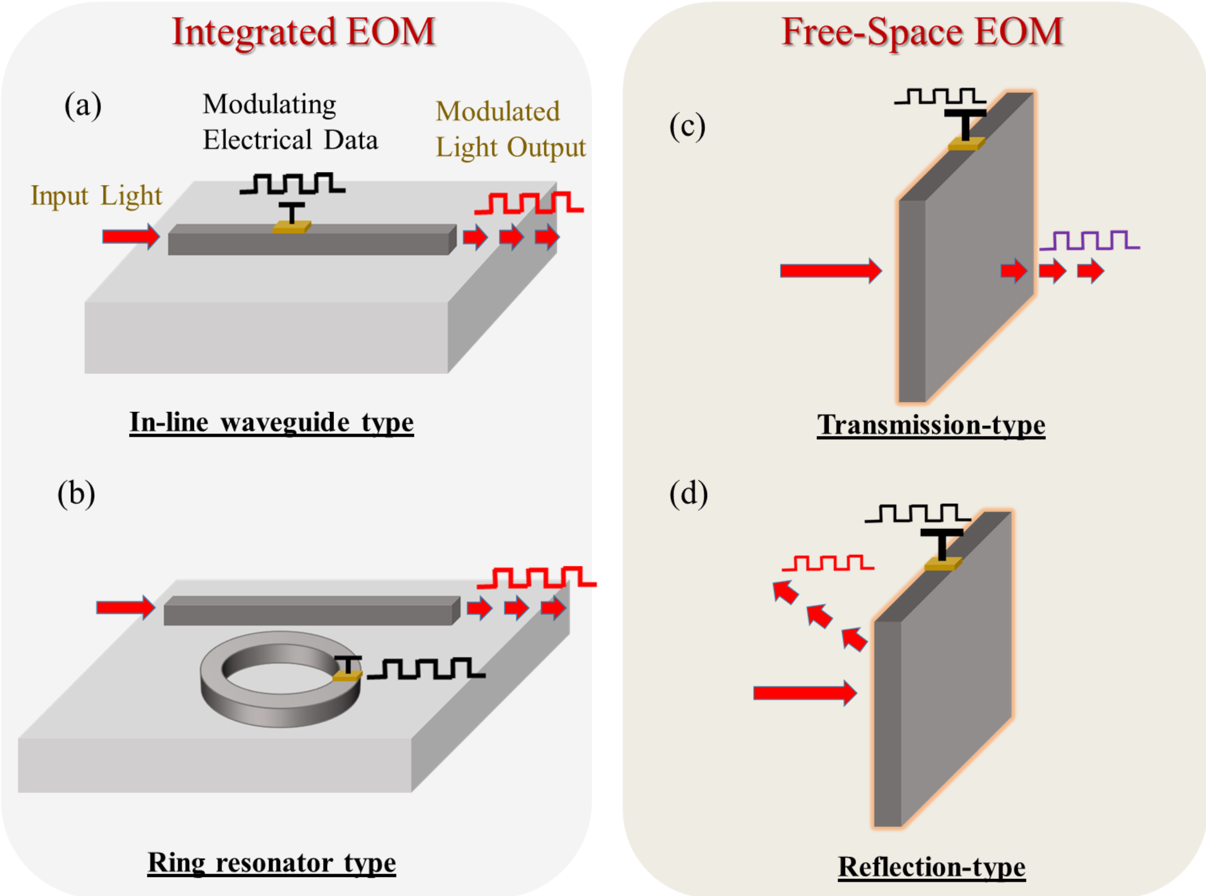

Figure 1.3: Broad classification of electro-optical modulators (EOMs) showing a few examples of integrated waveguide-based modulators *viz.* (a) in-line waveguide type and (b) ring resonator type, and a few examples of free-space modulators *viz.* (c) transmission-type and (d) reflection-type.

Figure 1.3. Over the few decades, several waveguide-based integrated EOMs have been demonstrated, such as lithium-niobate Mach-Zehnder modulators, silicon (Si) waveguide modulators [16]–[23], quantum-confined Stark-effect based electro-absorption modulator, and so on [24], [25]. On the other hand, InGaAs quantum-well surface-normal modulators [26] and photonic crystal spatial light modulators [27] are a few examples of the free-space EOMs demonstrated till date.

As the name suggests, the integrated EOMs, as shown in Figure 1.3(a) and (b), can be used for intra-chip optical communications facilitated by silicon photonics platform. Due to cost-effective photonics–electronics integration enabled by matured CMOS (complementary-metal-oxide-semiconductor)-technology, the integrated silicon-photonics based devices have emerged to address the major bottlenecks of electrical interconnects such as limited bandwidth, high energy consumption, and electrical cross-talk. These integrated EOMs can get benefits from light–matter interaction over the entire length of the waveguide, which may help in realizing high-speed modulation with high extinction ratio or modulation depth — although increasing the device footprint. However, most of the integrated EOMs either suffer from the dependency on a particular polarization (typically imposed by the boundary conditions) or a high-voltage requirement to acquire the needed refractive index change. While the dependency on a single state of polarization increases the overall system complexity by introducing additional requirement of maintaining polarization state, the large voltage requirement, on the other hand, results in the high energy consumption.

On the other hand, for free-space EOMs, shown in Figure 1.3(c) and (d), the direction of light propagation is typically normal to the active material layer — leading to a restricted propagation length. Therefore, it is challenging to design a free-space EOM as the restricted propagation length leads to a limited modulation depth. In order to attain a high modulation depth, we require a high-voltage amplifier (up to few hundreds of volts), which eventually increase the power consumption and system complexity. Moreover, the conventional scheme of free-space optical communication involves several additional bulk optical components, *eg.* polarizers, quarter wave plates, mirrors, and so on, due to their polarization-sensitivity [28]. This makes the overall footprint of the system very large for packaging altogether in a single module. Additionally, the conventional free-space EOMs are themselves bulky due to the limitation of the optical properties (such as weak electro–optic coefficient, polarization-sensitivity, *etc.*) of the natural materials used for modulation.

In short, the challenges posed by the large footprint, polarization-sensitivity, and high-voltage requirement of EOMs motivated the researchers to explore ultra-compact alternative nanophotonic devices based on artificially-engineered materials or 'metamaterials' [29]–[31]. In the last few years, tunable metamaterials have emerged as a potential candidate to realize such ultra-compact nanophotonic free-space EOMs, due to their capabilities to control light–matter interactions at a scale smaller than or comparable to the wavelength of light, by engineering their meta-atoms [29].

The thesis mainly focuses on the various challenges and limitations in designing of integrated and free-space modulators for nanophotonic applications, and finding some potential solutions by leveraging electro-tunable metamaterials overcoming the limitations of natural materials.

1.2.2. Epsilon-Near-Zero (ENZ) effect for Optical Modulation

Various designs of electro-tunable metamaterials have been demonstrated for realizing EOMs by integrating several emerging materials such as two-dimensional materials (graphene) [15], phase-change materials [32], transparent conducting oxides (TCOs) [33], and so on. Among these, degenerately-doped TCOs have gained enormous attention in nanophotonic applications due to their electrical conductivity and optical transparency at the near-infrared wavelength regime [33]–[35].

TCOs, such as indium tin oxide (ITO), dysprosium-doped cadmium oxide (Dy-CdO), aluminium-doped zinc oxide (AZO), and gallium-doped zinc oxide (GZO), which are from wide-bandgap semiconductor family, are widely adopted in smartphone touchscreens [36], solar-cell transparent contacts [37], and energy-saving window glasses [38]. The use of TCOs has been extended to the field of flexible electronics, transformation optics, and many photovoltaic applications. Moreover, being low-loss and compatible with standard CMOS technology, TCOs bring enormous possibilities to enter into the foundry process for realizing various nanophotonic devices.

The optical properties of the TCOs can be modulated by applying external stimuli such as optical pumping or electrical biasing. Importantly, by tuning the optical properties of TCOs, we can exploit an exciting phenomenon named as 'epsilon-near-zero (ENZ) effect', where the real part of permittivity becomes vanishingly small at a certain wavelength. The variation of permittivity using electrical biasing opens the doors to design electro-optic modulators for nanophotonic applications. On the contrary, upon applying optical pumping, nonlinear-effect in TCOs (operating at the ENZ-region) induced by the intraband electronic transitions enables the realization of all-optical modulators. Thus, the ENZ-materials can open a new realm to realize several tunable nanophotonic devices.

1.2.2.1. Electro-Optic Intensity Modulation

The optical properties of a TCO can be defined by the Drude model, given as [33], [39]

$$\varepsilon_{\mathrm{TCO}} = \left(\varepsilon_{\infty} - \frac{\omega_{\mathrm{p}}^2}{(\omega^2 + \mathrm{j}\Gamma\omega)}\right), \tag{1.1}$$

where high-frequency permittivity, plasma frequency, oscillation frequency, and damping constant are represented by ε_{∞}, ω_{p}, ω, and Γ, respectively [29]. The plasma frequency, ω_{p} varies with carrier concentration (N) and effective electron mass m_{e}^*, and can be given by

$$\omega_{\mathrm{p}} = \sqrt{\frac{N\mathrm{e}^2}{m_{\mathrm{e}}^*\varepsilon_0}} \tag{1.2}$$

To unravel the electro-tunable optical response of TCOs, Atwater *et al.* experimentally demonstrated a large refractive index tuning method in a metal-oxide-

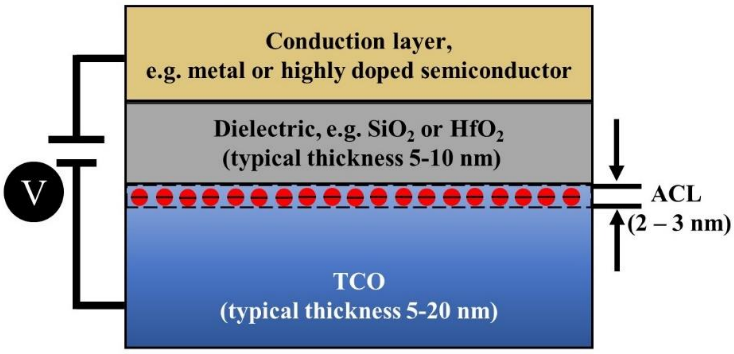

Figure 1.4: A MOS capacitor multilayer stack, forming an accumulation layer (ACL) at TCO–dielectric interface

semiconductor (MOS) configuration with TCO acting as an active material [39]. Under the influence of an applied electrical bias in the MOS-type configuration, the free-electrons (majority carriers) of the TCO will get accumulated at the TCO–dielectric interface, thus, forming an ultra-thin (~2–3 nm) accumulation layer (ACL), as represented in Figure 1.4.

The variation in optical properties of the ACL with changing free-charge carrier concentration distributions (N) can be estimated by the Drude model. Figure 1.5 depicts the modulation of the complex permittivity of ITO (as a TCO-material having the initial value of $N = 3 \times 10^{19}$ cm^{-3}) with the variation of carrier concentration distributions. The ENZ-region can be referred to the real part, $\Re e$ ($\varepsilon_{\mathrm{ITO}}$), of the permittivity ranging from –1 to +1. Thus, a transition from dielectric-like behaviour (positive permittivity) to metallic-like behaviour (negative permittivity) can be seen. On the other hand, the imaginary part of the permittivity is relatively low as compared to the noble metals. The electro-tunable optical response while maintaining negative real part of permittivity and low imaginary part of permittivity indicate TCOs to be less-lossy conductive active material — which is a desirable feature for realizing transmission- and reflection-type free-space modulators. Moreover, the ENZ-effect based devices have gained ample

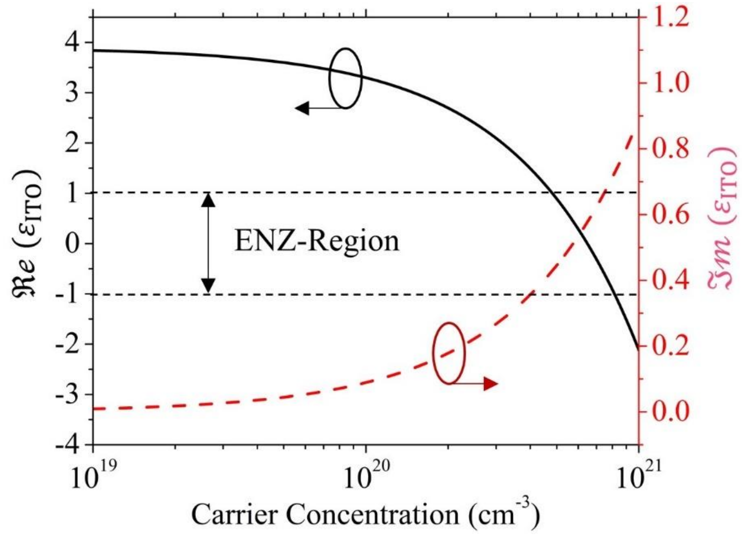

Figure 1.5: Variation of real ($\Re e(\varepsilon_{\mathrm{ITO}})$) and imaginary ($\Im m(\varepsilon_{\mathrm{ITO}})$) parts of permittivity of a TCO-material (here, ITO) as a function of its free-charge carrier concentration at 1.55 μm wavelength. Note**:** ENZ-region is shown for $-1 < \Re e\,(\varepsilon_{\mathrm{ITO}}) < +1$.

attention due to their exceptional electro-optic properties at the telecommunication wavelength region, *i.e.*, C-band ranging from 1530 nm to 1565 nm.

The most highlighting feature of this MOS-type configuration is the ability to confine light at the ultra-thin ACL at the TCO–dielectric interface by enhancing the electric field distributions. TCOs, while exhibiting the ENZ-effect, impose unusual boundary conditions at TCO–dielectric interface. This leads to an enhancement of local electric field inside the ENZ-layer, which ensures strong light–matter interactions. The electric field enhancement can be described by applying boundary conditions, where the normal component of the electric flux density ($D^{\mathrm{n}} = \varepsilon E^{\mathrm{n}}$) is continuous at the TCO–dielectric interface. Thus, the enhancement factor of the electric field can be written as [40]:

$$\frac{|E_{\mathrm{ITO}}^{\mathrm{n}}|}{|E_{\mathrm{Al_2O_3}}^{\mathrm{n}}|} = \frac{|\varepsilon_{\mathrm{Al_2O_3}}|}{|\varepsilon_{\mathrm{ITO}}|} \tag{1.3}$$

where $\varepsilon_{\mathrm{ITO}}$ and $\varepsilon_{\mathrm{Al_2O_3}}$ denote the permittivity of ITO (as TCO-material) and Al_2O_3 (as dielectric material), respectively. It should be noted that at ENZ-condition, the enhancement factor will reach its maximum value due to the negligibly small denominator in Eq. (1.3). Thus, by accumulating free carriers in the TCO-films electrically, we can confine the optical fields within a tightly confined ENZ-region.

By leveraging the ENZ-effect in the MOS-type configuration, several designs have been demonstrated in recent years for integrated and free-space electro-optic modulation [9], [41]–[43]. Though the waveguide-based modulators can attain a large propagation length leading to strong light–TCO interactions at the ultra-thin ACL, the interaction length is quite small for free-space modulators (at the 2–3 nm thick ACL). This results in a weaker electro-optic effect (leading to lesser electro-tunable optical response) for free-space EOMs than that of the waveguide-based devices. Therefore, a promising technique needs to be adopted for free-space modulation of light at a sub-wavelength scale.

To mitigate this issue, the ENZ-materials can be integrated into a resonating nano-structure, which could help in enhancing the light–TCO interactions by confining the electromagnetic fields while operating at the resonant-wavelength. Recently, various designs have been demonstrated for efficient free-space electro-optic modulation by merging the ENZ-effect with either gap-plasmon resonance mode [9] or Huygens resonance modes in dielectric nanostructures [44] or guided-mode resonance (GMR) in grating structures [5], [45].

However, the previously reported nanophotonic free-space EOMs suffer from several limitations, such as low modulation depth, high energy-consumption, incident angle-sensitivity, stringent dependency on polarization state of light, low modulation speed, high-voltage requirement, etc. These fundamental research problems regarding the design and realization of free-space EOM for nanophotonic applications need to be solved.

In this dissertation, the opportunities and challenges towards achieving efficient electro-optic modulation for various nanophotonic applications have been presented by leveraging the ENZ phenomenon of TCOs integrated with several resonating metamaterials.

1.2.2.2. Ultra-Fast All-Optical Intensity Modulation

Over the last few decades, integration of photonics and electronics paved the way towards the realization of high-speed optoelectronic devices [11]. However, due to the involvement of required electronics, the EOMs suffer from limited bandwidth and high power consumption [46]–[49]. Hence, all-optical modulation brings in the possibility to realize ultra-fast and energy-efficient next-generation optical computing systems by overcoming the fundamental limits of electronics [50]–[53]. To achieve ultra-fast control of light, several all-optical modulation schemes have been demonstrated by using nonlinear effects such as Kerr effect, two-photon absorption, etc. [11], [54]. However, the traditional all-optical intensity modulators or switching devices usually require large footprint to accumulate the required refractive index change.

In recent years, plasmonic metamaterial based all-optical modulators have emerged as potential replacements for conventional bulky elements due to their capabilities to confine light beyond the diffraction limit [6]. In this direction, TCOs, operating at the ENZ-regime have gained massive consideration due to their sub-picosecond nonlinear response with large refractive index tuning capabilities [33], [55]. Recently, Boyd *et al.*, demonstrated plasmonic metasurfaces for realizing ultra-fast all-optical switching by incorporating the intraband-transition induced optical nonlinearities in the ENZ-material [56]. On application of a femtosecond laser pump-pulse, optical nonlinearities in the ENZ-material can be seen due to the intraband electronic transition, where the absorbed photon energy leads to a rise in the electron-

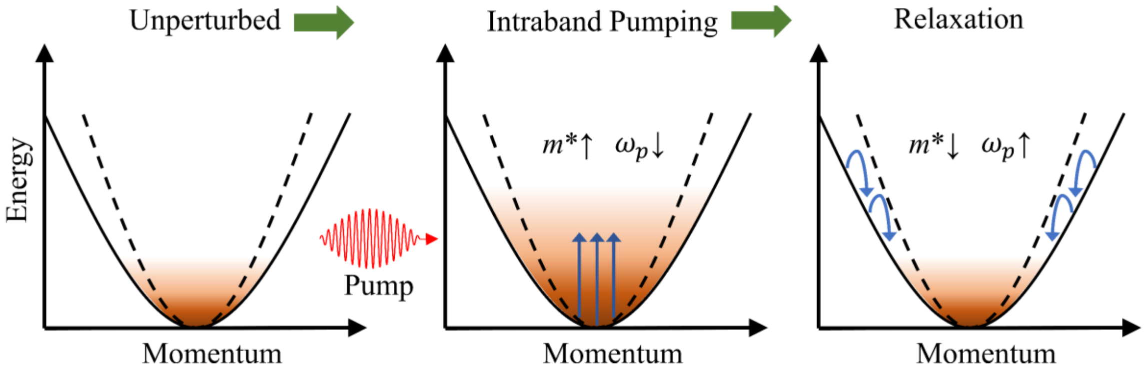

Figure 1.6: Schematic representation of the intraband transitions in the ENZ-material on applying a pump signal depicting the initial unperturbed energy state, intraband transition, and consequent relaxation process of the free electrons in the conduction band. The black dashed line represents the parabolic approximation of the conducting band.

temperature and reallocates the electrons in a non-parabolic conduction band as presented in Figure 1.6.

In other words, the electron effective mass (*m**), which decides the plasma frequency (ω_p), will no longer be constant upon applying pump-signal, rather it will be dependent on the electron temperature [57], [58]. This results in an increase in the electron effective mass and a decrease in the plasma frequency. In the absence of the pump signal, the excited free-electrons undergo relaxation to their original unperturbed condition, causing the *m**, and ω_p to return to their initial steady-state values. Thus, the optical properties of the ENZ-material can be altered by applying an ultra-fast pump-pulse. Moreover, if the ENZ-material is integrated with a resonating nanostructure, the resonance phenomenon can be tuned by leveraging the pump-signal induced optical nonlinearities in the ENZ-medium. This opens a new door to realize all-optical switching at the resonance wavelength.

Based on this astonishing properties, several designs have been demonstrated to realize all-optical modulation of polarization, phase, and amplitude [55], [59]–[63].

However, the state-of-the-art all-optical intensity modulators are either suffering from low modulation depth or high pump-fluence requirement [33], [55]. Thus, the realization of femtosecond all-optical switching with high modulation depth (> 0.8) and low pump-fluence requirement (~ few μJ/cm^2) simultaneously, remains a challenging task. To bridge this gap, in this dissertation, a proper design-strategy based on plasmonic metamaterial has been implemented by leveraging the nonlinear effects of ENZ material.

1.2.2.3. Electro-Optic Polarization Modulation

Until now, various research problems and challenges in realizing an efficient nanophotonic electro-optical or all-optical intensity modulation have been discussed, where the ENZ-effect of TCOs may find potential solutions. Apart from the intensity, different polarization states are also vital electromagnetic properties of light. The polarization state of light is determined by the orientation of its oscillating electric field [64], [65]. Control of polarization states of light is essential for any photonic system.

The polarization-controlling elements are crucial components for many applications, such as optical imaging, optical communication, data transmission, and so on [7], [29], [40], [66], [67]. The most common approach to control light polarization is either by using the Kerr effect or the Faraday effect [68]. These traditional polarization-controlling devices suffer from bulkiness and static operations, *i.e.*, they offer only a fixed degree of polarization control. Though one can utilize acousto-optical or electro-optical effects to realize dynamic polarization-switching components, these devices are not compatible with nanophotonics systems due to their large footprints [69]. On the other hand, metasurface has shown potential towards realizing nanophotonic devices for polarization-control in nanoscale by introducing birefringence and chirality [70]–[74].

To date, many researchers have demonstrated several metasurface-based designs for polarization conversion, which find a wide range of applications, including holographic displays [75], polarization imaging [66], Stokes parameters detection [76], and many more. However, most of these metasurface-based polarization controlling components have typically been limited by passive operation, *i.e.*, a fixed control over the degree of polarization [70]–[74], [77].

Extensive research has been performed in the recent years to demonstrate dynamic control over the polarization state of light by incorporating numerous emerging materials such as phase-change materials, graphene, and so on [78]. However, most of the previously reported metasurface-based active polarization controllers are designed for mainly far-infrared [79], and mid-infrared [80] wavelengths. Active polarization controlling devices at visible and near-infrared wavelengths are essential for quantum and nanophotonic applications.

Recently, a few metasurface-based dynamic polarization modulators have been demonstrated suitable at near-infrared (NIR) wavelengths by leveraging the ENZ-effect [81]. Nevertheless, the previously reported metasurfaces for dynamic polarization conversion come at the costs of low intensity of reflected light and high bias-voltage requirement. Therefore, realization of an effective and energy-efficient active metasurface for polarization modulation remains a great challenge. The ENZ phenomenon can be utilized to enable dynamic polarization rotation with small electrical biasing while maintaining low insertion loss. In this dissertation, the opportunities towards accomplishing a new direction for energy-efficient flat optical components for electro-optic polarization modulation have been presented by leveraging the ENZ phenomenon of TCOs.

1.3. Problem Statements and Objectives

As discussed in the previous section, several fundamental research problems regarding the design and realization of nanophotonic optical modulators still need to be addressed, such as stringent dependency on polarization state of light, incident angle-sensitivity, low modulation depth, high energy-consumption, low modulation speed, high-voltage requirement, *etc.*

The study described in this thesis seeks to achieve five different objectives (listed below) by proposing a few potential solutions to these challenges and limitations (divided into five subproblems) in designing nanophotonic integrated and free-space modulators, by leveraging the ENZ phenomenon of TCOs integrated with different resonating metamaterials.

- **Subproblem I:** Over the last two decades, the most preferable wavelength band for designing EOMs is C-band (1.535 μm – 1.565 μm) due to the revolution of fiber-optic communication systems. In order to modulate optical signal at both the primary telecom wavelength bands, *i.e.*, C-band and O-band (1.26 μm – 1.36 μm), separate components need to be employed in the nanophotonic system. This would translate into a large device footprint and, thus, would increase overall system complexity due to added components. Therefore, it is crucial to investigate the design of a *dual-band* electro-optic modulator, which can operate in both C-band and O-band.

  Objective I: Design of ENZ-Material based Metasurface for ***Dual-band*** Electro-Optic Intensity Modulation.

- **Subproblem II:** Most of the previously reported active nanophotonic EOMs are dependent on polarization states of incident light. This stringent dependency on polarization imposes several limitations on reducing the footprint of a nanophotonic system due to the need for extra polarization-maintaining components. Hence, the research on designing *polarization-insensitive* EOMs with high modulation depth is essential to mitigate the limitation arising from the extra polarization-controlling elements in the nanophotonic systems.

Objective II: Design of ENZ-Material based Metasurface for ***Polarization-insensitive*** Electro-Optic Intensity Modulation.

- **Subproblem III:** The realization of a femtosecond energy-efficient all-optical modulator with high modulation depth and low required pump-fluence simultaneously remains a challenging task. Therefore, the investigation of designing ultra-fast and energy-efficient all-optical switching modulators schemes is crucial for next-generation optical computing systems.

  Objective III: Design of ENZ-material based Nonlinear Metamaterial for Ultra-Fast ***All-Optical Intensity Modulation.***

- **Subproblem IV:** Integrated EOMs are the key elements for an optical communication system and are potential candidates for high bandwidth- and power-hungry interconnects at data center networks. However, the state-of-the-art designs for integrated EOMs either suffer from stringent dependency on polarization state of waveguide modes or suffer from large footprint due to weak electro-optic effect. Therefore, the design of a *dual-polarization integrated* EOM using silicon photonics platform is crucial for the integrated nanophotonic systems.

  Objective IV: Design of ENZ-material based Dual-Polarization ***On-Chip*** Electro-Optic ***Intensity Modulation*** for Integrated Photonics

- **Subproblem V:** Control of polarization states of light is crucial for any photonic system. The conventional polarization-controlling elements are usually bulky **and thus impose limitations to incorporate them into the nanophotonic systems.** Metasurfaces have the potential to realize polarization control in nanoscale. However, most of the metasurface-based polarization controlling components have typically been limited by passive operation, *i.e.*, a fixed control over the degree of polarization. Therefore, the designing of an electro-tunable metasurface for dynamic polarization-switching remains a great challenge.

  Objective V: Design of ENZ-Material based Metasurface for Electro-Optic ***Polarization Modulation*** to realize dynamic control of polarization states of reflected waves

1.4. Research Methodology

This thesis explores designs of various active nanophotonic devices to harness the ENZ effect for optical modulation. Numerous design-strategies have been explored for enabling active control of light–matter interactions at nanoscale. Computational electromagnetics may assist us in solving both straightforward and difficult issues in order to acquire the optical responses of the optical systems. In particular, it is difficult to anticipate the optical response in the case of the multi-layered and patterned nanostructures without executing the numerical computer simulations.

Two essential techniques for full-wave electromagnetic simulations are the finite-difference time-domain (FDTD) approach and the finite element method (FEM). Typically, these solvers divide the domain of the structure into the shape of a grid (or mesh) in order to solve Maxwell's equations. Extensive simulations can be conducted using commercially available simulation tools such as Lumerical FDTD®, CST Microwave Studio®, and COMSOL Multiphysics®.

To understand the electrical properties of the TCOs upon applying external bias-voltage, a set of electrostatic simulations needs to be carried out, where the spatial distribution of the free-carrier concentration inside the TCO-layer can be calculated when configured as MOS-type structure. This can be done by using Lumerical Device (Charge) solver. The electrostatic simulations can give us the variation of the free-carrier concentration of the TCO-layer, which can be incorporated into the Drude model to obtain the optical properties of the layer. To theoretically analyze the optical properties of the proposed nanophotonic devices, several analytical approaches along with the numerical simulations have been used.

To estimate the resonance wavelengths of gap-plasmon supporting structures in metal–insulator–metal configuration, the RLC-equivalent circuit modeling can be easily deployed after calculating the corresponding value of the lumped elements: resistance (R), capacitance (C), and inductance (L). In this theoretical modeling, the unit-cell or meta-atom of the proposed structure can be assumed as an equivalent RLC-circuit. It should be noted that a close-match between the theoretically estimated resonant wavelength with that of numerically simulated data could validate the findings.

Effective medium theory (EMT) may be used to define the macroscopic characteristics of a composite medium in the theoretical modeling of designed nanostructures. Using this method based on the relative volume fractions and permittivity of two separate media, one may determine the effective permittivity of a homogenized medium. This approach may potentially be used to mimic any patterned structure at the sub-wavelength scale and could provide a pretty realistic approximation.

In the case of the guided-mode-resonance based structures, a semi-analytical method can be adopted by combining the EMT-approximation with modal analysis. In this approach, the dielectric sub-wavelength grating can be modeled as an effective medium with a uniform permittivity. Then, by using modal analysis in the Lumerical Mode solver, the effective refractive index of the guided-modes can be calculated. It should be noted that the resonance wavelength can be predicted for those wavelengths that satisfy the grating equation.

To understand the optical response of the magnetic-plasmon-resonance based structure, the EMT-approximation can be adopted by considering the metamaterial as an inhomogeneous two-port network. Then, the S-parameters can be incorporated into the EMT-modelling, which can accurately predict the effective permittivity of the whole metamaterial structure. In other words, by using this approach, one can replace the multi-layered inhomogeneous metamaterial structure by a homogeneous layer of an effective medium with uniform permittivity, which mimics the optical properties of the whole structure. The choice of design parameters is typically not simple and involves careful consideration of the device's dimensions. To cut down on the total cost and production time, it is ideal to minimize the thickness of each material. Keeping all other parameters constant, a parametric sweep may be performed to determine the ideal geometrical parameters (such as width and thickness) of each layer.

1.5. Major Contribution of this Thesis

We adopted several innovative approaches to design electro-tunable metamaterials for optical modulation with high modulation depth and low energy-consumption by exploiting ENZ phenomenon of TCOs.

i. By leveraging the ENZ effect in TCOs along with gap-plasmon resonance of metal–insulator–metal structure, a novel plasmonic electro-tunable metamaterial absorber is designed that can be used to simultaneously modulate the amplitude of reflected light at both O-band and C-band wavelengths.

ii. By harnessing the ENZ phenomenon of TCOs combined with guided-mode resonance of grating waveguide, a dual-band electro-tunable metamaterial has been presented that can be used for optical intensity modulation as well as narrowband tunable optical filtering purposes.

iii. Two innovative approaches have been adopted based on ENZ-effect to design polarization-insensitive metamaterials for free-space electro-optic modulation, which can mitigate the limitation arising from the requirement of extra polarization-controlling elements in the nanophotonic systems.

a. The plasmonic metasurface based polarization-insensitive, reflection-type design can be operated with a wide variation of incident angle — indicating the angle-insensitivity of the device.

b. The guided-mode resonance based all-dielectric polarization-insensitive modulator can operate in both transmission and reflection modes, *i.e.*, supports dual-mode of operation.

iv. A novel electro-tunable metasurface has been introduced to enable dynamic control of polarization states of reflected light by leveraging the electro-optic properties of the ENZ materials. The designed metasurface can dynamically switch among the three linear polarization states of the reflected wave upon applying external electrical biasing, allowing a tri-state polarization modulation.

v. A novel dual-polarization electro-absorption modulator has been designed for integrated photonic systems. The device has been designed by leveraging hybrid integration of ENZ-material in a standard silicon waveguide. The presented modulator may help reducing the footprint of integrated photonic systems by eliminating extra polarization controlling devices.

vi. To enable ultra-fast all-optical switching using nonlinear phenomena in ENZ-material, a novel magnetic plasmon based energy-efficient metamaterial has been proposed which can operate with ultra-fast response time in subpicosecond scale.

vii. Our comprehensive theoretical modeling framework based on effective medium theory and RLC-circuit model can be extended to accurately predict the spectral characteristics of any guided-mode resonance and gap-plasmon based nanostructures.

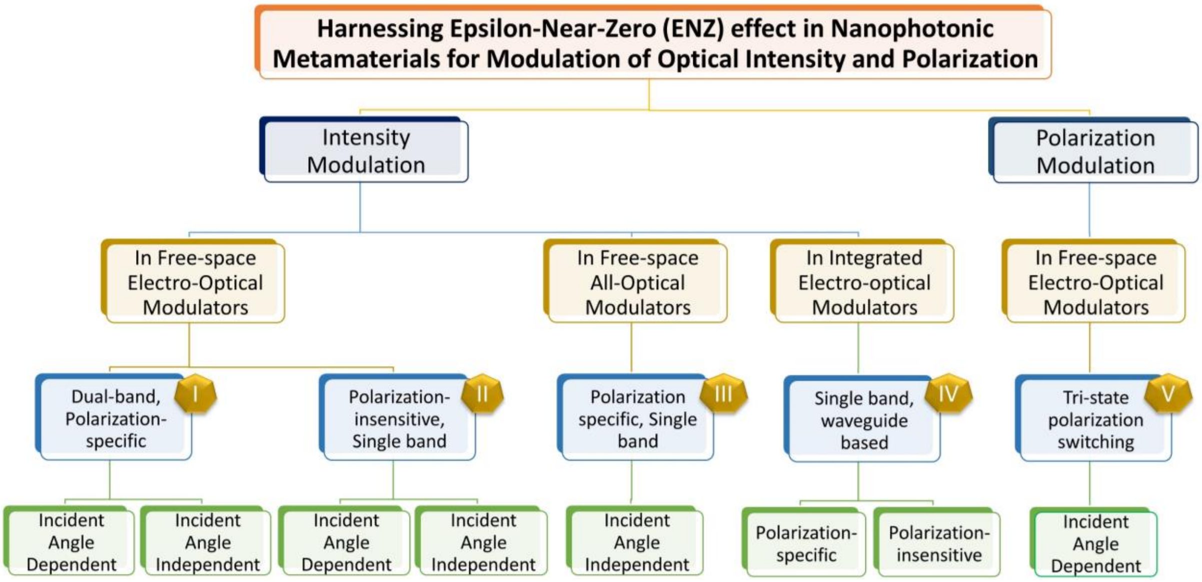

Figure 1.7: Thesis flow at a glance. Note that the five different objectives proposed in this thesis work have been represented as roman-numbering format from I to V.

1.6. Thesis Outline

The scope of this thesis work can be broadly categorized into two sections, as represented in. The "intensity modulation" section covers distinct strategies to enable optical intensity modulation using ENZ-material. This section is further categorized into three sub-sections *viz.* "free-space EOMs", "free-space AOMs", and "integrated EOMs". The electro-optic properties of ENZ-material is utilized for realizing the free-space and integrated EOMs. On the other hand, the nonlinear phenomenon of ENZ-materials is leveraged for realizing the all-optical modulators (AOMs). The objectives proposed in this dissertation have been marked in roman-numbering format, as denoted in Figure 1.7.

In the sub-section of free-space EOMs, the first two research objectives are covered by integrating the ENZ-materials into various resonating metamaterials. Then, the third objective of designing femtosecond all-optical intensity modulator has been covered. The sub-section classified as integrated EOMs covers the fourth objective of designing on-chip modulators for integrated photonic system. Finally, the fifth objective of electro-tunable polarization switching is covered in the free-space polarization modulation section.

The thesis work has been sub-divided into eight chapters. The thesis chapters are organized as follows:

Chapter 1 gives an overview of the thesis work. This chapter includes a brief introduction to the broad field of nanophotonics and metamaterials, research motivation, methodology, problem statements, identified research gaps and objectives, summarizes the major contribution of this thesis, and presents the thesis organization.

Chapter 2 introduces the broad field of nanophotonics and metamaterials. This chapter also introduces the emerging epsilon-near-zero (ENZ) materials and their capability in active control of light–matter interactions, followed by a literature review on ENZ-material based nanophotonic meta-devices for modulation of optical intensity, phase, and polarization. Further, this chapter discusses relevant theoretical background and numerical techniques adopted during the research work.

Chapter 3 discusses ENZ-material based dual-band free-space electro-optic intensity modulation at both the primary telecommunication wavelength bands, *i.e.*, C-band and O-band with high modulation depth. Two innovative approaches have been adopted for enabling dual-band free-space electro-optic intensity modulation.

First, a unique design of dual-band electro-tunable metasurface has been presented by leveraging the ENZ phenomenon of TCOs combined with guided-mode resonance effect of grating waveguides. Effective medium theory combined with a modal analysis is used to study the resonance dips in the optical reflectance spectrum. Then, by combining ENZ effect with gap-plasmon resonance mode, an electro-tunable metamaterial absorber has been introduced for dual-band optical intensity modulation with wide incident angle-insensitivity for *x*-polarized light.

Chapter 4 investigates ENZ-material based different approaches to realize polarization-insensitive electro-tunable metasurfaces for free-space optical intensity modulation.

The first section presents a guided-mode resonance based all-dielectric modulator that can operate in both transmission and reflection modes, *i.e.*, dual-mode of operation, under the influence of random polarization angle of normally incident light. Then, in the next section, a novel design of GPR based electro-tunable metasurface has been discussed for polarization- and angle-insensitive optical intensity modulation.

Chapter 5 presents the investigation of ultra-fast all-optical intensity modulation based on nonlinear phenomena in ENZ materials. To enable ultra-fast all-optical intensity modulation, a novel magnetic-plasmon-resonance based metamaterial has been designed by integrating an ENZ-material. The intra-band transition-induced optical nonlinearities in the ENZ-medium lead to a high modulation depth at the telecom wavelength with ultrafast response time in subpicosecond scale. Effective medium theory has been explored to study the nonlinear behavior of the device.

Chapter 6 deals with the realization of ENZ-material based integrated electro-optic intensity modulation. Two different directional coupler based devices have been explored for intensity modulation based on the hybrid integration of ENZ-material in a standard silicon waveguide by utilizing the silicon photonics platform.

First, an energy-efficient design has been presented that can modulate only the TM mode of the input waveguide. Then, a parallel directional coupler based dual-polarization design has been discussed for modulating both TM and TE modes of the input waveguide. This may help in reducing footprint of the integrated photonic systems by eliminating the requirements of extra polarization controlling devices.

Chapter 7 presents the realization of an ENZ-material based nanophotonic device to enable free-space electro-optic polarization modulation of reflected light. In unbiased condition, excitation of gap-plasmon resonance in the metasurface leads to rotation of *x*-polarized incident light to orthogonally polarized reflected light (*i.e.*, *y*-polarized) at 1.55 μm. With an *x*-polarized incident wave, the reflected light from the metasurface can be dynamically switched among the three linear polarization states of the reflected wave, allowing a tri-state polarization switching (*viz. y*-polarization at 0 V, –45° linear polarizations at 2 V, and *x*-polarization at 5 V). The Stokes parameters are also calculated to show real-time control over polarization states of reflected light.

Chapter 8 summarizes the thesis work highlighting major findings and contributions in the design of ENZ material based nanophotonic devices for optical intensity and polarization modulation. This chapter also presents potential directions for future research.

2

Theoretical Background and Literature Review

Contents

This chapter first provides a quick overview of the developing field of nanophotonics. Then, the relevant theoretical background, a review of the literature and analytical methodologies are discussed that are needed for conducting research in the emerging field of metamaterial based active nanophotonic devices. In the beginning of the section for theoretical background, a brief overview of relevant electromagnetic theory, starting from the Maxwell's equation to the boundary conditions and wave equation, is presented. Next, a discussion on the polarization optics is provided. To approximate the relative permittivity of the metals and TCOs, Drude model is then deployed. Then, an elaborate discussion is provided to introduce the electro-optic properties of the ENZ-materials, followed by a literature survey on ENZ-material based electro-tunable metamaterials for the free-space applications. After that, a quick overview is presented on the ENZ-material based on-chip integrated electro-optic modulators. In what follows, a literature survey on the emergence of the ultra-fast all-optical switching using ENZ-material is presented. Finally, several relevant theoretical and analytical techniques are discussed that can be adopted to study the optical responses of different metamaterial-inspired nanophotonic devices.

2.1. Nanophotonics and Metamaterials: An Overview

As mentioned in the previous Chapter, the field of nanophotonics has the potential to support extremely high operating speeds with minimal device dimensions by overcoming the limitations of both semiconductor electronics and dielectric photonics. Plasmonics, a sub-field of nanophotonics, uses optical properties of metallic nanostructures to manipulate light–matter interactions at the sub-wavelength scale [2]. Since the pioneering research works carried out by G. Mie in 1908 to describe optical scattering phenomena of small colloidal particles and R. Ritchie in 1957 to investigate the plasma losses in thin films, the research field to study the electromagnetic effects at metal–dielectric interfaces had been widely recognized [1]. In 1980s, researchers observed the propagation of light waves is possible at the metal–dielectric interface due to the resonant interaction of light waves with the free electrons at the metal surface. This phenomenon has been termed as ‘plasmonics’, named after the quantum of electron oscillations called plasmon [1], [2]. The promise of plasmonics is to ensure a minimal device dimension by breaking the diffraction limit of light [2], [67], [82]–[88].

In the same direction, metamaterial or artificially engineered materials have found potential applications by breaking the limitations of natural materials that typically restrict the researchers from attaining a desired optical response, as discussed in the previous Chapter. In 2000, Smith *et al.* coined the term ‘metamaterial’ as a structured material inspired from the Greek word ‘meta’, which means ‘beyond’ [89]. As the name suggests, metamaterials can exhibit unusual electromagnetic properties, depending upon structural units, which cannot be observed in naturally available materials [4].

A broad categorization of materials on the basis of their intrinsic properties is presented in Figure 2.1(a). The naturally existing dielectrics and metals are presented in first and second quadrants, respectively. On the other hand, two different special cases

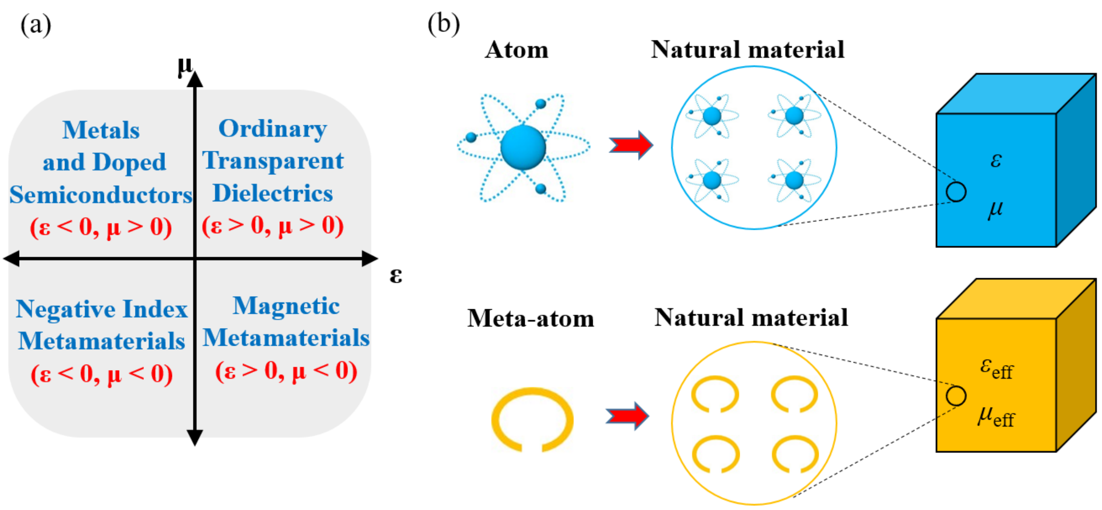

Figure 2.1: (a) Broad classification of materials based on the real parts of permittivity and permeability [3], (b) Pictorial representation for comparison between natural materials and metamaterials.

of the metamaterials can be seen in third and fourth quadrants [3]. As represented in Figure 2.1(b), an atom defines the optical properties of a natural material. In contrast, the optical properties of metamaterials, and their two-dimensional counterparts known as metasurfaces, are decided by their unit cells or 'meta-atoms', which are sub-wavelength in scale [3]. This gives a lot of freedom to the engineers to customize the optical transmittance, reflectance, and absorption [80], [82], [90]–[122].

Recent technological advancements in both experimental and computational methods in the field of nanophotonics have paved the way toward the realization of active metamaterial and plasmonic based devices for controlling light–matter interactions at the nanoscale [4]. Over the years, several metamaterials have been included as integral parts of plasmonic nanostructures, such as cut wire antennas, split-ring resonators, and so on [1]. The all-dielectric metamaterials have also been implemented to get over the optical losses for metallic structures [106]. Due to their exceptional abilities to control light–matter interactions at the sub-wavelength scale, metamaterials have gained enormous attention for the realization of flat optical components such as multifunctional meta-lens [7], hyperspectral imaging [8], electro-optic modulators [9], optical sensors, filters [10], and so on. Thus, plasmonics and metamaterials have accelerated the pathway to realize next-generation optical components for nanophotonic system.

2.2. Relevant Theoretical Background

After the myriad of research carried out for fundamental reasons behind the source of electromagnetic field, and the relationship between electric and magnetic fields by pioneer scientists Ampere, Coulomb, Faraday and Gauss, the revolution in the electromagnetic fields happened when James Clerk Maxwell proposed a set of fundamental equations in 1865. This is arguably one of the most crucial scientific contributions in the field of physics and modern science in 19th century [64].

2.2.1. Maxwell's Equations

The Maxwell's equations are valid for both static and dynamic electromagnetic fields in a medium. Over several decades, Maxwell's equations have been extensively used to investigate the light–matter interactions over the whole electromagnetic spectrum. However, these equations are relevant for the classical domain and have limitations in predicting the quantum phenomena. The set of equations determining the relationship between electric field (**E**), magnetic field (**H**), electric displacement (**D**), and magnetic flux density (**B**), are given by [64]:

Gauss's law
$$\nabla . \mathbf{D} = \rho_v \tag{2.1}$$

Gauss's law for magnetism
$$\nabla . \mathbf{B} = 0 \tag{2.2}$$

Maxwell–Faraday equation
$$\nabla \times \mathbf{E} = -\frac{\partial \mathbf{B}}{\partial t} \tag{2.3}$$

Ampere's circuit law with Maxwell's modification
$$\nabla \times \mathbf{H} = \frac{\partial \mathbf{D}}{\partial t} + \mathbf{J} \tag{2.4}$$

where, ρ_v is the volume charge density and $\mathbf{J}$ is the electric current density. The Maxwell's equations are enough for describing the electric and magnetic field distributions in both time and space.

These macroscopic equations discard the fundamental interactions between charged particles and electromagnetic fields while considering a microstructure. Thus, the material intrinsic properties need to be further linked to the above macroscopic equations. The relationship between electric field **E** and electric flux density **D** in a medium depends on polarization **P**, the macroscopic sum of the electric dipole moments induced by electric field. Analogously, the relationship between magnetic field **H** and magnetic flux density **B** depends on the magnetic property of a medium magnetization **M**. The material dependency of the electric and magnetic fields can be given by:

$$\mathbf{D} = \varepsilon_0 \mathbf{E} + \mathbf{P} \tag{2.5}$$

$$\mathbf{B} = \mu_0 \mathbf{H} + \mu_0 \mathbf{M} \tag{2.6}$$

where, the constants $\varepsilon_0 \approx 8.854 \times 10^{-9}$ F/m and $\mu_0 \approx 4\pi \times 10^{-7}$ H/m are the vacuum dielectric permittivity and magnetic permeability, respectively. The magnetization, **M,** can be ignored for nonmagnetic media. Moreover, in the case of vacuum, there is no polarization, **P**, which leads to the above two equations as $\mathbf{D} = \varepsilon_0\mathbf{E}$ and $\mathbf{B} = \mu_0\mathbf{H}$.

Finally, if we limit the discussion by considering the media as linear, homogeneous, non-magnetic and isotropic, then, the polarization **P** can be written as:

$$\mathbf{P} = \varepsilon_0 \chi \mathbf{E} \tag{2.7}$$

Thus,

$$\mathbf{D} = \varepsilon_0 (1 + \chi) \mathbf{E} = \varepsilon_0 \varepsilon_r \mathbf{E} \tag{2.8}$$

where, χ is the electric susceptibility and is related to relative permittivity ε_r.

2.2.2. Wave Equation and Boundary Condition

Each scalar component of electric and magnetic field must need to satisfy the wave equation, obtained from the Maxwell's equations, and is given by:

$$\nabla^2 \mathbf{E} = \mu_0 \varepsilon_0 \, \varepsilon_r \frac{\partial^2 \mathbf{E}}{\partial t^2} \tag{2.9}$$

$$\nabla^2 \mathbf{H} = \mu_0 \varepsilon_0 \, \varepsilon_r \frac{\partial^2 \mathbf{H}}{\partial t^2} \tag{2.10}$$

The electric or magnetic field for a given region may be obtained by solving one of these wave equations, while Maxwell's equations can be used to determine the other. When employing frequency domain solvers, the time dependence can be assumed to be harmonic, where $\partial/\partial t \rightarrow i\omega$. The wave equation then can be called as Helmholtz equation. The time domain solvers, on the other hand, make use of Maxwell's curl equations. In case of waveguides, the solutions of wave equations determine the guided modes field distributions. The wave equations, for instance the Eq.(2.9), can be further simplified as:

$$\nabla^2\mathbf{E} = \frac{1}{c^2}\,\varepsilon_r\,\frac{\partial^2\mathbf{E}}{\partial t^2} \tag{2.11}$$

where, $c = \sqrt{1/\mu_0\varepsilon_0}$ is the speed of light in vacuum. Furthermore, the refractive index, n, of a given non-magnetic medium can be defined as the ratio of the speed of light in the vacuum to that in the medium, and can be written as:

$$n = \frac{c}{v} = \sqrt{\frac{\mu_0\varepsilon_0\,\varepsilon_r}{\mu_0\varepsilon_0}} = \sqrt{\varepsilon_r} \tag{2.12}$$

In most practical scenarios, it is essential to solve the equations for electromagnetic wave propagation over different mediums. One way to solve electromagnetic problems is to find the solution of Maxwell's equations in a finite region of interest with appropriate boundary conditions at the interface of two different media. By applying Gauss' and Stokes' theorem with the presence of surface charge density (ρ_s) and surface current density (J_s), the boundary conditions at the interface of two different media (1 and 2) can be shown as [123]:

$$D_{1n} - D_{2n} = \rho_s \tag{2.13}$$

$$B_{1n} - B_{2n} = 0 \tag{2.14}$$

$$E_{1t} - E_{2t} = 0 \tag{2.15}$$

$$H_{1t} - H_{2t} = J_s \tag{2.16}$$

where, suffix ‘t’ and ‘n’ denotes tangential and normal components of corresponding vector fields, respectively.

2.2.3. Metals and Linear Dispersive Media

The optical properties of metals may be described by a plasma model across a large frequency range, in which a fixed background of positive ion cores is accompanied by a gas of free electrons with number density N. The lattice potential and electron–electron interactions are not taken into consideration in the plasma model. Rather, the model considers a simplistic assumption such that each electron's effective mass (m) comprises certain characteristics of the band structure. When an electromagnetic field is applied, the electrons exhibit damped oscillations with a typical collision frequency of $\Gamma = 1/\tau$. The relaxation time of the free electron gas, denoted by τ, is usually around 10^{-14} s at ambient temperature, corresponds to $\Gamma = 100$ THz.

The equation of motion for electron gas with an external time harmonic electric field $\mathbf{E} = \mathbf{E}_0 \exp(-i\omega t)$ can be given as [124]:

$$m\frac{d^2\mathbf{r}}{dt^2} + m\Gamma\frac{d\mathbf{r}}{dt} = -e\mathbf{E} \tag{2.17}$$

where, Γ is the collision frequency, e and m are the charge and effective mass of electron, respectively. The displacement $\mathbf{r}$ due to the oscillation, can be given by:

$$\mathbf{r} = \frac{e}{m}\frac{\mathbf{E}}{(\omega^2 + i\Gamma\omega)} \tag{2.18}$$

The resultant macroscopic polarization ($\mathbf{P}$) due to this displacement, can be given as:

$$\mathbf{P} = -eN\mathbf{r} = \frac{-\mathrm{N}e^2}{m(\omega^2 + i\Gamma\omega)}\mathbf{E} \tag{2.19}$$

where, N is the free electron density. Thus, the constitutive relationship in Eq.(2.5), can be written as:

$$\mathbf{D} = \varepsilon_0 \left(1 - \frac{Ne^2}{\varepsilon_0 m} \frac{1}{(\omega^2 + i\Gamma\omega)}\right) \mathbf{E} = \varepsilon_0 \left(1 - \frac{\omega_p^2}{(\omega^2 + i\Gamma\omega)}\right) \mathbf{E} \qquad (2.20)$$

where, $\omega_\mathrm{p} = \sqrt{N\mathrm{e}^2/m\varepsilon_0}$ is the plasma frequency of the free electron gas.

This plasma model is also known as Drude model for metals. We can obtain frequency dependent Drude permittivity as:

$$\varepsilon(\omega) = \left(1 - \frac{\omega_\mathrm{p}^2}{(\omega^2 + i\Gamma\omega)}\right) \qquad (2.21)$$

It should be noted that in this free-electron model, we assume $\varepsilon \to 1$, for $\omega >> \omega_\mathrm{p}$. However, this model needs to be expanded in the case of $\omega > \omega_\mathrm{p}$ for noble metals such as gold and silver, where the existence of a positive background of the ion cores leads to a residual polarization. This residual polarization can be described by adding the expression, $\mathbf{P}_\infty = \varepsilon_0 (\varepsilon_\infty - 1) \mathbf{E}$, to the Eq.(2.5), where **P** now signifies polarization solely owing to free electrons. This phenomenon can be described by a dielectric constant ε_∞, which is usually ranging between 1 and 10. In that case, modified Drude permittivity can be given as:

$$\varepsilon(\omega) = \left(\varepsilon_\infty - \frac{\omega_p^2}{(\omega^2 + i\Gamma\omega)}\right) \qquad (2.22)$$

The validity limits for the Drude permittivity model are defined by comparing the real and imaginary parts of $\varepsilon(\omega)$ with the experimental data measured by Johnson and Christy for noble metals such as, silver and gold [125], as presented in Figure 2.2.

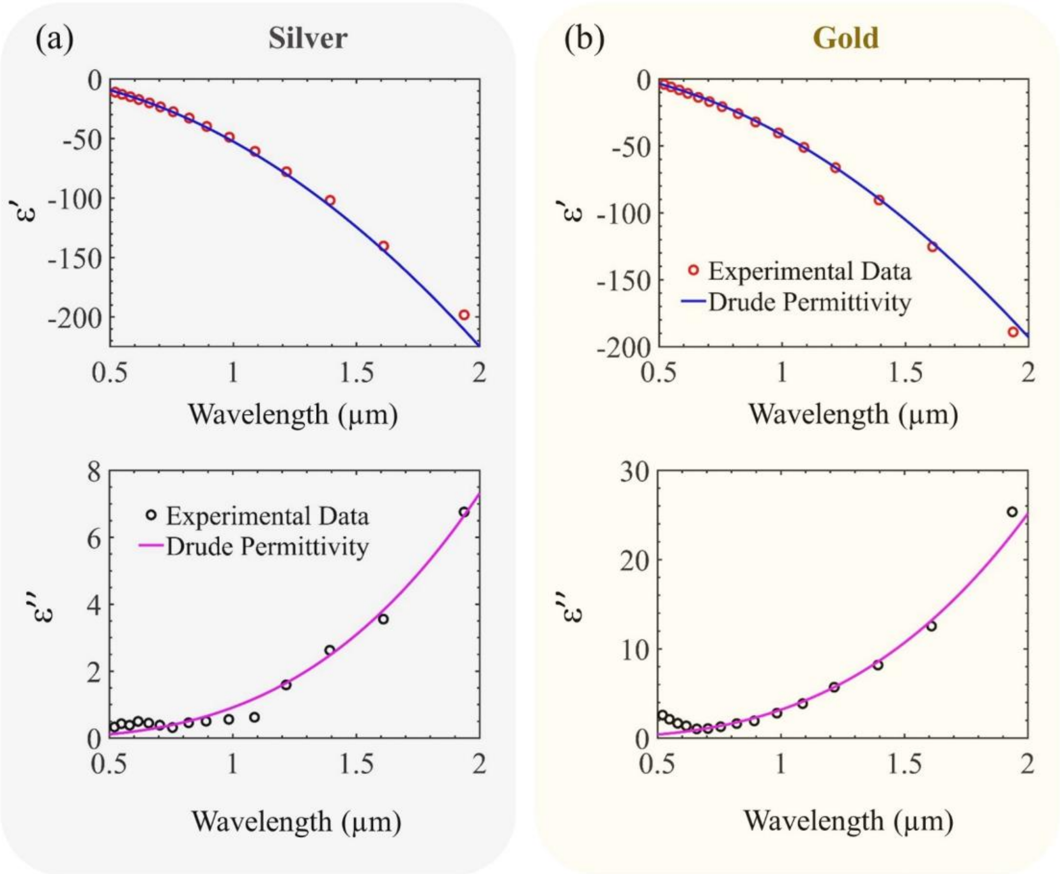

Figure 2.2: Validation of the Drude model. The real ε' and the imaginary ε'' parts of the permittivity, as a function of wavelength, for (a) silver and (b) gold. The experimental data (represented by circles) are taken from the ref. [125] measured by Johnson and Christy. To fit the Drude permittivity functions (denoted by solid lines), as per Eq.(2.22), the parameters are taken for silver as $\varepsilon_\infty = 5$, $\omega_p = 1.43 \times 10^{16}$ rad/s, and $\Gamma = 0.3 \times 10^{14}$ rad/s; and for gold as $\varepsilon_\infty = 9.5$, $\omega_p = 1.35 \times 10^{16}$ rad/s, and $\Gamma = 1.169 \times 10^{14}$ rad/s.

The complex permittivity of the material can be further linked to the refractive index as $n = \; n' + in'' = \sqrt{\varepsilon} = \sqrt{\varepsilon' + i\varepsilon''}$. Thus, we can get

$$\varepsilon'(\omega) = \left(n'(\omega)\right)^2 - \left(n''(\omega)\right)^2 \;, \qquad \varepsilon''(\omega) = 2n'(\omega)n''(\omega) \qquad (2.23)$$

where, $\varepsilon'(\omega)$ and $\varepsilon''(\omega)$ are the real and imaginary parts of the permittivity. The real part of the refractive index, $n'(\omega)$, is responsible for the dispersion in the material, whereas the imaginary part, $n''(\omega)$, decides the absorption in the medium.

2.3. Properties of Light while Travelling through Different Materials

The thesis work focuses on the active control of the electromagnetic properties of light, *viz.* intensity, phase, and polarization, by using the ENZ effect of TCOs. This subsection briefly describes some fundamentals that define these electromagnetic properties of light while travelling in different media. If light travels within a medium in z-direction with an angular frequency ω, we can define the electric field vector as

$$\mathbf{E}\,(z,t) = \mathfrak{Re}\{\mathbf{E_0} \exp\left[-i(kz-\omega t)\right]\} \tag{2.24}$$

where, k is the propagation constant and $\mathbf{E_0}$ is the complex envelope of the electric field that is related to the amplitude, and hence intensity of light.

The objectives I to IV of the thesis work, as mentioned in the previous Chapter, revolve around various design strategies of nanophotonic devices to dynamically control the intensity of light (in terms of reflectance and transmittance) by leveraging ENZ effect of TCOs. Thus, this section first introduces the intensity of light within a medium, followed by the variation in intensity at the interface of two different media. Finally, the polarization state of light and the corresponding phases, which are related to the Objective V of the thesis, will be discussed.

2.3.1. Intensity of Light within a Lossy Material

As the light travels through a lossy medium, it experiences attenuation due to absorption if the material refractive index is a complex quantity. Thus, the propagation constant is also be a complex quantity and can be described as $k = \beta - i\alpha/2$. The real part of the refractive index, n', and the imaginary part, n'', of the refractive index of the medium are related to the complex propagation constant as $\beta = k_0 n'$ and $\alpha = -2k_0 n''$, where k_0 is the propagation constant in vacuum.

Thus, the Eq.(2.24) can be further expressed as:

$$\mathbf{E}\,(z,t) = \mathfrak{Re}\{\mathbf{E_0}\, \exp\,[-\alpha z/2] \exp\,[-i(\beta z - \omega t)]\} \qquad (2.25)$$

The amplitude of the light decays exponentially as it propagates along the z direction. The real part of propagation constant describes the propagation characteristics such as phase velocity, $v = \omega/\beta$. Thus, the parameter β is known as phase constant. Whereas, the imaginary part of k is responsible for attenuation along the z direction. The intensity of light (**I**) is proportional to the $|\mathbf{E}\,|^2$, which leads to $\mathbf{I} \propto |\mathbf{E_0}\exp\,[-\,\alpha z/2]|^2 \approx \mathbf{E}_0^2\exp\,[-\alpha z]$. Thus, the parameter α is known as absorption coefficient (also known as attenuation coefficient). It should be noted that when the medium has a negligible imaginary part of the permittivity, such as glass or SiO_2, then the attenuation of light is also insignificant, and the medium can be referred to as a lossless medium.

2.3.2. Intensity of Light at the Interface of Two Media

When light strikes the interface between two media with different refractive index, it may be reflected back to the first medium or transmitted to the second medium depending on the refractive indices of the two media. The angle of reflection will be same as the angle of incidence. Whereas, the angle of transmission or refraction will depend on the refractive index of the second medium. If the light is travelling through a medium with refractive index n_i and striking an interface of second medium with an angle θ_i, then as per Snell's law, $n_i\sin\theta_i = n_t\sin\theta_t$, where θ_t and n_t are the angle of transmission and refractive index of the second medium, respectively. As the light crosses the boundary of two different materials, the θ_t will be either greater than or smaller than the θ_i depending on the refractive index of each material.

In describing the reflection and refraction when light strikes the interface between two media, the plane of incidence is very crucial, which is defined by the plane

Table 2.1: The reflection coefficient, *r*, and transmission coefficient, *t*, as per Fresnel equations

Light Polarization	For Oblique incidence	For Normal incidence
TE polarized	$r_{\perp} = \dfrac{n_i \cos\theta_i - n_t \cos\theta_t}{n_i \cos\theta_i + n_t \cos\theta_t}$	$r_{\perp} = \dfrac{n_i - n_t}{n_i + n_t}$
	$t_{\perp} = \dfrac{2n_i \cos\theta_i}{n_i \cos\theta_i + n_t \cos\theta_t}$	$t_{\perp} = \dfrac{2n_i}{n_i + n_t}$
TM polarized	$r_{\parallel} = \dfrac{n_i \cos\theta_t - n_t \cos\theta_i}{n_i \cos\theta_t + n_t \cos\theta_i}$	$r_{\parallel} = \dfrac{n_i - n_t}{n_i + n_t} = r_{\perp}$
	$t_{\parallel} = \dfrac{2n_i \cos\theta_i}{n_i \cos\theta_t + n_t \cos\theta_i}$	$t_{\parallel} = \dfrac{2n_i}{n_i + n_t} = t_{\perp}$

that contains the propagation vector and the surface normal. If the direction of the electric field is perpendicular to the plane of incidence, then the light is said to be perpendicularly polarized or TE polarized. Similarly, the parallel or TM polarized light means the orientation of electric field is parallel to the plane of incidence. Both of these conditions are special cases of linear polarized light, as will be described in next subsection. To know the intensity of light after reflection and refraction or transmission, the Fresnel equations may be employed, where the reflection coefficient, *r*, and transmission coefficient, *t*, are defined as per Table 2.1.

For TE polarized light, the reflection coefficient and transmission coefficients are defined as $r_{\perp}$ and $t_{\perp}$, respectively. Similarly, for TM polarized light, the coefficients are defined as $r_{\parallel}$ and $t_{\parallel}$, respectively. Moreover, if we consider a normal incidence where

$\theta_i = 0$, we have $r_\perp = r_\parallel$ and $t_\perp = t_\parallel$. The transmittance (T) and reflectance (R), which measure the intensity of the transmitted and reflected light, can be attained using $T = |t|^2(n_t\cos\theta_t/n_i\cos\theta_i)$ and $R = |r|^2$, respectively. The absorbance (A) can also be calculated as $A = 1 - R - T$.

2.3.3. Polarization State of Light and Corresponding Phase

Polarization is an important characteristic of light, which is described by the orientation of oscillating electric field vector as function of time at a given point in space. Based on the geometrical shape traced by the tip of electric field vector, polarization of light can be classified as linearly or circularly or elliptically polarized. If a monochromatic light travels in z direction with an angular frequency ω, we can determine the polarization state of the light by tracing the endpoint of electric field vector, $\mathbf{E}\,(z,t)$, as a function of time at each position of z.

The electric field, $\mathbf{E}\,(z,t)$, can be expressed by the Eq.(2.24), where $\mathbf{E_0}$ is the complex envelope of the electric field composed of two complex components, E_x and E_y. Expressing each term with corresponding magnitude and phase, such that $E_x = E_{x0}\exp(i\varphi_x)$ and $E_y = E_{y0}\exp(i\varphi_y)$, we get:

$$\mathbf{E}\,(z,t) = E_x\hat{x} + E_y\,\hat{y} \tag{2.26}$$

where

$$E_x = E_{x0}\cos(\omega t - kz + \varphi_x) \tag{2.26.i}$$

$$E_y = E_{y0}\cos(\omega t - kz + \varphi_y) \tag{2.26.ii}$$

Here, E_{x0}, E_{y0} are the magnitudes, and φ_x, φ_y are the corresponding phases of E_x and E_y components, respectively.

The two equations, Eq.(2.26) and (2.26), can be described as parametric equations of ellipse

$$\frac{E_x^2}{E_{x0}^2} + \frac{E_y^2}{E_{y0}^2} - 2\cos\left(\frac{E_x E_y}{E_{x0} E_{y0}}\right) = \sin^2\varphi \qquad (2.27)$$

For a fixed value of z, the polarization ellipse can be defined by tracing out the tip of the electric field vector that periodically rotates in the x-y plane. The phase difference (φ) and complex-envelope (R**)** are two determining factors while describing polarization ellipse to find out the polarization state of light and can be written as:

$$\varphi = \varphi_y - \varphi_x = \arg\{E_y\} - \arg\{E_x\} \qquad (2.28)$$

and,

$$R = \frac{E_{y0}}{E_{x0}} = \frac{|E_y|}{|E_x|} \qquad (2.29)$$

When the polarization ellipse reduces to a straight line, it is referred to as linearly polarized (LP) light. In other words, if the geometrical shape traced by the tip of the instantaneous electric field vector is a straight line, it is called linearly polarized light. On the other hand, if the geometrical shape is a circle, then it is referred to as circularly polarized (CP) light. If the electric field rotates in a clockwise direction, it is called as right circularly polarized when observed from the direction toward which the light is approaching. Similarly, a counter clockwise rotation of electric field indicates the left circularly polarized light. In all other conditions, the light can be called as elliptically polarized (EP) light.

Table 2.2: Examples of different polarization states of light

Complex-envelope (R)	Phase difference (φ)		Polarization states
$R = 0$ or ∞	Any arbitrary value		Linearly polarized with parallel or perpendicular polarization
$R = 1$	$\varphi = 2m\pi$, where m is an integer		Linearly polarized with $\pm 45^0$ polarization angle
$R \neq 1$	$\varphi = 2m\pi$, where m is an integer		Linearly polarized with an arbitrary polarization angle
$R = 1$	$\varphi = (2m+1)\ \pi/2$	when m is a positive integer	Right circularly polarized
		when m is a negative integer	Left circularly polarized
$R \neq 1$ or 0	$\varphi \neq 2m\pi$	when m is a positive integer	Right elliptically polarized
		when m is a negative integer	Left elliptically polarized

Stokes Parameters

There are certain limitations on polarization ellipses as they are applicable when we consider completely polarized light beams. Polarization ellipse is not appropriate for the incoherent or unpolarized or partially polarized light. Moreover, the two real quantities, R and φ, can describe only the polarization state of light, and they do not contain any information about the intensity of the light. Therefore, it is desirable to describe polarization state of light in terms of measurable quantities which contain such information. The representation via Stokes parameters contains such information.

In 1852, Sir George Gabriel Stokes observed that any polarization state of an electromagnetic wave can be defined by four parameters, referred to as Stokes parameter, and given as:

$$S_0 = E_{x0}^2 + E_{y0}^2 = |E_x|^2 + |E_y|^2 \tag{2.30}$$

$$S_1 = E_{x0}^2 - E_{y0}^2 = |E_x|^2 - |E_y|^2 \tag{2.31}$$

$$S_2 = 2E_{x0}E_{y0}\cos\varphi = 2\,\Re e\{E_x E_y\} \tag{2.32}$$

$$S_3 = 2E_{x0}E_{y0}\sin\varphi = 2\,\Im m\{E_x E_y\} \tag{2.33}$$

where E_{x0}, E_{y0} are the corresponding magnitudes, and φ_x, φ_y are corresponding phases of E_x and E_y components, respectively, as mentioned in Eq.(2.27). The Stokes

Table 2.3: The significance of the four Stokes parameters [113]

Stokes Parameter	**Optical observation**
S_0	Total irradiance (polarized + unpolarized)
S_1	Horizontal or vertical linear polarization (with $S_1 = 1$ as horizontal and $S_1 = -1$ as vertical polarization)
S_2	Linear polarized wave (with $S_2 = \pm 1$ as $\pm \pi/4$ polarization to the previous orientation)
S_3	Circular Polarization (with ellipticity $X = S_3 / S_0 = 1$ as left circular polarization and $X = -1$ as right circular polarization)

parameters can be used to describe the different states of polarization of light as presented in Table 2.3 [113].

Here, we emphasize that the Objective V of the thesis work mainly revolves around the dynamic control of polarization state of light by leveraging ENZ effect of TCOs incorporated into a nanophotonic structure.

2.4. Transparent Conducting Oxide: Emerging ENZ material

Searching for materials that are simultaneously electrically conductive and transparent to light indicates a ‘conflict’. A material must need to have a large carrier concentration and mobility in order to be conductive. However, these properties of a material lead to the plasma frequency occurring at the lower wavelengths, which suppresses the transparency and causes substantial losses. Transparent conducting oxides (TCOs) circumvent this limitation with their large bandgap, enabling the transmission of light when made into thin films [33], [39], [55], [99], [126]–[131]. Therefore, the search for alternative plasmonic materials over the past decade has led us to the emergence of low-loss TCOs, which belong to the wide bandgap semiconductor family and can provide optical transparency and electrical conductivity at the same time [132].

2.4.1. Brief Introduction

TCOs are basically degenerately doped metal-oxides such as indium tin oxide (ITO), dysprosium-doped cadmium oxide (Dy-CdO), aluminium-doped zinc oxide (AZO), and gallium-doped zinc oxide (GZO) [55]. Table 2.4 depicts a comparative overview of a few widely used TCOs (ITO, CdO) with noble metals (Au and Ag) and semiconductor (Si) as per the Drude permittivity modelling at the telecom wavelength of 1550 nm.

Table 2.4: Comparison of the properties of a few widely-used TCOs with parameters from their Drude permittivity model mentioned in Eq. (2.22)

MATERIAL		$\Re e(\varepsilon)$ at 1550 nm	$\Im m(\varepsilon)$ at 1550 nm	ε_∞	N (cm^{-3})	ω_p (rad/s)	E_g (ev)
TCO [144], [210]	ITO	3.5	0.07	3.9	7×10^{19}	8×10^{14}	2.8
	CdO	4.3	0.03	5.6	7×10^{19}	1×10^{15}	2.36
Metal [124], [125]	Au	–116	11.3	9.5	7×10^{22}	1.35×10^{16}	--
	Ag	–130	3.3	5	7×10^{22}	1.43×10^{16}	--
Semiconductor [25]	Si	11.9	0	11.8	2×10^{10}	1×10^{13}	1.11

*Here, $\Re e(\varepsilon)$ and $\Im m(\varepsilon)$ refer to the real and imaginary part of the permittivity of the corresponding material at C band of wavelength. The parameter ε_∞ refers to the permittivity at the high frequency. N, ω_p, and E_g refer to the carrier concentration, plasma frequency, and bandgap energy, respectively.

As mentioned in the previous chapter, TCOs exhibit an exciting phenomenon named as 'epsilon-near-zero (ENZ) effect', where the real part of permittivity becomes vanishingly small at a certain wavelength. The range of wavelength for which the real part of the permittivity lies in between –1 and +1 can be referred to as ENZ-region [29]. Thus, a transition from dielectric-like behaviour (positive permittivity) to metallic-like behaviour (negative permittivity) can be seen. On the other hand, the imaginary part of the permittivity is relatively low as compared to the noble metals, which indicates TCOs to be less-lossy conductive material [131]. More importantly, the optical properties of the TCOs can be modulated by applying external electrical biasing. To understand the variation in optical properties under the influence of the external electric field, an example can be seen in the next sub-section, where an in-detailed procedure has been discussed to incorporate the electrostatic simulation data to obtain the optical properties of TCOs.

2.4.2. Tuning Permittivity using Electrical Biasing — Electro-Optic Effect

The ENZ-effect of TCOs can be harnessed at the near infrared (NIR)wavelength region by accumulating free-carriers when configured as a MOS type configuration, as discussed in Chapter 1 (sub-section 1.2.2). The variation in the carrier-concentration distribution of a TCO-layer, can be studied by doing electrostatic simulations in commercially available solver, Lumerical Device tool. To demonstrate the electro-optic properties, an n-doped ITO-layer (as TCO material) with an initial carrier-concentration (N) of ~7×10^{19} cm^{-3} has been considered to ensure a positive real part of permittivity at the NIR wavelength region.

2.4.2.1. Electrostatic simulations to study electro-optic properties of TCO

The Au–Al_2O_3–ITO stack forms a MOS-type structure, as depicted in the inset of Figure 2.3(a). To witness the accumulation of free-electrons at ITO–Al_2O_3 interface upon applying external bias-voltage (V), the electrostatic device physics simulations have been conducted by solving drift-diffusion equations.

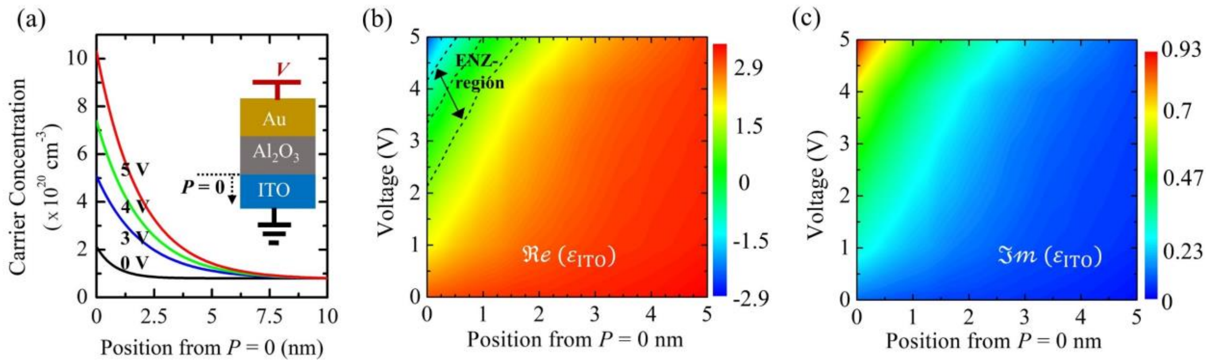

Figure 2.3: Variation of permittivity of ITO upon applying external bias. (a) The spatial distributions of ITO layer carrier concentration (N) from position P = 0 to 10 nm for distinct bias-voltages. Here, inset illustrates the MOS-type configuration consisting Au–Al_2O_3–ITO layers, where Al_2O_3–ITO interface is marked as P = 0. The contour plots of spatial distributions of (b) real ($\Re e(\varepsilon_{\text{ITO}})$) and (c) imaginary ($\Im m(\varepsilon_{\text{ITO}})$) parts of the permittivity of ITO at the wavelength of 1.55 µm from P = 0 to 5 nm for different biasing states. Note that the ENZ-regime is depicted as $-1 < \Re e(\varepsilon_{\text{ITO}}) < 1$.

Figure 2.3(a) depicts the carrier concentration distributions, N, as a function of applied bias-voltage for the first 10 nm region inside the ITO layer from the ITO–Al_2O_3 interface. To accurately estimate the optical properties of **ac**cumulation **l**ayer (ACL), the carrier concentration distributions are translated to the spatial distributions of permittivity *via* Drude model, given as [39]

$$\varepsilon_{\text{TCO}} = \left(\varepsilon_{\infty} - \frac{\omega_{\text{p}}^2}{(\omega^2 + i\Gamma\omega)}\right), \qquad \omega_{\text{p}} = \sqrt{\frac{Ne^2}{m_{\text{e}}^*\varepsilon_0}} \tag{2.34}$$

where high-frequency permittivity, plasma frequency, oscillation frequency, and damping constant are represented by ε_∞, ω_{p}, ω, and Γ, respectively [29]. The ω_{p} varies with carrier concentration (N) and effective electron mass m_e*. In the electrostatic simulations, the electron effective mass of ITO is assumed to be $m_e^* = 0.35m_e$ (where m_e is the mass of an electron). The electron mobility and bandgap of ITO are set to 30 $cm^2V^{-1}S^{-1}$ and 2.8 eV, respectively [29]. Due to the degenerately-doping, we can assume there is no substantial contribution of holes to be seen in the physical processes. Thus, effective mass of holes can be taken as m_e and mobility of hole is set to 10 $m^2V^{-1}S^{-1}$. In addition, the electron affinity of ITO is taken as 4.8 eV, whereas, the DC-permittivity of ITO and Al_2O_3 are set to 9.3 and 9, respectively [29]. The work function of Au is assumed to be 5.1 eV [128]. Due to the initial or bulk carrier-concentration (N) of ~7 × 10^{19} cm^{-3}, the ITO-layer behaves as a conductive transparent layer in unbiased condition at the NIR-wavelength region.

The spatial distribution of real ($\Re e(\varepsilon_{\mathrm{ITO}})$) and imaginary ($\Im m(\varepsilon_{\mathrm{ITO}})$) parts of permittivity of ITO at the wavelength of 1.55 μm are depicted in Figure 2.3(b) and (c), respectively, as a function of bias-voltage for the first 5 nm from ITO–Al_2O_3 interface. The range, $-1 < \Re e\,(\varepsilon_{\mathrm{ITO}}) < +1$, is denoted as ENZ-region. With increasing bias-voltage, the $\Re e(\varepsilon_{\mathrm{ITO}})$ can change its sign, which indicates the transition from dielectric-like behavior to metallic-like characteristics. Moreover, when $\Re e(\varepsilon_{\mathrm{ITO}})$ decreases, the imaginary part of permittivity increases as per the fundamental Kramers–Kronig relation. In addition, with the negative value of $\Re e(\varepsilon_{\mathrm{ITO}})$ inside the ACL upon applying external bias-voltage, the $\Im m(\varepsilon_{\mathrm{ITO}})$ doesn't acquire a large value, which reveals less-lossy metallic properties of the ACL.

2.4.2.2. Homogenization of the carrier accumulation layer

To accurately predict the optical properties of the inhomogeneous ACL, a two-layer model can be adopted, similar to ref. [133], [134], where a close-match with experimental results were obtained. In the two-layer model, the inhomogeneous ACL can be estimated as an equivalent ultra-thin layer (~2 to 3 nm) of uniform carrier concentration distribution based on the modified Thomas–Fermi approximation (MTFA) [133], [134]. Thus, the 10 nm ITO layer can be divided into two regions, namely ITO_{ACL} and ITO_{Bulk} corresponding to a 3 nm ACL and a 7 nm bulk ITO-region, respectively.

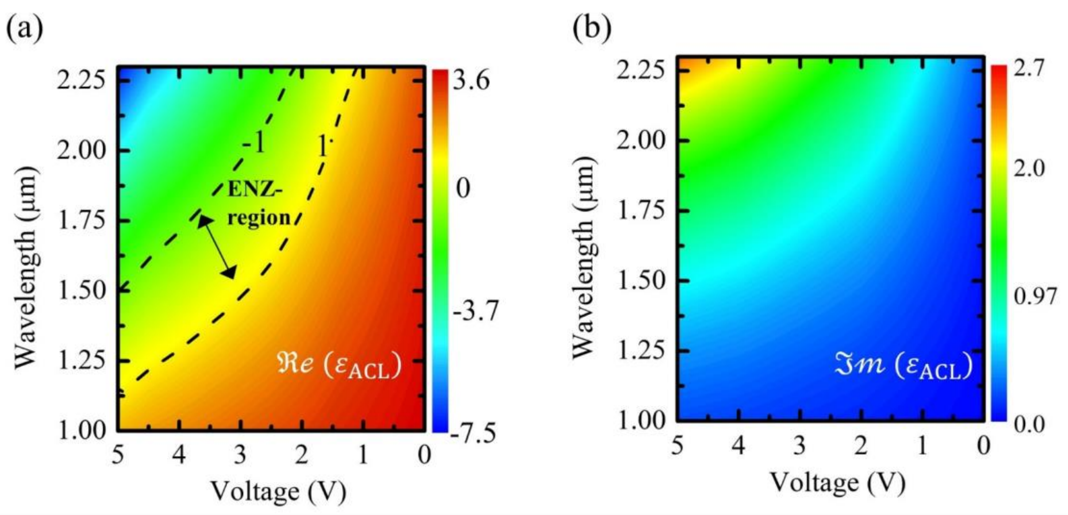

Figure 2.4: Variation of complex permittivity in a homogenous ACL. Voltage-dependency of real (a) ($\Re e(\varepsilon_{ACL})$) and (b) imaginary ($\Im m(\varepsilon_{ACL})$) parts of permittivity of accumulation layer in ITO.

If we consider the voltage-dependent carrier concentration distributions as Figure 2.3(a), we can estimate a uniform charge carrier concentration distribution (a median value for different voltage) inside the 3 nm thin ACL. These homogenous carrier concentration distributions are then translated to the distributions of permittivity *via* Drude model, given in Eq. (2.34).

The variation in real ($\Re e(\varepsilon_{ACL})$) and imaginary ($\Im m(\varepsilon_{ACL})$) parts of permittivity of ACL as a function of bias-voltage can be seen in Figure 2.4(a) and (b), respectively. Here, the ENZ-region can be referred to the wavelength-range for which the $\Re e(\varepsilon_{ACL})$ is in between –1 to +1 [29]. To analyse the optical properties of the MOS-structure based nanophotonic devices, these optical properties of ITO as a function of external electrical biasing can be incorporated into the electromagnetic simulation tools such as Lumerical FDTD®, CST Microwave Studio Suite®, and COMSOL Multiphysics®.

2.4.2.3. Choice of the gate-dielectric material

In order to design MOS-based electro-optic modulators, as depicted in the inset of Figure 2.3(a), the choice of gate-dielectric material plays a crucial role. The gate-dielectric material brings a trade-off between voltage requirement and capacitance limited electrical bandwidth. If we choose a dielectric layer with high DC-permittivity (like hafnia or HfO_2), we can achieve low-voltage driven modulator but at the cost of low operational 3-dB modulation bandwidth. It should be noted that with the higher DC-permittivity, the capacitance of the device will increase, which results in a large RC-time delay and limits the modulation bandwidth [29].

On the contrary, to increase the bandwidth, we can use dielectric material having a low DC-permittivity (like alumina or Al_2O_3), which requires a relatively high bias-voltage. In addition to the consideration of bandwidth while choosing a proper gate-dielectric material, the breakdown field of the material is also a major constraint. Both HfO_2 and Al_2O_3 are widely used in the field-effect transistor technology. Though alumina exhibits high breakdown field of up to 10 MV/cm, hafnia exhibit a relatively low breakdown field of 3.1 MV/cm [29]. Therefore, a proper choice of the gate-dielectric material should be taken into consideration while designing TCO based electro-tunable nanophotonic devices.

2.5. Literature Survey

In the last few years, metasurfaces have accelerated the development of active nanophotonic components such as electro-optic and all-optical modulators due to their exceptional abilities to control light–matter interactions at the sub-wavelength scale. As mentioned earlier, metasurfaces are ultra-thin optical scatterers that can manipulate the intensity and phase of the light scattered from the surface. This section reviews several design strategies reported in the literature for active control of electromagnetic properties (*viz.* intensity, phase, and polarization) of light using metasurfaces based on ENZ-materials.

2.5.1. Free-Space Electro-Optic Modulation using ENZ Effect

Over the last few years, several active metasurfaces have been proposed to demonstrate free-space electro-optic modulation by leveraging the ENZ-effect of TCOs [33], [132]. These electro-tunable metasurfaces have opened new doors to realize active nanophotonic devices by engineering their sub-wavelength meta-atoms. As discussed in Chapter 1 (sub-section 1.2.2), the major challenge to realize a free-space EOM is the limited interaction of incident light with active material (here, TCO) along the thickness (few nanometers) of the device[111], [128], [135]–[145]. Therefore, it is challenging to design an EOM as the restricted light–TCO interaction length leads to low modulation depth and high voltage requirement. To overcome these limitations, several state-of-the-art design strategies have been demonstrated, which can be seen in this sub-section.

2.5.1.1. Gap-Plasmon Resonance based EOMs

The gap-plasmon resonance (GPR) based metasurfaces have gained myriad attention from researchers working in a wide-variety of frequency regime over the last decade [146]. The GPR-based metasurfaces, a sub-class of plasmonic nanostructure, consist of a sub-wavelength metallic grating on top of a dielectric spacer layer deposited on an optically-thick metal ground-plane [146]. Thus, these structures can be seen as a metal–insulator–metal (MIM) type configuration. Over the years, several passive and tunable metamaterials have been reported by leveraging GPR-effect for a wide-variety of nanophotonic applications, *viz.* beam steering, broadband absorption, holographic imaging, high-resolution color printing, ultra-thin metalens, and electro-tunable metasurfaces [146]–[148]. Among these, the electro-tunable metasurface absorbers have been demonstrated as reflection or absorption type EOMs [149].

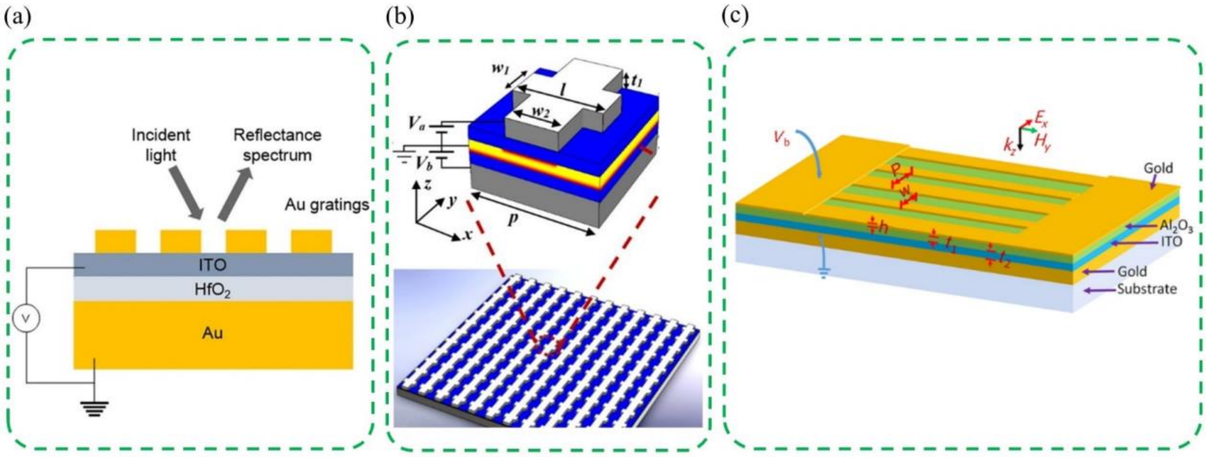

Figure 2.5: A few recently reported gap-plasmon resonance (GPR) based metamaterials for electro-optic modulation**:** (a) an electro-tunable metafilm absorber for intensity modulation. Adapted with permission from: [149] Copyright © 2015, The Author(s), under exclusive license to Springer Nature Limited. (b) A dual-gated metamaterial with fishbone pattern of Al-nanoantenna for phase modulation. Adapted with permission from: [29] Copyright © 2018, American Chemical Society (c) An ITO-coupled metamaterial absorber for dual-band intensity modulation. Adapted with permission from: [9] Copyright © 2020, Springer Nature Limited.

In literature, both intensity and phase modulators have been demonstrated by leveraging ENZ-phenomena of TCOs combined with GPR-effect. As shown in Figure 2.5(a), Park *et al*. experimentally demonstrated an electro-tunable 'metafilm absorber' for optical intensity modulation by combining GPR-effect with ENZ-phenomenon of ITO in the mid-infrared wavelength regime [149]. To modulate the reflected light in the near-infrared regime, Shirmanesh *et al.* proposed a metasurface with fishbone pattern of Al-nanoantenna on top of a multi-layered heterostructure (consisting of dielectric–ITO–dielectric layers) deposited on Al-back reflector, as shown in Figure 2.5(b) [29]. They used a special type of gate-dielectric layer named as hafnium-aluminum oxide laminate (HAOL), which is basically a composite of Al_2O_3–HfO_2 and can avail benefits from Al_2O_3 of having large breakdown field as well as benefits from HfO_2 of having large DC-permittivity. By leveraging the electro-optic properties of ITO, they experimentally demonstrated the modulation of the phase of reflected light from 0 degree to 303 degrees at 1550 nm wavelength.

To modulate the intensity of the reflected light at the near-infrared wavelength regime, Chen *et al.* proposed an ITO-integrated GPR-based metamaterial, as depicted in Figure 2.5(c) [9]. With an increase in the carrier concentration of the ACL from N_{Bulk} (= 1×10^{20} cm^{-3}) to N_{ACL} (=7×10^{20} cm^{-3}) upon applying external biasing, the ENZ-wavelength had been tuned to the vicinity of GPR-wavelength — leading to a strong coupling between the GPR-mode and the ENZ-mode. They had shown an enhancement of the absorption characteristic of the metamaterial due to the coupling of GPR-mode and ENZ-mode, which results in multi-band modulation of the reflected light with a modulation depth of ~0.52 and ~0.39 at 1.45 μm and 1.61 μm wavelength, respectively. Here it should be noted that this GPR based device could be useful not only for optical modulation but also for the dynamic control of the absorption properties of light.

2.5.1.2. Guided-Mode Resonance based EOMs

To modulate the optical signal, the ENZ-material can also be integrated with guided-mode resonance (GMR) based structure. A GMR-structure usually consists of a sub-wavelength grating on top of a high-index waveguide core [5], [141]. A sharp dip (peak) in the transmission (reflection) spectrum can be seen due to the coupling of incident light and waveguide mode, as discussed later in sub-section 2.6.1. It should be noted that the GMR based filters are widely adopted nanophotonic devices, and the dynamic response of these devices could help in realizing active components for various applications. The resonance response of the GMR-based metamaterial can be tuned by incorporating an active layer such as ENZ-materials or phase-change materials.

Several design strategies have been demonstrated for modulating transmitted or reflected light by combining GMR-effect of the grating waveguides and ENZ-effect of

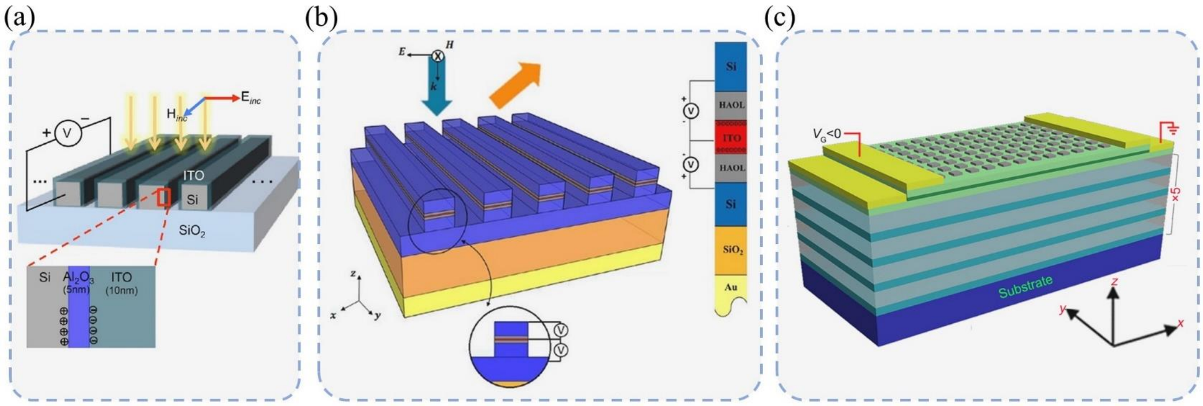

Figure 2.6: A few recently reported guided-mode resonance (GMR) based metamaterials for electro-optic modulation**:** (a) an ITO-integrated waveguide-grating structure for intensity modulation. Adapted with permission from: [5] Copyright © 2017, Optica Publishing Group. (b) A dual-gated metamaterial for intensity and phase modulation. Adapted with permission from: [30] Copyright © 2019, American Chemical Society. (c) An ITO-coupled distributed Bragg-reflector based metamaterial for intensity modulation. Adapted with permission from: [45] Copyright © 2021, IEEE.

TCOs configured as MOS-type structures [30], [31], [45], [141]. Researchers have demonstrated that if the ENZ-wavelength of TCOs can be tuned to the vicinity of the GMR-wavelength, the resonance phenomena will disappear [5]. This is due to the fact that when TCOs exhibit the ENZ-effect, the imaginary part of the permittivity solely decides the optical properties of the ACL, which increases optical absorption. Thus, when the ENZ-wavelength of TCO is tuned to the vicinity of the GMR-wavelength, the modal loss of the guided-mode will get increased due to the strong light–matter interactions at the absorptive ACL. The drastic increase in the modal loss of the guided-mode is responsible for the disappearance of the resonance phenomenon. Over the years, this electrically tunable resonance phenomenon has been utilized for the modulation of optical intensity and phase at a particular wavelength region.

Recently, Brongersma *et al.* demonstrated active control on the intensity of the reflected light by leveraging ENZ-effect of ITO incorporated into a GMR-based structure, as shown in Figure 2.6(a) [5]. The ENZ-effect was achieved by accumulating free-carriers at the ITO–Al_2O_3 interface upon applying an external bias voltage. They theoretically demonstrated that when the ENZ-wavelength of the ITO had been tuned at the vicinity of the GMR-wavelength, the resonance phenomenon disappeared. By utilizing this astonishing phenomenon, they have shown the intensity modulation of reflected light with a modulation depth of 0.82. Forouzmand *et al.* demonstrated a guided-mode resonance mirror based metamaterial for reflection-type electro-optic amplitude and phase modulation, as shown in Figure 2.6(b) [30]. They achieved intensity modulation at 1537 nm wavelength with modulation depth as high as 0.8 for a –15 V bias-voltage. In addition, they had also shown the phase modulation with a variation in the phase of reflected light as high as ~210 degrees for a voltage range of –15 V to +24 V.

Various designs have been demonstrated for energy-efficient modulation. For instance, Vatani *et al.* reported a design strategy by leveraging GMR-effect of a waveguide grating critically-coupled with a 20-pair quarter wavelength distributed Bragg-reflector, as presented in Figure 2.6 (c) [45]. The presented reflection-type device could exhibit ~0.99 modulation depth at 1550 nm wavelength with only 0.1 V biasing.

To achieve intensity modulation of transmitted light, Qiu *et al.* theoretically demonstrated a transmission type EOM by integrating ENZ material into a GMR based structure [141]. In another ITO-integrated GMR based work, Hu *et al.* showcased a novel design strategy that could control over the transmitted light from 0.02 to 0.86 under the influence of electrical biasing at 1550 nm wavelength [31].

2.5.1.3. Research gaps identified

Though various designs have been demonstrated for free-space EOM by merging the ENZ-effect with various resonance phenomena, these state-of-the-art works suffer from several limitations, such as low modulation depth, high energy-consumption, incident angle-sensitivity, stringent dependency on polarization state of light, low modulation speed, high-voltage requirement, and most importantly single wavelength band modulation [30], [31], [45], [141]. These fundamental research problems regarding the design and realization of free-space EOM for nanophotonic applications need to be solved.

In this dissertation, the opportunities and challenges towards achieving efficient electro-optic modulation (with high modulation depth, low-voltage driven, high modulation speed, and low energy consumption) for various nanophotonic applications have been presented by leveraging the ENZ phenomenon of TCOs integrated with several resonating metamaterials.

2.5.2. Integrated Electro-Optic Modulation using ENZ Effect

With the emergence of the research area named as silicon photonics, the design of high-speed on-chip optical modulators gained enormous attention for integrated photonics applications. Integrated EOMs are the key elements for the optical communication system and potential candidates for the replacement of bandwidth- and power-hungry electrical interconnects at data center networks (DCNs) [150], [151]. Several hybrid integrated modulators such as Pockels effect based modulators and plasma dispersion effect based modulators have been demonstrated by altering real-part of the refractive index of the corresponding active materials [16], [24]; whereas, quantum-confined Stark effect based and Franz-Keldysh effect based electro-absorption modulators (EAMs) have been demonstrated by controlling absorption coefficient of the materials [152].

However, Pockels effect based silicon Mach–Zehnder modulators (MZM) suffer from larger footprint and limited performance due to moderate perturbation of refractive index [24]. On the other hand, resonator based designs, such as microring resonators [153] and photonic-crystal cavity based modulators [154] can effectively reduce device footprint and energy requirement by sacrificing spectral bandwidth.

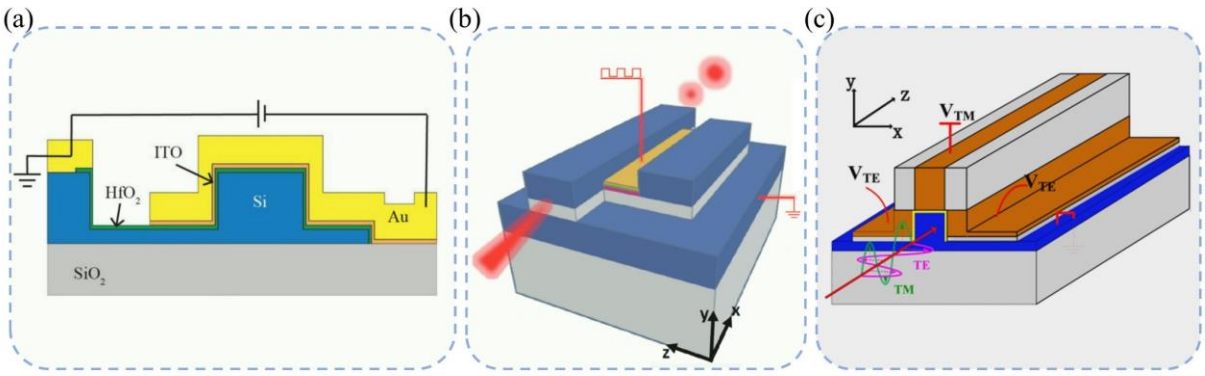

Figure 2.7: A few recently reported ENZ-material based integrated electro-optic intensity modulators using silicon photonics platform: (a) an ITO-integrated high-speed hybrid plasmonic intensity modulator. Adapted with permission from: [13] Copyright © 2020, IEEE. (b) A directional coupler based intensity modulator. Adapted with permission from: [162] Copyright © 2018, IEEE. (c) A polarization-insensitive intensity modulator. Adapted with permission from: [28] Copyright © 2020, IEEE.

To mitigate these research problems, over the years, numerous design strategies have been adopted to realize energy-efficient and high bandwidth EOMs by incorporating ENZ effect of TCOs into the silicon photonics platform [41]–[43], [155]–[167]. For instance, Sorger *et al.* experimentally demonstrated an ultra-compact energy-efficient EOM by leveraging ENZ phenomenon of ITO while configuring in a MOS-type structure with a power consumption as low as 57 fJ/bit [43]. To demonstrate high modulation speed, Zhou *et al.* presented a plasmonic modulator by using ENZ effect of ITO on silicon photonics platform, as shown in Figure 2.7(a) [13]. With 100 fJ/bit energy-consumption, they achieved 3.5 GHz modulation bandwidth. In another work, Swillam *et al*. theoretically demonstrated a directional coupler based EOM by using electro-tunable ENZ-effect, as shown in Figure 2.7(b) [162]. In this direction, various state-of-the-art works showcased high-speed energy-efficient modulation with large modulation depth [13], [134], [162], [163], [165], [168]. However, these designs are limited to a particular polarization state of light.

The polarization-sensitivity of an EO-modulator leads to the requirement of extra polarization controlling elements in the integrated photonic system, which increases the overall footprint and system complexity. In this direction, a few designs have been demonstrated by leveraging ENZ effect [28], [41], [161], [166], [169]. For instance, Qiu *et al.* presented an ITO-based dual-polarization intensity modulator, as shown in Figure 2.7(c) [28]. They achieved simultaneous modulation of both TE and TM polarizations with a modulation depth of ~10 dB for 75 μm active length.

Though some initial studies have been demonstrated for TCO-based polarization-insensitive modulators [28], [41], [161], [166], [169], these EOMs either suffer from the large footprint or low modulation depth and high energy consumption. Therefore, it remains highly challenging to design a compact polarization-insensitive modulator, which is capable of simultaneous modulation of both TM and TE modes while maintaining low power consumption and high modulation bandwidth.

2.5.3. Free-Space All-Optical Intensity Modulation using ENZ Effect

Till now, we have seen the state-of-the-art designs for realizing free-space and integrated EOMs by leveraging the electro-optic properties of ENZ-materials. Though the EOMs are crucial for a nanophotonic system, their bandwidth are limited by the RC-delay due to the involvement of required electronics [46], [47]. Hence, all-optical modulation brings in the possibility to realize ultra-fast next-generation optical computing systems by overcoming the fundamental limits of electronics [50]. In this sub-section, an overview of ultrafast all-optical modulators is discussed by leveraging the intraband transition induced optical nonlinear effects of ENZ-materials.

Recently, the ENZ-materials have gained massive consideration in realizing all-optical modulators due to their sub-picosecond nonlinear response with large refractive index tuning capabilities. The ultra-fast hot electron dynamics and nonlinear response of ENZ-material had been experimentally demonstrated by Boyd *et al.* in ref. [58]. The researchers have considered a 310 nm thick ITO-layer (as ENZ-material) deposited on silica glass substrate. They have considered the ENZ-wavelength of ITO to be 1240 nm.

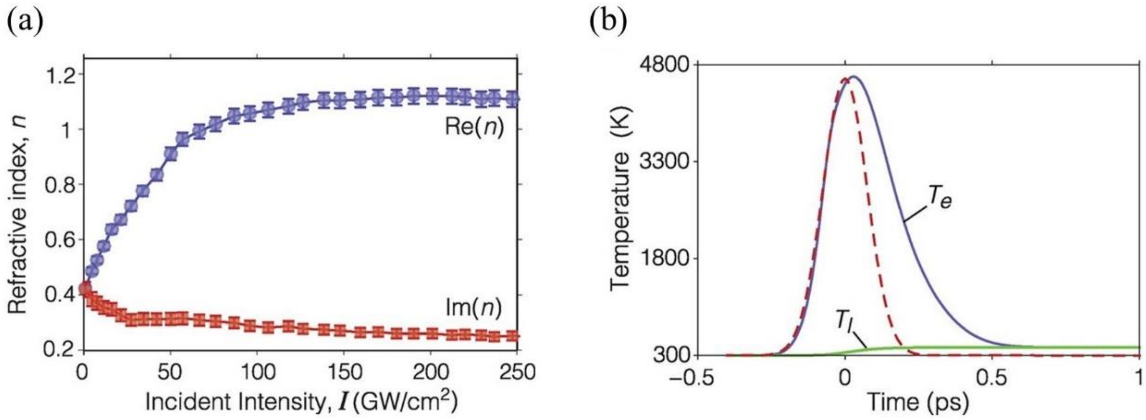

Figure 2.8: Nonlinearities in the ENZ material for intraband electronic transitions depicting**:** (a) the incident pump intensity dependent real and imaginary parts of refractive index of an ITO thin film and (b) ultra-fast transient response of the electron and lattice temperature upon illumination of a pump pulse with an intensity of 66 GW/cm^2. Adapted with permission from: [58] Copyright © 2016, The American Association for the Advancement of Science.

With a Gaussian pump pulse excitation, they had experimentally shown that the optical properties of the ITO-film can be altered with the variation in the incident pump intensity, *I*, as depicted in Figure 2.8(a). Upon illumination of pump-pulse with an intensity of 66 GW/cm^2, the electron temperature increases with a peak value of 4500 K at 1.2 ps and then gradually decays to its steady-state value of 300 K, as depicted in Figure 2.8(b). The increase in the electron temperature leads to an increase in the effective electron mass, and thus the plasma frequency decreases. Therefore, this ultra-fast variation in the optical properties in the ENZ-material can be utilized to realize femtosecond all-optical modulation.

By leveraging this nonlinear response of ENZ-material, Alam *et al.* demonstrated a plasmonic metasurface for realizing ultra-fast all-optical intensity modulation, as shown in Figure 2.9(a) [56]. They achieved a sub-picosecond response time while maintaining a low pump-fluence requirement of a few pJ/μm^2. They showcased that the nonlinear phenomenon of ENZ-material can be enhanced by integrating it into a resonating metasurface.

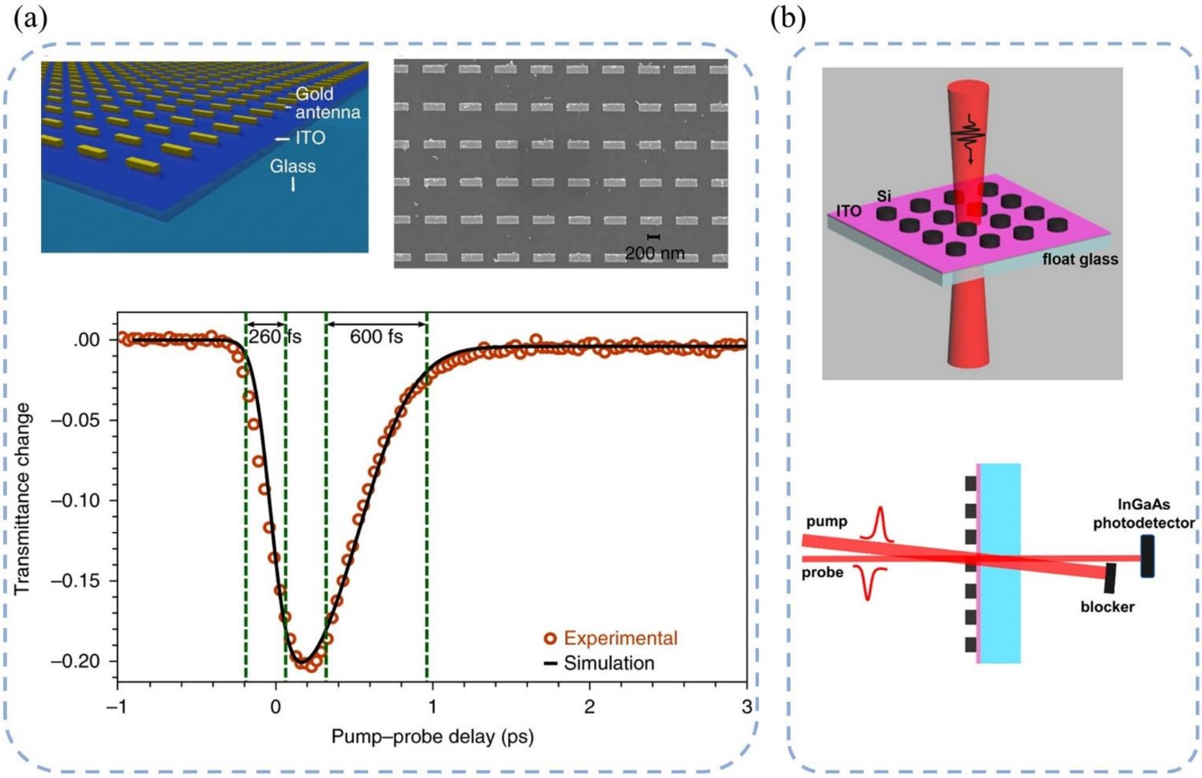

Figure 2.9: A few recently reported metamaterials for ultra-fast all-optical modulation using nonlinear phenomena in ENZ-material**:** (a) an ITO-coupled metamaterial with Au-nanoantenna for energy-efficient intensity modulation. Adapted with permission from: [56] Copyright © 2018, Springer Nature Limited (b) A silicon nano-disk array based metamaterial for ultra-fast intensity modulation. Adapted with permission from: [170] Copyright © 2022, American Chemical Society.

Based on this incredible scheme, several metasurface designs have been demonstrated in the recent years to realize all-optical modulation of polarization, phase, and amplitude [55], [59]–[63], [170]. For instance, Vatani *et al.* theoretically showcased a reflective type all-optical intensity modulator by utilizing nonlinear phenomena of AZO [63]. They attained a modulation depth of 0.5 with a pump-fluence requirement of

2.39 mJ/cm^2. In another work, Wang *et al.* demonstrated a silicon nano-disk array based ITO-coupled metamaterial for ultra-fast all-optical intensity modulation, as depicted in Figure 2.9(b) [170]. They revealed that the intensity-dependent effective optical nonlinear coefficient can be enhanced by more than 3 orders of magnitude in their coupled-system than that of bulk ITO thin-film.

However, the state-of-the-art all-optical intensity modulators are either suffering from low modulation depth or high pump-fluence requirement [55], [59]–[63], [170]. Thus, the realization of femtosecond all-optical switching with high modulation depth (> 0.8) and low pump-fluence requirement (~ few μJ/cm^2) simultaneously, remains a challenging task. To bridge this gap, a proper design-strategy needs to be implemented by incorporating the nonlinear effects of ENZ material into a plasmonic metamaterial structure that exhibits a strong resonance effect at the vicinity of the ENZ wavelength.

2.5.4. Free-Space Electro-Optic Polarization Modulation using ENZ Effect

Controlling polarization states of light is crucial for photonic systems. The oscillating electric field determines the polarization states of light. To date, many researchers have demonstrated several metasurface-based designs for polarization conversion, which find a wide range of applications, including holographic displays [75], polarization imaging [66], Stokes parameters detection [76], and many more. However, most of these metasurface-based polarization controlling components have typically been limited by passive operation, *i.e.*, a fixed control over the degree of polarization [70]–[74], [77].

Extensive research has been performed in recent years to demonstrate dynamic control over the polarization state of light by incorporating numerous emerging materials such as phase-change materials, graphene, and ENZ-materials [78]. However, most of the previously reported metasurface-based active polarization rotators are designed for mainly far-infrared [78], [79], and mid-infrared [80] wavelength regimes.

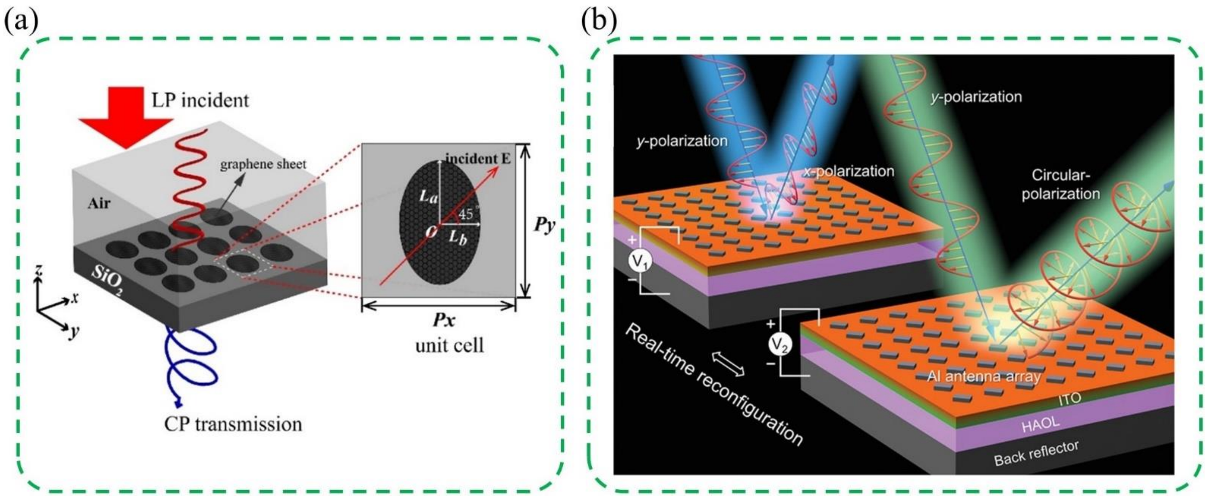

Figure 2.10: A few recently reported metamaterial based polarization modulators: (a) A graphene-assisted metamaterial for linear-to-circular polarization switching. Adapted with permission from: [78] Copyright © 2019, Optical Society of America (b) An ITO-coupled metamaterial for electro-optic polarization modulation. Adapted with permission from: [81] Copyright © 2021 Wiley-VCH GmbH.

For instance, Yao *et al.* presented a graphene-assisted metamaterial for linear-to-circular polarization switching for the far-infrared wavelength regime, as shown in Figure 2.10(a) [78]. The realization of active polarization controlling devices at visible and near-infrared wavelength regimes is essential for quantum and nanophotonic applications.

In this direction, Atwater *et al.* recently demonstrated a metasurface-based dynamic polarization controlling device at near-infrared (NIR) wavelengths by integrating an ENZ material, as shown in Figure 2.10(b) [81]. They have experimentally demonstrated the modulation of polarization state of reflected light from the metasurface under the influence of external electrical biasing. They showcased a y-polarization to x-polarization conversion with the variation of applied bias within the range of −4 and 3 V. Whereas, for the bias voltage ranging between 12 and 16 V, they demonstrated the conversion of the illuminated linearly polarized light into a circularly polarized light when reflected from the metasurface.

Nevertheless, the previously reported ENZ material-based metasurfaces for dynamic polarization conversion come at the cost of low intensity of reflected light and high bias-voltage requirements. Therefore, realization of an effective and energy-efficient active metasurface for polarization modulation remains a great challenge.

2.6. Analytical Methods

This section introduces some theoretical methods that have been considered for analyzing optical responses of the numerically simulated nanophotonic structures. These theoretical and analytical approaches can be extended to find resonance wavelengths of GMR and GPR based metasurfaces.

2.6.1. Effective Medium Theory for GMR based Structure

A guided-mode resonance (GMR) based structure usually consists of a sub-wavelength grating on top of a high-index waveguide core, as illustrated in Figure 2.11(a). The resonance phenomenon in the GMR-structure is associated with leaky waveguide modes [63], [171]–[175]. Without any grating layers, the waveguide core-layer supports bounded modes. On the other hand, energy from an incident plane wave could couple into the waveguide mode. Thus, the resonance phenomenon can be seen when the energy from the diffracted wave is coupled into a leaky mode [171]–[173]. A sharp dip in the transmission (reflection) spectrum can be seen due to the constructive interference of the leaking fields, as illustrated in Figure 2.11(a).

Over the years, silicon has been the most preferable choice as the high-index material for waveguide core-region, which enabled CMOS-compatibility. Here, an in-detailed semi-analytical methodology is discussed to estimate the resonant wavelength of a GMR-based device by combining effective medium theory (EMT) with modal analysis.

The EMT approximation can be adopted to estimate the effective permittivity of a medium consisting of different materials. On the basis of the permittivity and relative fractions of different media, the effective permittivity of a homogenized medium can be estimated using mixing formulae.

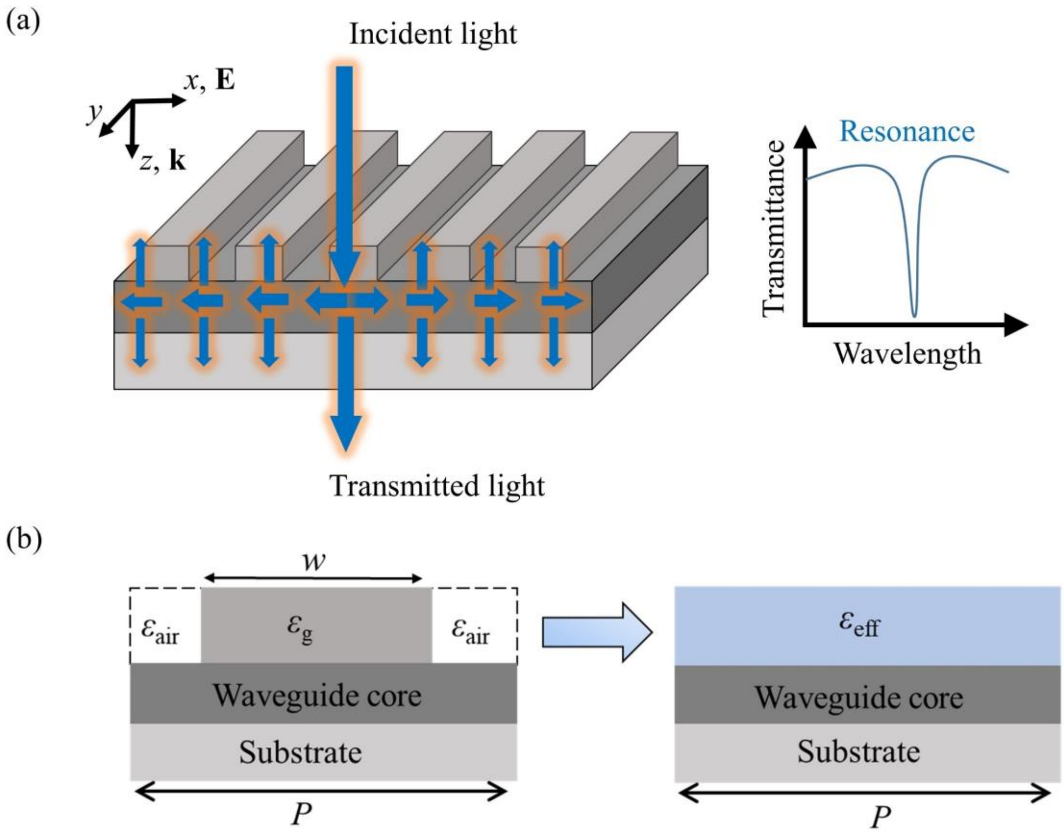

Figure 2.11: A pictorial representation of guided-mode resonance (GMR) based metamaterial showing: (a) A perspective view of the metamaterial depicting the physical mechanism behind the sharp dip in the transmission spectrum, (b) Side-view of the unit cell, where effective medium approximation models the grating as a homogenous layer of permittivity ε_{eff}.

For example, as presented in Figure 2.11(b), the EMT approximation assumes a periodic array of subwavelength grating (in a GMR-based metamaterial structure) as a homogeneous layer with an effective permittivity ($\varepsilon_{\mathrm{eff}}$) defined by the following set of complementary equations [171], [176]:

$$\varepsilon_{\mathrm{eff}}^{\parallel} = f(\varepsilon_{\mathrm{g}}) + (1-f)\varepsilon_{\mathrm{air}} \tag{2.35}$$

$$\frac{1}{\varepsilon_{\mathrm{eff}}^{\perp}} = \frac{f}{\varepsilon_{\mathrm{g}}} + \frac{(1-f)}{\varepsilon_{\mathrm{air}}} \tag{2.36}$$

where ε_{g} is the permittivity of the grating material, $\varepsilon_{\mathrm{air}}$ is the permittivity of air, the $\varepsilon_{\mathrm{eff}}^{\parallel}$ and $\varepsilon_{\mathrm{eff}}^{\perp}$ are the effective permittivity along the parallel and perpendicular direction of incident light polarization, respectively. The parameter f is the filling fraction, which depends on grating width (w) and period (P) as $f = w^2/P^2$.

If we consider the incident light is parallel-polarized or x-polarized, as presented in Figure 2.11(a), then we can estimate the effective permittivity of the grating by using Eq.(2.35). Then, we may estimate the resonant wavelength of this multilayered homogenized structure.

The resonance feature can be seen at the wavelength that satisfies the grating equation, defined as [31]:

$$\lambda_{\mathrm{GMR}} = (n_{\mathrm{mode}} - n\sin\theta)P \tag{2.37}$$

where λ_{GMR} is the resonant wavelength, n_{mode} is the effective modal index of a particular waveguide mode, θ is the incident angle, n is the background refractive index, and P is the grating period. Here, the effective modal index (n_{mode}) of a particular guided mode decides the resonant wavelength. The effective modal index may be obtained from the modal analysis using any simulation tool such as Lumerical Mode solver.

For a normally incident light, θ (= 0^0), with a background medium of air, the Eq.(2.37), reduces to $\lambda_{\text{GMR}} = n_{\text{mode}}P$. This analytical approach gives a reasonably precise approximation to find the resonant wavelength of the GMR based device.

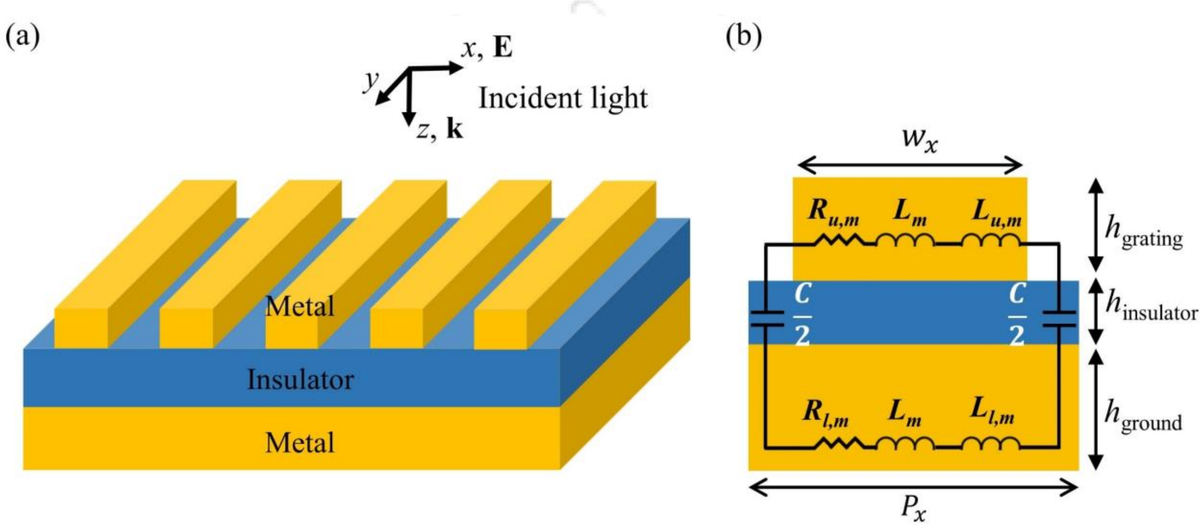

Figure 2.12: A pictorial representation of gap-plasmon resonance (GPR) based metamaterial showing: (a) a perspective view of the metamaterial considering an *x*-polarized incident light propagating along the z axis, (b) the equivalent RLC-circuit model of the unit cell, where $R_{u,m}$ ($R_{l,m}$) denotes the ohmic resistance, L_{m} denotes the Faraday inductance, $L_{u,m}$ ($L_{l,m}$) denotes the kinetic inductance, and *C* denotes the equivalent capacitance. Note that the subscript '*u*' and '*l*' are used to denote the lumped elements corresponding to the upper and lower metallic-layers, and *m* denotes the resonance mode number.

2.6.2. RLC Equivalent Circuit Modelling for GPR based Structure

The gap-plasmon resonance (GPR) based metasurfaces, a sub-class of plasmonic nanostructure, consist of a sub-wavelength metallic grating on top of a dielectric spacer layer deposited on an optically-thick metal ground-plane [146]–[148]. To estimate the resonant wavelength of such metal–insulator–metal (MIM) based structures, a RLC-equivalent circuit modeling is convenient by calculating the corresponding value of the lumped elements: resistance (*R*), capacitance (*C*), and inductance (*L*). Here, an in-detailed analytical methodology is discussed by providing an example using the equivalent RLC-circuit modelling.

Let us consider that an *x*-polarized incident light propagating along *z*-direction is used to excite the GPR-mode for the structure shown in Figure 2.12(a). The subwavelength unit cell can be modelled as an equivalent RLC-circuit, as shown in Figure 2.12(b). The unit cell comprises a metallic grating with a period (P_x) and width (w_x) along x-direction. The corresponding thickness (or height) of the metallic grating and insulator layer are denoted as h_{grating} and $h_{\text{insulator}}$, respectively. The ground metal layer thickness, h_{ground}, should be more than its effective skin depth (δ_{metal}). Note that the subscripts '*u*' and '*l*' are used to denote the lumped elements corresponding to the upper and lower metallic-layers, and *m* denotes the resonance mode number.

In the equivalent circuit model, $R_{u,m}$ ($R_{l,m}$) denotes the ohmic resistance, L_m denotes the Faraday inductance, $L_{u,m}$($L_{l,m}$) denotes the kinetic inductance due to the drifting of electrons within the skin depth of the metallic layer, and C specifies the equivalent capacitance between the upper and lower metal-blocks. Here, we have assumed the adjacent unit-cells are far enough from each other, and thus we can exclude the electromagnetic coupling between them.

Based on the resonance analysis theory, the parameters of the equivalent circuit model can be given as [177]–[179]:

$$C = \frac{\alpha \varepsilon_i \varepsilon_0 w_x l_y}{m h_{\text{insulator}}} \tag{2.38}$$

$$L_{u,m} = \frac{-w_x}{m\delta_{\text{metal}}\omega^2 l_y \varepsilon_0} \times \left\{\frac{\varepsilon'}{(\varepsilon')^2 + (\varepsilon'')^2}\right\}_{\text{metal}} \tag{2.39}$$

$$L_{l,m} = \frac{-1}{m\delta_{\text{metal}}\omega^2 \varepsilon_0} \times \left\{\frac{\varepsilon'}{(\varepsilon')^2 + (\varepsilon'')^2}\right\}_{\text{metal}} \tag{2.40}$$

$$L_m = \frac{0.5\mu_0 w_x h_{\text{insulator}}}{m l_y} \tag{2.41}$$

$$R_{u,m} = \frac{-w_x}{m\delta_{\text{metal}}\omega^2 l_y \varepsilon_0} \times \left\{\frac{\varepsilon''}{(\varepsilon')^2 + (\varepsilon'')^2}\right\}_{\text{metal}} \tag{2.42}$$

$$R_{l,m} = \frac{-1}{m\delta_{\text{metal}}\omega^2 \varepsilon_0} \times \left\{\frac{\varepsilon''}{(\varepsilon')^2 + (\varepsilon'')^2}\right\}_{\text{metal}} \tag{2.43}$$

where, ω is the angular frequency of the incident wave, ε_0 and μ_0 are the vacuum permittivity and permeability, respectively. The real and imaginary parts of permittivity of the metal layer are denoted as $\varepsilon'$and ε'', respectively.

The parameter α ($0.2 < \alpha < 0.3$) is the tuning factor of the effective capacitance, which depends on the resonance mode number (m) [177]. The unit length of the metamaterial grating along the y-direction is taken as l_y. In the equivalent circuit, the input impedance can be given as [178]:

$$Z_i = R_{u,m} + R_{l,m} + \frac{1}{j\omega C} + 2i\omega L_m + i\omega\left(L_{u,m} + L_{l,m}\right) \tag{2.44}$$

The circuit impedance will be perfectly matched at the resonance condition and the imaginary part of Z_i will be '0'. The resonant wavelength, λ_{GPR}, can be calculated as [177]:

$$\lambda_{\mathrm{GPR}} = 2\pi c\sqrt{C\left(L_{\mathrm{m}} + L_{u,m} + L_{l,m}\right)} \tag{2.45}$$

where c is the speed of light in vacuum. This method also provides vital information that the resonance wavelength proportionally varies with the grating width.

3

ENZ-Material based Metasurfaces for Dual-band Electro-Optic Intensity Modulation

Contents

This chapter presents different designs of ENZ-material based dual-band free-space electro-optic intensity modulation at both the primary telecommunication wavelength bands, *i.e.*, C-band and O-band with high modulation depth. Two innovative approaches have been adopted for enabling dual-band free-space electro-optic intensity modulation. Section 3.1 discusses a unique design of dual-band electro-tunable metasurface for optical intensity modulation by leveraging the ENZ phenomenon of TCOs combined with guided-mode resonance (GMR) effect of grating waveguides. By nature, GMR based devices are incident angle specific. Section 3.2 introduces an electro-tunable metamaterial absorber with wide incident angle-insensitivity for dual-band optical intensity modulation by combining ENZ effect with gap-plasmon resonance mode.

3.1. Guided Mode Resonance based Modulator: Incident-Angle Specific Design

In this section, we introduce a unique design strategy of dual-band electro-optic intensity modulation by leveraging the ENZ phenomenon combined with guided-mode resonance effect. The designed metasurface exhibits a dual-band intensity modulation with modulation depth as high as ~22.3 dB (~19.5 dB) at 1.55 µm (1.31 µm).

3.1.1. Background

As mentioned in the previous Chapter, electro-tunable metasurface opened new doors to manipulate electromagnetic properties of light (such as intensity, polarization, and phase) at the nanoscale by engineering sub-wavelength ‘meta-atoms’ [29]. Over the last few years, several metasurfaces have been reported for designing active flat optical components for modulation of reflected and transmitted light [9], [10]. In order to achieve dynamic control of optical properties of an incoming light, ENZ-phenomenon has been merged with guided-mode resonance (GMR) effect [5], Huygens resonance modes [44], gap-plasmon resonance (GPR) modes [149], and so on.

However, the metasurface based electro-optic modulators reported so far are either operated at a particular wavelength or multi-wavelengths within the same band [5], [30], [31], [45], [149].[180] With the revolution of optical fiber communication, the most preferable wavelength band to design electro-optic intensity modulators is C-band (1.535 μm – 1.565 μm) over the last few decades [45], [141]. However, due to the high chromatic dispersion coefficient, C-band wavelengths suffer from signal distortion for high-speed communication beyond 10 Gbps [181]. To mitigate such distortion, several signal processing components such as equalizers and delay interferometers need to be employed. This will increase system complexity and overall costs. In contrast, a more cost-efficient solution can be realized if we utilize low dispersion characteristic of O-band (1.26 μm – 1.36 μm) [181]. Nevertheless, to exploit benefits from both the two key telecommunication wavelength bands, *i.e.*, O-band and C-band, separate active devices need to be employed in a photonic system. This again increases system complexity and leads to a larger footprint due to the extra active components. Therefore, it is crucial to investigate the design of a *dual-band* electro-optic intensity modulator, which can operate in both C-band and O-band.

To bridge these gaps, we present an electrically-tunable metasurface that can simultaneously modulate the reflected light intensity in both of the key telecom wavelength bands, *i.e.*, O-band and C-band. The dual-band optical modulation is realized by leveraging the ENZ-phenomenon of ITO in a guided-mode resonance mirror (GMRM) structure.

3.1.2. Design and Operating Principle

A GMRM-structure usually consists of a dielectric grating on top of a stack of high-index guiding core and a reflective substrate. Figure 3.1(a) shows the perspective view of the proposed GMRM-based metasurface, which consists of silicon-nitride (Si_3N_4) nanograting on top of Si–ITO–Al_2O_3 stack deposited on an optically thick Au-layer. The

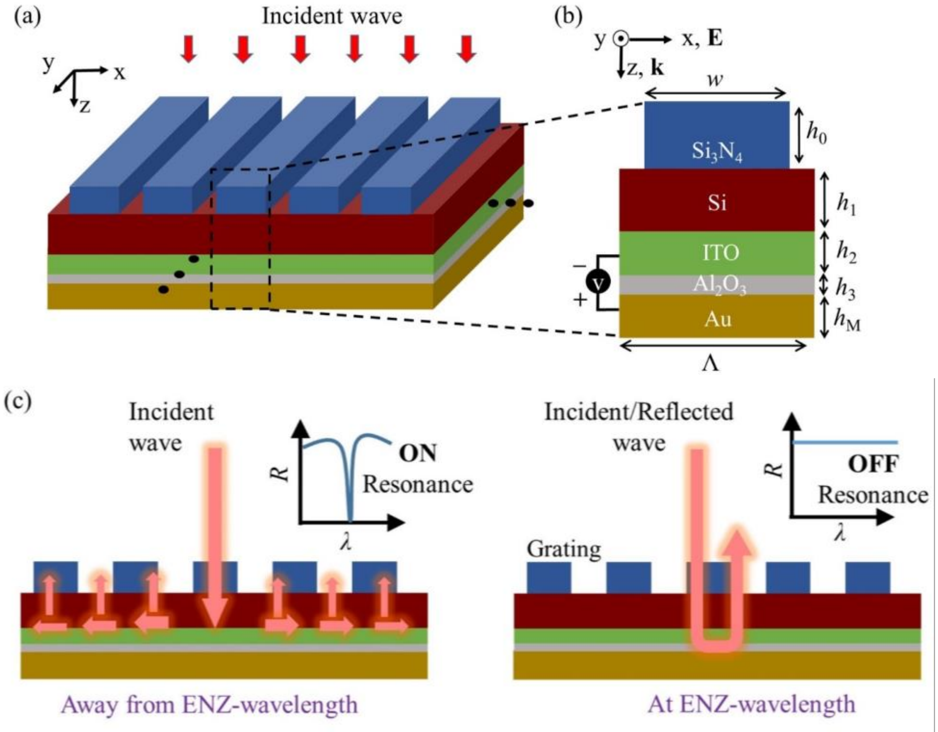

Figure 3.1: Schematic overview of the proposed electro-tunable metasurface based on guided-mode resonance mirror (GMRM) structure, showing (a) a perspective view, where a unit cell is represented by a black dashed rectangle, and (b) a cross-sectional view (*x*-*z* plane) of a unit cell with electrode configuration. The design consists of Si_3N_4 nanograting on top of $Si/ITO/Al_2O_3$ layers deposited on optically thick Au-layer, where x-polarized incident beam propagates along z-direction. The grating has a width (*w* = 600 nm) and periodicity (Λ= 800 nm) along x-direction. Here, h_0 = 510 nm, h_1 = 305 nm, h_2 = 70 nm, h_3 = 5 nm, and h_M = 70 nm. (c) Pictorial representation of the physical mechanism behind an ITO-integrated GMRM structure. Note that when the ENZ-wavelength of ITO is tuned to the operational wavelength band, the resonance dip in reflectance (*R*) spectrum is disappeared [180].

x-polarized normally incident plane wave, propagating along z-direction, can be coupled to the ITO-integrated Si-waveguide —leading to excitation of different guided modes. This results in a dip in the reflection spectrum at resonant wavelength of each mode. The resonance response can be tuned by accumulating free-carriers at the ITO–Al_2O_3 interface by applying an external bias voltage. The unit cell (*x*-*z* view) with electrode configuration is shown in Figure 3.1(b), where Si_3N_4 nanograting has a width of (*w* = 600 nm) and periodicity of (Λ= 800 nm) along *x*-direction.

Figure 3.1(c) depicts the pictorial representation of the physical mechanism behind an ITO-integrated GMRM-structure, where the coupling of incident light into the guided mode results in a resonance dip in the reflectance (*R*) spectrum. We refer to it as the ON-resonance condition. In contrast, when the ENZ-wavelength of ITO is tuned at the operational wavelength-band by applying bias-voltage, we can introduce large modal loss, which diminishes the coupling of incident plane wave to guided modes. Therefore, the incident light is primarily reflected by the mirror-substrate, and we can refer to it as the OFF-resonance condition. This enables the modulation of spatial light when we electrically switch between ON-resonance and OFF-resonance conditions.

3.1.3. Electro-Optic Properties of ITO

In order to estimate the optical properties of any TCO based metasurface under applied bias, the electrical properties of the TCO layer need to be extracted by doing electrostatic simulation in Lumerical Device. In our device physics simulations, the parameters assumed for ITO (as TCO material) are identical as the ones revealed in Chapter 2 (section 2.4). The bulk carrier concentration of ITO is taken as $N = 7 \times 10^{19}$ cm^{-3}. The formation of a MOS-type structure containing Au–Al_2O_3–ITO layers is illustrated in the inset of Figure 3.2(a). The voltage-dependent carrier concentration distributions can be seen in Figure 3.2(a) for the first 10 nm from ITO–Al_2O_3 interface inside the ITO-layer.

After calculating the charge carrier distributions under the influence of applied biases, we employ the two-layer model to accurately predict the optical properties of the inhomogeneous accumulation layer (ACL), similar to the procedure as mentioned in Chapter 2 (sub-section 2.4.2). As discussed previously, in the two-layer model, the inhomogeneous ACL can be estimated as an equivalent ultra-thin layer (~3 nm) of uniform carrier concentration distribution based on the modified Thomas–Fermi approximation [133], [134]. Then, the charge distributions inside the ACL of 3 nm

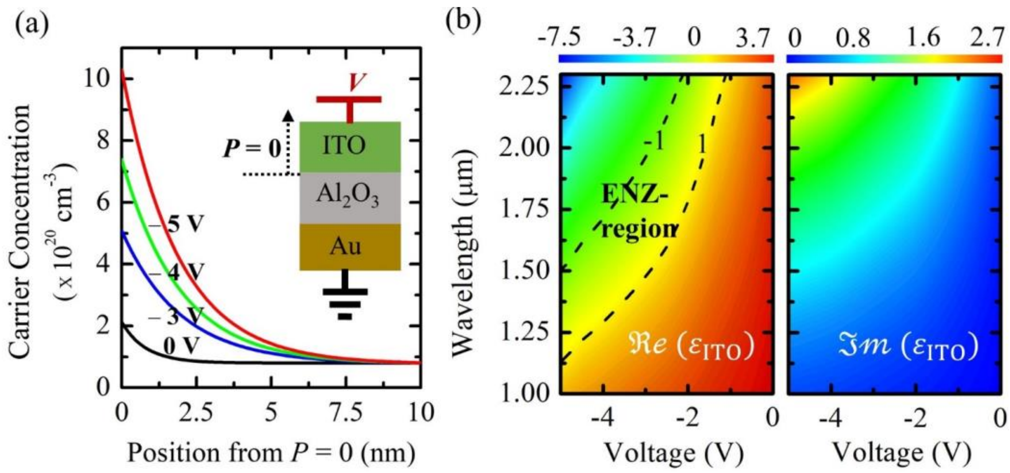

Figure 3.2: (a) The variation in carrier concentration distribution, N (cm^{-3}), of ITO layer at the position from P = 0 to 10 nm for different bias voltages (V). The formation of MOS-type structure containing Au–Al_2O_3–ITO layers is shown in the inset, where P = 0 represents the ITO–Al_2O_3 interface. (b) The color contour plots showing the variation in real and imaginary parts of permittivity of carrier accumulation layer for different bias-voltages. The range, –1 < $\Re e\,(\varepsilon_{ITO})$ < +1, is shown as ENZ-region [180].

thickness are translated to the optical properties via Drude permittivity model, given by Eq. (2.34) of Chapter 2. The variation in real ($\Re e(\varepsilon_{ITO})$) and imaginary ($\Im m(\varepsilon_{ITO})$) parts of permittivity of charge accumulation layer as a function of bias-voltage can be seen in Figure 3.2(b). Here, the ENZ-region can be referred for the wavelength-range for which the $\Re e(\varepsilon_{ITO})$ is in between –1 to +1 [29]. In our further analyses, we consider that with a bias-voltage of –4 V and –5 V, the ENZ-wavelength can be tuned to 1.55 μm and 1.31 μm, respectively, as shown in Figure 3.2(b).

3.1.4. Theoretical Modelling

Effective medium theory (EMT) combined with modal analysis is adopted to observe the guided-mode resonance response. As the grating period of the structure is comparable to operating wavelength region, *i.e.*, $\lambda > \Lambda$ (where λ and Λ are the free-space wavelength of incident light and the grating period, respectively), the analytical method using EMT modelling stated in Chapter 2 (sub-section 2.6.1) cannot be used. Thus, a second-order expression for EMT is considered here, as mentioned in ref. [172], [173], where the effective permittivity can be expressed as a function of the λ and Λ.

The inset of Figure 3.3(a) illustrates the perspective view of the device, where the Si_3N_4 nanograting is modelled as an effective medium with uniform permittivity, given by [173]:

$$\varepsilon_{\mathrm{eff},\parallel}{}^{(2)} = \varepsilon_{0,\parallel} + \frac{\pi^2}{3} f^2 (1-f)^2 \times \left(\frac{1}{\varepsilon_{\mathrm{s}}} - \frac{1}{\varepsilon_{\mathrm{Air}}}\right)^2 \varepsilon_{0,\parallel}^3\, \varepsilon_{0,\perp} \left(\frac{\Lambda}{\lambda}\right)^2 \tag{3.1}$$

where $\varepsilon_{\mathrm{eff},\parallel}{}^{(2)}$ denotes the second-order effective permittivity of nanograting for parallel or *x*-polarized light [173], [176]. Whereas, the $\varepsilon_{0,\parallel}$ and $\varepsilon_{0,\perp}$ are the zero-order effective permittivity for *x*- and *y*-polarized light, respectively, given by [35]:

$$\varepsilon_{0,\parallel} = f(\varepsilon_{\mathrm{s}}) + (1-f)\varepsilon_{\mathrm{Air}} \tag{3.2.i}$$

$$\varepsilon_{0,\perp} = \varepsilon_{\mathrm{s}}\varepsilon_{\mathrm{Air}} / [f(\varepsilon_{\mathrm{Air}}) + (1-f)\varepsilon_{\mathrm{s}}] \tag{3.2.ii}$$

where ε_{s} and $\varepsilon_{\mathrm{Air}}$ are the permittivity of silicon-nitride and air, respectively, and λ is the free-space wavelength. The filling fraction (*f*) is calculated as $f = w^2/\Lambda^2 = 0.75$ for grating period (Λ) and width (*w*) of 800 nm and 600 nm, respectively. The refractive indices of Si_3N_4, Si, Al_2O_3, and Au are taken from literature [182], [183]. For a normally incident light, it is observed that only TM-modes are excited in the proposed structure for the considered wavelength regime.

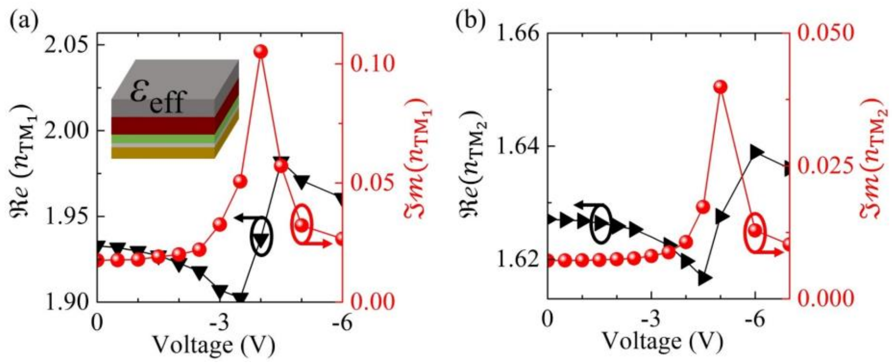

Figure 3.3: The real and imaginary part of modal index as a function of bias-voltage for guided TM_1-mode (a) and TM_2-mode (b). Here, the modelling of the silicon-nitride grating as a homogeneous medium with permittivity of ε_{eff}, by using effective medium approximation, is shown in inset of (a). Note that, the operating wavelength is taken as 1.55 µm for (a) and 1.31 µm for (b) [180].

The resonance responses (dips in the reflectance spectrum) at the wavelengths (λ_{TM}) may be observed that satisfy the first order (*i.e.*, $m = \pm 1$) grating equation, expressed as [31]:

$$\lambda_{\text{TM}} = |n_{\text{TM}}\Lambda/m| = n_{\text{TM}}\Lambda \tag{3.3}$$

where n_{TM} is the effective mode index and λ_{TM} denotes the free-space excitation wavelength of the guided TM-mode for a normally incident light. To observe the multiple resonances due to the excitation of waveguide-modes, we have combined the EMT-approximation with modal analysis, where the eigenvalue-equations are solved by using Lumerical Mode. Without applying any bias-voltage, we find that an *x*-polarized normally incident light can excite the TM_1-mode and TM_2-mode with effective index (n_{TM}) of ~1.932 and ~1.629, respectively. This leads to the resonance dips in the reflection spectrum at the vicinity of 1.55 µm and 1.31 µm, as per Eq.(3.3).

The resonance wavelengths can be tuned by applying external bias-voltage. Figure 3.3(a) and (b) illustrate the variation of complex modal index (both real and imaginary parts) as a function of bias-voltage for TM_1-mode (at 1.55 μm) and TM_2-mode (at 1.31 μm), respectively. Both real and imaginary parts of modal index (n_{TM}) play vital roles to provide active tuning of the resonance conditions.

Here, we would like to emphasize that when we tune the ENZ-condition to the resonant wavelength, a rise in the imaginary part of modal index is observed — leading to the large propagation loss (α) along the waveguide, given by [34], [40]:

$$\alpha = 10\left|\log\left(e^{\left(-\frac{4\pi}{\lambda}\Im m(n_{\mathrm{TM}})\right)}\right)\right| \quad \left(\frac{\mathrm{dB}}{\mu\mathrm{m}}\right). \tag{3.4}$$

The rise in modal loss results in a very short propagation length of the guided TM_1- and TM_2-modes. In those cases, the coupling of incident light to the waveguide modes diminishes, resulting in an OFF-resonance condition.

3.1.5. Simulation Results: Dual-Band Modulation

To investigate the modulation of reflected light intensity, a 3D finite-difference time-domain (FDTD) simulation model is adopted by considering perfectly matched layer (PML) boundary conditions along the z-directions and periodic boundary conditions along x- and y-directions. We have considered a very fine meshing at the ITO–Al_2O_3 interface. The variation in the reflectance (R) spectra with respect to the bias-voltage can be seen in Figure 3.4(a) and (b). At the unbiased state (0 V), due to the coupling of incident light to TM_1- and TM_2-mode, we can see resonance dips in the reflectance spectra at 1.55 μm and 1.31 μm, respectively, which we refer to as ON-resonance conditions.

On the other hand, when ITO exhibits ENZ-phenomenon at the vicinity of 1.55 μm for –4 V biasing, the resonance dip for TM_1-mode in the reflectance spectra will disappear due to high propagation loss, as shown in Figure 3.4(a), *i.e.*, OFF-resonance condition. Similarly, if we further tune the ENZ-wavelength at the vicinity of 1.31 μm

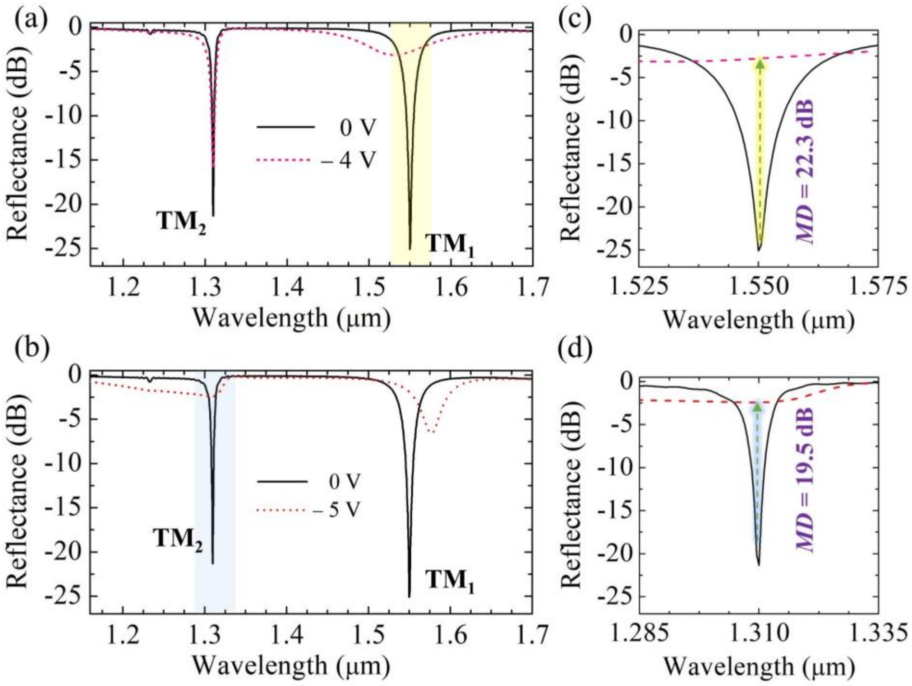

Figure 3.4: Reflectance (*R*) spectra, in dB, of the proposed metasurface showing the variation of resonance responses as a function of applied bias voltages considering (a) modulation at 1.55 μm (highlighted in yellow background) while switching between 0 V and –4 V bias and (b) modulation at 1.31 μm (highlighted in blue background) while switching between 0 V and –5 V bias. Here, at 0 V bias, the resonance responses occur at 1.55 μm and 1.31 μm for TM_1-mode and TM_2-mode, respectively. The modulation depth (MD) at (c) 1.55 μm and (d) 1.31 μm are shown as enlarged view of highlighted portions of (a) and (b) [180].

by applying –5 V, the resonance dip for TM_2-mode will disappear, as shown in Figure 3.4(b). This results in a modulation of incident light by switching ON-resonance (0 V biasing) and OFF-resonance (biased at ENZ-condition) states at the corresponding wavelength. The modulation depth (MD) can be defined by:

$$\text{MD}\,(\lambda) = 10\log\left|\frac{I_{\text{ON}}\,(\lambda)}{I_{\text{OFF}}\,(\lambda)}\right| \quad (\text{dB}), \tag{3.5}$$

where $I_{\text{OFF}}\,(\lambda)$ and $I_{\text{ON}}\,(\lambda)$ denote the intensity of reflected light for OFF- and ON-resonance conditions, respectively, as a function of wavelength. We achieve a MD as high as ~22.3 dB (~19.5 dB) at 1.55 μm (1.31 μm) while switching between 0 V and –4 V (–5 V) external biasing states, as shown in Figure 3.4(c) and (d).

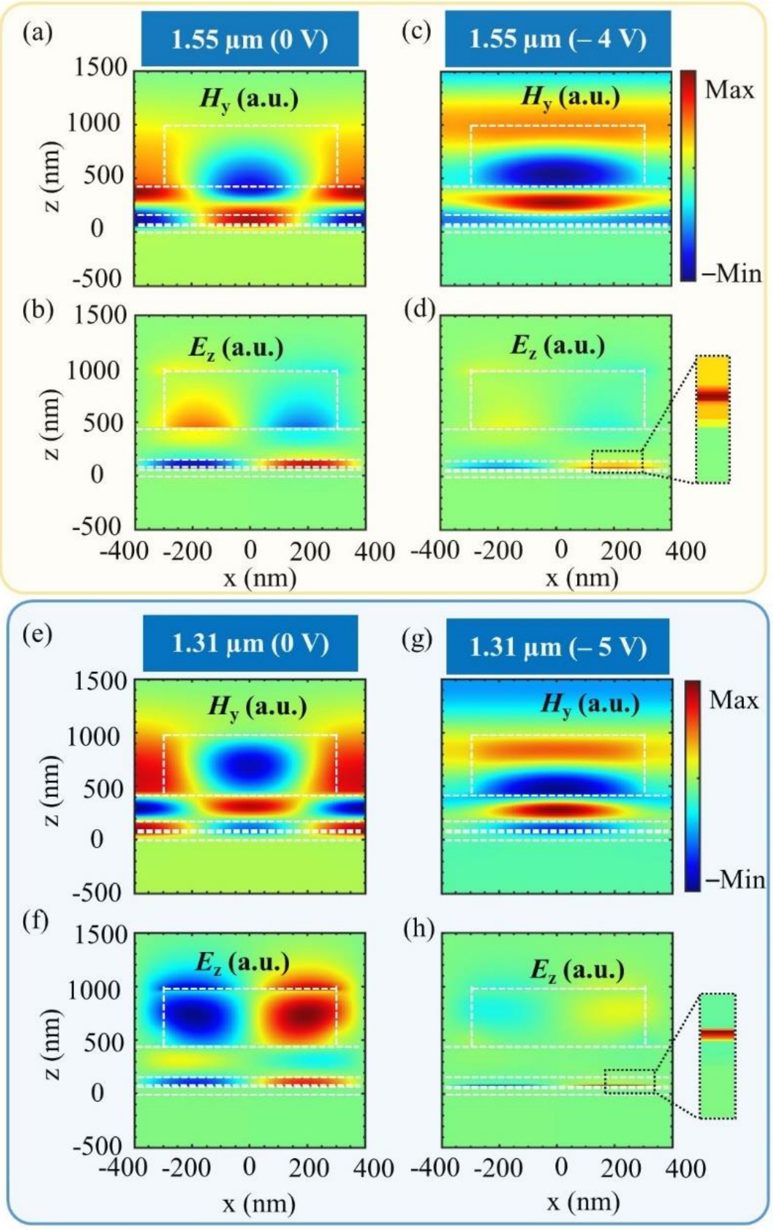

Figure 3.5: Normalized magnetic field (H_y) and electric field (E_Z) distributions in x-z plane for (a and b) 0 V and (c and d) –4 V biasing states at 1.55 μm. Normalized H_y- and E_Z-field distributions in x-z plane for (e and f) 0 V and (c and d) –5 V biasing states at 1.31 μm. The E_Z-field confinement at the ENZ-layer is shown by the enlarged view of (d) and (h). Here, the white dashed lines refer to the underlined structure [180].

The normalized magnetic field (H_y) and normalized electric field (E_z) distributions at 1.55 µm and 1.31 µm are shown in Figure 3.5(a–h) for different biasing conditions. At the unbiased state (0 V), as shown in Figure 3.5 (a–b) and (e–f), we can see the excitation of TM_1-mode and TM_2-mode due to the coupling of incident light at 1.55 µm and 1.31 µm, respectively. On the other hand, if we apply –4 V bias, the GMR-effect disappeared at 1.55 µm, as depicted in Figure 3.5(c) and (d). Similarly, at –5 V biasing condition, the resonance phenomenon at 1.31 µm disappears, as shown in Figure 3.5(g) and (h). Moreover, an enhancement of electric field is observed inside the ENZ-layer due to the strong light–matter interactions at ITO–Al_2O_3 interface, as illustrated in the enlarged view of Figure 3.5(d) and (h). This electric field enhancement can be described by applying boundary conditions, where the normal component of the electric flux density is continuous at ITO–Al_2O_3 interface, as discussed in Chapter 1 (sub-section 1.2.2). The enhancement factor will reach its maximum value at the ENZ-condition, as per Eq. (1.3), and the coupling of incident light to the waveguide modes diminishes due to high modal loss. Thus, the device behaves as a multi-layered structure with a reflective back-plane.

3.1.5.1. Requirements of Minimum Number of Grating Periods

The smallest lateral dimensions of the device, or more specifically the minimum number of grating periods (P_N), required to sustain a sharp guided-mode resonance depends on the Q-factor of the resonance, which can be given by [175]:

$$P_N > Q/\pi , \qquad \text{where, } Q = \lambda_{TM}/\Delta\lambda \tag{3.6}$$

Here, λ_{TM} is the resonant wavelength and $\Delta\lambda$ is the spectral bandwidth, which can be expressed by [175]:

$$\Delta\lambda = \frac{\lambda_0 \Lambda}{\pi L} , \tag{3.7}$$

where Λ is the grating period and L is the propagation length (or loss length) of the particular guided-mode, which can be expressed by [31]:

$$L = \frac{\lambda_{\mathrm{TM}}}{2\pi \times \Im m(n_{\mathrm{TM}})}, \tag{3.8}$$

where $\Im m(n_{\mathrm{TM}})$ is the imaginary part of modal index at the resonant wavelength λ_{TM}. Without applying any bias-voltage, we find that normally incident *x*-polarized plane wave can excite TM_1-mode and TM_2-mode with effective index of (1.932 + 0.01732713i) and (1.629 + 0.008573i), respectively. Accordingly, the loss length of the TM_1-mode can be calculated as ~15 µm, which results in a spectral bandwidth $\Delta\lambda \approx 26$ nm. Thus, the Q-factor of the resonance for TM_1-mode is 59 — leading to $P_N = 19$.

On the other hand, with a higher Q-factor of 96 for TM_2-mode, the minimum number (P_N) of grating periods required to sustain a sharp resonance is around 30. So, for our dual-mode design we require at least 30 periods. Therefore, to accommodate 30 periods of the grating with 800 nm periodicity we need to have a device dimension of around 25 × 25 µm^2 to sustain sharp resonances for both TM_1-mode and TM_2-mode at the vicinity of 1.55 µm and 1.31 µm, respectively. Furthermore, a conical mounting arrangement (when the grating vector is not parallel to the incidence plane) may be used to achieve a large focussing angle in the proposed GMR based structure [184], [185].

3.1.5.2. Electrical Bandwidth and Speed of the Device

It should be noted that due to the ultrafast formation of the carrier accumulation layer, the 3-dB modulation bandwidth is impeded by the RC-time constant of the modulator (here, *R* is the equivalent device resistance, and *C* is the capacitance formed by MOS-type structure) [45]. To find the *RC*-limited electrical bandwidth of the modulator while maintaining minimum number of grating periods required to sustain a sharp GMR-effect, the effective device resistance (*R*) and capacitance (*C*) need to be estimated. The capacitance per unit cell area is estimated as ~10.97 fF/µm^2 by performing electrostatic simulations on Lumerical Device. Thus, for a device having dimensions of 25 × 25 μm^2, the total capacitance (C) is approximated as ~6.8 pF.

The effective resistance of the device can be approximated as $R = (R_{ITO} + R_{Gold})/2$, where R_{Gold} is the resistance for the gold layer and R_{ITO} is the resistance for the ITO layer [45]. The value of R_{ITO} can be estimated as the parallel combination of R_{ITO} (for bulk ITO-layer) and R_{ACL} (for charge-accumulation layer) with a carrier concentration, N, of 7 × 10^{19} cm^{-3} and 6.46 × 10^{20} cm^{-3}, respectively.

Then, for each corresponding layer, the resistance can be derived by using $R_0 = (\rho l_0/t w_0)$, where w_0 and l_0 are the width and length of the device, respectively. Here, t is the thickness and ρ is the resistivity of the corresponding layer. The resistivity of gold layer can be approximated as 2.2 × 10^{-8} Ω.m [186]. In contrast, the resistivity of a semiconductor depends on the carrier mobility (μ), given by, $\rho = (e\mu N)^{-1}$.

Thus, the resistivity of bulk ITO-layer (with μ = 19.5 cm^{2}V^{-1}s^{-1}) and accumulation layer (with μ = 13 cm^{2}V^{-1}s^{-1}) can be calculated as 4.57 × 10^{-5} Ω.m and 7.5 × 10^{-6} Ω.m, respectively [133]. This results in an effective device resistance (R) of ~280 Ω — leading to a 3-dB bandwidth, $f_{3dB} = (2\pi RC)^{-1}$, of ~83.5 MHz. We have also approximated the bit-rate (BR) as ~167 Mbps by applying Nyquist theorem ($BR = 2 \times f_{3dB} \times \log_2 \kappa$, where $\kappa = 2$ denotes the number of signal levels).

The energy consumption, E_b (J/bit) = $\left| CV_{bias}^2/4 \right|$, is also another aspect that needs to be considered while designing an electro-optic modulator to estimate the energy required to switch a bit in the modulation scheme [136]. With a maximum applied voltage as –5V and the effective capacitance (C) of ~6.8 pF, the energy consumption (E_b) of the modulator can be estimated as ~4300 fJ/bit.

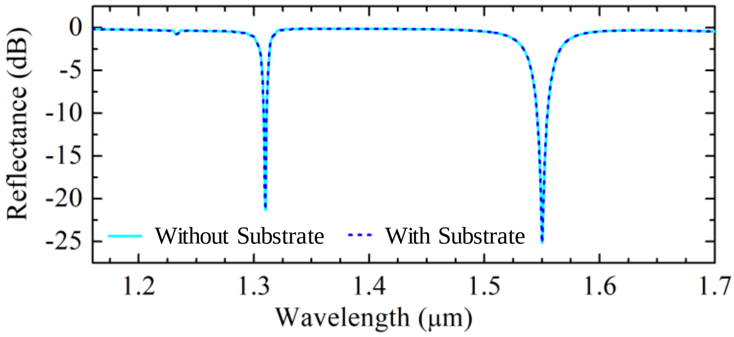

Figure 3.6: Reflectance (*R*) spectra, in dB, of the proposed metasurface with a 500 nm thick silica substrate at 0 V bias. The resonance responses occur at 1.55 μm and 1.31 μm for TM_1-mode and TM_2-mode, respectively [180].

3.1.5.3. Effect of Substrate

The numerical simulation results reveal that due to the presence of an optically thick Au back-plane, there will be no effect on the resonance dips in the reflectance spectra if we include a 500 nm thick silica substrate, as shown in Figure 3.6. Inclusion of a substrate will provide mechanical strength of the device without effecting the resonance dips in the reflection spectra.

3.1.5.4. Study of Fabrication Imperfection due to Rounded-edges

Here, we would like to emphasize on the fact that while studying optical properties through numerical simulation analysis, we assume that there will be sharp edges at the nanograting pattern. However, in practical scenario, these sharp edges may not be achieved after fabrication. Thus, to study and incorporate the fabrication imperfections and roughness that arise from the rounded-edges of the nanograting, we have simulated our design by rounding the edges (with a 10 nm and 20 nm rounding radius) [56].

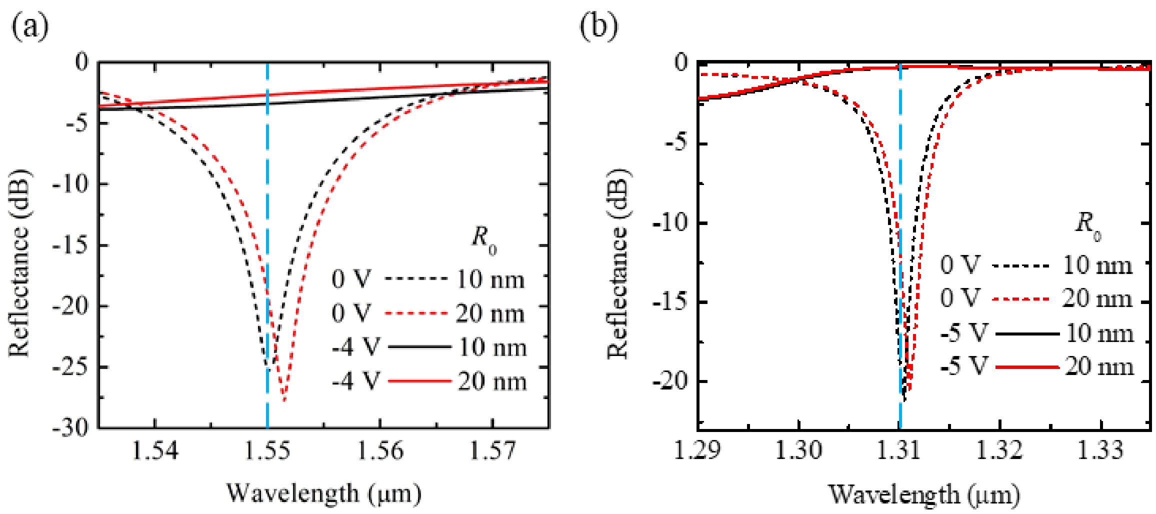

Figure 3.7: Reflectance (R) spectra, in dB, of the proposed metasurface with two different rounding radius (10 nm and 20 nm) at the edges of the nanograting, showing the variation of resonance responses as a function of applied bias voltages considering (a) modulation at 1.55 μm while switching between 0 V and –4 V bias and (b) modulation at 1.31 μm while switching between 0 V and –5 V bias. Note that the dashed vertical lines depict the wavelength of (a) 1.55 μm and (b) 1.31 μm.

Figure 3.7 (a) depicts the modulation of light at 1.55 μm while switching between 0 V and –4 V bias with rounding radius (R_0) of 10 nm and 20 nm. Note that the dashed vertical line depicts the wavelength of 1.55 μm. At the unbiased state (0 V), we can see resonance dips in the reflectance spectra are getting red-shifted from 1.55 μm with the increase of the rounding radius. On the other hand, when ITO exhibits ENZ-phenomenon at the vicinity of 1.55 μm for –4 V biasing, the resonance dip in the reflectance spectra will disappear as we predicted before, *i.e.*, OFF-resonance condition. This results in a modulation depth of ~21.7 dB and ~19.5 dB at 1.55 μm with rounding radius of 10 nm and 20 nm, respectively, while switching between 0 V and –4 V bias, which indicates that we can still maintain a modulation depth of around 20 dB at 1.55 μm.

Similarly, Figure 3.7(b) depicts the modulation of light at 1.31 μm while switching between 0 V and –5 V bias with rounding radius of 10 nm and 20 nm. We have witnessed the red-shift of the resonance dips from 1.31 μm at the unbiased state (0 V) with the increase of the rounding radius. With an electrical bias of –5 V, the resonance dip in the reflectance spectra will disappear leading to a modulation depth of ~17 dB and ~13.7 dB at 1.31 μm with rounding radius of 10 nm and 20 nm, respectively.

3.1.5.5. Comparative Analysis

A comparative overview with a few recently reported ENZ-material based optical modulators can be seen in

Table 3.1: Comparative Overview of a Few Recently Reported Theoretical Designs of ENZ-material based Modulators

Ref.	λ (μm)	MD (dB)	Speed (Mbps)	Dual-band Operation
Forouzmand *et al.* [30]	1.537	~12.5	NA	No
Kim *et al.* [5]	1.480	~13.3	NA	No
Vatani *et al.* [45]	1.550	24	~80	No
Forouzmand *et al.* [145]	1.547, 1.564	23.3, 23.7	NA	No
Qiu *et al.* [141]	1.510, 1.512	14, 20	NA	No
This Work	1.550, 1.310	**~22.3, ~19.5**	**~167**	**Yes**

Here, MD: modulation depth, λ: operational wavelength, and NA: not available.

Table **3.1**. Here, we would like to emphasize on the fact that most of the previously reported designs are either operated on a single wavelength orual-wavelengths restricted to a single band. In contrast, our design can operate in both C-band and O-band of wavelength region while maintaining a MD as high as ~22.3 dB (at 1.55 µm) and ~19.5 dB (at 1.31 µm), respectively.

3.1.6. Summary

We theoretically presented a **tunable metasurface for dual-band electro-optic intensity modulation** by leveraging the ENZ-phenomenon of ITO and GMR-effect of grating waveguide. Effective medium approximation combined with modal analysis was utilized to study the multiple resonance responses because of the excitation of waveguide modes by coupling of incident light. We observed a rise in the modal loss if ENZ-wavelength of ITO is electrically-tuned to the operating wavelength-band. This rise in the modal loss is responsible for the disappearance of GMR-effect. Thus, we could achieve a **modulation depth as high as ~22.3 dB (~19.5 dB) at 1.55 µm (1.31 µm) with ~167 Mbps modulation speed**. To the best of our knowledge, such a dual-band (operating at both C-band and O-band wavelength region) metasurface for electro-optic intensity modulation is presented here for the first time. The metasurface could find potential applications towards realization of active flat optical components in nanophotonic systems.

3.2. Gap Plasmon Resonance based Modulator: Incident-Angle Insensitive Design

In the previous Section, a GMR based design has been introduced to achieve dual-band electro-optic intensity modulation by leveraging the ENZ phenomenon. Though the design could exhibit a high modulation depth, the major bottleneck comes from the incident angle sensitivity of the design. More specifically, the presented GMR based device can only be operated with the normally incident light. With the change of incident light angle, the resonance wavelengths will get shifted from the operating wavelength regime. This angle-specific nature of a device introduces several limitations, such as it may increase the overall cost and footprint of the photonic system due to the requirement of complex arrangements of several opto-mechanical components. Moreover, due to the narrow band resonance phenomena of the GMR based structure, the intensity modulation of reflected light couldn't achieve for the whole C-band and O-band of wavelength regime.

This section introduces a gap plasmon resonance (GPR) based electro-tunable metamaterial that can modulate the reflected light intensity for a wide variation of incident angle operating at both C-band and O-band of wavelength regime. We leverage GPR mode of a metal–insulator–metal (MIM) structure and ENZ phenomenon of ITO to enable dynamic control of reflected light intensity. The operating principle of the typical GPR based design relies on the confinement of electromagnetic field inside the insulator layer sandwiched between two metallic layers having the top layer as a sub-wavelength grating arrangement. In this case, we can get a wide incident angle insensitivity due to the fact that the incident beam with different incident angles can be absorbed to satisfy the resonance condition.

The coupling of GPR-mode with ENZ-mode is observed when an external bias-voltage is applied. This results in a broadening of resonance with more than 80% absorption over a 370 nm spectral window ranging from 1.25 μm to 1.62 μm.

Such dynamic control of absorption properties is then utilized for intensity modulation of the reflected light. The metamaterial exhibits dual-band intensity modulation of reflected light with an extinction ratio (or modulation depth) as high as 20.5 dB and 16.6 dB at 1.55 μm and 1.31 μm of wavelength, respectively, while switching between 0 V and 5 V biasing conditions. Most importantly, this GPR based device can be operated with a wide range of incident angle (up to 60 degrees) for *x*-polarized light. This tunable metamaterial could help in realizing incident angle-insensitive optical modulators operating at different wavelength bands for nanophotonic systems.

3.2.1. Structural Overview

The 3D schematic of the proposed electro-tunable metamaterial absorber is illustrated in Figure 3.8(a). The design consists of an array of Au-nanograting on cascaded layers of an Al_2O_3 oxide-layer, an ITO active layer, a SiO_2 buffer layer deposited on a highly

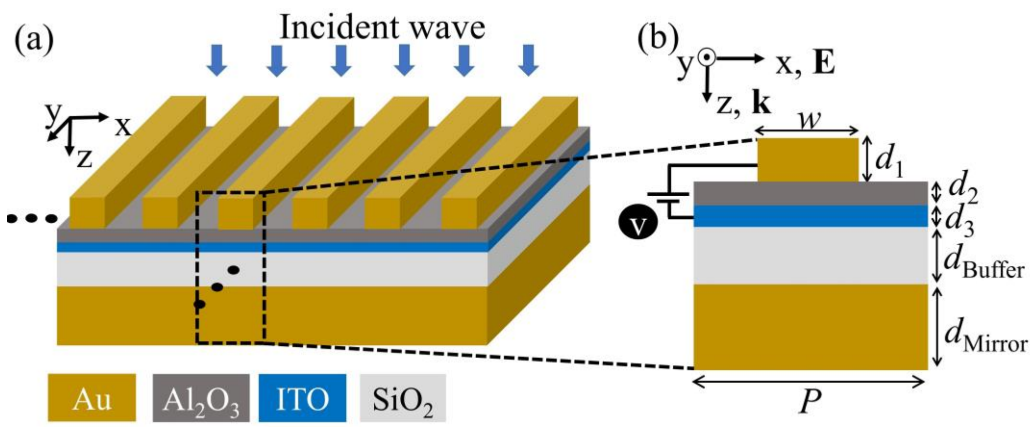

Figure 3.8: Schematic of the designed gap-plasmon resonance based electro-tunable metamaterial absorber consisting of an array of Au-nanograting on top of Al_2O_3–ITO–SiO_2 stack deposited on an optically-thick Au-layer. (a) A 3D view of the metamaterial considering incident light propagating along the *z* axis. Here, the black dashed rectangle depicts a unit cell structure. (b) Side view of a unit cell with electrical biasing [189].

reflective Au-layer. The refractive indices of SiO_2, Al_2O_3 are taken as 1.445 and 1.745, respectively [183]. Whereas, the refractive index of Au is taken from the experimental data mentioned in Ref. [125]. The unit cell (side view) with periodicity P (= 700 nm) along x-direction is illustrated in Figure 3.8(b), where d_1 (100 nm) and w (230 nm) depict the height and width of Au-nanograting, respectively. The thickness of Al_2O_3 oxide-layer, ITO layer, SiO_2 buffer layer, and Au-ground plane are denoted by d_2 (= 5 nm), d_3 (= 10 nm), d_{Buffer} (= 30 nm), and d_{Mirror} (= 100 nm), respectively.

It should be noted that one can use other noble metals also as a metal back-plane and top grating layer. However, after exploring a few metals (such as gold, silver, aluminum, *etc.*) for as a metal back-plane, it was evident from the simulation trials (not shown here) that the use of gold is providing the desirable optical response to achieve the objective I, *i.e.*, a dual band modulation at the wavelengths of interest.

3.2.2. Electro-Optical Properties of ITO

In order to obtain the optical properties of ITO under the influence of applied bias, we have done the electrostatic simulation in Lumerical Device. In the device physics simulations, the parameters assumed for ITO are similar as the ones revealed in Chapter 2. The bulk carrier concentration of ITO is taken as $N = 7 \times 10^{19}$ cm^{-3}. The formation of a MOS-type structure containing Au–Al_2O_3–ITO layers is illustrated in the inset of Figure 3.9(a). The voltage-dependent carrier concentration distributions can be seen in Figure 3.9(a) at different positions inside the ITO layer from Al_2O_3–ITO interface.

Then, the charge carrier distributions inside the ITO layer are translated to the optical properties via Drude permittivity model, given by Eq. (2.34) of Chapter 2. The variation of real ($\Re e(\varepsilon_{\mathrm{ITO}})$) and imaginary ($\Im m(\varepsilon_{\mathrm{ITO}})$) parts of permittivity of ITO at the resonant wavelength (1.43 μm) are depicted in Figure 3.9(b) and (c), respectively, as a function of external biasing for the first 5 nm distance from the Al_2O_3–ITO interface. With increasing bias-voltage, the $\Re e(\varepsilon_{\mathrm{ITO}})$ changes its sign, which indicates

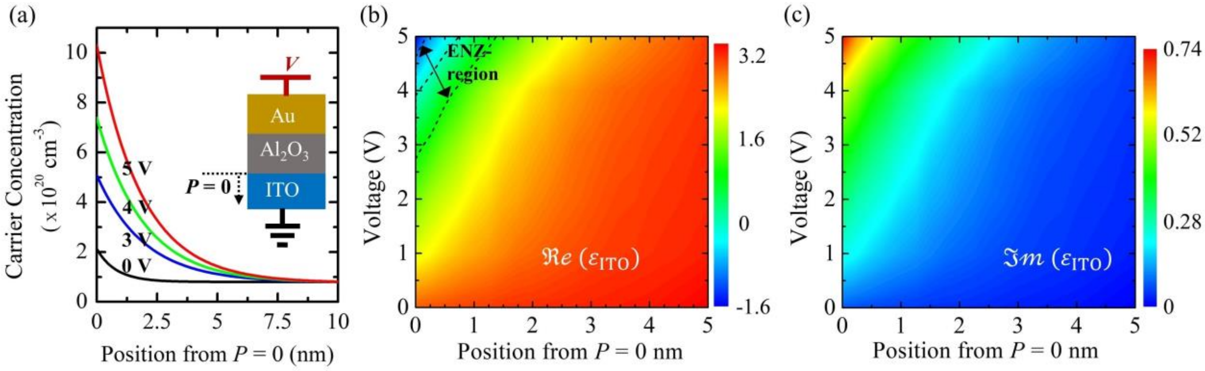

Figure 3.9: (a) The spatial distributions of ITO layer carrier concentration (*N*) from *P* = 0 to 10 nm for distinct bias-voltages. Here, the inset illustrates the MOS-type configuration consisting Au–Al_2O_3–ITO layers, where Al_2O_3–ITO interface is shown as *P* = 0. The contour plots of spatial distributions of real (b) and imaginary (c) parts of permittivity of ITO at the resonant wavelength (1.43 μm) from *P* = 0 to 5 nm for different biasing states. Note that the ENZ-regime is depicted as $-1 < \Re e(\varepsilon_{\mathrm{ITO}}) < 1$ [189].

the transition from dielectric-like behavior to metallic-like characteristics. The electrostatic simulations reveal that for a 5 V external biasing, a maximum ~4.35 MV/cm electric field is obtained across the Al_2O_3 layer, which is below than the breakdown field of Al_2O_3 [29]. Finally, we employ the two-layer model to accurately predict the optical properties of the inhomogeneous accumulation layer (ACL), similar to the procedure as mentioned in Chapter 2 (sub-section 2.4.2). As discussed previously, in the two-layer model, the inhomogeneous ACL can be estimated as an equivalent ultra-thin layer (~3 nm) of uniform carrier concentration distribution to study the optical performance of the TCO based device.

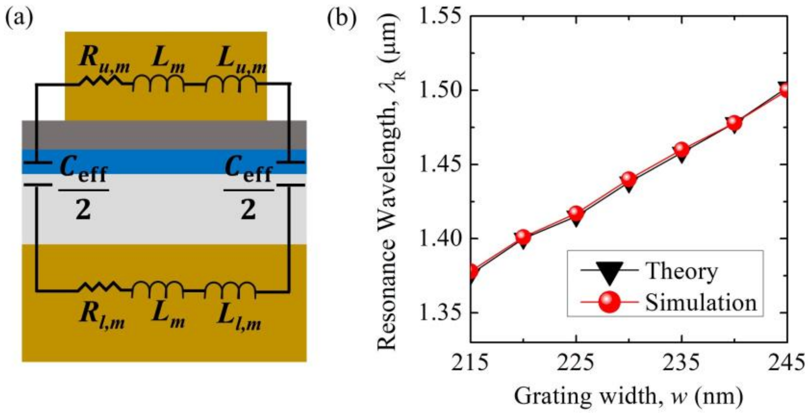

Figure 3.10: (a) The equivalent RLC-circuit model of the unit cell, shown in Fig. 3.7(b), where $R_{u,m}$ (or $R_{l,m}$) denotes the ohmic resistance, L_m denotes the Faraday inductance, $L_{u,m}$ (or $L_{l,m}$) denotes the kinetic inductance, and C_{eff} denotes the equivalent capacitance. Note that the subscript '*u*' and '*l*' are used to denote the lumped elements corresponding to the upper and lower metallic-layers, and *m* denotes the resonance mode number. (b) Resonance wavelengths (λ_R) predicted by the equivalent circuit model (black triangle block) and calculated by the FDTD simulation (red spherical blocks) [189].

3.2.3. Theoretical Framework

The *x*-polarized incident light propagating along z-direction is used to excite the GPR-mode. The subwavelength unit cell is modelled as an equivalent RLC-circuit in a similar way discussed in Chapter 2 (sub-section 2.6.2), and as is presented in Figure 3.10(a). Note that the subscripts '*u*' and '*l*' are used to denote the lumped elements corresponding to the upper and lower metallic-layers, and *m* denotes the resonance mode number. In the equivalent circuit model, $R_{u,m}$ ($R_{l,m}$) denotes the ohmic resistance, L_m denotes the Faraday inductance, $L_{u,m}$ ($L_{l,m}$) denotes the kinetic inductance due to the drifting of electrons within the skin depth of Au, and C_{eff} specifies the equivalent capacitance between the Au-blocks. Here, we can assume the adjacent unit-cells are far enough from each other and thus we can exclude the electromagnetic coupling between them.

With an initial carrier concentration of ~7×10^{19} cm^{-3}, we can assume ITO-layer as a dielectric layer due to the negligible imaginary part of permittivity in the operating wavelength region. Therefore, we can estimate an effective permittivity for the cascaded dielectric layers of Al_2O_3–ITO–SiO_2, given as:

$$\varepsilon_{\text{eff}} = \frac{\varepsilon_{\text{Al}_2\text{O}_3} \times d_2}{d_{\text{total}}} + \frac{\varepsilon_{\text{ITO}} \times d_3}{d_{\text{total}}} + \frac{\varepsilon_{\text{SiO}_2} \times d_{\text{Buffer}}}{d_{\text{total}}} \tag{3.9}$$

where the permittivity of the cascaded dielectric layers of Al_2O_3, ITO, and SiO_2 are denoted as $\varepsilon_{\text{Al}_2\text{O}_3}$, ε_{ITO}, and $\varepsilon_{\text{SiO}_2}$, respectively, and d_{total} (= $d_2 + d_3 + d_{\text{Buffer}}$) denotes the total dielectric thickness.

Based on the resonance analysis theory, the parameters of the equivalent circuit model can be given as [177]–[179]:

$$C_{\text{eff}} = \frac{\alpha \varepsilon_{\text{eff}} \varepsilon_0 w l_y}{m d_{\text{total}}} \tag{3.10}$$

$$L_{u,m} = \frac{-w}{m\delta_{\text{Au}}\omega^2 l_y \varepsilon_0} \times \left\{\frac{\varepsilon'}{(\varepsilon')^2 + (\varepsilon'')^2}\right\}_{\text{Au}} \tag{3.11}$$

$$L_{l,m} = \frac{-1}{m\delta_{\text{Au}}\omega^2 \varepsilon_0} \times \left\{\frac{\varepsilon'}{(\varepsilon')^2 + (\varepsilon'')^2}\right\}_{\text{Au}} \tag{3.12}$$

$$L_m = \frac{0.5\mu_0 w d_{\text{total}}}{m l_y} \tag{3.13}$$

$$R_{u,m} = \frac{-w}{m\delta_{\text{Au}}\omega^2 l_y \varepsilon_0} \times \left\{\frac{\varepsilon''}{(\varepsilon')^2 + (\varepsilon'')^2}\right\}_{\text{Au}} \tag{3.14}$$

$$R_{l,m} = \frac{-1}{m\delta_{\text{Au}}\omega^2 \varepsilon_0} \times \left\{\frac{\varepsilon''}{(\varepsilon')^2 + (\varepsilon'')^2}\right\}_{\text{Au}} \tag{3.15}$$

where, ω is the angular frequency of the incident wave, ε_0 and μ_0 are vacuum permittivity and permeability, respectively. The real and imaginary part of permittivity of Au-layer are denoted as ε' and ε'', respectively, which are taken from the experimental data [125].

To simplify the metamaterial modelling, we have taken a unit length of l_y (= 600 nm) along the *y*-direction. The effective skin depth of Au (δ_{Au}) in the near-infrared range is taken as 24.5 nm and α ($0.2 < \alpha < 0.3$) is the tuning factor of the effective capacitance, which depends on the resonance modes[178]. For fundamental resonance mode ($m = 1$), we have taken $\alpha = 0.2$ [177].

In the equivalent circuit, the resonance wavelength can be calculated as [177]:

$$\lambda_R = 2\pi c\sqrt{C_{\text{eff}}\left(L_m + L_{u,m} + L_{l,m}\right)} \tag{3.16}$$

where *c* is the speed of light in vacuum. Figure 3.10(b) illustrates that the resonance wavelength (λ_R) increases with grating width (*w*), which also demonstrates a good agreement with the FDTD simulations.

3.2.4. Results and Discussion

To study the optical performance of the proposed metamaterial, we use a 3D finite-difference time-domain numerical simulation model and solve the wave equations considering an *x*-polarized incident light propagating along the *z*-axis. The periodic boundary conditions are used in *x*- and *y*-axis while considering perfectly matched layer in the *z*-axis to reduce the scattering of light due to the simulation domain confinement. The unusual boundary conditions enforced by the ENZ-phenomenon enable strong light–matter interactions. An adequately fine meshing was used at the Al_2O_3–ITO interface to accurately observe the enhancement of electric field.

3.2.4.1. Tunable Broadband Metamaterial Absorber

It should be noted that with a very small real part of permittivity at the ENZ-condition, the optical properties of the ultra-thin accumulation region are solely decided by the imaginary part of the permittivity. This results in an absorption-dominated optical

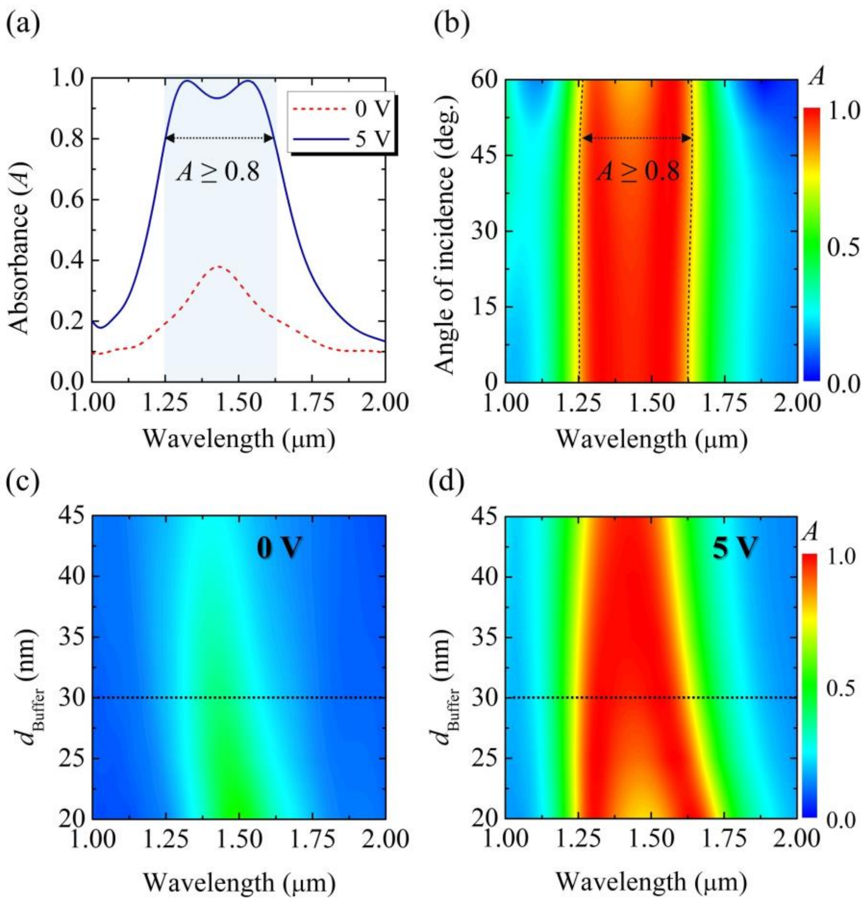

Figure 3.11: (a) Absorbance spectra (between 1 μm and 2 μm) at normal incidence for 0 V and 5 V bias voltages. Note: the shaded region depicts a 370 nm-wide wavelength window, where absorbance (*A*) is more than 0.8 for 5 V bias. (b) Color contour plot of absorbance spectrum as a function of incidence angle for 5 V biasing condition. Contour plot of absorbance spectrum as a function of buffer layer thickness (d_{Buffer}) for (c) 0 V and (d) 5 V biasing conditions. Here, horizontal black dashed lines represent optimized value of d_{Buffer} [189].

response leading to dynamic control of absorption properties of light at nanoscale. Thus, the proposed device can be treated as an electro-tunable metamaterial absorber. The existence of an optically-thick Au-ground layer ensures zero transmittance and thus, the reflectance (*R*) and absorbance (*A*) of the proposed structure are related by $A(\lambda) = 1 - R(\lambda)$ [187], [188].

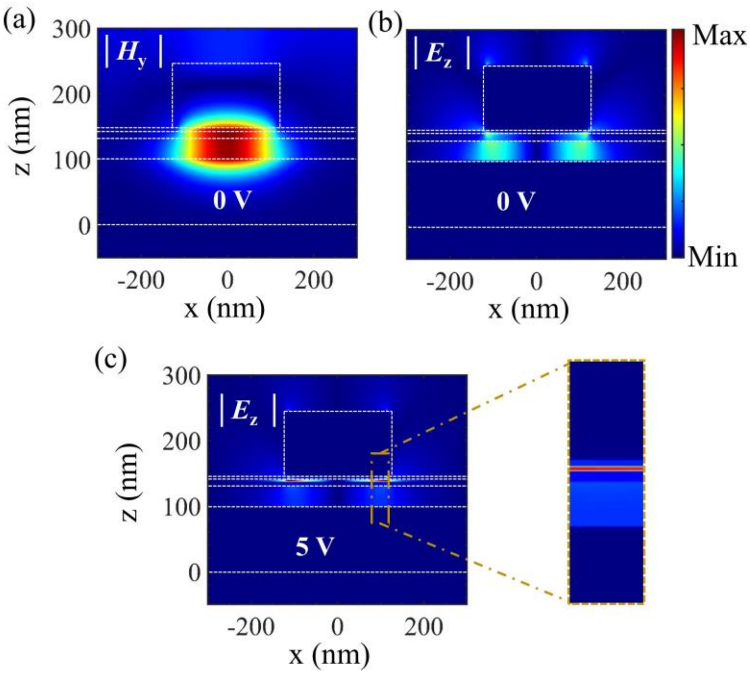

Figure 3.12: The normalized (a) magnetic (H_y) and (b) electric (E_z) field distributions at the resonance wavelength (1.43 µm) for 0 V biasing condition. Note that the underlined structure is presented by white dashed lines. (c) Normalized electric (E_z) field distributions at 1.43 µm wavelength for 5 V biasing condition, where enhancement of electric field is shown by an enlarged view [189].

The variations in the absorbance (*A*) spectrum for 0 V and 5 V are shown in Figure 3.11(a). At the unbiased condition, we can see the gap-plasmon resonance wavelength appears at 1.43 µm. On the other hand, when a 5 V bias-voltage is applied, a dramatic enhancement of absorbance can be seen due to the coupling of GPR-mode with ENZ-mode. Thus, we achieved more than 80% of absorbance (*A)* over a 370 nm wavelength window ranging from 1.25 µm to 1.62 µm, as shown in Figure 3.11(a).

To understand the device performance under the influence of oblique incidence angle of the impinging light, we have studied the absorbance spectrum for a wide incident angle ranging from 0 degrees to 60 degrees for 5 V bias, as shown by color contour plot in Figure 3.11(b). The wavelength region for which the absorbance can be achieved more than 0.8, is shown in Figure 3.11(b) — indicating the wide angle-insensitivity of the device.

The variation in the absorbance (*A*) spectrum with respect to the buffer layer thickness (d_{Buffer}) for 0 V and 5 V biasing states can be seen in Figure 3.11(c) and (d), respectively. At the unbiased state (0 V), the gap-plasmon resonance wavelength decreases with the increase of buffer layer thickness (d_{Buffer}). On the other hand, at 5 V biasing condition, we observe an enhancement and broadening of resonance response in the absorbance spectrum. We have chosen the buffer layer thickness (d_{Buffer}) as 30 nm to achieve absorbance of more than 0.8 (or equivalently 80%) for a 370 nm-wide wavelength region ranging from 1.25 µm to 1.62 µm.

Figure 3.12(a) and (b) depict the normalized magnetic (H_y) and electric (E_z) field distributions, respectively, at the resonance wavelength (1.43 µm) for 0 V biasing condition. The confinement of H_y-field inside the cascaded dielectric layers reveals the excitation of GPR-mode. Whereas, at 5 V biasing condition, due to the ENZ-mode excitation, an enhancement of E_z-field has been observed at the Al_2O_3–ITO interface, as presented by the enlarged view of Figure 3.12(c).

This electric field enhancement can be described by applying boundary conditions, where the normal component of the electric flux density is continuous at ITO–Al_2O_3 interface, as discussed in Chapter 1 (sub-section 1.2.2). When ITO exhibits ENZ-effect, the denominator of Eq. (1.3) is negligible, which leads to the enhancement of electric field at the Al_2O_3–ITO interface, as shown by the red hot-spot region seen in the enlarged view of Figure 3.12(c).

3.2.4.2. Dual-Band Optical Intensity Modulation

Figure 3.13(a) shows the pictorial representation of an electro-optic intensity modulator based on tunable absorption in the proposed metamaterial. Here, we would like to emphasize that the existence of an optically-thick Au-ground layer ensures zero transmittance and thus, the reflectance (*R*) and absorbance (*A*) are related by $A(\lambda) = 1 -$

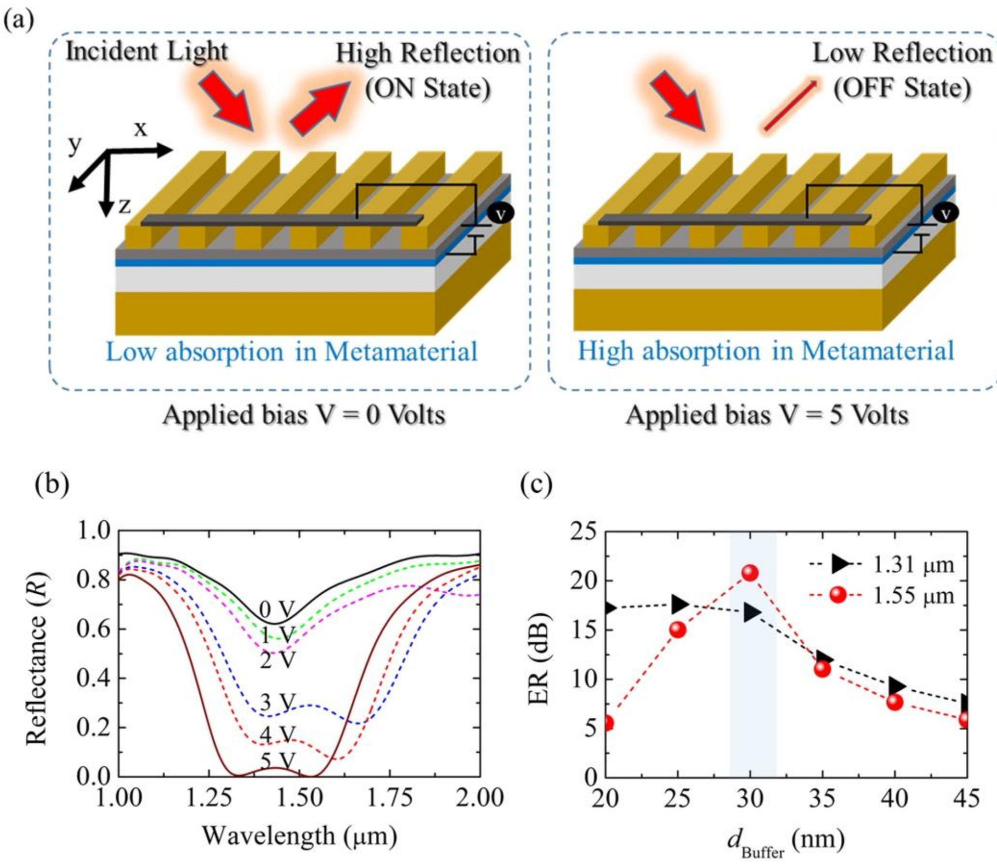

Figure 3.13: (a) Schematic of an electro-optic intensity modulator based on tunable absorption in the proposed metamaterial, where the metamaterial strongly reflects incident light at 0 V bias (left) and strongly absorbs the incident light at 5 V bias (right)—leading to intensity modulation of the reflected light. (b) The variation in the light intensity at the reflectance spectrum with respect to applied bias-voltages. (c) The extinction ratio (*ER*) as a function of buffer layer thickness (d_{Buffer}) for 1.55 μm and 1.31 μm. Note that the shaded region denotes the preferred buffer layer thickness, d_{Buffer} = 30 nm, for which we obtain $ER \approx 20.5$ dB at 1.55 μm while maintaining $ER \approx 16.6$ dB at 1.31 μm [189].

R(λ). This enables a modulation of reflected light when the metamaterial absorbs the incident light under the influence of applied bias-voltage.

In other words, if we place a receiver (photodetector) at the reflection port (as output port), we can establish a free-space intensity modulation scheme, as depicted in Figure 3.13(a). At 0 V bias, the metamaterial reflects most of the input light, which can be referred as "ON-state". Whereas, if we apply a 5 V bias, the metamaterial absorbs the input light — leading to near-zero reflectance at the output. We refer it as "OFF-state". Therefore, by utilizing the dynamic control of absorption properties, we can realize the modulation of output light intensity.

The variation in the intensity at the reflectance spectrum with respect to various voltages can be seen in Figure 3.13(b). We have optimized our design to maintain reflectance level more than 0.7 at the output for 1.55 μm and 1.31 μm wavelengths simultaneously, when there is no bias-voltage (0 V) for the gap-plasmon resonance wavelength of 1.43 μm. On the other hand, with the increase of bias-voltage, the ENZ-wavelength of ITO shifts towards the operating wavelength region. This leads to the coupling of ENZ-mode with GPR-mode and results in a broadening of resonance dip in the output spectrum. For 5 V biasing, when the ENZ-wavelength of ITO perfectly coincides with the gap-plasmon resonance wavelength, we observe an enhancement of resonance response due to the strong coupling of GPR-mode with ENZ-mode, as shown in Figure 3.13(b).

Here, we would like to emphasize that for 5 V applied bias, the broadening of the resonance dip covers both of the two key telecommunication wavelength bands, *i.e.*, O-band and C-band. Thus, we can modulate intensity of reflected light at both these wavelength bands while switching between the two external biasing states: 0 V (ON-state) and 5 V (OFF-state). Moreover, the variation in the extinction ratio (*ER*) or modulation depth as a function of buffer layer thickness, d_{Buffer}, can be seen in Figure 3.13(c), which is defined by:

$$ER\ (\lambda) = 10\log\left|\frac{I_{\text{ON}}(\lambda)}{I_{\text{OFF}}(\lambda)}\right| \tag{3.17}$$

where $I_{\text{ON}}\ (\lambda)$ and $I_{\text{OFF}}\ (\lambda)$ denote the intensity of the reflected light as a function of wavelength for 0 V (ON-state) and 5 V (OFF-state) external biasing states, respectively. With a buffer layer thickness of 30 nm, we have achieved *ER* as high as ~20.5 dB and

~16.6 dB at 1.55 µm and 1.31 µm, respectively, while switching between 0 V and 5 V biasing states, as shown in the shaded region of Figure 3.13(c). Moreover, this GPR based device can be operated with a wide range of incident angle (up to 60 degrees) as previously depicted by in Figure 3.11(b), where a high absorbance for 5V bias is achieved for a broadband wavelength regime covering the C-band and O-band — indicating the wide angle-insensitivity of the device.

Till now, we have emphasized about the modulation of reflected light at the two key telecommunication wavelength bands, *i.e.*, O-band and C-band. However, as can be seen from Figure 3.13(b) the device may also be useful for optical intensity modulation at other wavelength bands which lies within the spectral-window of 1.25 µm to 1.62 µm where strong absorption in the biased condition would result in negligible output intensity of the reflected light.

3.2.4.3. Electrical Bandwidth and Speed of the Device

To estimate the modulation speed of the proposed device which is restricted by *RC*-time constant, the equivalent capacitance (*C*) and resistance (*R*) of the device need to be calculated. The equivalent capacitance per unit area of a unit cell (C_{UC}) is approximated as ~10.2 fF/µm^2 by condcuting electrostatic simulations on Lumerical Device tool. Assuming a total device dimension of 10 × 10 µm^2, we can approximate the equivalent capacitance as $C \approx 1.02$ pF for a maximum bias voltage of 5V.

We can estimate the equivalent resistance (*R*) of the device, as $R = (R_{ITO} + R_{Au})/2$, where R_{ITO} and R_{Au} are the resistance of ITO and Au layers, respectively. The R_{ITO} can be seen as a parallel combination of R_{Bulk} (for bulk ITO-region) and R_{acl} (for accumulation layer). Here, we assume the carrier concentration for bulk ITO region as 7 × 10^{19} cm^{-3} and for accumulation region as 6.7 × 10^{20} cm^{-3}. Each corresponding layer has a resistance of $R_0 = (\rho L/dW)$, where *W* and *L* are the total device width and length, respectively. Here, ρ and *d* denote the resistivity and thickness of respective layers. The R_{Au} can be calculated by assuming resistivity of Au layer as ~2.2 × 10^{-8} Ω.m [186]. On

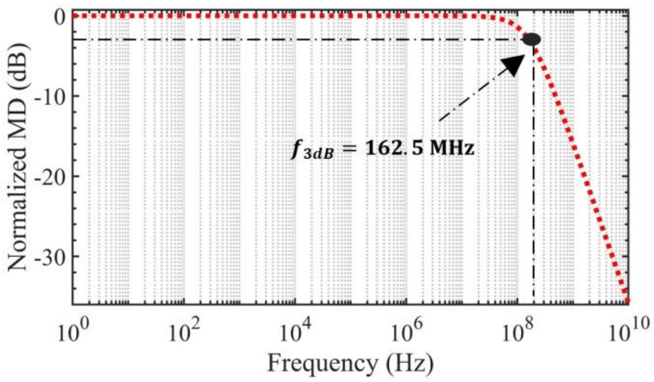

Figure 3.14: Frequency response of the modulator for input electrical bias signal (with frequency up to 10 GHz), where the 3-dB electrical bandwidth f_{3dB} = 162.5 MHz, is shown by the arrowed dashed-dot line [189].

the other hand, the resistivity (ρ) of ITO depends on electron mobility (μ), given as: $\rho = (e\mu N)^{-1}$.

Thus, we can calculate the resistivity of bulk ITO region as ~4.57×10^{-5} Ω.m (for $N = 7 \times 10^{19}$ cm^{-3}) and for accumulation layer as ~7.13×10^{-6} Ω.m (for $N = 6.7 \times 10^{20}$ cm^{-3}) [45]. This leads to the equivalent resistance (R) of 960 Ω. To analyze the frequency-response of the device, the normalized modulation depth (MD_N) of the device as a function of electrical signal frequency can be useful, which is defined by [45]:

$$\mathrm{MD_N} \approx |1 + j\omega RC|^{-1} = (1 + 2\pi f_0 RC)^{-1} \tag{3.18}$$

where ω (= $2\pi f_0$) denotes the frequency of input electrical data. The frequency response of the proposed device can be seen in Figure 3.14 for input signal frequency up to 10 GHz. It should be noted that the electrical bandwidth of the device can be calculated when the MD_N = –3dB (or 0.5).

Thus, the 3-dB electrical bandwidth of the device can be estimated as, $f_{3dB} = (2\pi RC)^{-1} \approx 162.5$ MHz, as shown in Figure 3.14. Moreover, by employing Nyquist

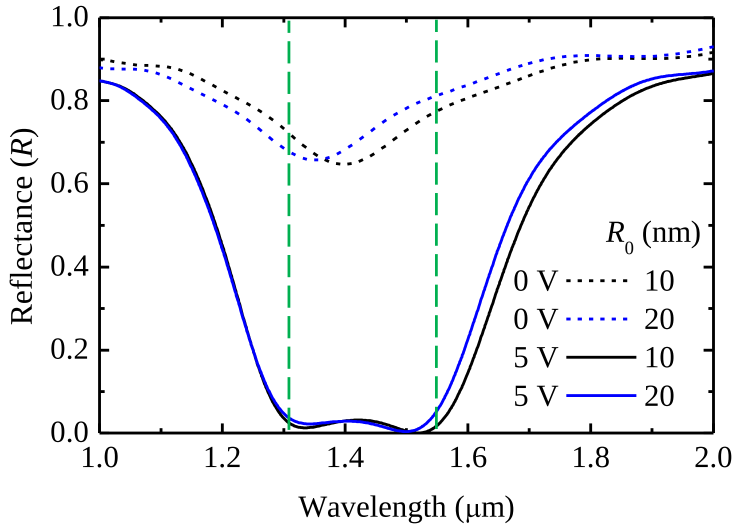

Figure 3.15: Reflectance (*R*) spectra of the proposed metasurface with two different rounding radius (10 nm and 20 nm) at the edges of the nanograting, showing the variation of resonance responses as a function of applied bias voltages while switching between 0 V and 5 V bias. Note that the dashed vertical lines depict the wavelength of 1.55 μm and 1.31 μm.

theorem, we can also estimate the bit-rate (*BR*) of the modulator as $BR = 2 \times f_{3dB} \times \log_2 S \approx 325$ Mbps (where, $S = 2$ denotes the bias voltage signal levels).

3.2.4.4. Study of Fabrication Imperfection due to Rounded-edges

Here, we would like to emphasize on the fact that while studying optical properties through numerical simulations, we modelled nanograting pattern with sharp edges and corners. However, in practical scenario, these sharp edges and corners may not be achieved after fabrication. Thus, to study and incorporate the fabrication imperfections and roughness that could arise from the rounded-edges of the nanograting, we have simulated our design by rounding the edges (with two different rounding radii, R_0 of 10 nm and 20 nm)[56].

Figure 3.15 depicts the modulation of light while switching between 0 V and 5 V bias with rounding radius (R_0) as 10 nm and 20 nm. Note that the dashed vertical lines depict the wavelengths of 1.55 µm and 1.31 µm. At the unbiased state (0 V), we can see resonance dips in the reflectance spectra are getting slightly blue-shifted with the increase of the rounding radius. On the other hand, as mentioned previously, when the ENZ-wavelength of ITO perfectly coincides with the gap-plasmon resonance wavelength for 5 V biasing, we observe an enhancement of resonance response due to the strong coupling of GPR-mode with ENZ-mode, as shown in Figure 3.15.

Here, we would like to emphasize that for 5 V applied bias, the broadening of the resonance dip still covers both of the two key telecommunication wavelength bands, *i.e.*, O-band and C-band. Thus, we can still maintain intensity modulation of reflected light at both these wavelength bands while switching between the two external biasing states: 0 V (ON-state) and 5 V (OFF-state) while maintaining an extinction ratio (*ER*) or modulation depth as high as ~18.5 dB (~17 dB) and ~15 dB (~13.7 dB) with rounding radius of 10 nm (20 nm) at 1.55 µm and 1.31 µm, respectively.

3.2.5. Summary

A broadband electro-tunable metamaterial absorber is presented here, which can be used to simultaneously modulate the intensity of reflected light at both O-band and C-band. By leveraging gap plasmon resonance of a metal–insulator–metal structure and ENZ phenomenon of ITO, we have shown dynamic control of absorbance spectrum for an incoming *x*-polarized light. The proposed device consists of an array of Au-nanograting on top of the Al_2O_3–ITO–SiO_2–Au stack. At the unbiased condition, we have seen the gap-plasmon resonance wavelength appears at 1.43 µm, which also can be predicted by the equivalent circuit model.

On the other hand, when a 5 V bias-voltage is applied, the coupling of GPR-mode with ENZ-mode is observed as we tune the ENZ-wavelength of ITO to the vicinity of the GPR wavelength by applying an external bias-voltage. This leads to a dramatic enhancement of absorbance and we achieved more than 80% of absorption over a 370 nm wavelength window ranging from 1.25 μm to 1.62 μm. Based on this tunable absorption, a **dual-band intensity modulation in the reflected light** (with an extinction ratio as high as 20.5 dB and 16.7 dB at 1.55 μm and 1.31 μm of wavelength, respectively) was realized when bias voltage switches between 0 V and 5 V. Most importantly, this GPR based device can be operated with a **wide range of incident angle** (up to 60 degrees). The proposed metamaterial could help in realizing multi-band and angle-insensitive active flat optical components for nanophotonic systems.

4

Polarization-insensitive Metasurfaces for Electro-Optic Intensity Modulation using ENZ-Material

Contents

Chapter 3 introduced two different metasurface design strategies for dual-band free-space electro-optic intensity modulation by leveraging ENZ phenomenon. Though the dual-band metasurfaces exhibit high modulation depth for both the telecom wavelength windows, the major bottleneck comes from the polarization sensitivity of the structure. The metasurfaces can only modulate the reflected beam for incident light with x-polarization. This Chapter investigates different approaches to designing of polarization-insensitive electro-tunable metasurfaces for free-space optical intensity modulation by harnessing ENZ phenomenon. Section 4.1 presents a novel guided-mode resonance based all-dielectric polarization-insensitive electro-tunable metasurface for intensity modulation. The metasurface can operate for random polarization of normally incident light in both transmission and reflection modes, *i.e.*, dual-mode of operation. Section 4.2 discusses a unique design of gap-plasmon resonance based electro-tunable metasurface for polarization-insensitive intensity modulation with wide incident angle-insensitivity.

4.1. Guided Mode Resonance based Incident-Angle Specific Design

This Section introduces a unique design strategy of polarization-insensitive all-dielectric electro-tunable metasurface that can be operated in dual-mode (both transmission- and reflection-mode). The metasurface can exhibit modulation depths (MDs) in reflection and transmission modes as high as $MD_R \approx 0.96$ and $MD_T \approx 0.85$, respectively, at 1.55 µm wavelength for both *x*- and *y*-polarized light by leveraging the ENZ phenomenon combined with guided-mode resonance effect.

4.1.1. Background

Metasurfaces provide an unprecedented degree of freedom by engineering meta-atoms at the sub-wavelength scale. However, most of the metasurface based electro-optic modulators are dependent on polarization states of incident light [9], [30], [31], [45],

[145]. This imposes several limitations to reduce the footprint of a nanophotonic system due to the need of extra polarization-maintaining components.

Though some initial studies have been proposed to overcome the stringent dependency on input light polarization [35], [141], they usually operate in a single-mode condition (either in transmission-mode or in reflection-mode) due to design constraints. This single-mode operation again imposes some restrictions in various nanophotonic applications where a robust and multi-functional device is necessary to reduce system complexity. Therefore, it is crucial to investigate the design of a polarization-insensitive electro-tunable metasurface that can be operated in dual-mode (both transmission- and reflection-mode) condition.

To address these limitations, we present a novel polarization-insensitive all-dielectric electro-optic modulator that can operate in both transmission and reflection modes. We leverage the GMR-effect of grating structure combined with ENZ-effect of ITO to realize electro-optic modulation. Moreover, the operating wavelength can be blueshifted or redshifted by utilizing the frequency-scaling property of the proposed design. The proposed structure offers a great degree of freedom to control the incoming light and thus finds potential applications in nanophotonic systems.

4.1.2. Design and Operating Principle

The architectural schematic of the proposed GMR based electro-tunable metasurface is shown in Figure 4.1(a). Our design features a 2D array of silicon-nitride (Si_3N_4) nanograting on cascaded layers of an active layer (ITO) with a thickness of t_1, an oxide-layer of alumina (Al_2O_3) with a thickness of t_2, a silicon guiding core with a thickness of t_3, and a silica (SiO_2) substrate. The Si_3N_4 nanograting has dimensions of $w \times w \times h$. Table 4.1 shows the structural and physical parameters used for numerical simulations.

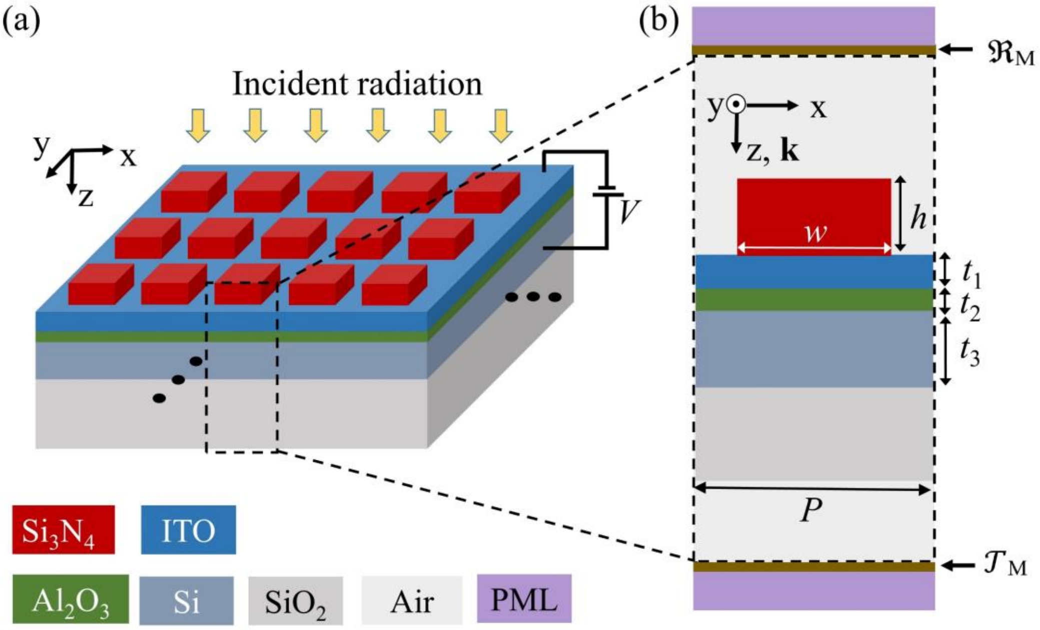

Figure 4.1: Schematics of the proposed guided-mode resonance based electro-tunable metasurface with a nanograting (2D array of Si_3N_4) on top of ITO–Al_2O_3 layers deposited on silicon-on-insulator platform. (a) A 3D view of the proposed design with electrode configuration, where incident plane wave propagates along the z direction. A unit cell is shown using a black dashed rectangle. (b) Side view (*x*-*z* view) of the unit cell, where PML (perfectly matched layers) are used at the top and bottom of unit cell. Note that a normally incident plane wave propagating along *z*-direction is considered here and the overall transmission (reflection) is measured by using a field-monitor denoted as $\mathcal{T}_M$ ($\Re_M$). [35]

The refractive indices of silicon, Al_2O_3, Si_3N_4, and SiO_2 are taken from literature [182], [183]. The side view (*x*-*z* view) of a unit cell with periodicity *P* (= 700 nm) along *x*- and *y*-directions is depicted in Figure 4.1(b). A 3D FDTD (finite-difference time-domain) numerical simulation model is adopted here by considering normally incident plane wave propagating along the *z*-direction. PML (perfectly matched layer) absorbing boundary condition is used in the *z*-direction to minimize the scattering due to the confinement of simulation domain. The periodic boundary conditions are applied in *x*- and *y*-directions. The overall transmission and reflection are measured by using field-monitors $\mathcal{T}_M$ and $\Re_M$, respectively, as shown in Figure 4.1(b).

Table 4.1: The Structural and Physical Parameters used for Numerical Simulations

Parameter	Value	Unit
*Grating period ($P_x = P_y = P$)	700	nm
Grating height (*h*)	450	nm
*Grating width ($w_x = w_y = w$)	620	nm
ITO-layer thickness (t_1)	10	nm
Al_2O_3-layer thickness (t_2)	5	nm
Silicon guiding core thickness (t_3)	220	nm
Carrier concentration (*N*) of bulk ITO	6×10^{19}	cm^{-3}
DC permittivity of Al_2O_3 [29]	9	-
Electron mobility (μ) of bulk ITO [133]	19.5	$cm^2V^{-1}s^{-1}$

*The subscripts *x* and *y* refer to the parameters along corresponding directions.

4.1.3. Electro-Optic Properties of ITO

In order to estimate the optical properties of ITO under the influence of applied bias in a metal-oxide-semiconductor (MOS) type configuration, the electrical properties of the ITO layer need to be extracted by doing electrostatic simulation. In the device physics simulations, the parameters assumed for ITO are same as the ones revealed in Chapter 2 (section 2.4.2). The bulk carrier concentration of ITO is taken as $N = 6 \times 10^{19}$ cm^{-3}.

The ITO–Al_2O_3–Si stack forms a MOS-type structure, as shown in the inset of Figure 4.2(a). To witness the carrier-accumulation at ITO–Al_2O_3 interface, the electrostatic simulations have been carried out by solving drift-diffusion and Poisson's equations in Lumerical Device tool. The variation of carrier concentration distributions of the ITO layer with respect to the external bias voltage (V_{bias}) can be seen in Figure

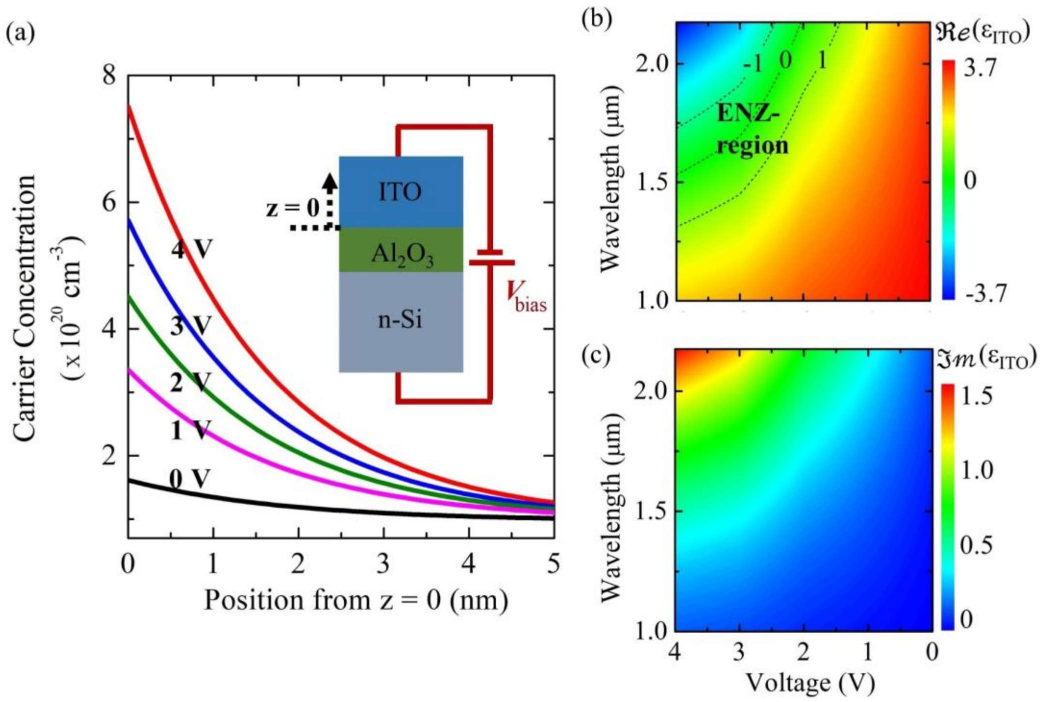

Figure 4.2: (a) The carrier concentration distribution (*N*) of ITO layer at different positions from $z = 0$ to 5 nm for varying bias voltages (V_{bias}). Here, $z = 0$ depicts the ITO–Al_2O_3 interface as shown in the inset, which illustrates the MOS-capacitor formation containing ITO–Al_2O_3–Si layers. The contour plots of real (b) and imaginary (c) parts of permittivity of ITO accumulation layer as a function of wavelength for distinct external biasing conditions. The ENZ-region is shown as $-1 < \Re e\,(\varepsilon_{ITO}) < 1$ [35]

4.2(a). Here, we consider the first 5 nm region of ITO-layer from the interface of ITO–Al_2O_3 to show the accumulation of electrons with the increase of bias voltage.

In order to accurately estimate the optical response of active ITO-layer, we employ a two-layer model, similar to the procedure mentioned in Chapter 2 (sub-section 2.4.2). The variation of real and imaginary parts of complex permittivity of ITO accumulation layer with respect to the external bias voltage are shown in Figure 4.2(b) and (c), respectively, by using Drude model defined in Eq. (2.34). A range of wavelengths can be denoted as “ENZ-region”, where the real part of permittivity of ITO lies in between –1 to +1 [29]. The electrostatic simulations show that for tuning the ENZ-region to the C-band of wavelengths, we need to apply a 4 V external bias voltage to the MOS-type capacitor structure. We consider a homogenized accumulation layer with ~6.2×10^{20} cm^{-3} carrier-concentration distribution for the 4 V external bias voltage. A maximum electric field of ~4.35 MV/cm is observed across the gate-dielectric (Al_2O_3) layer, which is much lower than the reported breakdown voltage of Al_2O_3 [29].

4.1.4. Theoretical Modelling

To observe the coupling of spatial light to the waveguide mode, we use temporal coupled mode analysis combined with effective medium theory (EMT) approximation as mentioned in Chapter 2 (sub-section 2.6.1). Figure 4.3(a) shows the side-view of the unit cell, where EMT approximation models the 2D-grating as a homogenous layer of permittivity ε_{eff}, defined as [171], [176]:

$$\varepsilon_{\text{eff}} = f(\varepsilon_2) + (1-f)\,\varepsilon_1\,, \qquad f = w^2/P^2 \tag{4.1}$$

where ε_1 is the permittivity of air, ε_2 is the permittivity of silicon-nitride, and f is the filling fraction of 2D grating, which depends on grating width (w) and period (P). For our design, we consider a filling fraction of f = 0.7845 (for w = 620 nm and P = 700 nm), with ε_1 = 1 and ε_2 = 3.98529 (at 1.55 μm wavelength).

For a normally incident plane wave, the resonance feature can be seen at the wavelength that satisfies the grating equation, defined as [31]:

$$\lambda_{\text{GMR}} = (\Re e(n_m) - n\sin\theta)P = \Re e(n_m)P \tag{4.2}$$

where n_m is a complex quantity denoting the effective index of guided mode, θ (= 0^0) is the incident angle, λ_{GMR} is the resonance wavelength, n is the background refractive index, and P is the grating period. Here, the effective index (n_m) of a particular guided mode decides the resonance wavelength. To study modal analysis, we solve eigenvalue-equations using Lumerical Mode solver. We observe that the normally incident plane

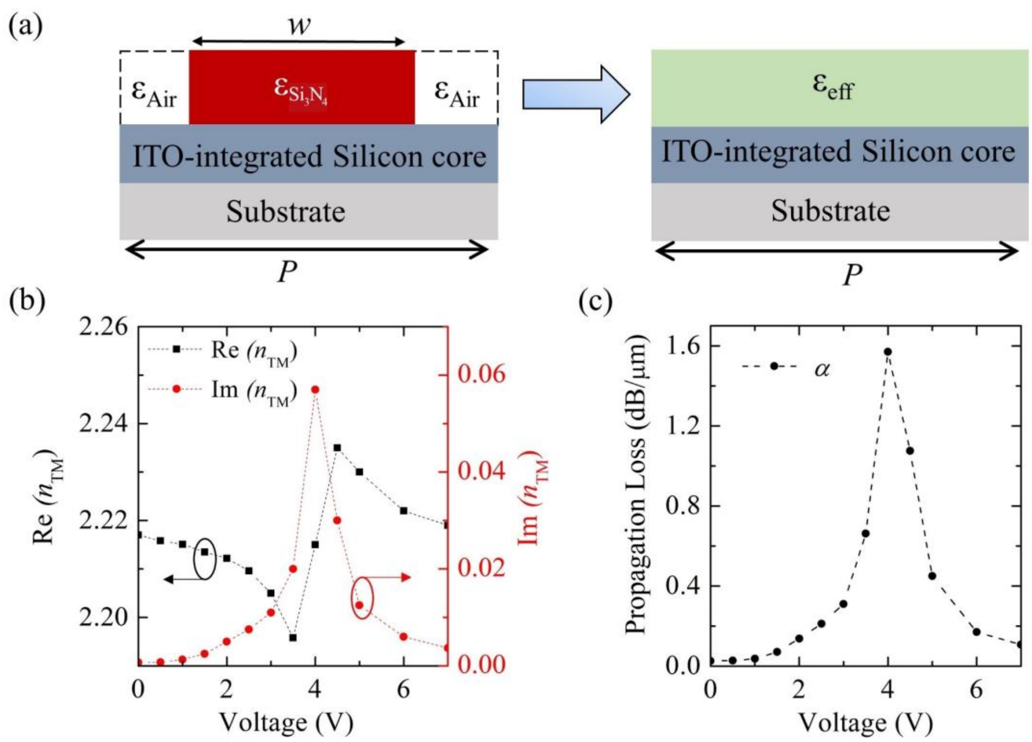

Figure 4.3: (a) Side-view of the unit cell, shown in Fig. 4.1 (b), where effective medium approximation models the grating as a homogenous layer of permittivity ε_{eff}. The voltage-dependent characteristics of fundamental guided TM-mode showing (b) the variation of real and imaginary part of effective modal index (n_{TM}), and (c) propagation loss (dB/µm) along the guiding core. Note that, ITO-integrated silicon layer is the guiding core and the operating wavelength is taken as 1.55 µm. [35]

wave can excite the fundamental TM-mode of ITO-integrated silicon waveguide with $n_m = n_{\text{TM}} \approx 2.217+ 0.0045i$ — leading to λ_{GMR} ~1.55 µm, by using Eq. (4.2). It should be noted that the design also supports higher-order waveguide-modes. These guided modes have lesser effective index than the fundamental mode, which leads to a significant blue-shift of the resonance wavelength beyond the spectral window (*i.e.* 1.5–1.6 µm wavelengths) considered in this work.

We further investigate the effect of external bias-voltage on GMR-phenomenon. The modulation of real and imaginary parts of effective modal index with external bias-voltage can be seen in Figure 4.3(b). A dramatic variation of the real part of effective modal index, $\Re e(n_{TM})$, can be seen — leading to the electro-tunable GMR-effect. In other words, as per Figure 4.3(b) and Eq. (4.2), the GMR wavelength can be tuned by varying the $\Re e(n_{TM})$ under the influence of external bias-voltage. On the other hand, due to the strong confinement of electric field at the absorptive ENZ layer, an increase in the imaginary part of effective modal index, $\Im m\,(n_{TM})$, is observed at 4 V biasing condition. This results in a high modal loss (α) of grating waveguide, defined as [34], [40]:

$$\alpha = \Gamma \alpha_{TM}, \quad \alpha_{TM} = 10 \left| \log^{\exp\left(-\frac{4\pi}{\lambda} \Im m\,(n_{TM})\right)} \right| \left(\frac{\mathrm{dB}}{\mu\mathrm{m}}\right) \tag{4.3}$$

where α_{TM} is the material loss and Γ denotes the modal confinement factor. The variation in modal propagation loss with respect to applied bias-voltage is shown in Figure 4.3(c). At ENZ-region, due to the large modal loss, the guided TM-mode has a very short propagation length. This is the fundamental reason behind the degeneration of resonance filtering response. Therefore, if we switch between unbiased and 4 V biasing states, a modulation of spatial light can be observed.

4.1.5. Simulation Results and Discussion

To evaluate the optical performance of the proposed unit cell, as shown in Figure 4.1(b), a 3D FDTD numerical simulation model is adopted here by considering normally incident plane wave propagating along the *z*-direction. PML (perfectly matched layer) absorbing_boundary condition is used in the *z*-direction to minimize the scattering due to the confinement of simulation domain. In order to accurately observe the ENZ-effect at the 3 nm thin charge accumulation layer, a minimum mesh size of 0.25 nm has been taken near the ITO–Al_2O_3 interface.

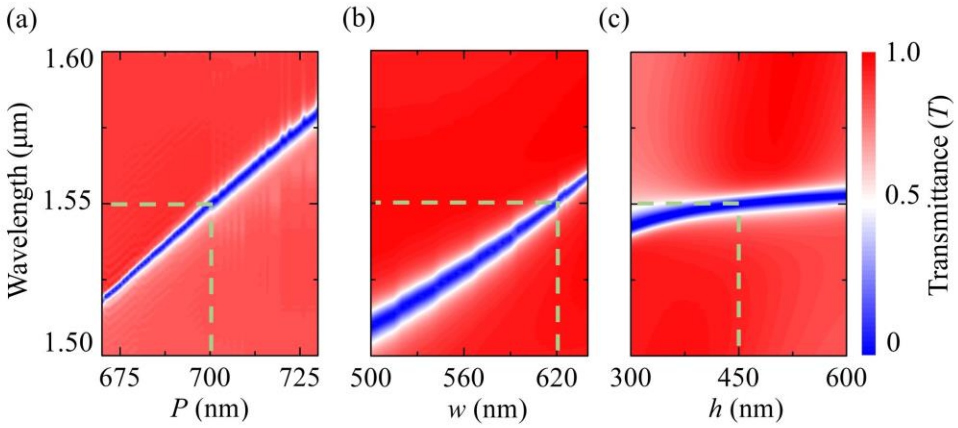

Figure 4.4: Parametric study, based on numerical simulation, showing contour plot to optimize the silicon-nitride nanograting dimensions by varying (a) grating-period, *P*, (b) width, *w*, and (c) height, *h*, keeping all other parameters constant. Here, the green dashed lines indicate the dimensions for which transmittance (*T*) is minimum at 1.55 μm wavelength. In all cases, the thickness of other layers of the proposed structure are kept constant. [35]

4.1.5.1. Parametric Analysis

In order to ensure that the proposed grating-based design exhibits GMR-effect with resonance wavelength (λ_{GMR}) at the vicinity of 1.55 μm wavelength, a careful selection of each geometrical parameter is necessary. We optimized the design based on numerical simulations, with no external bias voltage applied, as shown in Fig. 4.4. We varied a particular geometrical parameter keeping the other parameters constant to see the effect on resonance wavelength. The optimized parametric values, with λ_{GMR} = 1.55 μm, are marked by the green dashed lines in Figure 4.4(a)–(c). A redshift of the λ_{GMR} is observed, in the transmittance spectra, with the increase of grating period (*P*), as shown in Figure 4.4(a). This justifies the linear relation of grating period with resonance wavelength which can be seen in Eq. (4.2).

To understand the effect of variation in grating width (*w*) on λ_{GMR}, we can utilize the EMT approximation for grating structures. According to Eq.(4.1), an increase in *w* keeping *P* as constant will increase the filling fraction. This results in an increment in ε_{eff}, and hence a redshift of the λ_{GMR} is observed in the transmittance spectra, as shown in Figure 4.4(b). A much weaker redshift of the λ_{GMR} is observed if we increase the grating height (h), as shown in Figure 4.4(c). Here we emphasize that if we carefully choose a different set of values for 'w' and 'P', the optical bandwidth can be tuned while maintaining the center wavelength at 1.55 µm, as shown in Figure 4.4(a) and (b). Moreover, with the increase of silicon layer thickness (t_3), the effective index of guided mode will be increased leading to red-shift of the resonance wavelength, as per Eq. (4.2). Nevertheless, it should be noted that the value of t_3 (= 220 nm) is taken as a fixed value based on the commercially available standard silicon-on-insulator wafer thickness. The ITO-layer thickness has a very minimal effect on the resonance spectra if the dimension is varied within ± 50% deviation (results not shown). The value of t_2 is considered to be 5 nm, typical for a gate-dielectric layer for a MOS-type capacitor structure.

4.1.5.2. Dual-mode Polarization-insensitive Optical Modulation

The proposed metasurface design is symmetric along x-and y-directions. This indicates the polarization-insensitivity of the device. Figure 4.5(a) and (b) illustrate that the resonant wavelength will remain unchanged for any polarization angle of the incident light. Here, a polarization angle of 0 degree (90 degree) refers to the x-polarized (y-

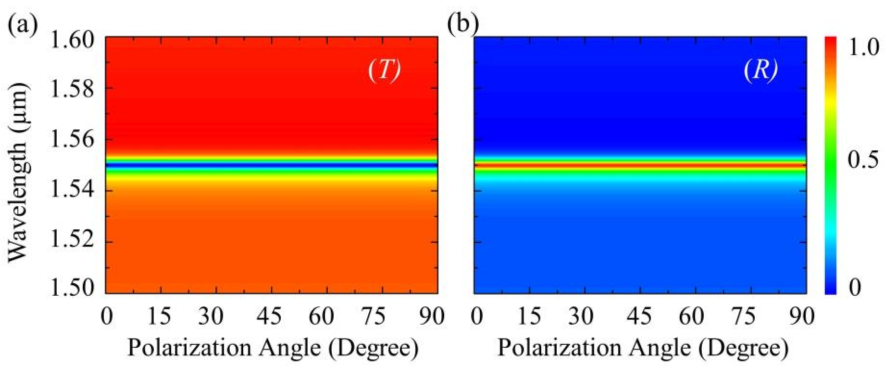

Figure 4.5: Color contour plot for (a) transmittance (T) and (b) reflectance (R) spectra, at 0 V bias, as a function of polarization angle. [35]

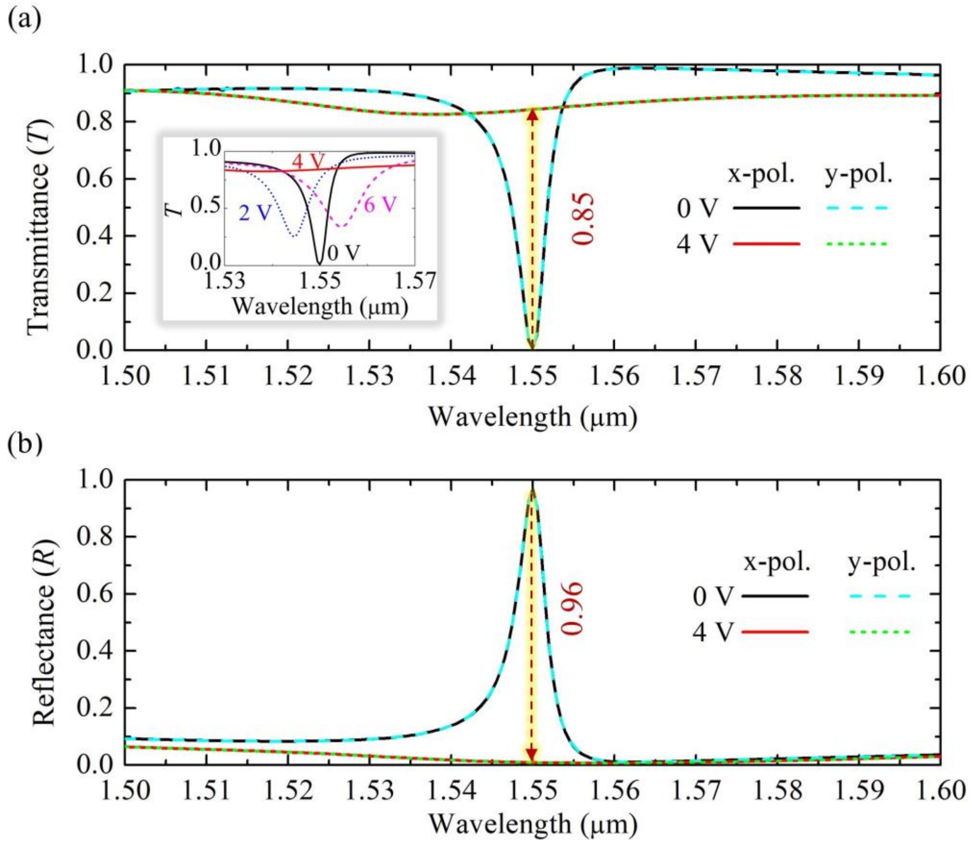

Figure 4.6: Simulation results of the proposed GMR-based modulator showing (a) transmittance (*T*) and (b) reflectance (*R*) spectra at 0 V and 4 V biasing conditions for both x- and y-polarized incident wave. The transmittance (*T*) spectrum at four different applied biasing conditions is shown as the inset of (a). Note that, ITO exhibits ENZ-effect when a 4 V bias is applied across the structure. [35]

polarized) normally incident light. This polarization-insensitive feature is useful for many nanophotonic applications to reduce system complexity. However, note that for off-normal incidence, the operating wavelength of this device will change [171].

Figure 4.6(a) and (b) illustrate the transmittance (*T*) and reflectance (*R*) spectra at 0 V and 4 V biasing conditions, respectively, for both *x*- and *y*-polarized incident waves. A sharp resonant dip (peak) in the transmittance (reflectance) spectra can be seen at 1.55 μm when no bias voltage is applied; referred to as resonance "ON" state. A significant variation of the resonant transmission dip with the changing bias voltage can be seen in the inset of Figure 4.6(a). The resonant dip (peak) in the transmittance (reflectance) spectrum gradually disappears as we tune the ENZ-wavelength of ITO at the vicinity of 1.55 μm by applying external bias voltage. At 4 V biasing, ITO exhibits ENZ-effect. The ENZ-effect imposes an unusual boundary condition at the ITO–Al_2O_3 interface—leading to an enhancement of electric field strength inside the ultra-thin absorptive charge accumulation layer. This results in a high propagation loss of the guided TM mode.

Thus, the resonance response disappears at the 4 V biasing condition, as mentioned before in the theoretical modeling. We refer to it as resonance "OFF" state. Therefore, if the device is switched between "ON" and "OFF" states, a modulation of reflected or transmitted light is observed, which are indicated by the arrow dashed lines in the transmittance and reflectance spectra. For both "ON" and "OFF" states, the transmittance and reflectance spectra remain unaffected by the change in polarization angle of incident plane wave — indicating the polarization-insensitivity of the design.

The normalized magnetic field (H_y) distributions, at 1.55 μm wavelength, for unbiased (ON state) and 4 V biased (OFF state) conditions are shown in Figure 4.7(a) and (b), respectively. At ON state, coupling of spatial light to the guided mode is observed, which is responsible for the filtering response. In contrast, the resonance phenomenon disappeared at the OFF-state due to the high modal loss. Thus, the device behaves as a transparent multi-layered structure, as shown in Figure 4.7(b). The normalized electric field (E_z) distributions at 1.55 μm wavelength, for ON and OFF states are shown in Figure 4.7(c) and (d), respectively.

Due to the enhancement of electric field inside the active ENZ layer, as shown in the enlarged view of Figure 4.7(d), strong interactions of light with the active region can be achieved. The enhancement of electric field can be described by applying boundary conditions at the ITO–Al_2O_3 interface, where the normal component of the

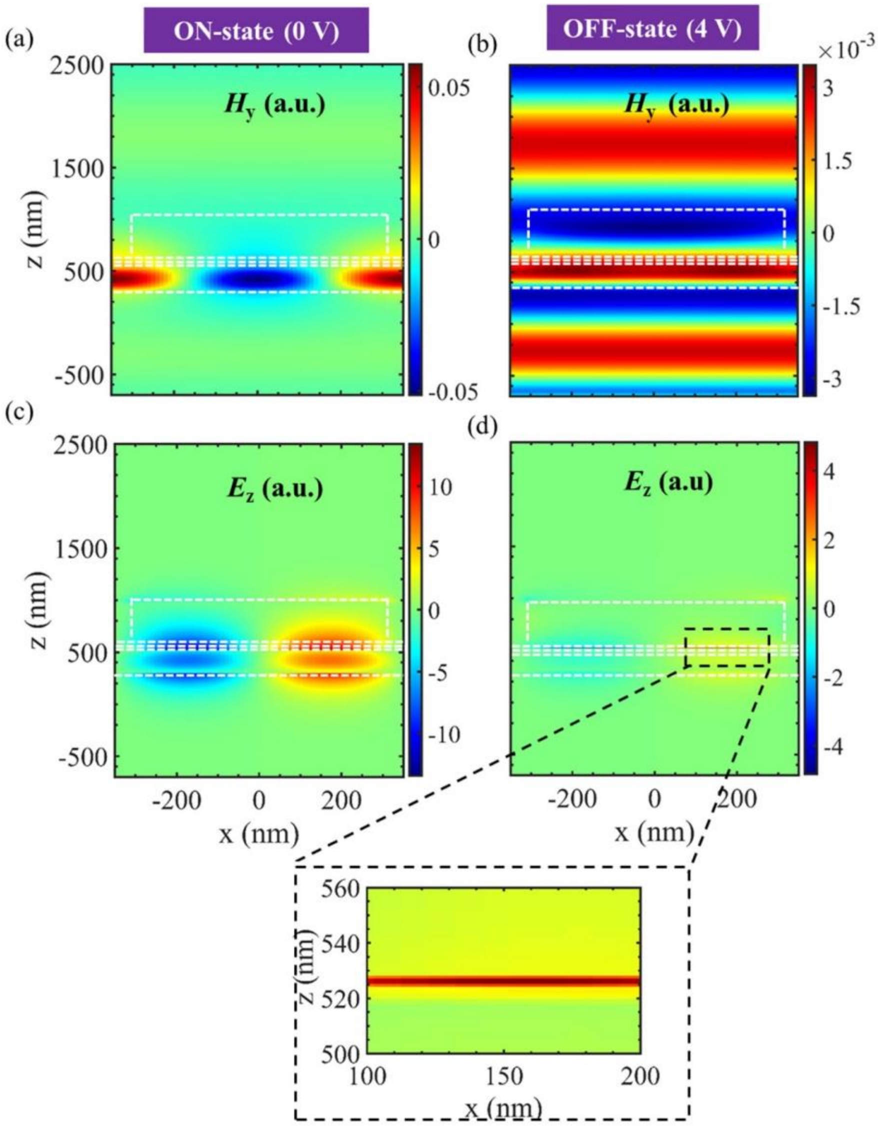

Figure 4.7: Normalized magnetic field (H_y) and electric field (E_Z) distributions in x-z plane for (a and b) 0 V and (c and d) –4 V biasing states at 1.55 µm. Normalized H_y- and E_Z-field distributions in x-z plane for (e and f) 0 V and (c and d) –5 V biasing states at 1.31 µm. The E_Z-field confinement at the ENZ-layer is shown by the enlarged view of (d) and (h). Here, the white dashed lines refer to the underlined structure. [35]

electric flux density is continuous at ITO–Al_2O_3 interface, as discussed in Chapter 1 (sub-section 1.2.2). According to Eq. (1.3), enhancement factor of the electric field will rise drastically when the real part of permittivity of ITO approaches zero (satisfying the ENZ condition) at the ITO–Al_2O_3 interface.

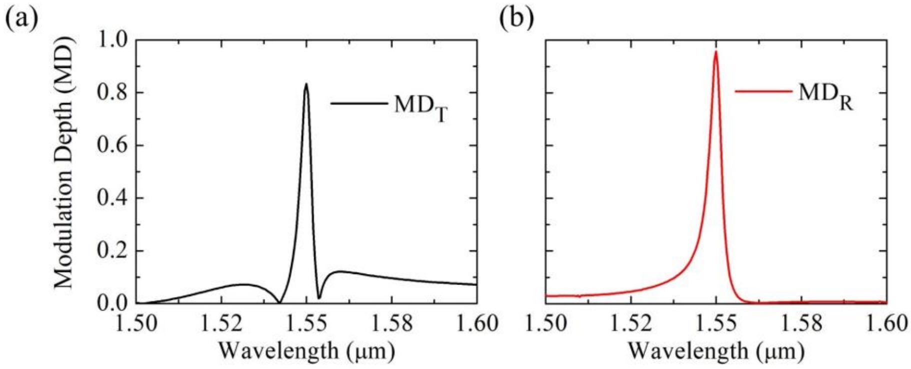

Figure 4.8: Modulation depth (MD) spectrum for (a) transmission-mode and (b) reflection-mode modulator. [35]

On the other hand, as mentioned earlier, the increase in the imaginary part of permittivity of ITO at the ITO–Al_2O_3 interface leads to a high propagation loss of guided mode and degenerates the resonance filtering response. Therefore, if the device is switched between "ON" and "OFF" states, a modulation of light is observed.

The modulation depth (*MD*) as a function of wavelength, can be defined as:

$$MD\ (\lambda) = \frac{\max\,[I_{\mathrm{ON}}\ (\lambda), I_{\mathrm{OFF}}\ (\lambda)]}{\min\,[I_{\mathrm{ON}}\ (\lambda), I_{\mathrm{OFF}}\ (\lambda)]}, \tag{4.4}$$

where I_{ON} (λ) and I_{OFF} (λ) refer to the intensity of light in the transmittance (or reflectance) spectrum for ON- and OFF-state, respectively. Figure 4.8(a) and (b) illustrate that we can achieve transmission-mode modulation depth (MD_T) and reflection-mode modulation depth (MD_R) as high as ~0.85 (16 dB) and ~0.96 (20 dB), respectively, at operating wavelength 1.55 µm.

4.1.5.3. Requirements of Minimum Number of Grating Periods

The smallest lateral dimensions of the device, or more specifically the minimum number of unit cells or grating periods (P_N), required to sustain a sharp guided-mode resonance depends on the Q-factor of the resonance, which can be given by [175]:

$$P_N > Q/\pi \,, \qquad \text{where, } Q = \lambda_{\mathrm{GMR}}/\Delta\lambda \tag{4.5}$$

Here, λ_{GMR} is the resonant wavelength and $\Delta\lambda$ is the spectral bandwidth, which can be expressed by [175]:

$$\Delta\lambda = \frac{\lambda_0 \Lambda}{\pi L} \,, \tag{4.6}$$

where Λ is the grating period and L is the propagation length (or loss length) of the particular guided-mode, which can be expressed by [31]:

$$L = \frac{\lambda_{\mathrm{TM}}}{2\pi \times \Im m(n_{\mathrm{TM}})} \,, \tag{4.7}$$

where $\Im m(n_{\mathrm{TM}})$ is the imaginary part of modal index at the resonant wavelength λ_{TM}. Without applying any bias-voltage, we find that normally incident light can excite TM-mode with effective index of (2.217 + 0.0039i). Accordingly, the loss length of the guided mode can be calculated as ~6.32 µm, which results in a spectral bandwidth $\Delta\lambda \approx$ 5.43 nm. Thus, the Q-factor of the resonance for guided TM-mode is ~286— leading to $P_N \approx 92$.

So, for our design we require at least 92 periods or unit cells. Therefore, to accommodate minimum number of unit cells with 700 nm periodicity, we need to have a device dimension of around 7 × 7 µm^2 (consisting of 100 unit cells). This device dimension will ensure that we can sustain the sharp resonance for guided mode at the vicinity of 1.55 µm.

4.1.5.4. Frequency Response and Operational Speed of the Modulator

To understand the operational speed of the modulator which is mainly limited by *RC*-time constant, we need to calculate the total equivalent capacitance and resistance of the device, as shown in Figure 4.9(a), where R_{ITO} and R_{Si} are the resistance of ITO layer and silicon layer, respectively. The parallel plate capacitor, for the part of dielectric layer sandwiched between ITO and Si layer, is shown as C_{eq}.

The capacitance of the device is estimated by electrostatic simulations done with Lumerical Device solver. With a maximum bias voltage (4V), capacitance per unit area for a unit cell ($C_{Unit\ Cell}$) is calculated as ~6.26 fF/μm^2. Assuming a total device width (W) and length (L) of 7 μm each (consisting of 100 unit cells), a total capacitance of $C_{eq} \approx 306.75$ fF can be approximated for gate-dielectric layer. Similarly, based on the electrostatic simulations, we can approximate the value of capacitor for the part of gate-layer under metal contacts as 2.05 fF, which is much smaller than C_{eq} and can be ignored.

The total equivalent resistance (R_{eq}) can be calculated by averaging the value of R_{ITO} and R_{Si}. Furthermore, due to the formation of accumulation layer, R_{ITO} can be represented as a parallel combination of resistance for accumulation layer (with $N = 6.2 \times 10^{20}$ cm^{-3}) and the resistance for bulk ITO layer (with $N = 6 \times 10^{19}$ cm^{-3}). The resistance of each layer can be calculated by using, $R = (\rho L/\ tW)$, where t and ρ are the thickness and resistivity of corresponding layer, respectively. The carrier mobility (μ) and carrier concentration (N) of a semiconductor material decide the resistivity as $\rho = (e\mu N)^{-1}$, where e is the electron charge. In our electrostatic simulations, we have considered the n-type silicon layer with a doping concentration of 1×10^{19} cm^{-3}. The total equivalent resistance for the design (consisting of 100 unit cells) can be approximated as $R_{eq} \approx 1.343$ kΩ, with electron mobility (μ) of 80 cm^{2}V^{-1}s^{-1}, 19.5 cm^{2}V^{-1}s^{-1}, and 13 cm^{2}V^{-1}s^{-1} for silicon-layer [127], bulk-ITO layer, and accumulation-layer of ITO [133], respectively.

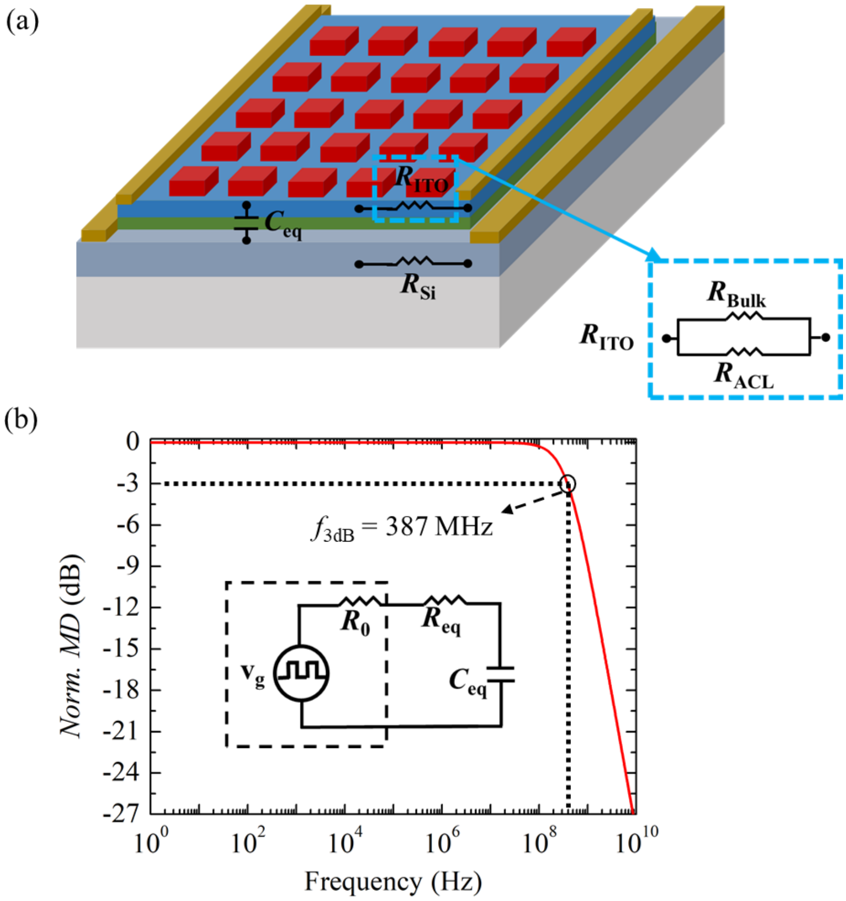

Figure 4.9: (a) The lumped circuit parameters approximation of the modulator for the part consisting ITO, silicon layer, and gate-dielectric layer. (b) The frequency response of the proposed modulator to calculate the 3-dB modulation bandwidth. The RC-limited bandwidth is highlighted by black circle indicating a –3 dB change in normalized modulation depth. Note: the equivalent circuit model is shown in the inset. [35]

The frequency response of the device can be analyzed by calculating normalized modulation depth considering R_0 (= 50 Ω) as the output impedance of the voltage source and ω (= 2π f_0) as the input signal frequency. The normalized modulation depth can be given as [45]:

$$Norm.MD \approx \left|1 + j\omega R_{eq}C_{eq}\right|^{-1} \approx \left(1 + 2\pi f_0 R_{eq}C_{eq}\right)^{-1} \qquad (4.8)$$

The frequency response of the device up to 10 GHz can be calculated by using MATLAB and is shown in Figure 4.9(b). We can estimate the modulation bandwidth at

Table 4.2: Comparative Overview of a Few Recently Reported Theoretical Designs of ENZ-material based EOMs

Ref.	λ (µm)	MD	Speed (Mbps)	Mode *(*T* or *R*)	P. I.
Forouzmand *et al.* [30]	1.537	0.8	NA	*R*-mode	No
Qiu *et al.* [141]	1.504	~0.8	NA	*T*-mode	Yes
Vatani *et al.* [45]	1.55	~0.99	80	*R*-mode	No
Kim *et al.* [5]	1.48	0.82	NA	*R*-mode	No
Forouzmand *et al.* [145]	1.547	0.86	NA	*T*-mode	No
Hu *et al.* [31]	1.55	0.85	NA	*T*- and *R*-mode	No
Chen *et al.* [9]	1.5	0.68	NA	*R*-mode	No
This Work	1.55	**0.96** (MD_R), **0.85** (MD_T)	**~774**	***T*- and *R*-mode**	**Yes**

*Modulator's operational mode. Here, *T*- and *R*-modes refer to transmission and reflection modes, respectively. P. I.: Polarization-insensitivity, λ: operational wavelength, MD: modulation depth, NA: not available.

which the *Norm. MD* is 0.5 (or –3dB), *i.e.* $f_{3dB} = (2\pi R_{eq}C_{eq})^{-1}$. Therefore, the calculated 3-dB bandwidth of our device is ~387 MHz, as marked in Figure 4.9(b). In addition, one can calculate the modulator bit-rate (*BR*) by employing Nyquist theorem, where $BR = 2\times f_{3dB}\times \log_2 m$ (here, $m = 2$ is the discrete levels of the input signal). With $f_{3dB} = 387$ MHz, we can achieve $BR = 774$ Mbps of the modulator.

4.1.5.5. Comparative Analysis

A comparative overview of a few recently reported electro-tunable metasurfaces for intensity modulation is shown in Table 4.2. It can be seen that most of the grating-assisted modulators operate in a single-mode condition (either in transmission-mode or in reflection-mode) due to their design constraints. Although a dual-mode operation of a modulator has been theoretically demonstrated by Hu *et al.* [31], the stringent dependency on polarization state of light is still a limiting factor. As seen in Table 4.2, our proposed design can be operated in both transmission- and reflection-mode simultaneously (dual-mode of operation) irrespective of the polarization angle of a normally incident plane wave.

4.1.5.6. Prospective Fabrication Process

The proposed modulator can be fabricated on a standard n-type silicon-on-insulator substrate with a doping concentration of 1×10^{19} cm^{-3}. To begin, the Al_2O_3 gate layer may be grown on top of silicon layer by atomic layer deposition [131]. Then, an ITO layer with 10 nm thickness could be deposited by radio frequency (RF) sputtering in an Argon/Oxygen (Ar/O_2) plasma environment [29]. The background carrier concentration of ITO can be controlled by Ar/O_2 flow rate. Then, the silicon-nitride layer with 450 nm thickness may be RF-sputtered on top of the layered structure. Afterward, the silicon-nitride layer could be patterned, to form a periodic square array, by using standard electron-beam lithography (EBL) and lift-off process. Finally, to provide electrical connections, the metal contacts (gold/aluminium) could be deposited by e-beam evaporation and patterned by a second round of EBL, followed by lift-off process [29], [43].

4.1.5.7. Frequency-scaling Property of the device

So far, we have theoretically demonstrated a polarization-insensitive electro-tunable metasurface which can operate in both transmission- and reflection-mode at 1.55 µm wavelength. Now, we would like to emphasize here that our proposed design exhibits

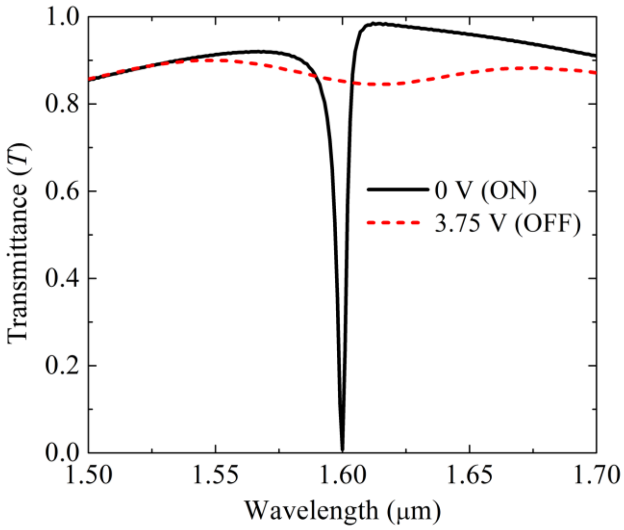

Figure 4.10: Simulation results of the scaled-up GMR-based modulator showing transmittance (*T*) spectra at two different applied biasing conditions, 0 V ("ON"-state) and 3.75 V ("OFF"-state). [35]

remarkable frequency-scaling property by which we can scaled-up or scaled-down the geometrical parameters to operate in different wavelength regimes. As a proof of the concept, we have studied a scaled-up design which can operate in L-band of wavelength. With a scaling factor of 1.0322, the resonance wavelength can be shifted from 1.55 μm (C-band) to 1.6 μm (L-band). Modulation of spatial light can be observed at 1.6 μm wavelength if the device is switched between "ON" and "OFF" states, as shown in Fig. Figure 4.10. Furthermore, it should be noted that the required external bias-voltage to observe ENZ-effect will be decreased (increased) if we scale-up (scale-down) the design.

4.1.6. Summary

An ENZ material based all-dielectric **polarization-insensitive** electro-optic intensity modulator is presented here**, which can operate in both transmission and reflection**

modes. The design comprises a nanograting (2D array of Si_3N_4) on top of ITO–Al_2O_3 layers deposited on silicon-on-insulator platform. By combining effective medium theory with temporal coupled-mode analysis, we have shown a normally incident plane wave can excite the fundamental TM-mode of grating waveguide, resulting in a guided-mode resonance effect at the vicinity of 1.55 μm wavelength. In contrast, an enhancement of electric field is observed at the ITO–Al_2O_3 interface due to the formation of an ultra-thin absorptive ENZ-layer upon applying external bias-voltage. This results in a large propagation loss of guided mode, and thus the resonance filtering response disappears.

We have achieved a modulation depth as high as ~0.96 (~0.85) in reflection (transmission)-mode at 1.55 μm operating wavelength for arbitrary polarization angle of normally incident plane wave. Our electrostatic simulations show that the device has a bit-rate of ~774 Mbps for binary modulation scheme. In addition, our proposed design is scalable. As a proof of the concept, we have demonstrated an up-scaled device with operating wavelength of 1.6 μm. To the best of our knowledge, such a scalable polarization-insensitive, electro-optic modulator is proposed for the first time, which can operate in both transmission and reflection modes (dual-mode). With large modulation depth and dual-mode operation, this scalable and multifunctional proposed design could find potential applications in flat optics and integrated nanophotonic systems.

4.2. Gap Plasmon Resonance based Incident-Angle Insensitive Design

In the previous Section, a GMR based design was discussed to achieve polarization-insensitive electro-optic intensity modulation by leveraging the ENZ phenomenon. Though the modulator could exhibit a high modulation depth and could find potential solution to overcome the stringent dependency on polarization of the input light, the incidence angle-sensitivity remains a limitation. As mentioned in the previous Chapter, the GMR based devices are incident-angle sensitive and the presented polarization-insensitive design can only be operated with normally incident light. The operating wavelength of this device will change for off-normal incidence. This angle-sensitivity nature of a device increases the cost and overall footprint of the nanophotonic systems due to the requirement of complex arrangements of several opto-mechanical components.

Moreover, while considering a polarization-insensitive structure, maintaining a low energy consumption is very challenging. To the best of our knowledge, an energy-efficient polarization-and angle-insensitive metasurface based electro-optic modulator is not demonstrated yet in the literature [5], [9], [30], [31], [45], [141]. In this direction, if we decrease the required external bias voltage, we may be able to reduce the capacitance per unit cell structure which eventually leads to an energy-efficient modulation.

This section introduces a gap plasmon resonance (GPR) based polarization-insensitive electro-tunable metasurface that can modulate the reflected light intensity for a wide variation of incident angle. Based on the free-carrier accumulation process upon applying external electrical biasing, we have attained a modulation depth of ~25 dB for random polarization angle of incident light while maintaining an energy-consumption as low as ~303 fJ/bit. In addition, the device can be over a wide range of oblique incidence angle (up to 50 degrees) for both *x*- and *y*-polarized light. The

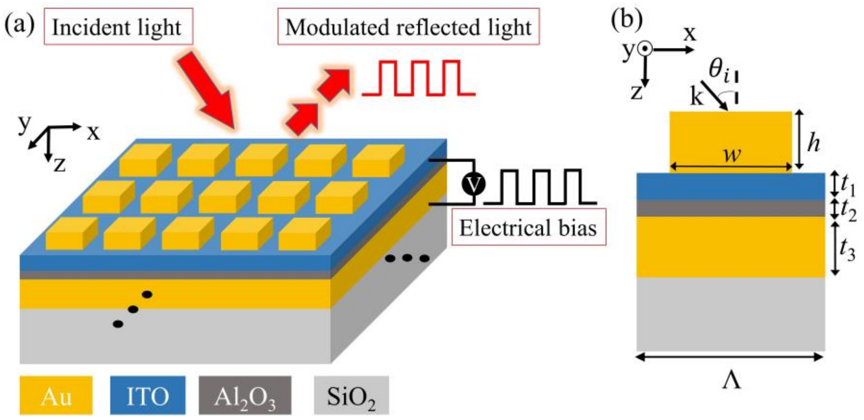

Figure 4.11: Schematic of the proposed gap-plasmon resonance based electro-tunable metasurface consisting of a two-dimensional array of Au-nanograting on top of ITO–Al_2O_3–Au stack deposited on SiO_2 substrate. (a) A perspective view of the metasurface, where an external electrical biasing modulates the reflected light. (b) Side view of a unit cell. Here, t_1 = 10 nm, t_2 = 5 nm, t_3 = 100 nm, and Λ = 700 nm. [207]

proposed device, thus, could help in realizing energy-efficient polarization-and angle-insensitive optical modulators for nanophotonic systems.

4.2.1. Structural Overview

The metasurface comprises a 2D array of Au-nanograting on cascaded layers of an ITO active region, an Al_2O_3 gate-dielectric layer, and an optically-thick gold (Au) layer deposited on SiO_2 substrate, as shown in Figure 4.11(a). The multi-layer deposition can be realized by using RF-sputtering. Then, patterning can be done by using electron-beam lithography and lift-off process to realize a of 2D array of Au-nanograting [29]. The refractive indices of Au [125], SiO_2 and Al_2O_3 [183] are taken from the experimental data reported in the literature. The unit cell (*x-z* view) with periodicity Λ along *x*- and *y*-axis is as shown in Figure 4.11(b), where width and height of the Au-nanograting are *w* (= 600 nm) and *h* (= 170 nm), respectively. We have adopted a 3D finite-difference time-domain simulation model while considering a plane wave source. The light incident on the metasurface with an angle of θ_i propagates along the *z*-direction. The

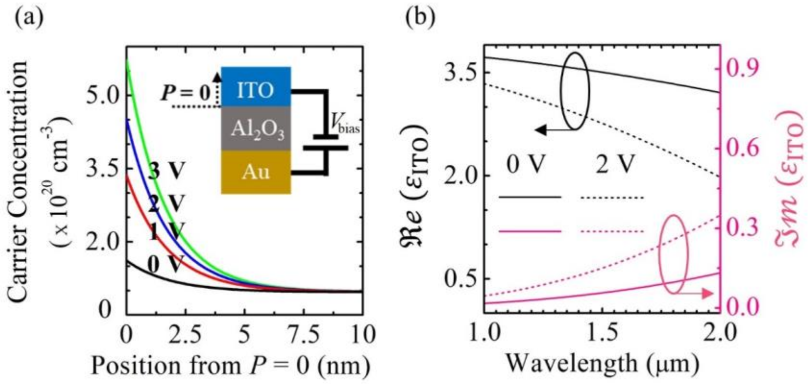

Figure 4.12: (a) The carrier concentration distribution, N (cm^{-3}), of ITO active region as a function of different bias voltages at different positions from P = 0 to 10 nm. The MOS-type configuration formation by ITO–Al_2O_3–Au stack is depicted in the inset, where the ITO–Al_2O_3 interface represents P = 0. (b) Voltage-dependent real ($\Re e(\varepsilon_{ITO})$) and imaginary ($\Im m(\varepsilon_{ITO})$) parts of permittivity of ITO-accumulation region for 0 V and 2V bias-voltages. [207]

periodic boundary conditions are used along *x*- and *y*-axis and perfectly matched layers are used in the *z*-axis.

4.2.2. Electro–Optical Properties of ITO

In order to obtain the electrically tunable optical properties of ITO, electrostatic simulations in Lumerical Device have been carried out by considering the parameters for ITO same as the ones mentioned in Chapter 2. For our study, we consider an n-doped ITO-layer with an initial carrier-concentration of ~3×10^{19} cm^{-3}. The ITO–Al_2O_3–Au stack forms a MOS-type configuration, as represented in the inset of Figure 4.12(a). Figure 4.12(a) depicts the spatial distributions of carrier concentration of ITO layer with the variation of bias-voltage for different positions from P = 0 to 10 nm, where the ITO–Al_2O_3 interface represents P = 0. We have estimated the **ac**cumulation **l**ayer (ACL) as an ultra-thin layer (~3 nm) with a uniform carrier-concentration distribution by using a two-layer model, as mentioned in Chapter 2 (sub-section 2.4.2). After that the optical properties of ACL are estimated by the Drude permittivity model, given in Eq. (2.34).

The voltage-dependent real ($\Re e(\varepsilon_{\text{ITO}})$) and imaginary ($\Im m(\varepsilon_{\text{ITO}})$) parts of permittivity of ACL are depicted in Figure 4.12(b).

4.2.3. Theoretical Framework

The subwavelength unit cell of the metasurface is modelled as an equivalent RLC-circuit in a similar way discussed in Chapter 2 (sub-section 2.6.2), and is presented in Figure 4.13(a). Here, R_m, L_m, $L_{e,m}$, and C_{eff} denote the Ohmic resistance, Faraday inductance, kinetic inductance, and equivalent capacitance, respectively [177], [178]. Note that m represents mode-number of the resonance. With negligible imaginary part of permittivity, the ITO-layer can be assumed as a dielectric layer.

Thus, for the cascaded dielectric layers of ITO–Al_2O_3, we can estimate an effective permittivity, given as:

$$\varepsilon_{\text{eff}} = \frac{\varepsilon_{\text{ITO}} \times t_1}{d_{\text{total}}} + \frac{\varepsilon_{\text{Al}_2\text{O}_3} \times t_2}{d_{\text{total}}} \tag{4.9}$$

where ε_{ITO} and $\varepsilon_{\text{Al}_2\text{O}_3}$ denote the permittivity of ITO and Al_2O_3 layers, respectively, and d_{total} (= t_1+t_2) denotes the total dielectric thickness. The gap-plasmon resonance wavelength can be estimated as [177]:

$$\lambda_{\text{R}} = 2\pi c\sqrt{C_{\text{eff}}\left(L_{\text{m}} + 2L_{e,m}\right)} \tag{4.10}$$

where c is the speed of light in vacuum. The parameters of the equivalent circuit model can be calculated as [177], [178], [189]:

$$C_{\text{eff}} = \frac{\alpha\varepsilon_{\text{eff}}\varepsilon_0 w^2}{m d_{\text{total}}} \tag{4.11}$$

$$L_{e,m} = \frac{-1}{m\delta_{\text{Au}}\omega^2\varepsilon_0} \times \left\{\frac{\varepsilon'}{(\varepsilon')^2 + (\varepsilon'')^2}\right\}_{\text{Au}} \tag{4.12}$$

$$L_m = \frac{0.5\mu_0 d_{total}}{m} \tag{4.13}$$

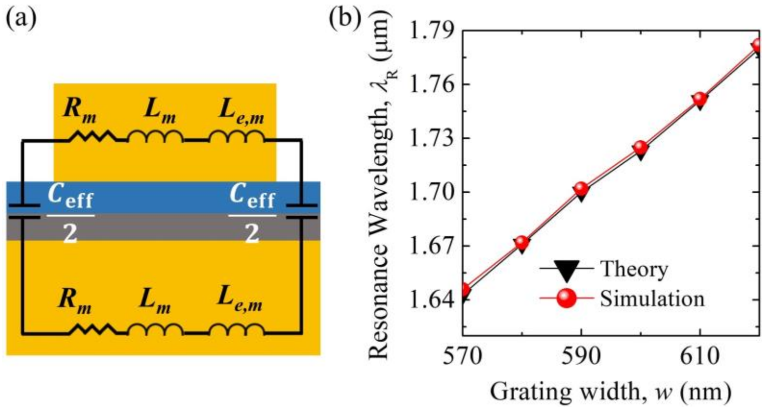

Figure 4.13: (a) The RLC-equivalent circuit model of the unit cell structure. (b) The resonance wavelengths (λ_R), as a function of grating width, calculated by the FDTD simulation (red spherical blocks) and predicted by the equivalent circuit model (black triangles). [207]

where, ω is the angular frequency of the incident wave, ε_0 and μ_0 are vacuum permittivity and permeability, respectively. where ω, w, ε_0, and μ_0 are the incident wave angular frequency, grating width, vacuum permittivity, and vacuum permeability, respectively. The $\varepsilon'$and ε'' depict the real and imaginary part of permittivity of Au-layer, respectively [125]. Here we have taken m = 3, corresponding to the third-order gap-plasmon resonance mode. We have considered the skin depth of Au (δ_{Au}) as 24.5 nm and the tuning factor as α = 0.13 [178]. Figure 4.13(b) shows that with the increase of grating width (w) the resonance wavelength (λ_R) increases, which also shows a close agreement with the FDTD simulations.

4.2.4. Results and Discussion

Figure 4.14 illustrates the reflectance (R) spectra for both x- and y-polarized incident light at 0 V and 2 V biasing conditions. Due to the excitation of gap plasmon resonance mode, a dip at 1.72 μm in the reflectance spectra can be observed at the unbiased state (0 V). We have optimized our design in such a way that a high reflectance at 1.55 μm wavelength can be achieved for 0 V biasing-state. Thus, we can refer to it as "ON" state.

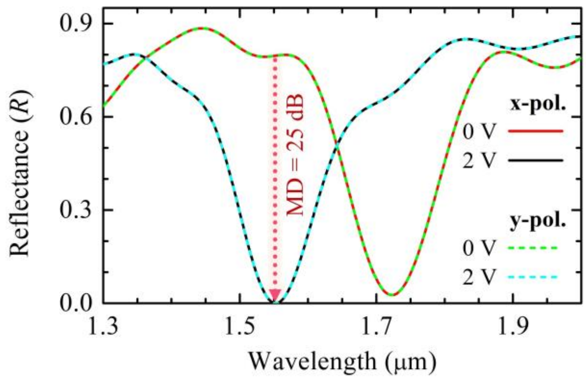

Figure 4.14: Simulation results of the proposed tunable metasurface for electro-optic modulation showing the reflectance (*R*) spectrum at 0 V and 2 V external bias-voltages for both *x*- and *y*-polarized incident light. Here, the modulation depth (MD = 25 dB) at 1.55 μm wavelength is shown by the arrowed dotted line. [207]

On the other hand, the resonance dip in the reflectance spectrum can be tuned to 1.55 μm by applying a 2 V bias. We refer to it as "OFF-state" due to negligible reflected light intensity. Therefore, if we switch between ON-state and OFF-state, we can accomplish a modulation depth ($MD = 10\log|I_{ON} / I_{OFF}|$) as high as ~25 dB, as shown by the arrowed dotted line in Figure 4.14. Here, I_{ON} and I_{OFF} denote the reflected light intensity for ON- and OFF-state, respectively. Moreover, due to the design symmetry along *x*- and *y*-directions, we can see a polarization-insensitive behavior in the reflectance spectra.

The normalized magnetic (H_y) and electric (E_z) field distributions are depicted in Figure 4.15(a) and (b), respectively, at the resonant wavelength (1.55 μm) for 2 V biasing condition—indicating the excitation of third-order GPR-mode [148]. To study the angle-sensitivity of the device, we have performed numerical simulations for a wide range of oblique incidence angle ranging from 0 degree to 60 degrees for 2 V biasing condition. Figure 4.15(c) and (d) depict the color contour plot of reflectance spectra under the influence of oblique incidence angle for *x*- and *y*-polarization of light, respectively. A slight blue-shift of the resonant wavelength is observed with the increase

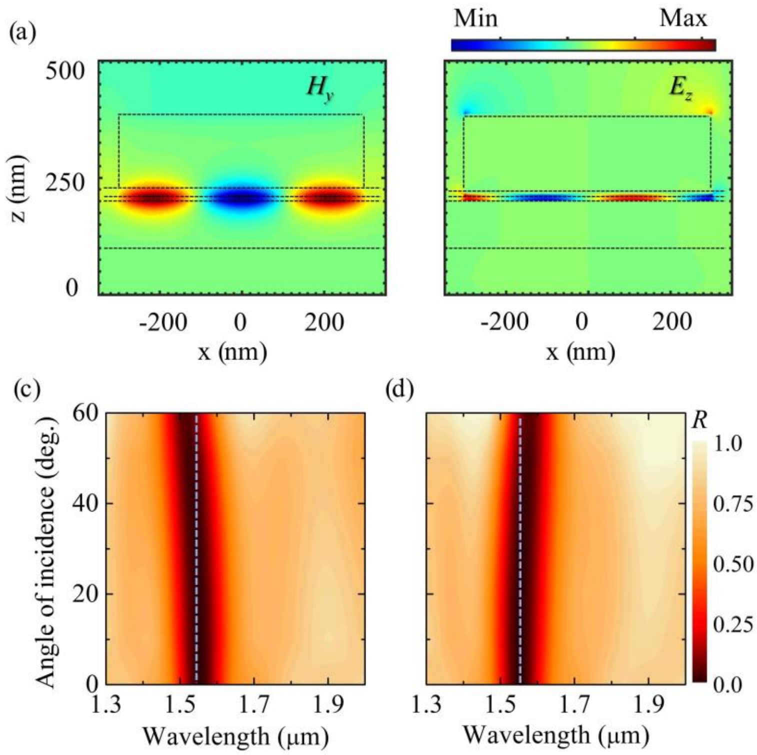

Figure 4.15: The normalized (a) H_y-and (b) E_z-field distributions at the third-order gap-plasmon resonance wavelength (1.55 μm) for 2 V biasing. Here, the black dashed lines indicate the underlying structure. Color contour plot of reflectance spectra at 2 V biasing state as a function of incidence-angle (θ_i) for (c) *x*- and (d) *y*-polarized incident plane wave. Here, the dashed line represents the operating wavelength (1.55 μm). [207]

of incidence angle for *x*-polarized light. Whereas, a red-shift in the resonance wavelength can be seen for *y*-polarized light. Nevertheless, we can maintain a very negligible reflected light intensity (OFF-state) at 1.55 μm for an oblique incidence angle up to 50 degrees in both *x*- and *y*-polarized cases—indicating a wide angle-insensitivity of the device.

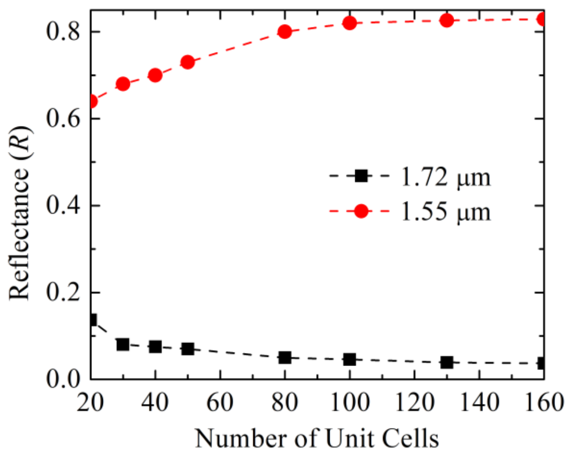

Figure 4.16: Simulation results to identify the minimum number of unit cells required to maintain the desired reflectance (> 0.8 at 1.55 µm and <0.03 at 1.72 µm at unbiased condition), as predicted with an infinite periodic conditions of a unit cell, shown previously in Figure 4.14 [207]

4.2.4.1. Requirements of Minimum Number of Grating Periods

To identify the minimum number of unit cells or grating periods required to sustain the resonance response, we have done a set of numerical simulations considering different device dimensions at the unbiased condition. While doing the FDTD simulations, we have taken a set of unit cells according to the lateral dimensions and considered PML boundary conditions in all directions. For instance, as shown in Figure 4.16, when we have considered a minimum device dimensions of 1.4 × 1.4 µm^2 (consisting 20 unit cells with 700 nm periodicity), a weak resonance response can be seen — leading to the reflectance of ~0.13 and ~0.62 at 1.72 µm and 1.55 µm, respectively. As expected, when we increase the number of unit cells, the reflectance decreases at 1.72 µm and increases at 1.55 µm. Thus, to maintain the desired reflectance (> 0.8 at 1.55 µm), (as predicted with an infinite periodic conditions of a unit cell shown previously in Figure 4.14), we need to have a device dimension of around 7 × 7 µm^2 (consisting of 100 unit cells).

4.2.4.2. Electrical Bandwidth and Speed of the Device

The electrical bandwidth of the modulator is mainly restricted by *RC*-time constant. The electrostatic simulation reveals that the proposed device has a capacitance per unit cell (C_u) of ~6.2 fF/μm^2. Hence, with a device dimensions of 7 × 7 μm^2 (consisting 100 unit cells), the effective capacitance (C) can be approximated as ~303 fF. The equivalent resistance (R) of the device can be estimated as $R = (R_{ITO} + R_{Au})/2$. The resistance for ITO layer (R_{ITO}) can be seen as a parallel combination of R_{Bulk} (corresponds to bulk ITO-region) and R_{ACL} (corresponds to accumulation layer). Then, the resistance for each region can be estimated by $R_0 = (\rho L/dW)$, where $W \times L$ represents the device dimensions consisting 100 unit cells. Here, ρ and d denote the resistivity and dielectric layer thickness, respectively.

The resistance of Au layer, R_{Au}, can be estimated by considering ρ as ~2.2×10^{-8} Ω.m [180]. Whereas, the resistivity of ITO, $\rho = (e\mu N)^{-1}$, depends on electron mobility (μ) [45], [189]. This leads to the equivalent resistance (R) as 1.16 kΩ. Thus, the 3-dB bandwidth of the modulator can be calculated as, $f_{3dB} = (2\pi RC)^{-1} \approx 450$ MHz. Then, by using Nyquist theorem, we can estimate the bit-rate as $BR = 2 \times f_{3dB} \times \log_2 m \approx$ 900 Mbps (where, $m = 2$ indicates the electrical signal levels). Moreover, with a maximum of 2 V biasing, we can attain a low energy-consumption ($E_b = CV^2 / 4$) of ~303 fJ/bit.

4.2.4.3. Comparative Analysis

Table 4.3 presents a comparative study among a few recently reported metasurface based electro-optic modulators. We can see that the modulators reported so far are either polarization-dependent or angle-sensitive. In contrast, the proposed design can be operated with a wide range of oblique incident angle irrespective of the polarization-states of incoming light while maintaining a large MD of ~25 dB.

Table 4.3: Comparative Overview of a Few Recently Reported Recently Reported Theoretical Designs of Metasurface based Electro-Optic Modulators

Ref.	λ (μm)	MD (dB)	Speed (Mbps)	P. I.	A. I.
Vatani *et al.* [45]	1.55	24	80	No	No
Kim *et al.* [5]	1.48	~14	NA	No	No
Chen *et al.* [9]	1.5	~17	NA	No	No
Bhowmik *et al.* [180]	1.55	23	167	No	No
Forouzmand *et al.* [30]	1.537	~13	NA	No	No
Mosallaei *et al.* [145]	1.564	23.7	NA	No	No
Qiu *et al.* [141]	1.512	20	NA	Yes	No
This Work	**1.55**	**25.2**	**~900**	**Yes**	**Yes (up to 50 degrees)**

λ: operational wavelength, MD: modulation depth, P. I.: Polarization-insensitivity, A. I.: Angle-insensitivity, NA: not available.

4.2.5. Summary

We presented a gap-plasmon resonance based polarization-insensitive electro-tunable metasurface that can modulate intensity of the reflected light by leveraging the electro-optic properties of ITO. The proposed metasurface features a 2D array of Au-nanograting on top of ITO–Al_2O_3–Au stack deposited on silica substrate. The numerical simulations reveal that the third-order gap-plasmon resonance is excited at 1.72 μm wavelength, which can be verified by the equivalent RLC-circuit model. The resonance wavelength can be tuned by applying external bias-voltage to accumulate the free-electrons at the ITO–Al_2O_3 interface.

With 2 V applied bias, we can tune the resonance wavelength to 1.55 µm wavelength leading to a modulation depth as high as ~25 dB for random polarization angle of incident light. The modulator exhibits a bit-rate of ~900 Mbps while maintaining a low energy-consumption of ~303 fJ/bit. In addition, the proposed device can be operated with a wide range of incident angle (up to 50 degrees) for both *x*- and *y*-polarized light. To the best of our knowledge, such an **energy-efficient polarization- and angle-insensitive** tunable metasurface based electro-optic modulator is presented here for the first time. The proposed device, thus, could find potential application in nanophotonic systems.

5

ENZ-material based Nonlinear Metasurface for Ultra-Fast Free-space All-Optical Intensity Modulation

Contents

Chapters 3 and 4 presented different designs of metasurfaces for free-space electro-optic intensity modulation by leveraging the electro-optic behaviour of ENZ materials. This Chapter introduces the investigation of ultra-fast all-optical intensity modulation based on nonlinear phenomena in ENZ-materials. To enable ultra-fast all-optical modulation, a novel metasurface has been designed by combining ENZ phenomenon with magnetic plasmon resonance. Section 5.1 presents an elaborated discussion on the theoretical framework and the underlying principle behind intraband transition-induced optical nonlinearities in an ENZ-medium that can be can be harnessed for designing all-optical modulator. Section 5.2 discusses a unique design of magnetic plasmon resonance based metasurface for energy-efficient all-optical modulation by integrating an ENZ-material. The ENZ-material coupled metasurface can operate with a high modulation depth and low pump-fluence at the telecom wavelength while maintaining ultrafast response time in sub-picosecond scale.

5.1. Nonlinear Effect in ENZ Materials —Theoretical Framework

In Chapter 1, it has been revealed that apart from the electro-optic properties, the TCOs also exhibit optical nonlinear phenomena or intensity-dependent refractive index in the ENZ-regime. This section introduces the theoretical framework for nonlinear-effects in ENZ-material induced by intraband electronic transitions. The intraband electronic transition induced plasma frequency shift in the ENZ materials are indeed considered as a nonlinear process due to the variation of the refractive index is not linear with the electric field rather it is dependent on the intensity of light. In other words, the change in the refractive index upon application of the external pump signal depends on the nonlinear susceptibility term, $\chi^{(3)}$, analogous to the optical Kerr effect [190]. Optical intensity-dependent refractive index (n_0) can be written as [33], [58]:

$$n = n_0 + n_2 I = n_0 + \Delta n \tag{5.1}$$

where, the change of refractive index ($\Delta n = n_2 I = \chi^{(3)}\eta_0 I/n^2$) depends on optical pump intensity (I).

It is always desirable to employ nonlinear materials with significantly large value of n_2 for low power applications. TCOs, operating at the ENZ regime have gained massive consideration due to their sub-picosecond nonlinear response with large refractive index tuning capabilities [33]. On application of a pump signal, we can see optical nonlinearity in the ENZ-material. If the optical pump signal has photon energy smaller than the TCOs bandgap energy, redistribution of carriers in conduction band have been observed due to the intraband transitions of electrons. The process causes electron heating and may increase effective mass (m_e*) of the electrons due to the conduction band's non-parabolicity nature, which results in a shift in the plasma frequency. This mechanism of tuning plasma frequency is capable to make significant changes of the material refractive index simply by reshaping material dispersion properties. The plasma frequency (ω_p) shifting mechanism described here is totally based on external optical pumping unlike to that of electrical biasing. The optical nonlinearities in ENZ-materials can be theoretically modelled by using a two-temperature model while considering an extended Drude-model.

5.1.1. Intraband Electronic Transitions — Extended Drude Model

The Drude model mentioned in Eq. (2.34), in Chapter 2, assumes that all free-electrons have the same effective mass, m_e*. However, in ENZ materials, the non-parabolic nature of the electron band causes m_e* to depend on energy, E [58]. Upon application of a pump signal, we can see optical nonlinearity in the ENZ-material induced by the intraband electronic transition, where the absorbed photon energy leads to a rise in the electron-temperature and reallocates the electrons in a non-parabolic conduction band

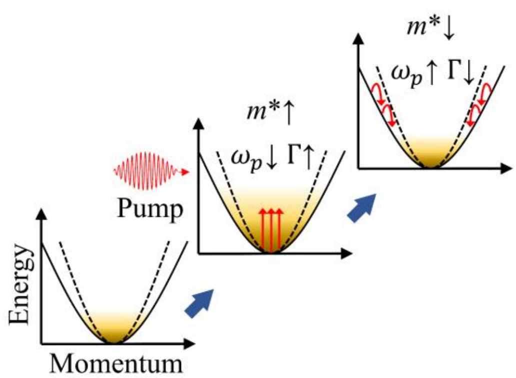

Figure 5.1: Schematic representation of the intraband transitions in a TCO film at ENZ region on applying a pump signal depicting the initial unperturbed energy state, intraband transition, and consequent relaxation process of the free electrons in the conduction band. The black dashed line represents the parabolic approximation of the conducting band. [210]

as presented in Figure 5.1. In other words, the electron effective mass, which decides the plasma frequency, will no longer be constant upon applying pump-signal, rather it will be dependent on the electron temperature [57], [58]. This results in an increase in the electron effective mass and a decrease in the plasma frequency as shown in Fig. 5.1. Furthermore, the mobility (μ) of the ENZ-material is related to m_e* by the degenerate form of the Brooks-Herring formula [191], and thus contributes to an increase in the damping frequency ($\Gamma = e/m_e^*\mu$) on optical pumping (where e is the charge of an electron).

In the absence of the pump signal, the excited free-electrons undergo relaxation to their original unperturbed condition, causing m_e*, ω_p, and Γ to return to their initial steady-state values. Thus, we cannot apply the conventional Drude model to a collection of electrons with different energies. Therefore, the optical nonlinearity due to intraband transitions in ENZ materials has to be modeled using an extended Drude model, where we consider a statistically averaged electron effective mass.

In this direction, we can consider the first-order non-parabolic approximation and model the E–k relationship for ENZ-material as [56]

$$\hbar^2 k^2/2m_0^* = \gamma(E) = E + CE^2 \tag{5.2}$$

where E is the electron energy referenced to the conduction band minimum, k is the wavevector, m_0^* is the electron effective mass weighted at the conduction band minimum, $\hbar$ is the reduced Planck's constant, and C is the first-order nonparabolicity factor. Thus, we can model the electron effective mass, m_e^*, that to be used in the extended Drude model as [192]

$$\frac{1}{m_e^*} = \frac{\int_0^\infty \frac{1}{m_D^*(E)} N_D f_{FD} dE}{\int_0^\infty f_{FD} N_D dE} \tag{5.3}$$

where $N_D = \gamma^{\frac{1}{2}}(d\gamma/dE)(2m_e^*/\hbar^2)^{\frac{3}{2}}(2\pi^2)^{-1}$ is the density-of-states (DOS) and $m_D^*(E) = m_0^*\, d\gamma/dE$ is the DOS effective mass.

The temperature-dependent m_e^* can be attributed to the Fermi–Dirac distribution, $f_{FD} = \left\{\exp\left(\left(E - \tilde{E}_F(T_e)\right)/(k_B T_e)\right) + 1\right\}^{-1}$, where $\tilde{E}_F(T_e)$ is the electron temperature-dependent chemical potential and k_B is the Boltzmann constant. It is known that the carrier density is temperature-independent in the absence of interband transitions [193], and its value is conserved for intraband transitions [56] leading to the expression $N(T_e = 0) = N(T_e) = \int_0^\infty f_{FD} N_D dE$. Therefore, by minimizing the function $|N(T_e = 0) - N(T_e)|$, the chemical potential $\tilde{E}_F(T_e)$ can be calculated as [194]

$$\tilde{E}_F(T_e) = E_F\left[1 - \frac{\pi^2}{12}\left(\frac{k_B T_e}{E_F}\right)^2 + \frac{\pi^2}{80}\left(\frac{k_B T_e}{E_F}\right)^4\right] \tag{5.4}$$

where E_F is the Fermi energy of the TCO film. Furthermore, in degenerate TCO thin films, ionized impurity scattering is the dominant scattering mechanism, which reduces the mobility, μ, of the TCO samples at room temperature [191]. This change in μ is represented by the degenerate form of the Brooks-Herring formula [191], which describes the ionized impurity scattering mobility of the TCO film:

$$\mu = \frac{24\pi^3(\varepsilon_s\varepsilon_0)^2\hbar^3 N}{\mathrm{e}^3 m_e^{*2} N_{\mathrm{ion}}\left[\ln[1+y(n)] - \frac{y(n)}{1+y(n)}\right]} \tag{5.5}$$

where $y(n) = \frac{2(3N\pi^8)^{1/3}\hbar^2\varepsilon_s\varepsilon_0}{\mathrm{e}^2 m_e^*}$, N_{ion} is the density of the ionized impurities, and ε_s is the static permittivity of the TCO film.

5.1.2. Ultra-fast Hot-Electron Dynamics using Two-Temperature Model

On irradiation with a femtosecond laser pulse, the ENZ material absorbs the laser energy causing generation of hot electrons, which acquire a non-thermal energy distribution and act as delayed energy sources. Thus, the non-linear response has a finite response time, and the maximum response is delayed with respect to the peak of the laser excitation [58].

The temperature dynamics of the conduction band electrons upon ultrafast excitation can be accurately described using the phenomenological coupled differential equations of the two-temperature model (TTM) [58], given as

$$C_{\mathrm{e}}\frac{\partial T_{\mathrm{e}}(t)}{\partial t} = -g_{\mathrm{ep}}\big(T_e(t) - T_{\mathrm{l}}(t)\big) + \frac{N(t)}{2\tau_{\mathrm{ee}}(t)} \tag{5.6}$$

$$C_l\frac{\partial T_l(t)}{\partial t} = g_{\mathrm{ep}}\big(T_{\mathrm{e}}(t) - T_{\mathrm{l}}(t)\big) + \frac{N(t)}{2\tau_{\mathrm{ep}}(t)} \tag{5.7}$$

$$\frac{\partial N(t)}{\partial t} = -\frac{N(t)}{2\tau_{\mathrm{ee}}(t)} - \frac{N(t)}{2\tau_{\mathrm{ep}}(t)} + P(t) \tag{5.8}$$

where C_{e} and C_{l} are the heat capacities of the electron and lattice, respectively, and g_{ep} is the electron–phonon coupling coefficient. The rate of energy exchange between the electrons and the phonons is defined using g_{ep}.The electron–phonon and electron–electron relaxation periods are τ_{ep} and τ_{ee}, respectively, and N is the non-thermal energy density stored in the excited electrons. The heat capacity of electron (C_e) is related to the electron temperature (T_{e}), and is defined as [58]

$$C_{\mathrm{e}} = \frac{3\pi^2 N k_{\mathrm{B}} T_{\mathrm{e}}}{\sqrt{36T_{\mathrm{F}}^2 + 4\pi^4 T_{\mathrm{e}}^2}} \tag{5.9}$$

where T_{F} is the Fermi temperature of the TCO film [59]. The energy exchange between the excited electrons and the lattice is represented using electron–phonon coupling coefficient (g_{ep}) as [58]

$$g_{\mathrm{ep}} = 0.562N \frac{k_{\mathrm{B}}^2 \theta_{\mathrm{D}}^2 v_{\mathrm{F}}}{L_{\mathrm{f}} T_{\mathrm{l}} \varepsilon_{\mathrm{F}}} \tag{5.10}$$

where θ_{D} is the Debye temperature, L_{f} is the electron mean free path, and v_F is the Fermi velocity of the ENZ-material. The electron–electron (τ_{ee}) and electron–phonon (τ_{ep}) relaxation times define the rate at which absorbed energy is exchanged between the electrons and the lattice, respectively, as given by [58]

$$\tau_{\mathrm{ee}} = C\left\{\frac{\omega^2}{4\pi^2\omega_{\mathrm{p}}}\left[1 + \left(\frac{2\pi \mathrm{k_B} T_{\mathrm{e}}}{\hbar\omega}\right)^2\right]\right\}^{-1} \tag{5.11}$$

$$\tau_{\mathrm{ep}} = 2\frac{C_{\mathrm{e}}}{g_{\mathrm{ep}}} \tag{5.12}$$

where ω is the frequency of the laser excitation and C is the scaling factor. We can estimate the value of the parameter C at room temperature by using the expression $1/\tau_{\mathrm{ee}} + 1/\tau_{\mathrm{ep}} = \Gamma$ as mentioned in ref. [58].

The effective absorbed power density $P(t)$ can be calculated as [47].

$$P(t) = \frac{F_0}{\tau_{\mathrm{p}}}\alpha e^{-2\left(\frac{t}{\tau_p}\right)^2} \tag{5.13}$$

where F_0 is the pump fluence of a Gaussian laser pulse excitation, τ_p is the pulse duration, and d is the thickness of the TCO-film. The parameter α is the effective absorption coefficient, which can be defined by $\alpha = -{}^{1}/_{d} \ln\left[{}^{T}/_{(1-R)^2}\right]$ as a function of transmittance (T) and reflectance (R) while illuminating light to a TCO-film with a thickness of d [195].

5.2. Ultra-Fast All-Optical Modulation using Nonlinearity from ENZ effect

In the previous section, the underlying principle behind the optical nonlinear effects of ENZ-materials and a relevant theoretical framework have been discussed. The ultra-fast change in refractive index of the ENZ-material upon applying external pump-signal can be useful to realize high-speed all-optical modulators and switches. If the ENZ-material is integrated with a resonating nanostructure, the resonance phenomenon can be tuned by leveraging the pump-signal induced optical nonlinearities in the ENZ-medium. This opens a new door to realize all-optical modulation at the resonance wavelength.

Based on this astonishing scheme, several metasurface designs have been demonstrated to realize all-optical modulation of polarization, phase, and amplitude [55], [59]–[63]. However, the state-of-the-art all-optical intensity modulators are either suffering from low modulation depth or requirement of high pump-fluence [33], [55]. Thus, the realization of femtosecond all-optical modulation with high modulation depth (> 0.8) and low pump-fluence (~ few µJ/cm^2) simultaneously, remains a challenging task.

To bridge these gaps, in this section, a novel design-strategy of plasmonic metasurface has been presented by leveraging the nonlinear effects of ENZ material combined with the magnetic plasmon (MP) resonance of metallic-grating structures. The proposed device can operate with a very low pump-fluence of 75 µJ/cm^2 to achieve a high modulation depth of 0.83 while maintaining an ultra-fast response time of 776 fs.

5.2.1. Structural Overview

Figure 5.2(a) depicts the perspective view of the proposed plasmonic metasurface for ultra-fast all-optical intensity modulation. The proposed device comprises a periodic array of two closely-spaced gold (Au) nanograting deposited on optically thick Au-layer

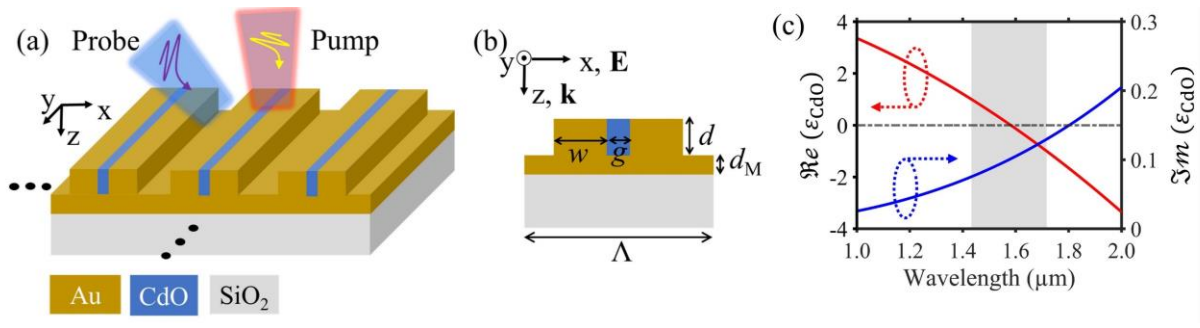

Figure 5.2: Schematics of the proposed magnetic-plasmon resonance based metasurface for all-optical modulation, showing (a) a perspective view, and (b) a cross-sectional view (*x*-*z* plane) of a meta-atom. The meta-atom consists of two closely-spaced Au-nanograting deposited on optically thick Au-layer, where the groove has been filled with cadmium-oxide (CdO). The width (w) of each Au-nanograting is 160 nm having a nanogroove of g = 50 nm wide and periodicity (Λ) of 700 nm along *x*-direction. We consider an *x*-polarized incident wave propagating along z-direction as probe beam. Here, d = 350 nm and d_M = 100 nm. (c) The real ($\Re e(\varepsilon_{\mathrm{CdO}})$) and imaginary ($\Im m(\varepsilon_{\mathrm{CdO}})$) parts of permittivity of the CdO film, where the ENZ-region is shaded in gray. [210]

on silica (SiO_2) substrate. The meta-atom or unit-cell structure is presented in Figure 5.2(b), with a periodicity of Λ = 700 nm along the *x*-direction. Under the illumination of *x*-polarized light, we have observed excitation of a strong magnetic plasmon resonance mode leading to a dip in the reflectance spectra. To enable optical nonlinearities and dynamic resonance response, the nanogrooves in the meta-atoms are filled with an ENZ-material, cadmium-oxide (CdO). Here, we would like to emphasize on the fact that the electron heat-capacity of the CdO is smaller than ITO [56] — leading to a larger variation in the electron temperature when all other parameters are kept constant. This motivated us to choose CdO over ITO as ENZ-material for our design.

We have considered a highly doped ($N \sim 7 \times 10^{20}$ cm^{-3}), high mobility (μ = 300 cm^{2}V^{-1}s^{-1}) CdO layer. Based on the Drude model, as mentioned in Eq. (2.34), the initial value of the real, $\Re e(\varepsilon_{\mathrm{CdO}})$, and imaginary, $\Im m(\varepsilon_{\mathrm{CdO}})$, parts of permittivity of CdO have been estimated for the wavelength range of 1 μm – 2 μm as shown in Figure 5.2(c). Here, we denote the zero-permittivity cross-over wavelength with λ_{ENZ} = 1.57 μm,

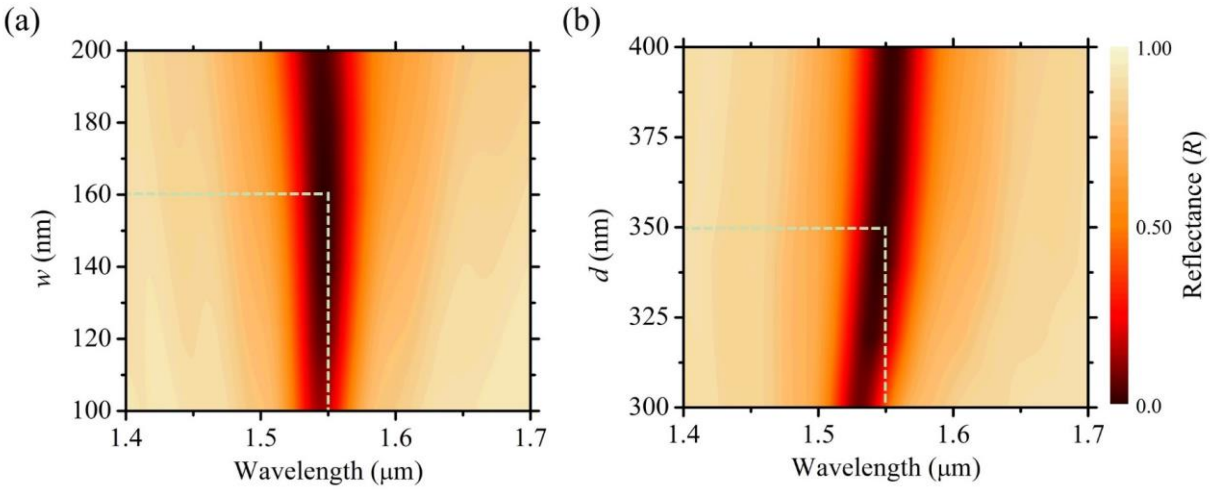

Figure 5.3: Parametric study, based on numerical simulations, showing contour plot of Reflectance for optimization of the metasurface dimensions by varying (a) grating width, *w* and (b) height, *d*, keeping other parameters constant. Here, the dashed lines indicate the dimensions for which the reflectance (*R*) is minimum at 1.55 μm wavelength. [210]

where the ENZ-region is shown for which $\Re e(\varepsilon_{CdO})$ is in between –1 to +1. The material dispersion effect has been considered while performing theoretical modelling and numerical simulations.

As mentioned in the previous section, on application of a laser pump signal, the free electrons in the conduction band of ENZ materials undergo intraband transitions to a higher energy state, causing an increase in the electron effective mass (m_e*), and a decrease in the plasma frequency (ω_p). We utilize this nonlinear phenomenon of CdO combined with magnetic plasmon resonance to demonstrate an ultra-fast all-optical intensity modulation.

5.2.2. Parametric Analysis

To study the optical performance of the proposed metasurface, we have performed 3D FDTD simulations considering periodic boundary conditions along *x*- and *y*-axis while keeping perfectly matched layer along *z*-axis. In order to ensure that the proposed metasurface exhibits magnetic plasmon resonance at the vicinity of 1.55 µm wavelength, a careful selection of each geometrical parameter is necessary. We optimized the design based on numerical simulations, with no external pump signal applied, as shown in Figure 5.3. We varied a particular geometrical parameter keeping the other parameters constant to see the effect on resonance wavelength. The optimized parametric values, with λ_{MP} at the vicinity of 1.55 µm, are marked by the dashed lines in Figure 5.3(a) and (b). Moreover, to incorporate the fabrication imperfection that arises from the rounded-edges of the nanograting, we have simulated our design by rounding the edges (with a 10 nm rounding radius).

5.2.3. Strong Light–Matter Interaction *via* Magnetic Plasmon Resonance

With an *x*-polarized incident plane wave having magnetic field along the *y*-direction, an oscillating current can be generated around the nanogrooves [196]. This induced current generates a strong magnetic field, *i.e.*, diamagnetism, as per Lenz's law [196]. Thus, a strong magnetic plasmon resonance can be observed.

The normalized magnetic ($|H_y|$) and electric field ($|E_x|$) distributions at the resonating wavelength (λ_{MP}) in the vicinity of 1.55 µm are shown in Figure 5.4(a) and (b) in the absence of the pump. The current-density and the instantaneous electric field vectors are represented by the arrows in Figure 5.4(a) and (b), respectively. We have used Maxwell's fourth law to calculate the current-density vectors, where we can see the vectors form a closed loop around the nanogrooves [196]. We observe that the strongest enhancement of the magnetic field occurs at the bottom of the nanogrooves due to the closed current loop. This hotspot of the field enhancement around the nanogrooves filled with CdO ensures strong light–CdO interactions at the vicinity of

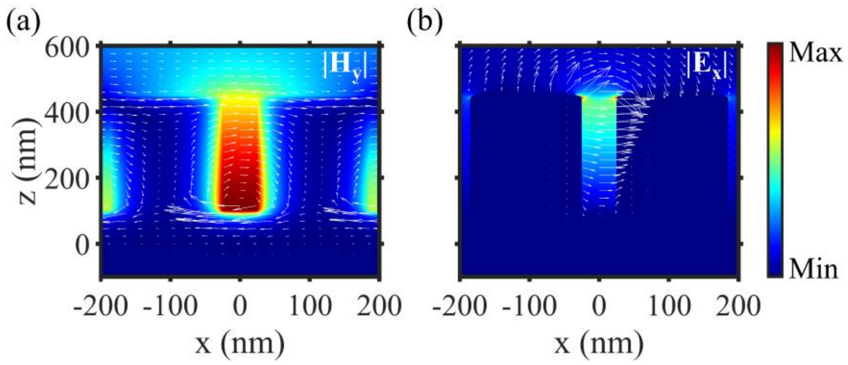

Figure 5.4: (a) Magnetic-field ($|H_y|$) and (b) Electric-field ($|E_x|$) profiles for *x*-polarized incident optical probe signal in *x-z* view for pump fluence, F_0 = 0 μJ/cm^2 at 1.55 μm. Here, the current-density and the instantaneous electric field vectors are shown by the arrows in (a) and (b), respectively. [210]

1.55 μm. Here, we leverage the pump-signal induced optical nonlinearities in the ENZ-medium to shift the resonance dip, which results in a new all-optical modulation scheme at the resonance wavelength.

5.2.4. Enhancement of Optical Nonlinearities in ENZ-materials

To study the hot-electron dynamics, we consider a Gaussian laser pump-pulse excitation of duration 100 fs with centre wavelength of 1.57 μm. The hot-electron dynamics can be precisely defined using the two-temperature model (TTM) as presented in the previous section [58]. In order to calculate the electron effective mass (m_e*) under the influence of an external pump signal, as mentioned in Eq.(5.3), we take m_0^* = 0.16 m_e, with m_e denoting the mass of an electron, and C = 0.5 eV^{-1} [46] for our CdO film. The value of Fermi energy (E_{F}) for our numerical calculations, as mentioned in Eq. (5.4), is taken from ref. [191]. Furthermore, the mobility (μ) is related to m_e* by the degenerate form of the Brooks–Herring formula [191], and thus contributes to the increase in the damping frequency ($\Gamma = \mathrm{e}/m_e^* \mu$) on optical pumping, as mentioned in Eq. (5.5). While using the Eq.(5.5), we have assumed N_{ion} = N_D, with N_D defined as the density of the

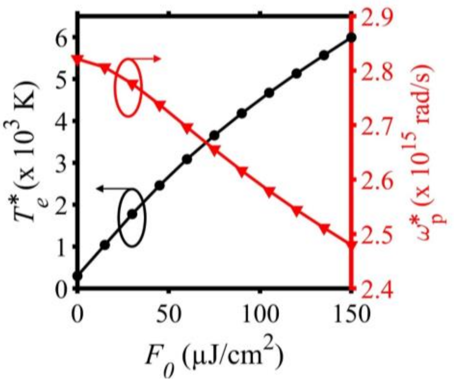

Figure 5.5: The dependence of electron temperature (T_e*) and plasma frequency (ω_p*) of CdO on the pump fluence (F_0) for the proposed structure. [210]

ionized donors. Additionally, the ionized donors have been assumed to be singly charged, and the static permittivity for CdO is assumed as ε_s = 21.9, as defined in ref. [197].

While calculating the electron–phonon coupling coefficient (g_{ep}) as shown in Eq.(5.10), the values of Debye temperature (θ_D), electron mean free path (L_f), and Fermi velocity (v_F) for the CdO film are taken from ref. [198], [199], and [191], respectively. In our theoretical calculations, the pump fluence (F_0) is varied from 0 to 150 μJ/cm^2. The corresponding variations in the electron temperature and the plasma frequency of the CdO-layer for our proposed structure have been calculated using the TTM equations, as illustrated in Figure 5.5.

The heat capacity of electron (C_e) of CdO is defined using Eq.(5.9) [200]. At T_e = 300 K, we calculate the value of C_e as 1056 Jm^{-3}K^{-1}. As mentioned earlier, the electron heat-capacity of the CdO is smaller than ITO [56], which results in a larger variation in the electron temperature when all other parameters are kept constant.

Due to integration of an ENZ-material with the structure, an extreme increase in the electron temperature of the ENZ-layer can be seen. It should be noted that the enhancement originates from the coupling of magnetic plasmon resonance with ENZ-

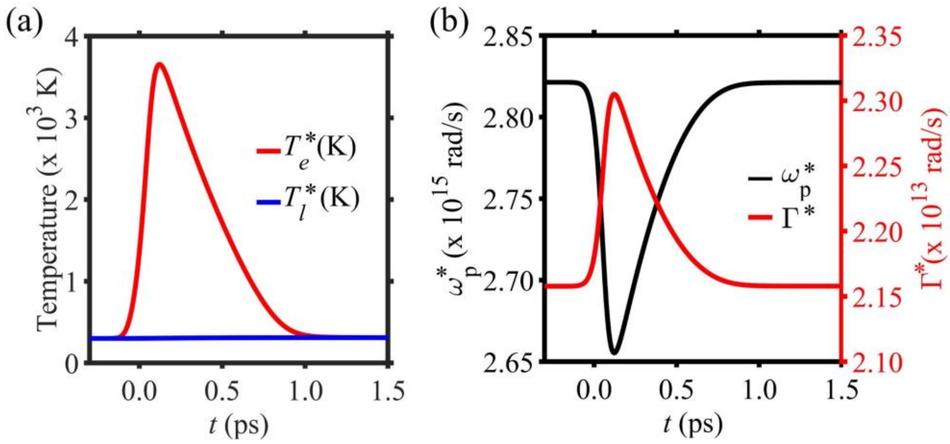

Figure 5.6: Transient response of the (a) electron (T_e*) and the lattice (T_l*) temperature, and (b) plasma frequency (ω_p*) and damping constant of the CdO-layer for the proposed structure. [210]

mode for our structure. This assures that we can achieve a much larger variation in the electron temperature in the CdO-layer with a lower pump-fluence for our structure than that of a bulk-CdO film. In other words, the plasma frequency (shown in Figure 5.5) is an effective variation for our structure after incorporating the electric field enhancement due to the magnetic plasmon resonance.

To highlight this fact, we have represented the modulated plasma frequency and electron temperature of CdO-layer as ω_p* and T_e*, respectively (see section A.01 of Appendix for more details). We observe an increase in the T_e* from its steady state value of 300 K to 5991 K with the variation of the pump fluence from 0 to 150 µJ/cm^2. The ω_p* decreases from its steady state value of 2.821 × 10^{15} rad/s (at F_0= 0 µJ/cm^2) to 2.480 × 10^{15} rad/s (at F_0=150 µJ/cm^2).

To maintain a high modulation depth with energy consumption as minimum as possible, we fix the pump fluence as F_0= 75 µJ/cm^2. Figure 5.6(a) shows the transient response of the electron (T_e*) and lattice (T_l*) temperatures of CdO-layer, respectively, for our structure. The T_e* reaches its peak of 3654 K at t = 0.12 ps and gradually decays to its steady-state value of 300 K after a duration of ~1 ps. The change in the T_l* is negligible compared to the variation in the T_e*. Furthermore, we define a constant lattice heat capacity (C_l) of 2.6 × 10^6 $Jm^{-3}K^{-1}$ such that $C_e \ll C_l$, which leads to $\Delta T_l \ll \Delta T_e$.

Similarly, Figure 5.6(b) displays the transient response of the ω_p* and Γ* for our device. We observe that on applying the pump signal, the ω_p* dips to its minimum value of 2.656 × 10^{15} rad/s at *t* = 0.12 ps before gradually increasing to its steady-state value of 2.821 × 10^{15} rad/s. On the contrary, the Γ* peaks to 2.305 × 10^{13} rad/s before gradually decreasing to its steady-state value of 2.158 × 10^{13} rad/s. We also check whether the pump induced optical nonlinearity of gold (Au) would affect the performance of our proposed structure. It should be noted that gold also has the nonlinear optical response at picosecond-to-nanosecond time scale. However, similar to the ref. [56], [59], the intrinsic nonlinearity of gold can be ignored for our study due to the negligible change in the electron-temperature of gold as compared to the ENZ-material CdO for our metasurface structure (see section A.02 of Appendix for more details). It should be noted that the previously reported (experimentally verified) laser power induced damaged threshold for a CdO film is 134 mJ/cm^2 [201], which is much higher than the considered pump-fluence (75 μJ/cm^2) in our study.

5.2.5. Results and Discussion — All-Optical Modulation

Due to the excitation of the magnetic plasmon resonance, we observe a resonance dip in the reflectance spectra at the vicinity of 1.55 μm for F_0 = 0 μJ/cm^2, as shown in Figure 5.7(a). We consider that our proposed device is at the “OFF” state owing to negligibly low reflectance at the operating wavelength of 1.55 μm. We have incorporated the theoretically obtained optical nonlinearities in the ENZ-medium into the FDTD simulations. Thus, the resonance dip can be tuned by applying external pump signal. We observe that the pump-induced plasma frequency variation in the CdO-layer causes a

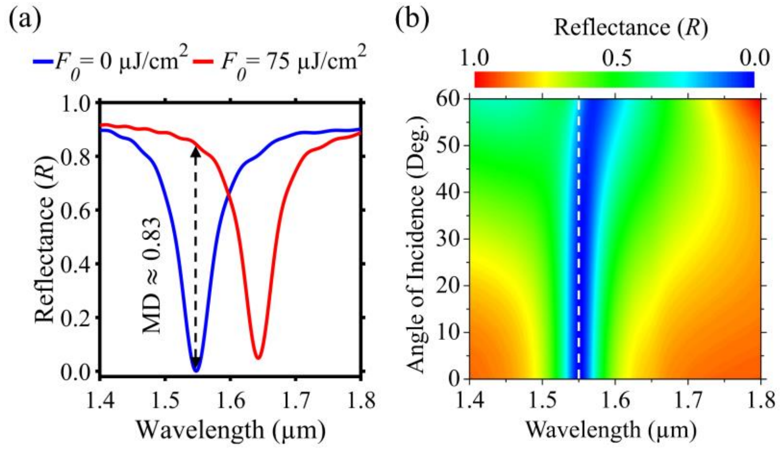

Figure 5.7: (a) Reflectance spectrum for *x*-polarized incident optical probe signal for OFF-state (at F_0= 0 μJ/cm^2) and ON-state (at F_0= 75 μJ/cm^2) pump fluences. The modulation depth (MD ≈ 0.83) at 1.55 μm is represented by an arrow-dashed line. (b) Color contour plot of reflectance spectrum for *x*-polarized incident optical probe signal as a function of oblique incidence angles (θ). Note: the dashed line depicts the wavelength of 1.55 μm. [210]

red-shift of the resonance dip in the reflectance spectra. This results in a high modulation depth of 0.83 (~21 dB) at 1.55 μm for pump fluence, F_0= 75 μJ/cm^2 — referred to as "ON" state. Thus, we can dynamically switch between the "ON" and "OFF" states of the device by applying external optical pumping.

To understand the device performance under the influence of the oblique incidence angle of the probe beam, we have done numerical simulations for various incidence angles ranging from 0º to 60º. Figure 5.7(b) represents the color contour plot of reflectance spectra with varying incidence angles of the *x*-polarized probe beam without applying any pump signal. We have observed a slight red-shift in the λ_{MP} with the increase of oblique incidence angle. Nevertheless, we can maintain a negligible reflectance at 1.55 μm with a probe beam having incidence angle of up to 50º. This indicates a wide angle-insensitivity of the design.

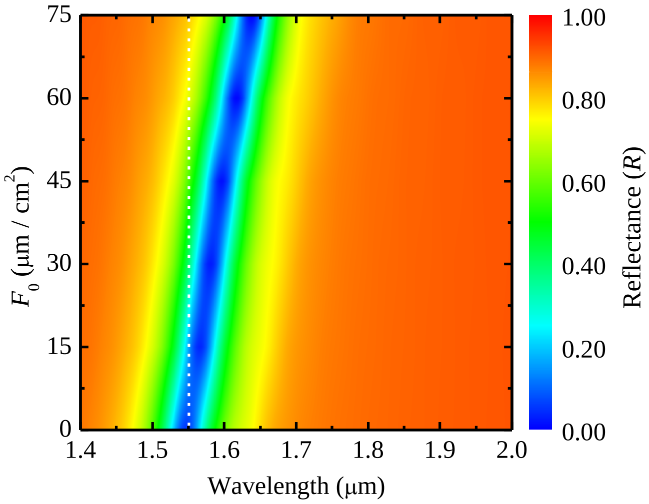

Figure 5.8: Color contour plot of reflectance spectrum for *x*-polarized incident optical probe signal as a function of pump fluence (F_0). Note: dashed line depicts wavelength of 1.55 μm.

Figure 5.8 illustrates the color contour plot of reflectance spectra for variation of the pump-fluence from 0 μJ/cm^2 to 75 μJ/cm^2. As mentioned previously, we can see a red-shift in the resonance dip in the reflection spectra with the increase of pump-fluence. Thus, we can dynamically tune the resonance condition by applying external optical pumping — indicating a nonlinear optical nonlinear phenomenon.

5.2.5.1. Effective nonlinearities of the metasurface using EMT approximation

To understand the nonlinear behaviour of our proposed ENZ-material coupled metasurface, we have used the effective medium theory approach for calculating the effective refractive index of the whole structure [202]. The theoretical approximation assumes that the metasurface can be replaced by a continuous material with a linear effective refractive index (n_{eff}) along the *x*-axis. This homogenized effective refractive index of the whole structure allows us to find the effective change in the refractive index

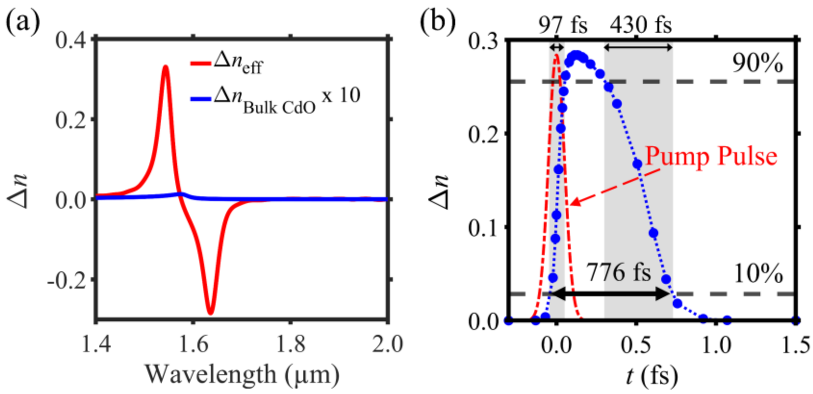

Figure 5.9: (a) Change in the effective refractive index of the proposed CdO-coupled structure (Δn_{eff}) and the refractive index variation of bulk CdO as a function of wavelength upon applying pump pulse with fluence (F_0) of 75 μJ/cm^2. (b) Transient response of Δn_{eff} , where the rise time and recovery time are shown as 97 fs and 430 fs, respectively, at 1.55 μm. The red dashed line shows the 100 fs Gaussian pump excitation at 1.57 μm. [210]

of the metasurface upon applying external pump signal. Using the *S*-parameter inversion method for an inhomogeneous system, we determine n_{eff} as [202]

$$n_{\mathrm{eff}} = \frac{1}{kd}\cos^{-1}\left[\frac{1}{2S_{21}}(1 - S_{\mathrm{av}}^2 + S_{21}^2)\right] \tag{5.14}$$

where k is the wave vector, d is the overall thickness of the proposed structure, and $S_{\mathrm{av}} = \sqrt{S_{11}S_{22}}$ is the averaged parameter used for inhomogeneous metasurface structures *i.e.*, $S_{11} \neq S_{22}$. Furthermore, S_{11}, S_{12}, S_{21}, and S_{22} are the S-parameters obtained from the FDTD simulations of the proposed metasurface structure.

Note that the parameters S_{11} and S_{21} are calculated for normal incidence. Similarly, the parameters S_{21} and S_{22} are calculated for reverse incidence. For calculating the change in effective refractive index (Δn_{eff}) of the metasurface, we calculate the S-parameters of our structure in the absence (F_0 = 0 μJ/cm^2) and presence (F_0 = 75 μJ/cm^2) of laser pump illumination, respectively, by making use of the two-temperature model and a series of FDTD simulations.

We compute the n_{eff} values at different points over the operating wavelength range for both the 'OFF' and 'ON' states. Finally, Δn_{eff} is calculated as the difference in the n_{eff} values between the 'ON' state and the 'OFF' states of our proposed structure over the operating wavelength range. In Figure 5.9(a), we can see the pump-intensity dependent change in the effective refractive index of the proposed CdO-coupled structure. Due to the excitation of the magnetic plasmon resonance, strong light–matter interactions can be assured at the resonance wavelength. This results in a large variation in the Δn_{eff} of the proposed CdO-coupled structure.

The peak variation in the Δn_{eff} can be seen at the wavelength of 1.545 μm as ~0.32, at the vicinity of our operating wavelength of 1.55 μm. To witness the enhancement of the nonlinearities in the CdO-coupled metasurface, we have also shown the change in refractive index of a 350 nm bulk CdO while illuminating a pump with fluence of 75 μJ/cm^2.

For calculating Δn for bulk CdO, we compute the shift in plasma frequency (ω_p) for a 350 nm CdO film using the two-temperature model and the electronic dispersion relation. Note that for calculating the absorption coefficient of the bulk CdO, we utilize the relation, $\alpha = (4\pi n'')/\lambda$, in the two-temperature model, where n'' is the imaginary part of the refractive index of CdO. From the obtained ω_p values, we further calculate the refractive index values for 'OFF' and 'ON' states by using the Drude model. Similar, to what has been previously done for our proposed structure, we calculate Δn for the bulk CdO by calculating the difference in the refractive index values for 'ON' and 'OFF' states, respectively, at different points over the operating wavelength range.

A direct comparison between the refractive index variation for the proposed structure (Δn_{eff}) and the bulk CdO (Δn) has been presented in Figure 5.9(a), which shows the increased nonlinearity obtained from our proposed metasurface structure. We observe that due to the coupling of ENZ-mode with the magnetic plasmon resonance, the change in the refractive index has been enlarged by a factor of ~100 compared to

Table 5.1: Comparative overview with a few recently reported ENZ-material based metasurfaces for all-optical modulation

Ref.	**λ (nm)**	**Structural Overview**	**Pump-Fluence (μJ/cm^2)**	**Switching Speed (fs)**	**MD**	**FOM (μJ^{-1}.cm^2)**	**A.I.**
[56]	1500	ITO-coupled plasmonic nano-antenna (experimental)	~ 21	~1100	0.18	8.7×10^{-3}	-
[59]	1500	ITO nano-resonator array (experimental)	7000	600	~0.2	0.028×10^{-3}	Yes
[60]	1240	ITO-coupled surface plasmon resonance based (theoretical)	~75	~660	0.36	4.8×10^{-3}	No
[63]	1310	AZO-coupled guided-mode resonance based (theoretical)	2410	Not given	0.45	0.18×10^{-3}	No
[211]	1240	ITO-coupled high-index contrast grating (theoretical)	3000	~660	0.41	0.13×10^{-3}	No
This work	**1550**	**CdO-coupled magnetic plasmon resonance based (theoretical)**	**75**	**717**	**0.83**	**11×10^{-3}**	**Yes**

*Here, λ: operational wavelength, MD: Modulation Depth, A.I.: Angle-insensitivity, and FOM: Figure-of-Merit

that of a bulk CdO layer. In Figure 5.9(b), the transient response of the Δn_{eff} can be seen. Upon applying the pump beam, we observe a peak value of ~0.29 at t = 0.12 ps for 1.55 μm. Furthermore, we can calculate the rise time (10% to 90% of peak Δn_{eff}) and recovery time (90% to 10% of peak Δn_{eff}) as 97 fs and 430 fs, respectively. Thus, the overall switching time can be estimated as 776 fs.

5.2.5.2. Comparative Analysis

To understand the overall performance of the device and to compare the metrics with the state-of-the-art designs, we define a figure-of-merit (FOM) that provides an optimum performance metric by incorporating the trade-off between the modulation depth (MD) and the pump-fluence (F_0) requirement, given by

$$\mathrm{FOM} = \mathrm{MD}/F_0 \quad (\mu\mathrm{J}^{-1}.\mathrm{cm}^2) \tag{5.15}$$

As shown in Table 5.1, our CdO coupled structure can outperform the previously reported TCO-based free-space all-optical intensity modulators. The FOM calculations shows that our proposed magnetic plasmon resonance based design has the highest value among the previously reported ENZ-material based all-optical intensity modulators. Moreover, our device is angle-insensitive and can operate with a wide-range of oblique incident angles of probe beam up to 50 degrees.

5.2.5.3. Investigating the Performance with Degraded CdO layer

It should be noted that we have considered the parameters of the CdO-layer as per the literature [46], [57], [203]. However, for our proposed structure, the CdO-layer need to be deposited on top of gold thin layer, which may eventually reduce the mobility value of CdO than that of the ideal cases. To understand the effect of reduced mobility value on the optical performance of the device, we have shown the optical response of the device for the set of reduced mobility values. We have taken three different reduced initial mobility values as ($0.9 \times \mu = 270$ cm^{2}V^{-1}s^{-1}), ($0.8 \times \mu = 240$ cm^{2}V^{-1}s^{-1}), and ($0.7 \times \mu = 210$ cm^{2}V^{-1}s^{-1}). It should be noted that the damping frequency (Γ) of CdO-layer is dependent on the mobility (μ) as Γ ($= e/\mu m_e^*$), where the statistically averaged electron's effective mass is denoted by m_e^*. Here, we would like to emphasize on the

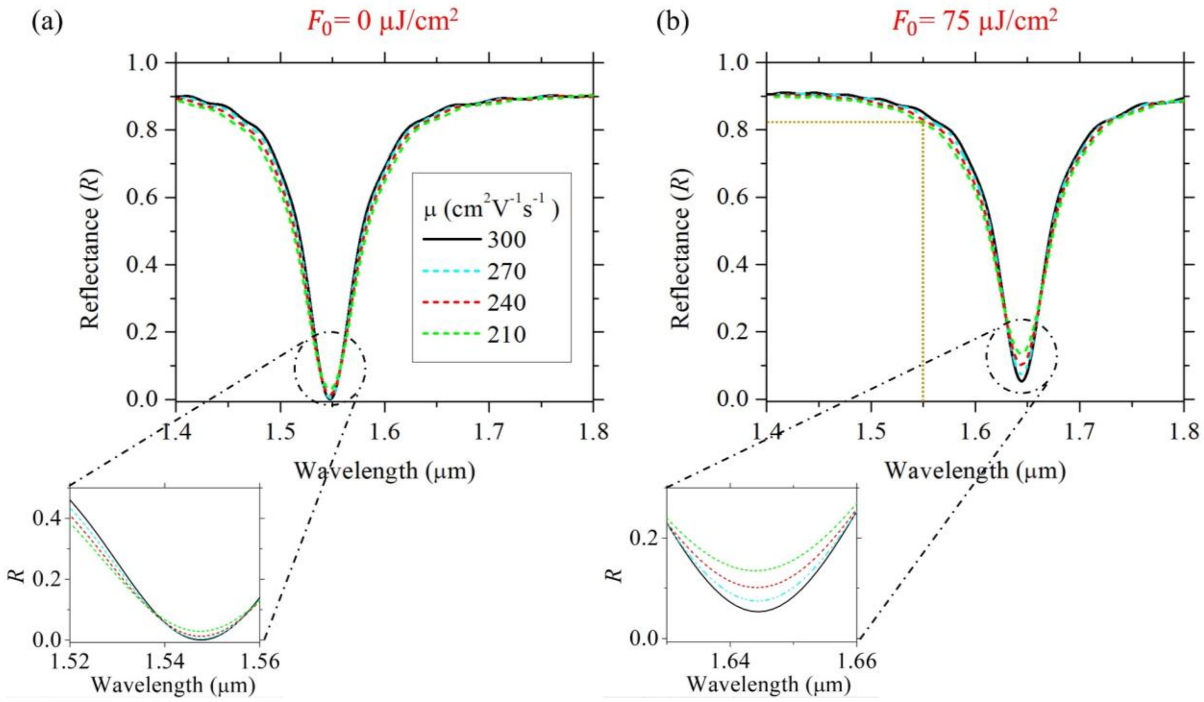

Figure 5.10: Reflectance spectra for *x*-polarized incident probe light signal for different mobility (μ) values as 300, 270, 240, and 210 cm^{2}V^{-1}s^{-1} for (a) OFF-state (at F_0= 0 μJ/cm^2) and (b) ON-state (at F_0= 75 μJ/cm^2). The dotted lines in (b) depicts the minimum reflectance value of ~0.82 achieved at 1.55 μm for different mobility values. The zoomed view for the resonance dip at different mobility values are shown for both cases. [210]

fact that a negligible reflectance (R), at the vicinity of 1.55 μm wavelength, still could be maintained with a 30% reduction of the mobility value when there is no pump signal applied (*i.e.*, at F_0= 0 μJ/cm^2), as shown in Figure 5.10(a). Thus, the metasurface will remain in the "OFF" state. It can also be observed that the reduced mobility value doesn't alter the magnetic plasmon resonance wavelength, rather it broadens the resonance phenomena due to the increased value of damping frequency (Γ).

The impact of the reduced mobility values for the "ON" state with a pump fluence, F_0= 75 μJ/cm^2, can be seen in Figure 5.10(b). It should be noted that while calculating the effective damping frequency (Γ*), we have incorporated the change in the effective electron mass. Then, the Γ* has been calculated for each reduced initial mobility value. The reflectance spectra for the F_0 = 75 μJ/cm^2 can be seen in

Figure 5.10(b). We observe that for the set of reduced mobility values, the reflectance (R) can be maintained more than 0.8 at 1.55 μm wavelength, as shown by the dotted lines in Figure 5.10(b). However, a reduction in the modulation depth from ~0.83 (with μ = 300 $cm^2V^{-1}s^{-1}$) to ~0.79 (with μ = 210 $cm^2V^{-1}s^{-1}$) can be observed. Nevertheless, we can still achieve a high-contrast modulation with degraded CdO having a 30% reduced mobility value of 210 $cm^2V^{-1}s^{-1}$. It should be noted that the experimentally measured mobility of the CdO-layer grown on gold thin film, in the ref. [57], is reported as 300 $cm^2V^{-1}s^{-1}$, which has been obtained from the Hall-measurement. This ensure that the mobility of the CdO-layer will not reduce much from our considered value.

5.2.6. Prospective Experimental Methods

Fabrication. The proposed metasurface can be fabricated on a standard silica substrate. To begin, the Au back-reflector with 100 nm thickness (as shown in Fig. 5.2) may be grown on top of the substrate by sputtering. Afterward, the CdO layer with thickness 350 nm can be grown by pulsed laser deposition. Then, the periodic array of CdO can be patterned by using standard electron beam lithography (EBL) and lift-off process [56], [59], [204]. We can define the periodicity of the unit-cell structure as 700 nm along x-axis while the width of the CdO grating as 50 nm for a 100 × 100 μm^2 total device area. Finally, a second round of EBL needs to be performed, followed by deposition of Au-layer (by e-beam evaporation) and lift-off process [56], [204] for patterning the Au-nanograting having the width of 160 nm.

Measurements. For the static reflectance measurements, we can use an infrared ellipsometer or an ultraviolet-visible-near-infrared spectrophotometer to record the spectral reflectance under x-polarized incident light. For the transient measurements, we can use an amplified laser source, with a central wavelength of 1500 nm, pulse duration of 100 fs and repetition rate of 1 kHz, feeding two identical optical parametric amplifier (OPAs). The idler output of one OPA can be used as the pump, and the idler output of the other OPA can be used as the probe [56], [57], [59]. The output wavelengths of the two OPAs can be controlled independently to generate pump and probe beam with different central wavelengths. The pump–probe delay could be generated by routing the pump beam through a controlled delay stage with a retro-reflector. After being reflected from the sample, the probe beam can be separated from the pump using an additional iris, and may be sent through a monochromator into an extended-range InGaAs photodiode for detection. The pump pulse energy needs to be tuned for obtaining required pump-fluence or pump-energy density. For example, with a beam area of ~0.02 cm^2, the pump pulse energy should be ~1.5 µJ, which corresponds to a pump-fluence of 75 $\mu J/cm^2$. The probe pulse energy needs to be kept below the damage threshold level of the InGaAs photodiode, which is usually in the order of a few nanoJoules. Here, we would like to emphasize on the fact that we can take the pump signal as a normally incident beam. Due to the angle-independency of the metasurface, the probe signal can have an oblique incidence during the pump-probe delay analysis in the experimental study.

5.2.7. Summary

We presented an ultra-fast all-optical modulation scheme based on magnetic plasmon resonance phenomena of the metasurfaces. The presented metasurface comprises a periodic array of two closely-spaced nanograting deposited on an optically thick ground-plane, where the nanogrooves formed between the consecutive nanogratings are filled with ENZ-material, CdO. We leverage the intraband transition induced optical nonlinearities of the ENZ-material. The intraband electronic transitions in the ENZ-material upon applying ultra-fast external pump signal cause an increase in the electron temperature, which leads to the modulation of plasma frequency. The temperature dynamics of electrons are studied by using a two-temperature model.

Due to the excitation of magnetic plasmon resonance strong light–matter interactions can be assured at the resonance wavelength. This leads to an enhancement of the nonlinear phenomenon of the proposed CdO-coupled structure. We have shown that the pump-induced refractive index change in the CdO-layer causes the red-shift of the resonance dip in the reflectance spectra leading to a high modulation depth of 0.83 at 1.55 µm wavelength. The transient study reveals that the device exhibits ultrafast switching speed of 776 fs while maintaining a very low pump-fluence of 75 µJ/cm^2. To the best of our knowledge, such a metasurface based high-contrast energy-efficient ultra-fast all-optical modulation scheme is proposed for the first time that can operate in the telecom wavelength band. The proposed device paves the way toward the realization of next-generation optical and quantum computation systems.

6

ENZ Effect based Integrated On-chip Electro-Optic Intensity Modulators

Contents

Chapters 3, 4, and 5 presented a few metasurface design strategies for free-space electro-optic and all-optical intensity modulation by leveraging electro-optic and nonlinear phenomena of ENZ-materials. This Chapter introduces the study of ENZ-material based *on-chip* electro-optic intensity modulators for integrated photonic system. Different directional coupler based devices have been explored for intensity modulation based on the hybrid integration of ENZ-material in a standard silicon waveguide by utilizing the silicon photonics platform.

Section 6.1 presents a polarization specific energy-efficient design that can modulate the intensity of guided transverse magnetic mode of the input silicon waveguide. Section 6.2 discusses a unique design of a dual-polarization device for modulating the intensity of both guided transverse magnetic (TM) and transverse electric (TE) modes of the input silicon waveguide. This device may help in the reduction of footprint of the integrated photonic systems by eliminating the requirements of extra polarization controlling devices. As the ENZ-material based on-chip modulators primarily alter the intensity of the guided modes by increasing the propagation loss under the influence of external electrical biasing, these electro-optic modulators are known as **electro-absorption (EA) modulators**.

6.1. Polarization Specific Integrated Electro-Absorption Modulator

This section introduces a unique design strategy for a compact (with a 17 μm active length) energy-efficient electro-absorption modulator by leveraging electro-tunable ENZ-effect of ITO. The proposed polarization-sensitive directional coupler based design exhibits energy consumption as low as 62.2 fJ/bit. With a ~10 dB extinction ratio at 1.55 μm wavelength, our design may find potential applications in the integrated nanophotonic system.

6.1.1. Background

Over the last few decades, optical communication systems undoubtedly witnessed explosive development covering the full spectrum of transmission systems ranging from long-haul links (such as transoceanic links) to short-haul links (such as optical interconnects). The overall capacity of such communication systems mostly depends on electro-optic modulator, where electrical data can be imprinted on optical signal. Due to mature silicon technology, silicon photonics based devices have gained enormous attention to design on-chip modulators [24]. However, the weak electro-optic effect of silicon (Si) leads to a high driving voltage (~10 to 50 V) and large propagation length (~ few hundreds μm) for achieving the required modulation depth [12].

Extensive research has been conducted to develop silicon photonics based electro-optic modulators by integrating several active materials such as two-dimensional materials (graphene) [15], phase-change materials [32], transparent conducting oxides (TCOs) [33]. Among these, TCOs are widely adopted in the integrated nanophotonic systems as they can provide optical transparency [37], [38] and can exhibit ENZ effect [33], [40]. Moreover, when the real part of permittivity is close to zero, the imaginary part of permittivity can solely decide the optical properties [162], [176]. This results in a strong optical absorption — leading to the realization of a special type of electro-optic modulators known as "electro-absorption (EA) modulators".

To mitigate the ever-increasing demand of bandwidth, several ENZ-material based modulators have been reported in recent years [33]. However, it is still a challenging task to realize an energy-efficient modulator (preferably with an energy consumption in the order of sub-femtojoule per bit) for power-hungry optical interconnects at data center networks [40]. In this study, we present a compact energy-efficient electro-absorption modulator by leveraging electro-tunable ENZ-effect of ITO. The proposed directional coupler based design exhibits energy consumption as low as 62.2 fJ/bit with a ~10 dB extinction ratio at 1.55 μm and 17 μm active device length.

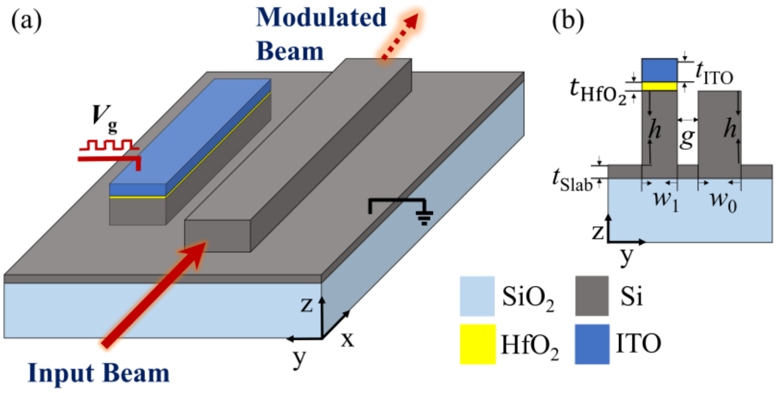

Figure 6.1: Schematics of our proposed coupling-assisted electro-absorption modulator showing a (a) perspective view and (b) cross-sectional view. Note: the guided TM-mode of input waveguide can be coupled to hybrid plasmonic waveguide (on left) and modulated by applying external voltage (V_g) [212].

6.1.2. Design Overview

Schematics of the proposed coupling-assisted electro-absorption modulator are shown in Figure 6.1(a) and (b). Our design consists of a standard silicon-on-insulator waveguide (as input bus waveguide) and a hybrid plasmonic waveguide (HPW) formed by ITO–HfO_2 (hafnia)–Si stack (as coupled waveguide). The input bus silicon rib-waveguide has a width (w_0) of 500 nm and a height (h) of 190 nm with a 30 nm thick slab. The HPW is 190 nm in height (h) and 400 nm in width (w_1) and located at a 100 nm separation gap (g) from the bus waveguide, as shown in Figure 6.1(b). The HfO_2 and ITO layers have thickness of 10 nm and 90 nm, respectively. The geometrical parameters are chosen in such a way that the guided fundamental transverse magnetic mode (TM) of the bus waveguide can couple to the HPW. To study the optical performance of the proposed modulator, a finite-difference time-domain based numerical simulator is used here by considering perfectly matched layers in all directions. We consider a very fine meshing around the ITO–HfO_2 interface.

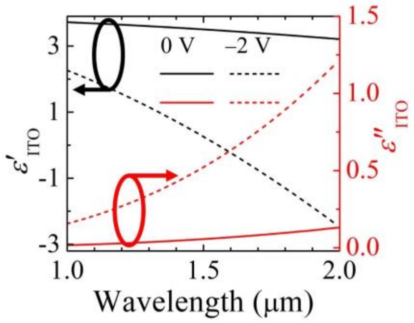

Figure 6.2: Voltage-dependent complex permittivity of ITO at the ultra-thin charge accumulation layer under unbiased and –2V biasing conditions [212].

6.1.3. Electro-Optic Properties of ITO

The ITO–HfO_2–Si stack forms a metal-oxide-semiconductor (MOS) type structure, where the cascaded layers of n-type doped silicon, HfO_2, and ITO act as a metal layer, gate-dielectric layer, and semiconductor layer, respectively. To witness the carrier-accumulation at the ITO–HfO_2 interface, the electrostatic simulations have been carried out in commercially available Lumerical Device tool®. In the device simulations, the parameters assumed for ITO are the same as the ones revealed in Chapter 2 (section 2.4.2). The bulk carrier concentration of ITO is taken as $N = 6 \times 10^{19}$ cm^{-3}.

The complex permittivity of ITO (ε_{ITO}) can be electrically-modified at the ITO–HfO_2 interface due to the formation of an ultra-thin charge **ac**cumulation **l**ayer (ACL). The inhomogeneous ACL can be approximated as a ~3 nm ultra-thin layer, similar to the two-layer model as mentioned in Chapter 2 (sub-section 2.4.2). With an external bias voltage (V_g) of –2 V (corresponding to $N \approx 6\times10^{20}$ cm^{-3}), the ultra-thin ACL exhibits ENZ-effect at 1.55 μm wavelength. The voltage dependent real (ε'_{ITO}) and imaginary (ε''_{ITO}) parts of the permittivity of ITO at the ACL are shown in Figure 6.2 by using the Drude model defined in Eq. (2.34). At –2 V, when real part of ε_{ITO} approaches zero at 1.55 μm wavelength, the imaginary part of ε_{ITO} mainly decides the optical properties of ITO. Therefore, an enhancement of optical absorption can be seen at the ultra-thin ENZ-layer. In other words, when ε'_{ITO} of ITO-ACL approaches the near-zero condition, the ultra-thin ACL behaves as a lossy medium due to Kramers-Kronig relationship. This is the fundamental principle behind realizing TCO-based electro-absorption modulators.

6.1.4. Simulation Results and Operation Principle

In a directional coupler-based design, a guided mode can be coupled back to the input waveguide when the effective device length is an even multiple of coupling length (L). Therefore, in the absence of any bias voltage, light can be first coupled to HPW and then coupled back to input bus waveguide with an effective length (L_{eff}) denoted as [40]:

$$L_{\text{eff}} = pL\,, \qquad p = 2,4,6,\ldots \tag{6.1}$$

$$L = \frac{\pi}{\beta_{\text{even}} - \beta_{\text{odd}}} = \frac{\lambda_0}{2(n_{\text{even}} - n_{\text{odd}})} = \frac{\lambda_0}{2\Delta n} \tag{6.2}$$

where λ_0 denotes the wavelength in vacuum, n_{even} (β_{even}) and n_{odd} (β_{odd}) refer to the effective index (propagation constant) of *even* or symmetric super-mode and *odd* or asymmetric super-mode, respectively, for fundamental guided TM-mode. By solving eigenvalue equations in the commercially available Lumerical Mode® solver, the difference (Δn) of the two effective indices can be found as ~0.1793, which translates to a coupling length of ~4.322 µm, as per Eq.(6.2).

The voltage-dependent modal loss due to the formation of absorptive accumulation layer at the ITO–HfO_2 interface is the primary reason behind this electro-absorption type modulation. The electric field distributions (E_z) at ON-state (unbiased) and OFF-state (–2 V biased) can be seen in Figure 6.3(a) and (b), respectively. An

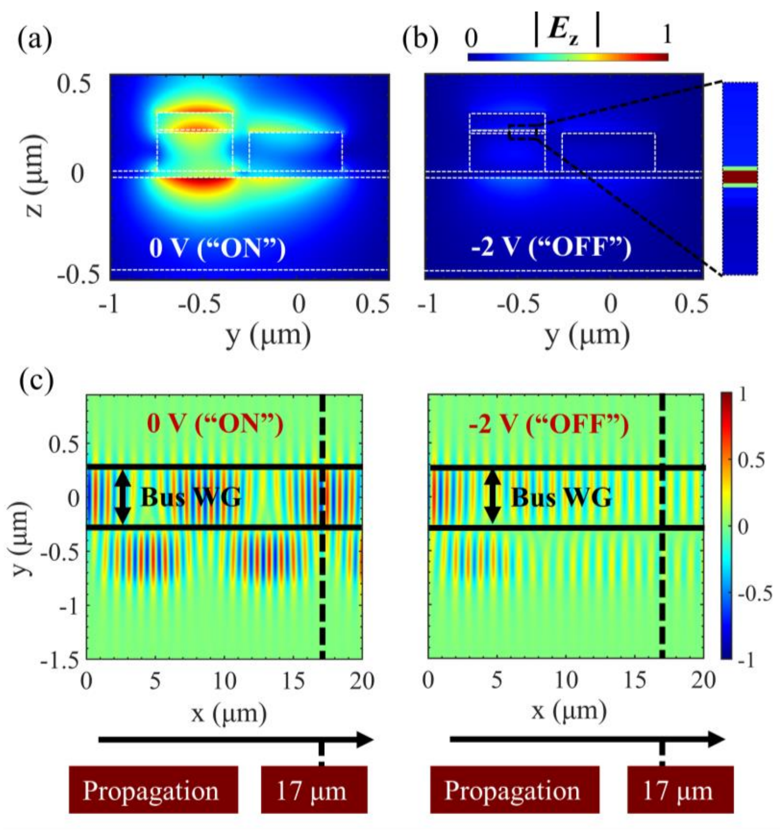

Figure 6.3: The electric field distributions (E_z) under unbiased (a) and –2V biased (b) conditions. Note: the white dashed lines represent the underlined structure and the inset of (b) shows the enhancement of electric field at the ITO–HfO_2 interface. (c) The electric field evolution along the modulator for both ON and OFF states at 1.55 μm wavelength [212].

enhancement of electric field at the ITO–HfO_2 interface can be seen as the enlarged view in the inset of Figure 6.3(b). This enhancement of electric field results in strong light–matter interactions at the accumulation layer. The electric field evolution along the electro-absorption modulator can be seen in Figure 6.3(c) for both "ON"- and "OFF"-states at 1.55 μm wavelength. The effective length of ~17 μm is marked as the black dashed lines.

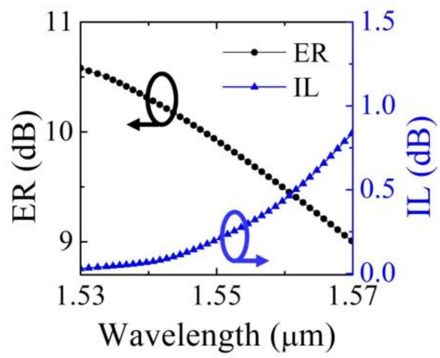

Figure 6.4: The variation of extinction ratio (ER) and insertion loss (IL), in dB, with respect to wavelength [212].

To achieve a high modal loss upon applying an external bias voltage, we have chosen an effective device length as ~17 μm, with p = 4 in Eq. (6.1). The extinction ratio (ER) and insertion loss (IL) of the device can be defined as:

$$\mathrm{ER} = 10\log\left(I_{0\mathrm{V}}/I_{-2\mathrm{V}}\right) \tag{6.3}$$

$$\mathrm{IL} = 10\log\left(I_{\mathrm{in}}/I_{0\mathrm{V}}\right), \tag{6.4}$$

where I_{in} is the optical intensity at the input, whereas $I_{0\mathrm{V}}$ and $I_{-2\mathrm{V}}$ are the output intensity at the unbiased and –2 V biasing conditions, respectively. The variation of extinction ratio and insertion loss values with respect to wavelength (covering the C-band from 1.53 μm to 1.57 μm) are shown in Figure 6.4. With a 0.21 dB insertion loss, our design exhibits an extinction ratio of ~10 dB at 1.55 μm wavelength, which yields a high modulation depth (MD = ER/L_{eff}) of ~0.59 dB/μm.

Moreover, the bandwidth, $f_{3\mathrm{dB}} = (2\pi RC)^{-1}$, and energy consumption, $E_{\mathrm{b}} = |CV^2/4|$, of the modulator (here, R is the equivalent device resistance, and C is the capacitance formed by MOS-type structure within the hybrid plasmonic waveguide) are the two key parameters for integrated photonic systems [40]. To calculate the effective capacitance of the ITO-integrated hybrid plasmonic waveguide, we have done electrostatic simulations on the commercial Lumerical Device® tool. The electrostatic simulations reveal that our device has an effective capacitance of 62.2 fF. On the other hand, we have assumed the equivalent device resistance for our design as 100 Ω, as reported in a similar type of directional coupler based modulator in the literature [162]. Thus, we can find the 3dB-modulation bandwidth of ~25.6 GHz. With a –2 V driving voltage, our device exhibits an energy consumption as low as 62.2 fJ/bit.

6.1.5. Summary

A coupling-assisted electro-absorption modulator is theoretically demonstrated by utilizing the ENZ-effect of ITO. The numerical results show that the proposed design exhibits energy consumption as low as 62.2 fJ/bit while maintaining a modulation bandwidth of 25.7 GHz. With a 17 µm active length, 0.21 dB insertion loss, and ~10 dB extinction ratio at 1.55 µm wavelength, our design could find potential applications in the integrated nanophotonic system.

6.2. Polarization-insensitive Integrated Electro-Absorption Modulator

In the previous section, a compact energy-efficient directional coupler-based design was discussed to achieve intensity modulation by leveraging the ENZ phenomenon of ITO. Though the presented electro-absorption modulator could exhibit a low energy consumption, the stringent dependency on light polarization remains a drawback.

Moreover, to address the ever-increasing demands for bandwidth in the optical communication system, wavelength-division-multiplexing (WDM) technique has been considered in last two decades. Similarly, polarization-division-multiplexing (PDM) technique has been adapted to maximize the link capacity over a single wavelength in the integrated photonic system. In the PDM-enabled photonic system, polarization-insensitivity of the electro-optic modulators is an essential feature to omit the requirement of polarization rotator and polarization beam splitter [164]. However, similar to our previously presented modulator, most of the ENZ-material based devices are dependent on particular polarization, which is imposed by the boundary conditions [134], [162], [163], [168]. This dependency on a single state of polarization increases system complexity in the hybrid PDM–WDM based data transmission.

Though some initial studies have been proposed for TCO-based polarization-insensitive modulators [41], [161], [166], [169], there is a trade-off between modulation bandwidth and device footprint. For instance, X. Qiu *et al.* proposed an ITO-based dual-polarization intensity modulator [28] at the cost of a very large active length. Moreover, in order to eliminate the polarization beam splitter element from the photonic system, separate electrical biasing is necessary for modulating TM and TE modes independently [164]. Therefore, it remains highly challenging to design a compact polarization-insensitive modulator that is capable of simultaneous modulation of both TM and TE modes with independent electrical-biasing while maintaining low power consumption and high modulation bandwidth.

To bridge these gaps, in this section, we present a novel design of a dual-polarization electro-absorption (EA) modulator based on ENZ effect of ITO. The proposed parallel directional coupler based design is capable of independent modulation of two fundamental modes (TE and TM) of a standard silicon (Si) rib waveguide. The numerical simulations show that the proposed design can be treated as a polarization-insensitive modulator due to its low polarization-dependent loss. The extinction ratio of TM (TE) is achieved as ~10.11 dB (9.66 dB) at 1550 nm wavelength, resulting in a very low (0.45 dB) polarization-dependent loss.

With a 27 μm active length, the modulation bandwidth and power-consumption are 122.75 GHz (107.91 GHz) and 773 fJ/bit (759 fJ/bit) for TM (TE)-modulation, respectively. To the best of our knowledge, such a low-dimensional coupling-assisted ENZ-material based dual-polarization electro-absorption modulator, is presented for the first time, which is capable of independent and parallel modulation of both polarizations simultaneously. The proposed design finds a potential solution to reduce footprint of the PDM-enabled integrated optical communication system by eliminating the requirements of both extra polarization rotators and polarization beam splitters.

6.2.1. Structural Overview

The architectural schematic of the proposed parallel directional coupler-based dual-polarization electro-absorption modulator is illustrated in Figure 6.5(a). The width and height of the input silicon bus waveguide are denoted as w_0 (= 500 nm) and h_0 (= 190 nm), respectively. The thickness of the silicon slab (t_{slab}) is taken as 30 nm. Light from a standard silicon rib waveguide (220 nm high and 500 nm wide), widely used in optical

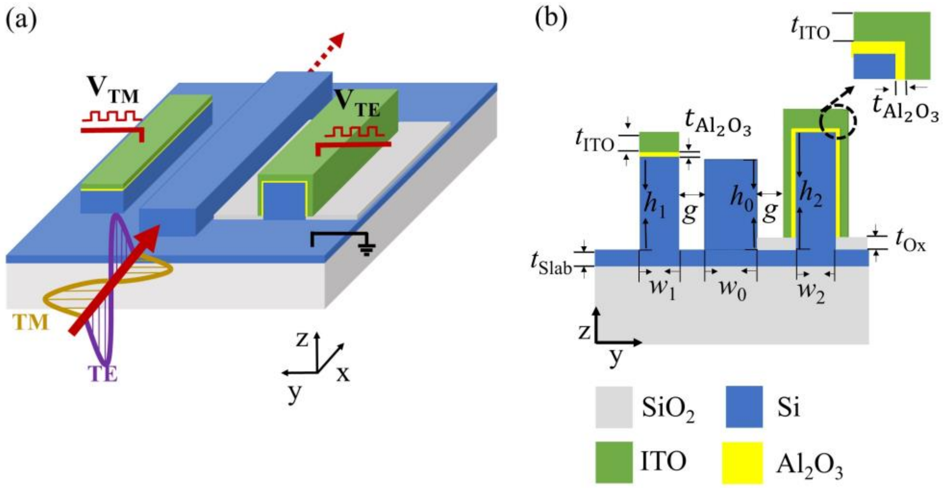

Figure 6.5: Schematics of the proposed parallel directional coupler based dual-polarization electro-absorption modulator. (a) three-dimensional (3D) layout of the proposed design, where V_{TM} and V_{TE} represent the corresponding bias voltages for HPW_1 and HPW_2, respectively. (b) 2D cross-sectional view of the proposed structure, where, h_0 =190 nm and w_0 = 500 nm are the height and width of the input bus silicon rib-waveguide, respectively. The slab thickness (t_{slab}) is taken as 30 nm. The corresponding width and height of the HPW_1 and HPW_2 are (w_1, h_1) and (w_2, h_2), respectively with a coupling gap between bus waveguide to each HPW is g = 100 nm. The thicknesses of ITO layer, Al_2O_3 and insulating layer are t_{ITO} = 35 nm, $t_{Al_2O_3}$= 5 nm, and t_{ox}= 30 nm, respectively [40].

on-chip communication, can be easily coupled to the bus waveguide without sacrificing light intensity in the form of coupling loss.

Two hybrid plasmonic waveguides (HPWs), consisting of ITO–Al_2O_3–Si based metal-oxide-semiconductor (MOS)-type capacitive structure, are placed parallel to the bus waveguide with a separation gap of g, as shown in Figure 6.5 (b). A 5 nm thick Al_2O_3 is taken as oxide layer in MOS-type structure to maintain a low capacitive effect without sacrificing the required tuning of carrier concentration with respect to applied external bias voltage [29], [30]. The n-type silicon-rib HPW_1 (HPW_2) is 210 nm (300 nm) in height and 370 nm (360 nm) in width, denoted as h_1 (h_2) and w_1 (w_2), respectively. An enlarged view of ITO cladding, with 35 nm thickness, covered on the Al_2O_3 layer is shown as insets of Figure 6.5 (b). Note that different ITO–Al_2O_3 coatings have been taken for two HPWs, keeping in mind the electric-field distributions of the TM and TE modes of bus waveguide. To provide insulation between Si-slab and ITO layer, two SiO_2 layers with thickness t_{ox} = 30 nm are placed on both sides of HPW_2 on the slab.

6.2.2. Electro-Optical Properties of ITO

The ITO/Al_2O_3/n-Si stack forms a MOS-type capacitor with ITO and Al_2O_3 acting as the transparent electrode and the gate dielectric layer, respectively, as shown in Figure 6.6(a). The bulk carrier concentration (N_0) is taken as ~3×10^{19} cm^{-3}. The refractive indices of Al_2O_3, SiO_2, and Si are taken from literature [183]. The voltage-dependent carrier concentration distributions of the ITO layer for the first 5 nm range from the interface of ITO–Al_2O_3 are shown in Figure 6.6(b).

The formation of charge **ac**cumulation **l**ayer (ACL) can be seen with the decrease of applied bias voltage (V_g). The numerical simulations have been carried out using the commercially available electrostatic solver — Lumerical Device®, where drift-diffusion and Poisson's equations have been solved to witness the accumulation of electrons at ITO– Al_2O_3 interface by considering the parameters for ITO same as the ones mentioned

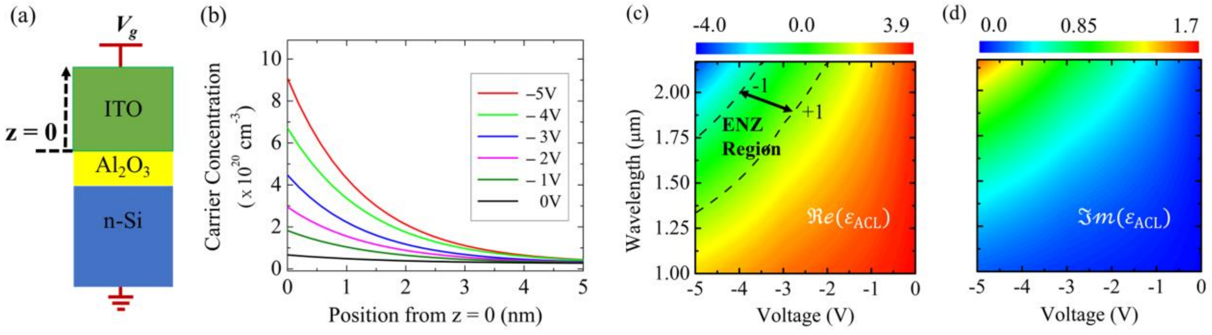

Figure 6.6: (a) The illustration of MOS-capacitor formation containing ITO/Al_2O_3/n-Si layers. (b) The carrier concentration distribution, N (per unit cm^3), of ITO layer at the position from z = 0 to 5 nm for different bias voltages, where z = 0 represents the ITO–Al_2O_3 interface. The real (c) and imaginary (d) parts of optical permittivity of charge **ac**cumulation **l**ayer (ACL) with respect to wavelength for different applied bias voltages. The ENZ Region is shown as $-1 < \Re e(\varepsilon_{ACL}) < 1$ [40].

in Chapter 2. The thickness of the ACL can be approximated as an equivalent homogenized ultra-thin layer (~3 nm) by using two-layer model based on modified Thomas–Fermi approximation (MTFA), as mentioned in Chapter 2 (sub-section 2.4.2) [133], [134].

The dependency of optical properties of ITO on carrier concentration can be explained by Drude model, as given in Eq. (2.34). The value of real part of permittivity of charge ACL, $\Re e(\varepsilon_{\mathrm{ACL}})$, approaches zero at 1550 nm wavelength when the carrier concentration of this ultra-thin ACL is ~ 6.4×10^{20} cm^{-3}. As shown in Figure 6.6(c), the range of wavelength at the vicinity of zero-permittivity crossover wavelength can be termed as "ENZ-region" [128].

As shown in Figure 6.6(d), the imaginary part of permittivity of ACL, $\Im m(\varepsilon_{\mathrm{ACL}})$, is negligible when no bias voltage is applied. Thus ITO behaves as a lossless medium with a bulk carrier concentration (N) of ~3×10^{19} cm^{-3}. On the other hand, if we apply external bias voltage, the formation of charge accumulation layer can be seen at the interface of ITO–Al_2O_3. Then, the imaginary part of permittivity of ITO starts increasing, which results in optical absorption. In other words, we can say when $\Re e(\varepsilon_{\mathrm{ACL}})$ of ACL approaches the near-zero condition, the layer behaves as a lossy medium. This is the fundamental principle behind realizing TCO-based electro-absorption modulators. Although a high $\Im m(\varepsilon_{\mathrm{ACL}})$ value can be acquired to design a more efficient electro-absorption modulator, unfortunately, the breakdown voltage of oxide layer becomes the limiting factor. In this study, the bias voltage (V_g) has been taken from 0 to –5 V that results in a maximum electric field of about 4.5 MV/cm across the Al_2O_3 layer, which is lower than the reported breakdown field [29].

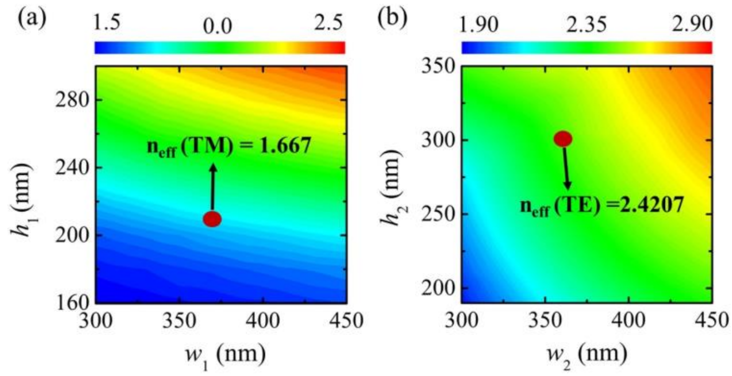

Figure 6.7: The effective refractive index (n_{eff}) variation of the plasmonic waveguides with different width and height. (a) Effective index variation of HPW_1, where the red marked dot at (w_1, h_1) = (370 nm, 210 nm) denotes the index matched (n_{eff} = 1.667) condition with the TM-mode of input bus waveguide. (b) Effective index variation of HPW_2, where the red marked dot at (w_2, h_2) = (360 nm, 300 nm) denotes the index matched (n_{eff} = 2.4207) condition with the TE-mode of input bus waveguide [40].

6.2.3. Parametric Study and Coupled Waveguide Analysis

The proposed directional coupler-based modulator has two parallel active coupling sections consisting of ITO-based HPW in each region. Each HPW is separated by a gap (g = 100 nm) from the input silicon rib-waveguide. The design is based on coupled mode theory (CMT) in a parallel directional coupler and complex refractive index modulation of ITO. Without any external biasing, the geometrical parametric analysis has been carried out in such a way that the effective index of fundamental TM-mode of HPW_1 can match the effective index of fundamental TM-mode of the input bus waveguide, as shown in Figure 6.7(a). This enables directional coupler based mode-coupling phenomena. Similarly, as shown in Figure 6.7(b), the fundamental TE-mode of input bus waveguide can be coupled to the HPW_2 by satisfying index matching condition.

Moreover, careful selection of physical parameters needs to be taken into consideration to minimize the possibilities of coupling of TE-mode of bus waveguide to HPW_1 and TM-mode of bus waveguide to HPW_2, which results in propagation loss and mode-crosstalk. Nevertheless, there are multiple choices for the selection of geometrical parameters for HPWs to satisfy parallel directional coupling. We have chosen the width and height of HPW_1, HPW_2 as (w_1, h_1) = (370 nm, 210 nm) and (w_2, h_2) = (360 nm, 300 nm), respectively, as shown by the red dot in Figure 6.7. The selection of parameters is made in such a way that the modulator can fulfill the requirements of polarization-insensitivity with independent bias voltage.

Two primary requirements need to be taken into consideration to design a directional coupler-based dual-polarization modulator. First, when no bias voltage is applied, the effective lengths of HPW_1 and HPW_2 should be the same — referred to as "ON" state. Thus, minimum insertion loss at the output port of input bus waveguide is observed for both TM and TE modes. Second, voltage-dependent change in modal losses (α_m) for TM and TE modes should be identical. This enables near-zero modulation-depth discrepancy between these two fundamental modes.

The modal loss (α_m) of a Si-waveguide based modulator can be defined as [34]:

$$\alpha_m = \Gamma\alpha, \tag{6.5}$$

where Γ denotes the confinement factor — a metric to measure how well a particular waveguide-mode overlaps with the active region or switching layer. Material absorption loss is denoted by α, which depends on the imaginary part of effective refractive index $\Im m$ (n_{eff}) at a particular wavelength (λ) and can be given as [28] :

$$\alpha = 10\left|\log\left(e^{\left\{-\frac{4\pi}{\lambda}\Im m(n_{\text{eff}})\right\}}\right)\right|\left(\frac{\text{dB}}{\mu\text{m}}\right). \tag{6.6}$$

According to CMT, if the directional coupler length is even multiple of coupling length, light will be coupled back to the input waveguide [205]. Therefore, to realize polarization-insensitive design based on the parallel directional coupler, the active length (L_{active}) of the modulator should be defined as a function of coupling length of each HPWs, and can be given as:

$$L_{\text{active}} = pL_{\text{TM}} = qL_{\text{TE}}\,, \qquad [p, q \;=\; 2, 4, 6, \dots] \tag{6.7}$$

where L_{TM} and L_{TE} are the coupling-lengths for TM and TE modes, respectively, and can be defined as [205]:

$$L_{\text{TM}} = \frac{\pi}{\beta_{\text{TM,e}} - \beta_{\text{TM,o}}} = \frac{\lambda_0}{2\left(n_{\text{TM,e}} - n_{\text{TM,o}}\right)} \tag{6.8.a}$$

$$L_{\text{TE}} = \frac{\pi}{\beta_{\text{TE,e}} - \beta_{\text{TE,o}}} = \frac{\lambda_0}{2\left(n_{\text{TE,e}} - n_{\text{TE,o}}\right)} \tag{6.8.b}$$

where λ_0 is the wavelength in vacuum, $\beta_{\text{TM,e}}$ ($n_{\text{TM,e}}$) and $\beta_{\text{TM,o}}$ ($n_{\text{TM,o}}$) are the propagation constant (refractive index) of symmetric *or even super-mode* and anti-symmetric *or odd super-mode* for TM-polarization, respectively, whereas, $\beta_{\text{TE,e}}$ ($n_{\text{TE,e}}$) and $\beta_{\text{TE,o}}$ ($n_{\text{TE,o}}$) are the propagation constant (refractive index) of symmetric and anti-symmetric super-modes for TE-polarization, respectively.

6.2.4. Results and Discussion

In this subsection, the analysis of individual mode-modulation is described first based on directional coupling mechanism. Then, by providing independent electrical biasing, simultaneous modulation of TM and TE modes have been discussed based on parallel directional-coupling. Finally, the fabrication tolerance study of our design is discussed.

6.2.4.1. Mode-coupling Analysis Independently for TE and TM Modes

To design a dual-polarization modulator based on parallel directional coupler, we need to first investigate each coupling section separately. Here, the performance analysis of

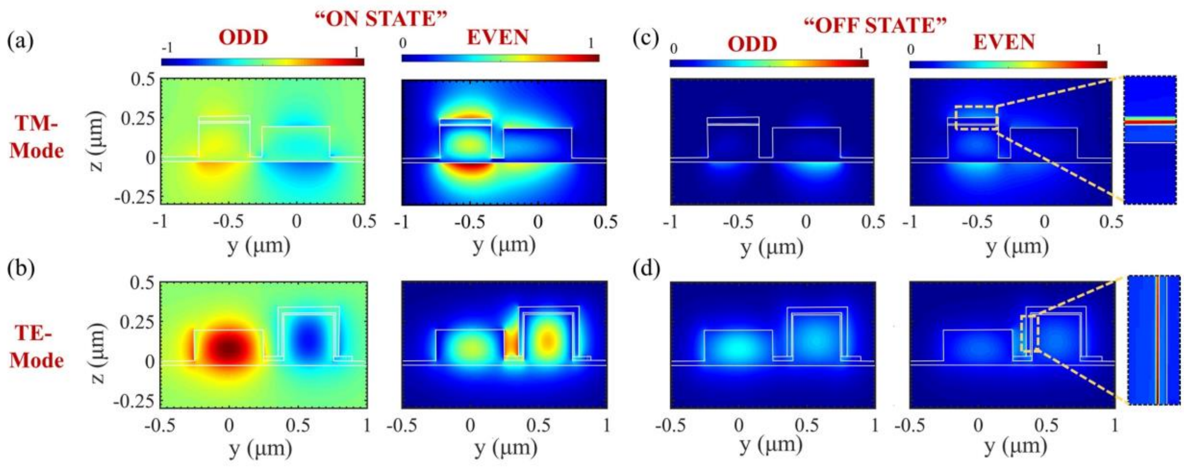

Figure 6.8: Electric field distributions of odd and even super-modes. (a) E_z–field distribution of odd and even super-modes of TM-polarization, when HPW_1 is taken into consideration for directional coupler based design at 0 V bias. (b) E_y–field distribution of odd and even super-modes of TE-polarization, when HPW_2 is taken into consideration at 0V bias. (c) and (d) are the counterpart electric field distributions of (a) and (b), respectively, at –5 V biased condition. Depending upon the mode field intensity at the input bus waveguide, the corresponding state is termed as "ON" or "OFF" state. Tight confinement of electric field at ITO–Al_2O_3 interface, due to the formation of absorptive-ACL, is shown by the enlarged view of (c) and (d). Note that, white solid lines are used for better visualization of the underlined structure [40].

individual mode-modulation has been discussed separately. For instance, directional coupler-based TM-mode modulator design can be considered with Si-bus waveguide as input waveguide and HPW_1 as coupled waveguide. In the TM-mode analysis, HPW_2 is not considered. Similarly, TE-mode modulation analysis has been carried out with HPW_2 as the coupled waveguide in the absence of HPW_1.

Figure 6.8(a) shows the numerically simulated E_z-field distribution of odd and even super-modes of TM-polarization supported by the directional coupler design when HPW_1 is taken into consideration. The effective refractive index differences (Δn) between even and odd super-modes can be found as ~0.1736 at operational wavelength 1550 nm, yielding coupling length $L_{TM} \approx 4.464$ μm, as per Equation (6.8.a).

Similarly, the E_y-field distribution of odd and even super-modes of TE-polarization are shown in Figure 6.8(b) when HPW_2 is taken into consideration. The effective refractive index differences (Δn) between even and odd super-modes for TE-polarization can be found as ~0.058. The coupling length can be determined by Equation (6.8.b) as $L_{TE} \approx 13.36$ μm. Thus, the effective active length for both HPWs can be estimated using Equation (6.7) to design dual-polarization modulator, where p and q are taken to be 6 and 2, respectively, yielding L_{active} to be at the vicinity of 27 μm. Therefore, these two directional coupler designs satisfy the first condition of independent and polarization-insensitive modulation.

To analyze the modal properties of the design, commercially available eigenmode solver-based Lumerical Mode® is used. The "OFF" state of each modulator section is enforced by the external electrical biasing. The enhancement of electric field is observed at ITO–Al_2O_3 interface, as shown in Figure 6.8(c) and (d), when –5 V bias is applied to the HPW_1 and HPW_2, respectively. Due to the unusual boundary condition imposed by the ENZ-effect, the waveguide modes overlap with the absorptive accumulation layer at the ITO–Al_2O_3 interface, resulting in a high modal loss. The strong enhancement of electric-field can be seen as the enlarged view in the insets of Figure 6.8(c) and (d).

6.2.4.2. Dual-Polarization Modulator: Performance Analysis

The electrode-configurations for TM- and TE-mode modulations are shown in the insets of Figure 6.9(a) and (b), respectively. The proposed parallel directional coupler-based design exhibits simultaneous modulation of TM and TE modes with independent electrical gating at HPW_1 and HPW_2, respectively. The dual-polarization modulation can be achieved by independent switching of V_{TM} from 0 to –5 V while keeping V_{TE} at 0 V and switching of V_{TE} from 0 to –5 V while keeping V_{TM} at 0 V.

With a 27 μm active length, the modal loss curves of the TM- and TE-modes, at three distinct operational wavelengths (1530 nm, 1550 nm, and 1570 nm), are shown in

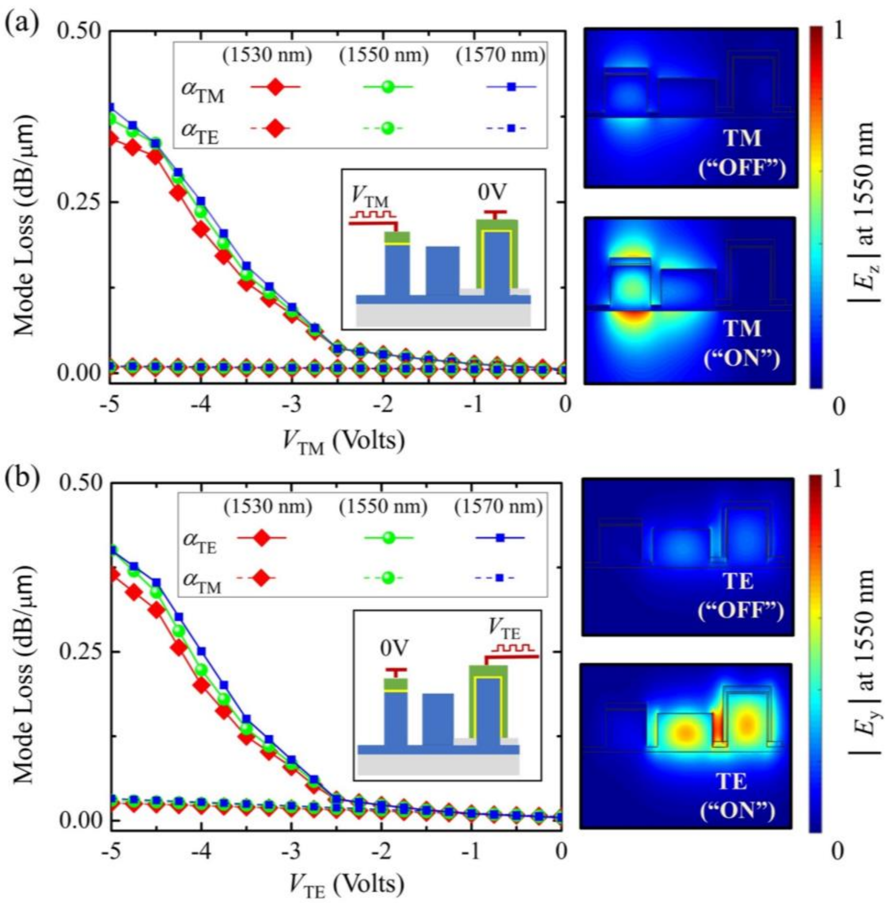

Figure 6.9: (a) Modal loss (dB/µm) as a function of external bias voltages for three different operational wavelengths (1530 nm, 1550 nm, and 1570 nm) in the case of (a) TM-mode modulation, and (b) TE-mode modulation. Electrode configurations are shown in the inset, where, (V_{TE}, V_{TM}) = (0 V, 0 to –5 V), and (V_{TE}, V_{TM}) = (0 to –5V, 0 V) for TM- and TE-mode modulations, respectively. For the TM-mode modulation, α_{TM} and α_{TE} denote the corresponding TM-mode and TE-mode loss, respectively. Similarly, for the TE-mode modulation, α_{TE} and α_{TM} denote the corresponding modal loss. The "ON"-state and "OFF"-state conditions are illustrated by the electric field distributions for TM or TE mode at bias voltage of 0 V and –5 V, respectively. Note that, solid black lines are used for better visualization of the underlined structure [40].

Figure 6.9(a) for TM-mode modulation, where V_{TE} = 0 V and V_{TM} is switching from 0 to –5 V. The E_z-field distributions are shown for TM-modulation and represented as "ON state" and "OFF state" at the bias voltage of V_{TM} = 0 V and –5 V, respectively. Due to the formation of absorptive-ACL located at the active coupling region of HPW_1, the modal loss for TM-mode (α_{TM}) keeps on increasing with the external bias changes from 0 to –5 V. On the other hand, TE-mode of the bus waveguide suffers very low loss (α_{TE}), which illustrates the independence of the applied V_{TM} over TE-mode.

Figure 6.9(b) illustrates the modal loss curves for TE-mode modulation at three distinct operational wavelengths with electrode configurations set as shown in the inset. The active propagation length for this study is the same as that of TM-modulation. E_y-field distributions of even super-modes are shown for TE-modulation and represented as TE-mode "ON" and "OFF" state at V_{TE} = 0 V and –5 V, respectively. With the coupling of TE-mode of bus waveguide to the HPW_2, higher modal loss (α_{TE}) can be achieved when V_{TE} decreases from 0 to –5 V. The insensitivity of TM-mode to the V_{TE} is seen from the low TM-mode loss (α_{TM}) curves.

However, Figure 6.9(a) shows a small variation of modal losses at the higher voltages for TE-mode, when TM-modulation is considered. Similar fluctuations are also observed for TM-mode loss at a higher voltage in Figure 6.9(b). These small fluctuations are due to mode-crosstalk (MC) and are negligible in comparison with the modal loss for respective mode-modulation. These small fluctuations are due to mode-crosstalk (MC) and are negligible in comparison with the modal loss for respective mode-modulation. The impact of one particular mode (TE or TM) modulation on the other mode (TM or TE) is described by mode crosstalk (MC) and can be given as [28]

$$MC = \frac{|\alpha_{TM/TE} + \alpha_{TE/TM}|}{2} \text{ (dB)}, \tag{6.9}$$

Here $\alpha_{TM/TE}$ is the TM mode loss when TE modulation is applied and $\alpha_{TE/TM}$ is the TE mode loss when TM modulation is applied. The variation of the mode crosstalk (MC) as a function of the applied voltage at the1550 nm is shown in Figure 6.10. It should be noted that the maximum mode crosstalk of the proposed modulator is estimated as 0.02 dB/µm, which is negligible than that of the modal loss for respective mode-modulation (having a maximum modal loss of ~0.39 dB/µm as shown in Figure 6.10.

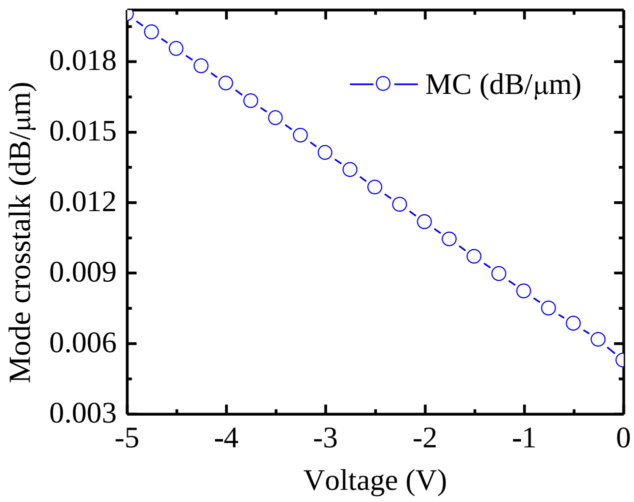

Figure 6.10: Mode-crosstalk (MC), in dB/µm, as a function of external bias voltages for operational wavelength of 1550 nm.

As the design attributes very low mode-crosstalk, independent mode modulation can be possible. The insertion loss (*IL*) of the modulator can be defined as:

$$IL = |P_0 - \alpha_0 L_{\mathrm{active}}| \ (\mathrm{dB}), \tag{6.10}$$

where P_0 denotes the input power at the modulator and α_0 denotes the modal loss of the modulator when no bias voltage is applied. Moreover, for an ideal polarization-insensitive dual-polarization modulator, it is highly desirable to maintain a low polarization dependent loss (*PDL*), which describes the discrepancy of extinction ratio between TM and TE modulations, and can be shown as:

$$PDL = |ER_{\mathrm{TM}} - ER_{\mathrm{TE}}| \ (\mathrm{dB}), \tag{6.11}$$

where ER_{TM} and ER_{TE} are the corresponding extinction ratio (*ER*) for TM and TE modulations, respectively.

The extinction ratio is very crucial parameter to design an intensity modulator and can be defined as a function of biased condition modal loss (α_b):

$$ER = |\alpha_b L_{active} - IL| \text{ (dB).} \quad (6.12)$$

Figure 6.11(a) and (b) illustrate the electric field **(**E_z) evolution for TM-mode along the modulator at "TM-ON" and "TM-OFF" states, respectively, at 1550 nm operational wavelength. The evolution of E_y-field along the modulator for TE-mode is shown in Figure 6.11(c) and (d) for "TE-ON" and "TE-OFF" states, respectively, at the 1550 nm operational wavelength. To ensure a negligible coupling loss while launching

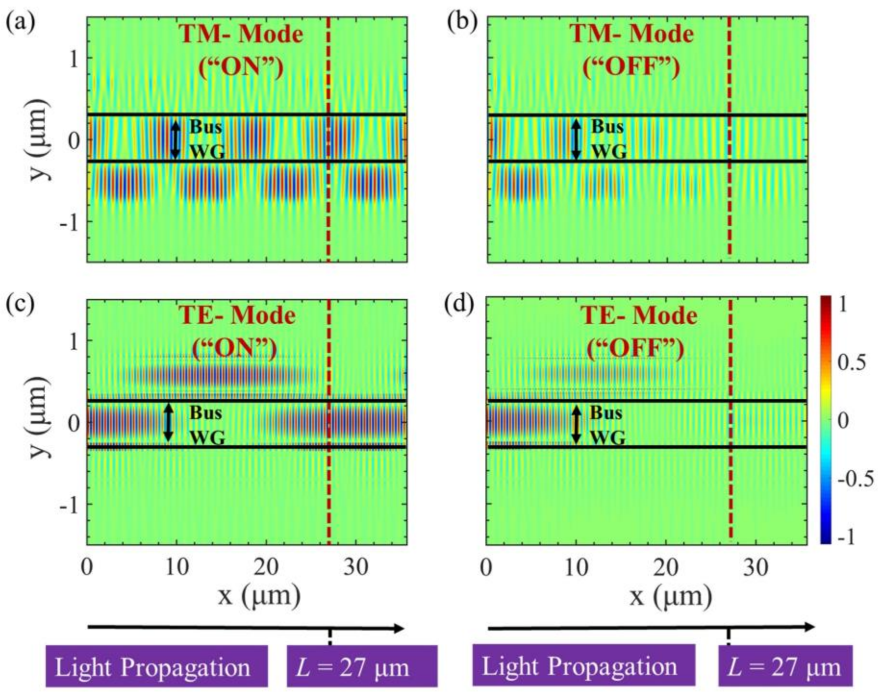

Figure 6.11: Electric field evolution along the propagation distance through the parallel coupled waveguides. (a) and (b), E_z-field propagation by coupling of TM-mode between bus waveguide and HPW_1 at V_{TM} = 0 V, and V_{TM} = –5 V, respectively, for TM-mode modulation. (c) and (d), E_y field propagation for TE-mode modulation at V_{TE} = 0 V and –5 V, respectively. Note that, for (a) and (b), TM-mode is the input at bus waveguide, whereas, for (c) and (d), TE-mode is the input at bus waveguide. The effective active length of the modulator section is L = L_{active} = 27 μm [40].

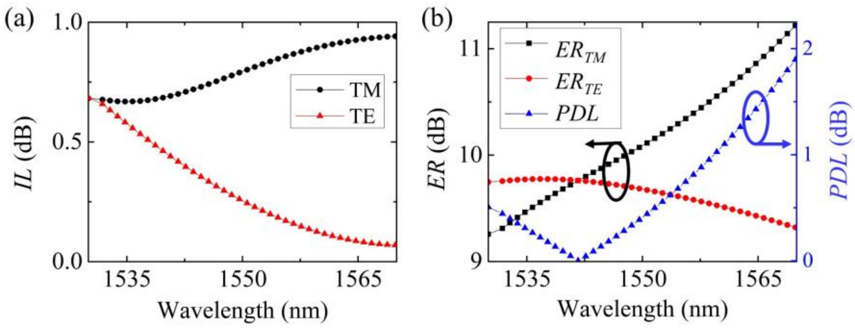

Figure 6.12: (a) Insertion loss (*IL*), in dB, as a function of wavelength for TM- and TE-mode modulations and (b) extinction ratio (*ER*), in dB, as a function of wavelength, covering the C-band, for TM- and TE-mode modulations, and corresponding polarization dependent loss (*PDL*). Note that, at 1550 nm wavelength, *PDL* between TM- and TE-mode modulations is 0.45 dB [40].

the light to the device, we have chosen the silicon bus waveguide with similar dimensions to the widely used standard silicon rib waveguide (500 nm wide and 220 nm high). A linearly polarized light can be launched from a standard silicon waveguide and can pass through the modulator section at "ON" state appearing at the output port of the bus waveguide.

In contrast, at "OFF" state, due to high propagation loss achieved by strong light–matter interactions around the absorptive-ACL, very low power is observed at the output port, located at L= 27 μm. To analyze the performance metrics of proposed parallel directional coupler-based dual-polarization electro-absorption modulator, 3D FDTD (finite-difference time-domain) method is used. With PML (perfectly matched layer) absorbing boundary condition, the structure is modeled by choosing a very fine mesh, with 0.25 nm minimum mesh size, around the ITO–Al_2O_3 interface.

The variations of insertion loss (IL) and extinction ratio (ER) as functions of wavelength ranging from 1530 to 1570 nm (covering the C-band) are shown in Figure 6.12(a) and (b) for both TM and TE-mode modulations, respectively. The polarization dependent loss (*PDL*) or extinction ratio-discrepancy can be calculated by using Equation (6.11), and the variation in polarization dependent loss as a function of wavelength is shown in Figure 6.12(b), where we can see the dual-polarization modulator can perform a broadband (1530 nm to 1570 nm) polarization-insensitive modulation with less than 2 dB extinction ratio-discrepancy. Moreover, due to the refractive index modulation, a slight shifting of coupling length at OFF-states of each modulation is noticed, which is incorporated with the extinction ratio (ER) of the design. At 1550 nm wavelength, ER_{TM} and ER_{TE} are 10.11 dB and 9.66 dB, respectively, resulting in the polarization dependent loss (*PDL*) to be 0.45 dB, which satisfies the second requirement of polarization-insensitive modulation.

6.2.4.3. Electrical Bandwidth and Energy Consumption of the Modulator

The operational speed of a modulator is one of the key parameters. Due to the ultrafast formation of the carrier ACL, the 3-dB modulation bandwidth, $f_{3dB} = (2\pi RC)^{-1}$ (Hz), is impeded by the RC-time constant of the modulator (here, R is the equivalent device resistance, and C is the capacitance formed by MOS-type structure) [162]. The power consumption $E = CV^2/4$ (J/bit) is also another aspect that needs to be considered while designing an electro-absorption modulator for a power-hungry integrated photonic system [41].

As the dual-polarization modulation is achieved by applying electrical gating at two parallel coupling regions consisting of two different HPWs, electrostatic analysis needs to be discussed separately for both mode-modulations. Based on electrostatic simulations on the commercial Lumerical Device® tool, the equivalent device resistivity and total capacitance per unit length can be estimated as 283.7 Ω.µm (327.58 Ω.µm) and 4.576 fF/µm (4.502 fF/µm) for TM (TE) modulation, respectively, which translates to a modulation bandwidth of 122.75 GHz (107.91 GHz) for TM (TE)-modulation. With an applied voltage ranging from 0 to –5V, the power consumption of the modulator can be estimated as 773 fJ/bit and 759 fJ/bit for TM- and TE-mode modulations, respectively.

6.2.4.4. Comparative Analysis

The performance comparison of the proposed ENZ material based electro absorption modulator with a few previously reported Mach–Zehnder interferometer based silicon free-carrier modulators can be seen in Table 6.1.

Table 6.1: Comparison of the Proposed EAM with a Few Previously Reported Silicon Waveguide-based Free-carrier Modulators

Design	**Wavelength (nm)**	***ER* (dB)***	***IL* (dB)***	***f*₃dB (GHz)**	**Dual-Polarization**
Si MZM **(Experimental)** [213]	1557	~7.5	~1.9	~30	No
Si MZM **(Experimental)** [214]	1557	~3.7	~2.6	~13	No
Si MZM **(Experimental)** [215]	1310	~5.0	~2.6	~10	No
Si MZM **(Theoretical)** [216]	1550	~3.0	~3.3	~13	No
ENZ Material based Directional Coupler **(This work)**	1550	TE: 0.358 TM: 0.375	TE: **8.30** TM: **5.75**	TE: 107 TM: 122	**Yes**

Note: Si modulators are Mach–Zehnder interferometer-based modulators (MZM), ER: extinction ratio, IL: insertion loss, f_{3dB}: 3-dB modulation bandwidth

The modulation depth (*MD*) of the device can be denoted as the extinction ratio (ER) per unit active length (L_{active}), *i.e.*, *MD* = ER/L_{active} (dB/μm). For obtaining larger *MD*, one can also opt for some other oxides with higher relative permittivity, such as HfO_2 (ε_r ~ 25). However, this will lead to larger capacitance, and thus modulation bandwidth gets affected. Thus, there is a trade-off between modulation bandwidth (f_{3dB}) and *MD* for the MOS-based optical modulators. To characterize the trade-off between these two parameters, a figure-of-merit (*FoM*) can be defined as:

$$FoM = MD.f_{3dB} \quad (\text{dB.GHz.}\mu\text{m}^{-1}). \tag{6.13}$$

This newly defined *FoM* can guide users for a careful selection of optical modulators with optimal performances.

In addition, to reduce the overall footprint and complexity of a PDM-enabled integrated photonic system, an independent biasing scheme also needs to be employed to modulate TE and TM modes separately. This will eliminate the requirement for extra polarization beam splitter elements. Here, we emphasize that our proposed parallel directional coupler-based design is capable of independent modulation of both polarizations with modulation bandwidth as high as 122.75 GHz (107.91 GHz) and power consumption as low as 773 fJ/bit (759 fJ/bit) for TM (TE)-modulation.

A comparative overview of a few recently reported TCO-based polarization-insensitive modulators is shown in Table 6.2. Note that all works compared in are Table 6.2 based on theoretical simulations. No experimental work on ENZ-material based dual polarization electro-absorption modulator has been reported to date to the best of our knowledge. Though the designs based on multilayered-MOS type structures provide high modulation depths, they are not capable of independent-modulation of TE and TM modes.

Moreover, the modulation bandwidth and power consumption are also affected due to the vertical stack of MOS-type structures. With a 27 μm active length and 10.11

Table 6.2: Comparison among a Few Recently Reported TCO-based Polarization-insensitive Integrated Modulators

Design	**Independent -biasing**	***MD* (dB/μm)***	**f_{3dB} (GHz)**	***FoM* (dB.GHz.μm^{-1})**	**Energy/bit (fJ/bit)**
Multi-layered MOS [161]	No	~1.0	16	~16.0	NA
Multi-layered MOS [41]	No	~3.1	7.1	~22.01	827
Single ITO coating [34]	No	~0.1	NA	NA	1300
Isolated active layers [28]	**Yes**	TE: 0.206 TM: 0.198	TE: 58 TM: 66	TE: 11.60 TM: 13.20	NA
Parallel coupling **(This work)**	**Yes**	TE: 0.358 TM: 0.375	TE: 107 TM: 122	TE: **38.30** TM: **45.75**	TE: 759 TM: 773

*MD (= ER/L_{active}) at 1550 nm wavelength. MOS: metal-oxide-semiconductor, f_{3dB}: 3-dB modulation bandwidth, NA: Not available, *FoM*: figure-of-merit.

dB (9.66 dB) extinction ratio for TM (TE) modulation at 1550 nm wavelength, we can calculate the modulation depth (*MD*) for both polarizations. The figure-of-merit (*FoM*) calculations show that our directional coupler-based design can outperform previously reported polarization-independent modulators. In addition, the optical bandwidth of this design can cover the whole C-band of wavelength with less than 1.5 dB polarization dependent loss (*PDL*). Therefore, our proposed design finds potential application in integrated nanophotonics systems for optical communication.

6.2.4.5. Potential Fabrication Process and Tolerance Study

The dual-polarization electro-absorption modulator consists of a silicon bus waveguide and two parallel HPWs with a separation gap of 100 nm each from the bus waveguide. The proposed device can be fabricated on a commercially available silicon-on-insulator (SOI) wafer with approximately 2 µm thick buried oxide. In the beginning, the silicon rib waveguides (bus waveguide, HPW_1, and HPW_2) with different physical dimensions can be patterned by electron-beam lithography (EBL) followed by reactive ion etching (RIE), leaving a 30 nm thick silicon slab for lower device contact [163], [206]. Two 30 nm thick SiO_2 insulation layers on both sides of HPW_2 can be deposited through thermal oxidation. The excess oxide layer can be wet-etched by dipping it into a hydro-fluoric solution [136]. Next, the input and output grating couplers may be defined by a second round of EBL and RIE to couple the light from optical fibers into the bus waveguide [167]. Then, the ITO–Al_2O_3 stack can be patterned by a third round of EBL, followed by atomic layer deposition of 5 nm thick Al_2O_3 and 35 nm thick ITO, and lift-off process [136]. To improve the film quality, the samples can be annealed for around 10 minutes at 400° C. Finally, the upper and lower metal contacts can be patterned using photolithography, followed by thermal evaporation and lift-off process to make electrical connections to the device [167].

After the completion of the fabrication process, a scanning electron microscope may be used to verify the thickness of each layer deposited over the substrate [163]. Then, the characterization of the device needs to be done without applying any bias voltage. Light from a C-band tunable light source can be coupled into and out of the silicon bus waveguide through the grating couplers using optical fibers. Polarization maintaining fibers may be used to observe the dual-polarization operation of the device.

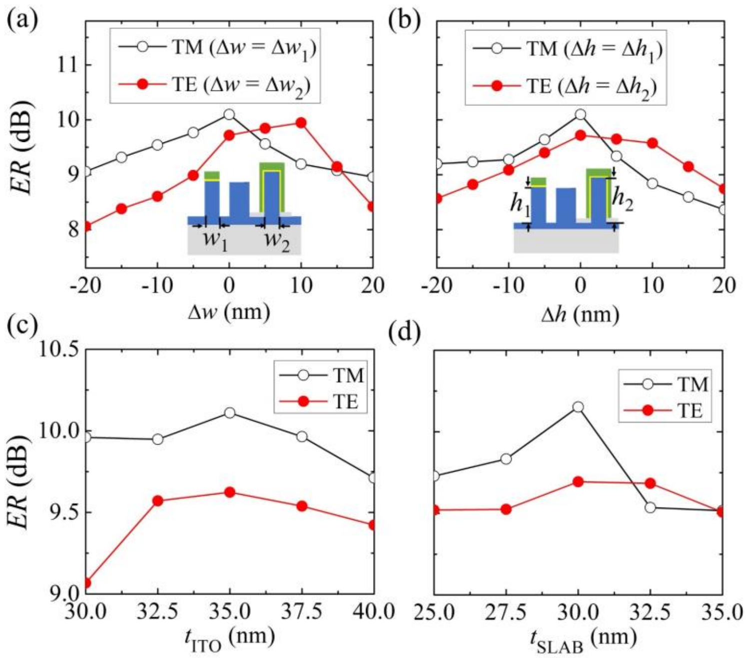

Figure 6.13: Fabrication tolerance study of rib width and height of HPWs. (a) extinction ratio (ER) for TM- and TE-mode modulations, as a function of the changing rib width by Δw_1 for HPW_1, and Δw_2 for HPW_2, respectively. (b) extinction ratio (ER) for TM- and TE-mode modulations, when rib height of HPW_1 and HPW_2 has changed to $h_1 \pm \Delta h_1$ and $h_2 \pm \Delta h_2$, respectively. extinction ratio (ER) for TM- and TE-mode modulations, considering ± 5 nm variation in thickness of (c) ITO-layer and (d) silicon slab, respectively. Note that, in case of (a) and (b) the ideal device can be represented by taking $\Delta w = \Delta w_1 = \Delta w_2 = 0$ and $\Delta h = \Delta h_1 = \Delta h_2 = 0$. All units are in nanometer, and the operating wavelength is 1550 nm [40].

Next, a –5V DC bias voltage can be applied on the ITO electrode, keeping the silicon slab contact grounded to observe the electro-optical response of the device. Then, the modulation of output light can be observed by optical spectrum analyzer [136].

As the device is based on the directional coupling-phenomena, the height and width of the HPWs are very crucial to decide the TM and TE modes coupling analysis. Therefore, we investigate the effect of inaccuracy in the fabrication process. Figure 6.13(a) depicts the impact on extinction ratio (ER) of dual-polarization modulation for ±20 nm deviations in silicon rib width (Δw) of both HPWs, where Δw_1 and Δw_2 represent the deviations of rib widths of HPW_1 and HPW_2, respectively. Similarly, the sensitivity of *ER* to the rib-height of the HPWs is shown in Figure 6.13(b), where Δh_1 and Δh_2 represent the corresponding deviations of heights of HPWs. Here, the tolerance study for TM-modulation has been done by considering rib-width (w_1 = 370 ± 20 nm) and height (h_1 = 210 ± 20 nm) of HPW_1. It can be seen that due to the maximum coupling efficiency, the ER_{TM} is maximum when $\Delta w_1 = 0$ (ideal device configuration). On the other hand, the variation in the ER_{TE} is shown with respect to the rib-width (w_2 = 360 ± 20 nm) and height (h_2 = 300 ± 20 nm) of HPW_2 for the TE-modulation. The lowest values of ER_{TM} and ER_{TE} in the tolerance analysis are 8.36 dB and 8.07 dB, respectively, allowing robustness to realize dual-polarization modulator within a ± 20 nm deviation in rib height and width of HPWs. Moreover, polarization-insensitivity comes from the extinction ratio-discrepancy of less than 2 dB. Figure 6.13(c) and (d) depict the impact on extinction ratio (ER) of dual-polarization modulation for ± 5 nm deviations in ITO-layer and silicon slab, respectively. It should be noted that there might be a variation in the ER value in the practical scenario due to roughness on the surface during fabrication process that leads to additional scattering losses in the directional coupler design.

6.2.5. Summary

We presented a novel design of parallel directional coupler-based dual-polarization electro-absorption modulator using ENZ-material. By applying independent external electrical bias at the corresponding coupling region consisting of ITO-based HPWs, enhancement of light–matter interactions yielding from ENZ-effect can be seen. Based on confining light in the absorptive accumulation layer, the design can be realized for independent and synchronized modulation of both polarizations. The design allows strong extinction ratio (ER) to insertion loss (IL) ratios for both TM and TE mode modulations. The extinction ratio (ER) of TM (TE) is achieved as 10.11 dB (9.66 dB) at 1550 nm wavelength of operation, resulting in a 0.45 dB polarization dependent loss or extinction ratio-discrepancy between two modulations.

With a 27 μm active length, the modulation bandwidth and power-consumption are 122.75 GHz (107.91 GHz) and 773 fJ/bit (759 fJ/bit) for TM (TE)-modulation, respectively. To the best of our knowledge, a parallel directional coupler based compact dual-polarization electro-absorption modulator is presented here for the first time, which is capable of independent and parallel modulation of both polarizations by leveraging the feature of electrically-tunable ENZ effect of ITO. In addition, the optical bandwidth of this design can cover the whole C-band of wavelength with less than 1.5 dB polarization dependent loss, which is a promising feature for dense-WDM and PDM-integrated optical communication systems.

7

ENZ-material based Metasurfaces for Electro-Optic Polarization Modulation

Contents

Until now, Chapters 3 to 6 have been dedicated to different designs for electro-optic or all-optical **intensity modulation** by leveraging the epsilon-near-zero (ENZ) effect of transparent conducting oxides (TCOs). Various design strategies have been adopted for achieving the free-space (metasurface-based) and integrated (waveguide-based) intensity modulation. Apart from the intensity, the polarization state is also one of the vital electromagnetic properties of light.

This Chapter is dedicated to the exploration of achieving **electro-optic polarization modulation** by harnessing the ENZ effect. Section 7.1 introduces the motivation behind the investigation of an electro-tunable, compact, free-space polarization modulator for nanophotonic systems. Section 7.2 discusses a unique design of a metasurface-based free-space **electro-optic polarization modulator or switching device**. This novel electro-tunable metasurface has been designed by combining the ENZ phenomenon of indium tin oxide (ITO) with gap plasmon resonance to enable a tri-state polarization switching mechanism.

7.1. Dynamic Control of Polarization State: A Brief Introduction

As discussed in Chapter 1, the polarization state of light is determined by the orientation of its oscillating electric field and is crucial for any photonic system [64], [65]. The polarization-controlling elements are the key components for many applications, such as optical imaging, optical communication, data transmission, and so on [7], [29], [40], [66], [67]. The most common approach to control the polarization state of light is either by using the Kerr effect or the Faraday effect [68]. These traditional polarizing devices suffer from bulkiness and static operations, *i.e.*, they offer only a fixed degree of polarization control. Though one can utilize acousto-optical or electro-optical effects to realize dynamic polarization-switching components, these devices are not compatible with nanophotonics systems due to their large footprints [69]. As discussed previously, metasurfaces have gained enormous attention in the recent years to tailor electromagnetic properties of light at the sub-wavelength scale by engineering their unit cells or ‘meta-atoms’ [102], [103], [189].

Metasurfaces are ultra-thin optical scatterers that can manipulate the amplitude and phase of the light scattered from the surface. Due to their exceptional abilities to control light–matter interactions at the sub-wavelength scale, metasurfaces have accelerated the development of ultra-thin flat optical components such as multifunctional meta-lens [7], hyperspectral imaging [8], spatial light modulators [9], optical sensors, filters [10], and so on. Thus, metasurface has the potential to realize polarization-control at the nanoscale by introducing birefringence and chirality [70]–[74]. To date, many researchers have demonstrated several metasurface-based designs for polarization conversion, which find a wide range of applications, including holographic displays [75], polarization imaging [66], Stokes parameters detection [76], and many more. However, most of these metasurface-based polarization controlling components have typically been limited by their passive mode of operation, *i.e.*, providing a fixed control over the degree of polarization [70]–[74], [77].

Extensive research has been performed in the recent years to demonstrate dynamic control over the polarization state of light by incorporating numerous emerging materials such as phase-change materials, graphene, and so on [78]. However, most of the previously reported metasurface-based active polarization controllers are designed mainly for far-infrared [79] and mid-infrared wavelengths [80]. Active polarization-controlling devices at the visible and near-infrared wavelengths are essential for quantum and nanophotonic applications.

To realize dynamic polarization rotation at optical frequencies, an all-dielectric metasurface based on the plasma dispersion effect of silicon has been proposed in [101]. Active tunability was demonstrated for linear-to-elliptical and linear-to-circular polarization conversions only. Recently, Atwater *et al.* demonstrated metasurface-based dynamic polarization control by integrating TCOs suitable at near-infrared (NIR) wavelengths [81]. Nevertheless, the previously reported TCO-based metasurfaces for dynamic polarization conversion come at the cost of low intensity of the reflected lights and requirement for high bias voltages.

Therefore, the realization of a low voltage-driven active metasurface for polarization modulation remains a great challenge. The ENZ phenomenon can be utilized to enable dynamic polarization rotation with small electrical biasing while maintaining a high intensity of reflected or transmitted light. To bridge these gaps, in the next Section, a low-voltage driven electro-tunable compact metasurface-based polarization converter has been introduced to enable a dynamic control over different linearly-polarized reflected light at 1.55 μm wavelength. This is achieved by tuning the accumulation process free-electrons in the ENZ material.

7.2. Electro-tunable Metasurface for Tri-State Dynamic Polarization Modulation

This Section presents a novel low-voltage driven electro-tunable metasurface-based polarization modulator that can operate at the key wavelength band of optical communication, *i.e.*, C-band. The proposed device comprises a two-dimensional array of elliptical silver (Ag)-nanopillars deposited on ITO–alumina (Al_2O_3)–Ag stack. We leverage gap-plasmon resonance effect combined with free-electrons accumulation process of ITO to achieve control over the three linearly polarization states of the reflected light, *i.e.*, a tri-state polarization switching (*viz. y*-polarization for 0 V, –45° linear polarizations for 2 V, and *x*-polarization for 5 V).

The normalized intensity of the reflected wave for both 0 V and 5 V biasing conditions are more than 0.7, and more than 0.5 for 2 V bias — implying low insertion losses in different biasing states. Such an electro-tunable metasurface is proposed for the first time, to the best of our knowledge, which is capable of switching among three different linear polarization states of the reflected light while maintaining sufficiently high intensity.

7.2.1. Structural Overview

The schematic of the electro-tunable metasurface-based polarization modulator is shown in Figure 7.1. The proposed metasurface consists of a two-dimensional array of elliptical-shaped Ag-nanopillars (with thickness t_0 = 215 nm) deposited on cascaded layers of ITO (with thickness t_{ITO} = 10 nm), Al_2O_3 (with thickness $t_{Al_2O_3}$ = 5 nm), and optically-thick metallic ground plane of Ag (with thickness t_M = 70 nm). The top view of the metasurface is shown in Figure 7.1 (a), where a meta-atom is shown in an enlarged view illustrating the periodicity (Λ = 500 nm) along both *x*-direction and *y*-direction,

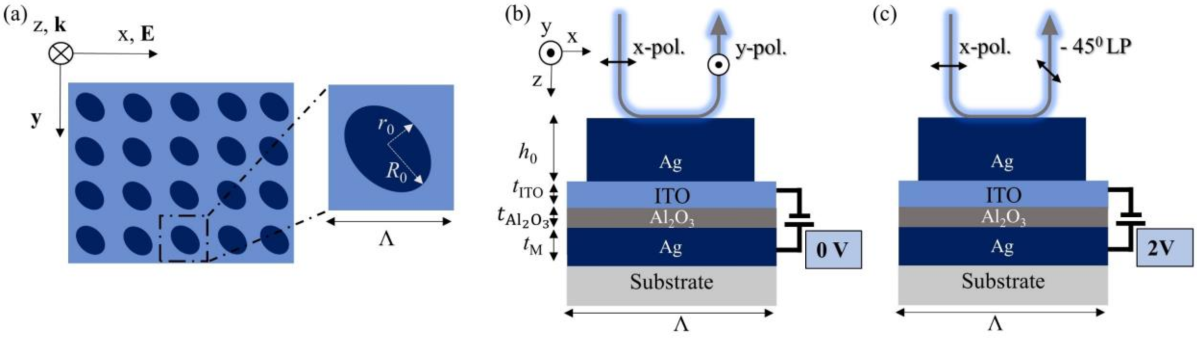

Figure 7.1: Schematics of the electro-tunable metasurface based polarization modulator consisting a two-dimensional array of elliptical Ag-nanopillars deposited on ITO–Al_2O_3–Ag stack. (a) Top view of the device, a square unit cell or 'meta-atom' with an elliptical Ag cylinder is shown in an enlarged view depicting the periodicity along *x*- and *y*-directions, and semi-major axis R_0 and semi-minor axis r_0. Cross-sectional view of the meta-atom of the proposed metasurface pictorially depicting polarization switching at (b) 0 V and (c) 5 V, where, we consider that the metasurface is illuminated by a normally-incident *x*-polarized light [208].

semi-major axis (R_0 = 125 nm) and semi-minor axis (r_0 = 105 nm). Here, we have considered an illumination of normally-incident *x*-polarized light propagating along the *z*-direction. The side-view of a meta-atom of the proposed structure describing a pictorial representation of polarization switching at 0 V and 2 V are shown in Figure 7.1(b) and (c), respectively. A 3D finite-difference time-domain simulation model is considered here. We have considered periodic boundary conditions along both *x*- and *y*-axis, and perfectly matched layers are used along the *z*-axis to minimize unwanted scattered light.

7.2.2. Electro-tunable ENZ-phenomenon of ITO

The ITO–Al_2O_3–Ag stack forms a metal–oxide–semiconductor (MOS)-type configuration, as presented in the inset of Figure 7.2(a). The refractive indices of Al_2O_3 and Ag are taken from the literature [125], [183]. To observe the accumulation of free-electrons at the ITO–Al_2O_3 interface upon applying bias-voltage, electrostatic device

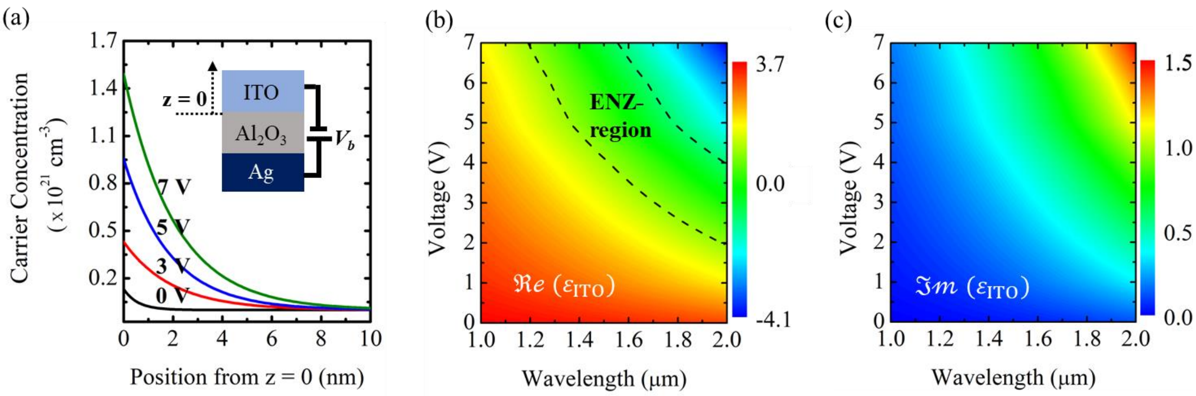

Figure 7.2: (a) Spatial distributions of carrier concentration (N) of ITO layer from z = 0 to 10 nm at different applied bias condition. Inset shows formation of MOS-type capacitor comprising ITO–Al_2O_3–Ag layers, where z = 0 indicates ITO–Al_2O_3 interface. The voltage-dependent real (b) and imaginary (c) parts of permittivity of the charge accumulation layer of ITO with respect to wavelength. The ENZ-region is displayed as $-1 < \Re e(\varepsilon_{\mathrm{ITO}}) < +1$ [208].

simulations have been conducted in the commercially available Lumerical Device® tool. For simulations involving device physics , the parameters assumed for ITO are identical to the ones considered in Chapter 2 (section 2.4.2). Here, the bulk carrier-concentration is taken as ~3×10^{19} cm^{-3}. The variation in the carrier-concentration distributions of the ITO layer from the ITO–Al_2O_3 interface is presented in Figure 7.2(a) as a function of electrical bias. The charge **ac**cumulation **l**ayer (ACL) is estimated as an ultra-thin region (~3 nm thickness) by applying modified Thomas–Fermi approximation [133], [134], where we employ a two-layer model similar to the procedure as mentioned in Chapter 2 (sub-section 2.4.2).

It should be noted that the ENZ-phenomena can be achieved by using different gate-dielectric materials (such as HfO_2). However, the breakdown voltage of the material needs to be carefully considered while choosing the gate-dielectric material in a MOS-type structure. For instance, the breakdown electric field for Al_2O_3 is 7.4 MV/cm [29]. On the contrary, the breakdown electric field for HfO_2 is 3.1 MV/cm, which is much lower than Al_2O_3. To verify that our device operates within the limit of breakdown voltage of Al_2O_3, we have done electrostatic simulations using Lumerical Device® tool. The numerical simulations reveal that the electric field across the Al_2O_3 layer is 5.2 MV/cm with a maximum of 5 V biasing, which is lower than the reported breakdown electric field.

After calculating the charge carrier distributions under the influence of applied bias voltages, the charge distributions inside the accumulation layer of 3 nm thickness are translated to the optical properties *via* Drude permittivity model, given by Eq. (2.34) of Chapter 2. Figure 7.2(b) depicts the variation of real, $\mathfrak{Re}\,(\varepsilon_{\mathrm{ITO}})$, part of the permittivity of accumulation layer with respect to the applied bias, where the zero-permittivity crossover wavelength is defined as "ENZ-region" [29]. Figure 7.2(c) depicts the variation of imaginary part of permittivity, $\mathfrak{Im}(\varepsilon_{\mathrm{ITO}})$, of the charge accumulation layer as a function of bias-voltage. We leverage the variation of the complex permittivity of ITO active layer (or accumulation layer ACL) to realize dynamic polarization control.

7.2.3. Results and Discussion —Tri-State Polarization Modulation

The proposed polarization rotating device is designed in such a way that the incident linearly polarized beam (with electric field along *x*-direction) forms a 45° angle with the *x*- and *y*-axes of the device (*i.e.*, with the major and minor axes of the elliptical nanopillars). This leads to decomposition of an incident *x*-polarized wave to its *x*- and *y*- components. Thus, the reflected wave has two components, namely co-polarized (R_{xx}) and cross-polarized (R_{yx}) for an *x*-polarized illumination. Figure 7.3 depicts the modulation of co-polarized (R_{xx}) and cross-polarized (R_{yx}) reflectance at 1.55 μm, and the corresponding phase difference, $\Delta\phi = \phi_{xx} - \phi_{yx}$, where ϕ_{xx} and ϕ_{yx} denote the phase of the R_{xx} and R_{yx} components, respectively, for an *x*-polarized illumination. Due to the excitation of gap-plasmon resonance mode at 1.55 μm wavelength (shown later in

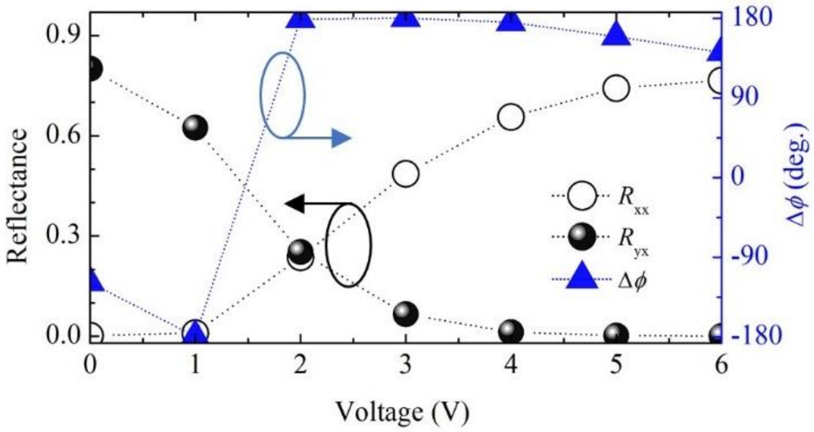

Figure 7.3: Variation of co-polarized (R_{xx}) and cross-polarized (R_{yx}) reflectance at 1.55 µm wavelength as a function of bias-voltage, and the corresponding phase difference, $\Delta\phi = \phi_{xx} - \phi_{yx}$, when illuminated with a normally-incident *x*-polarized light [208].

Figure 7.5) for 0 V bias, the co-polarized component acquires a negligible value — leading to a *y*-polarized reflected light.

By increasing the external bias-voltage, we can accumulate the free-electrons of ITO at the ITO–Al_2O_3 interface, which leads to modulation in phase and amplitude of the two orthogonal components of the reflected wave. At 2 V biasing state, the amplitude of the co-polarized (R_{xx}) and cross-polarized (R_{yx}) components are almost equal while the phase difference is $\Delta\phi = 180°$. This indicates the realization of a linearly polarized reflected light with –45° polarization angle [113]. On the other hand, if we further increase the electrical bias, we can achieve an *x*-polarized reflected light.

The reflectance spectra for co-polarized and cross-polarized components for 0 V, 2 V, and 5 V biasing conditions are shown in Figure 7.4(a), (b), and (c), respectively. Note that we have considered an *x*-polarized wave normally-incident on the metasurface while propagating along *z*-direction, as shown in the inset of Figure 7.4(c). Note that the electric field orientation of the reflected wave for each biasing state is depicted by the bi-directional arrows. Due to the excitation of the gap-plasmon resonance, a dip in the

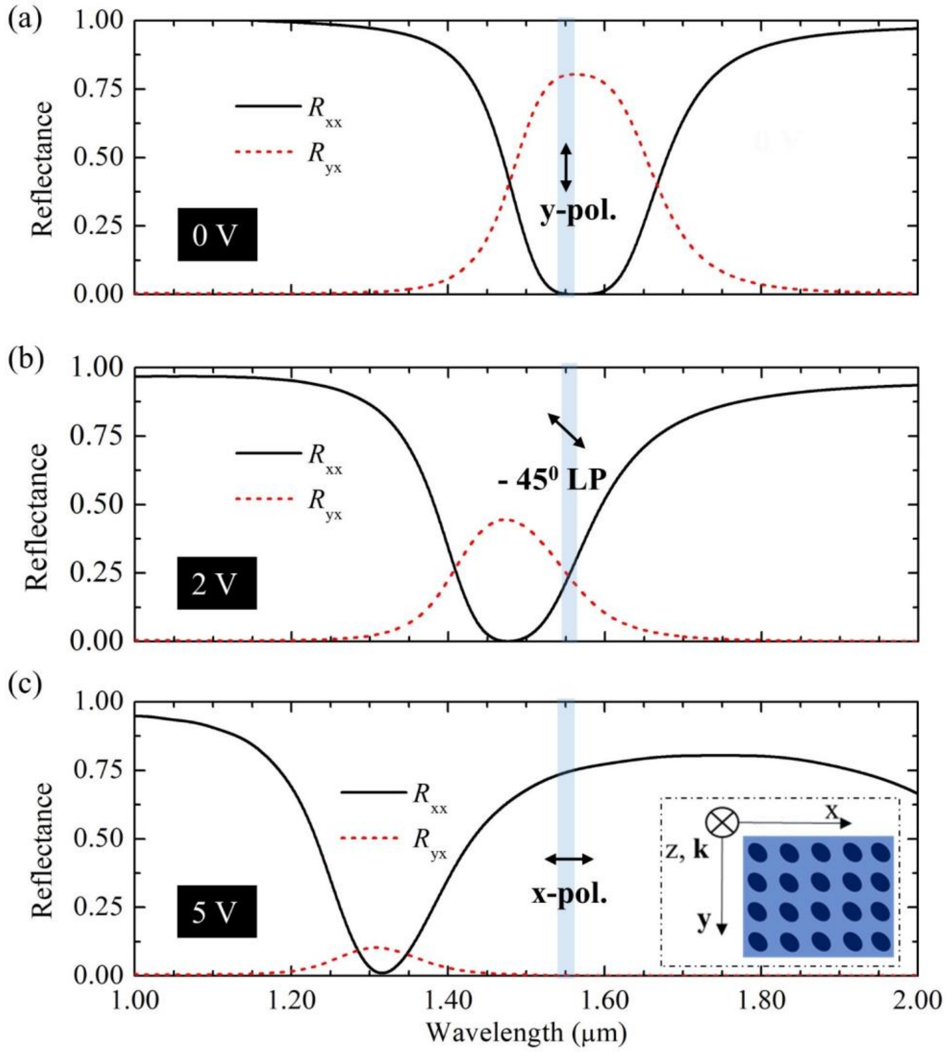

Figure 7.4: Reflectance spectra for co-polarized (R_{xx}) and cross-polarized (R_{yx}) components for (a) 0 V, (b) 2 V, and (c) 5 V biasing conditions. Note that the shaded region represents the operating wavelength regime, *i.e.*, the C-band of wavelength. The orientation of electric field of the reflected waves at different biasing are shown by bi-directional arrows. In all cases, we have considered an *x*-polarized wave normally incident on the metasurface, as shown in the inset of (c) [208].

co-polarized (R_{xx}) reflectance spectra at the operating wavelength region can be observed under 0 V biasing condition. On the other hand, the cross-polarized (R_{yx}) component of electric field intensity gets its peak at the 1.55 μm wavelength — leading to a *y*-polarized reflected wave.

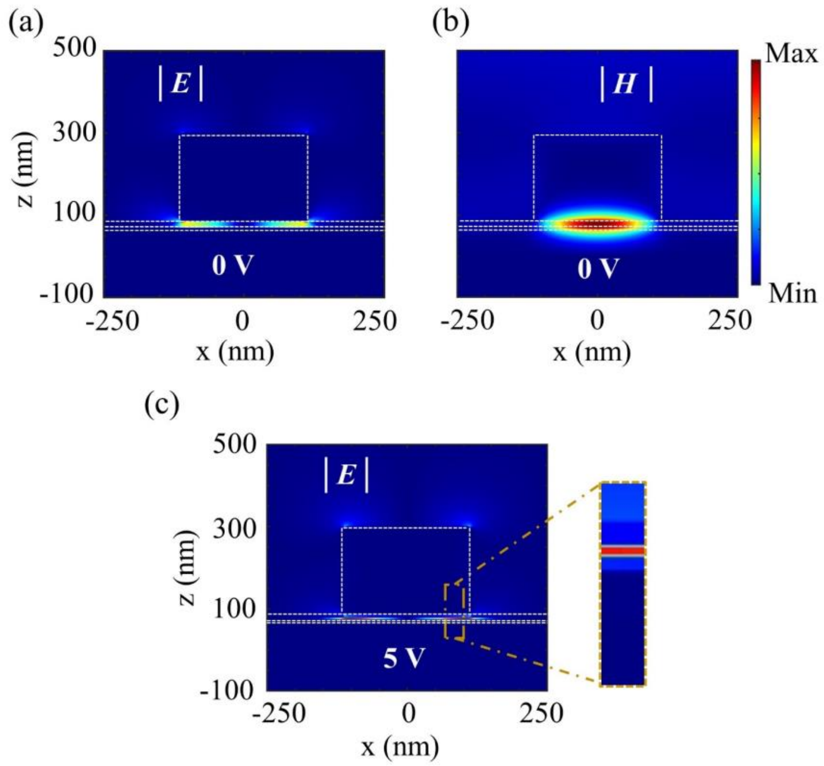

Figure 7.5: Normalized (a) electric (|E|) and (b) magnetic (|H|) field profiles at 1.55 μm wavelength for 0 V bias. (c) Normalized electric field profile at 1.55 μm for 5 V bias, where the field enhancement is displayed in an enlarged view. Note: white dashed lines represent the underlined structure [208].

Now, we can see a blue-shift of the plasmonic resonance dip with the increase of the bias voltage. At 2 V bias, when $R_{xx} \approx R_{yx}$ with $\Delta\phi \approx 180°$ at 1.55 μm wavelength, we can get a linearly polarized light with –45° polarization angle, as shown in Figure 7.4(b). It should be noted that with further increase of the bias-voltage, the charge accumulation region exhibits the ENZ-phenomenon at the operating wavelength region. This results in an alteration of resonance conditions of the orthogonal components of the reflected wave — leading to *x*-polarized reflected light at 5 V biasing condition.

Figure 7.5(a) and (b) represent the electric (|E|) and magnetic (|H|) field distributions for the unbiased (0 V) state at 1.55 μm wavelength. We can observe the excitation of gap-plasmon resonance, which leads to a resonance dip in the reflectance spectra corresponding to the co-polarized component and a peak in the cross-polarized component. Thus, the linearly polarized light (with electric field orientation along *x*-axis) will get rotated to its orthogonal state upon reflection from the metasurface, *i.e.*, providing a *y*-polarized reflected wave. On the other hand, the plasmonic resonance effect will get altered if we apply bias-voltage to accumulate free-electrons at the ITO–Al_2O_3 interface. Due to the enforcement of unusual boundary conditions, an enhancement of the electric field can be seen at the ultra-thin charge accumulation region, as discussed in Chapter 1 (sub-section 1.2.2). When the denominator of Eq. (1.3) is negligibly small (*i.e.*, at ENZ-condition), we can see an electric field enhancement at the ITO–Al_2O_3 interface, as displayed in an enlarged view of Figure 7.5(c) for 5 V biasing state.

7.2.3.1. Stokes Parameter Analysis

To further analyze the polarization states of the reflected wave at different biasing conditions, we can calculate the Stokes parameters, given by [73], [81], [113]:

$$S_0 = |r_x|^2 + |r_y|^2 = R_{\mathrm{xx}} + R_{\mathrm{yx}} \tag{7.1}$$

$$S_1 = |r_{\mathrm{x}}|^2 - |r_{\mathrm{y}}|^2 = R_{\mathrm{xx}} - R_{\mathrm{yx}} \tag{7.2}$$

$$S_2 = 2|r_{\mathrm{x}}||r_{\mathrm{y}}|\cos(\Delta\phi) \tag{7.3}$$

$$S_3 = 2|r_x||r_{\mathrm{y}}|\sin(\Delta\phi) \tag{7.4}$$

where r_x and r_y stand for the complex reflection coefficients with electric field orientation along *x*- and *y*-axis, respectively. Here, we have considered a normally-incident *x*-polarized wave propagating along the *z*-direction. The co-polarized and cross-

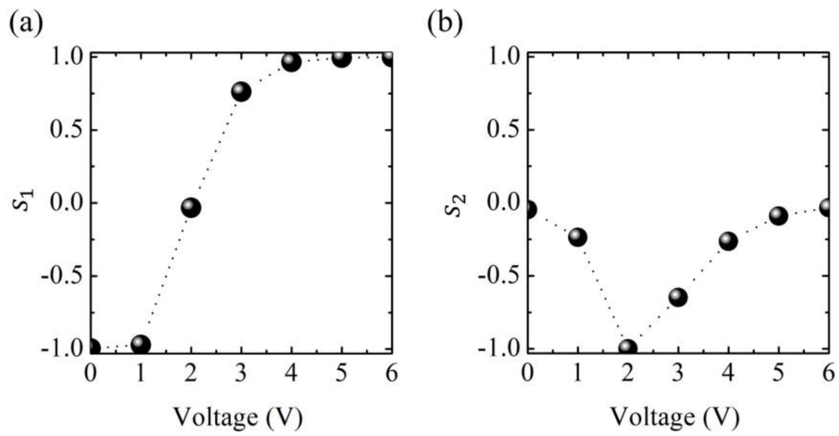

Figure 7.6: Normalized Stokes parameters: (a) s_1 and (b) s_2 for different bias voltages at 1.55 µm incident wavelength [208].

polarized components are denoted as R_{xx} and R_{yx}, respectively, and the $\Delta\phi$ (= $\phi_{xx} - \phi_{yx}$) denotes the corresponding phase differences.

To understand the orientation of the electric field of the linearly polarized light, we need to calculate the S_1 and S_2 parameters. The Stokes parameters can be normalized as s_1 (= S_1/S_0) and s_2 (= S_2/S_0) [113], where s_1 describes the linear polarization along x ($s_1 = +1$) or y ($s_1 = -1$) directions, and s_2 describes the linear polarization with an angle of ± 45° ($s_2 = \pm 1$), when illuminated with x-polarized light. The variation in the normalized Stokes parameters s_1 and s_2 are depicted in Figure 7.6(a) and (b), respectively, at different biasing states. It can be seen that with ($s_1 = -1$) and ($s_1 = +1$) for 0 V and 5 V bias, we can achieve linearly polarized reflected light with electric field orientation along y- and x-directions, respectively. On the other hand, with ($s_2 = -0.997 \approx -1$) for the 2 V biasing state, we can get the –45° linear polarized reflected light. Thus, if we switch among 0 V, 2 V, and 5 V bias voltages, we can dynamically switch among these three different linear polarization states of the reflected light.

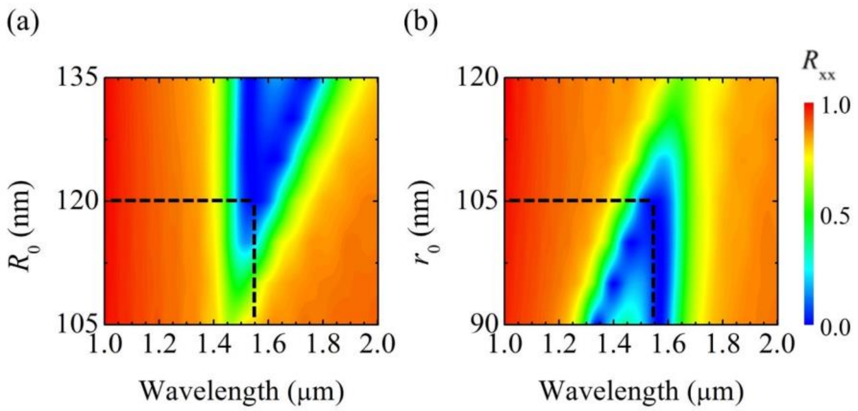

Figure 7.7: Reflectance spectra for co-polarized (R_{xx}) component depicting the fabrication tolerance study for (a) semi-major axis (R_0) and (b) semi-minor axis (r_0) with ±15 nm variation from the optimized parameters. Note: R_0 = 120 nm and r_0 = 105 nm are the optimized parameters of our design, which are represented by black dashed lines [208].

7.2.3.2. Parametric Tolerance Study

To understand the limits imposed on the geometrical parameters due to imperfections in the fabrication processes, we have conducted the parametric tolerance analysis of the elliptical-shaped Ag-nanopillars deposited on a multi-layered structure. We have varied the semi-major axis (R_0: from 105 to 135 nm) while keeping the semi-minor axis unchanged (*i.e.*, r_0 = 105 nm) to observe the variation in co-polarized (R_{xx}) reflectance component, as shown in Figure 7.7(a). Similarly, we have varied the semi-minor axis (r_0 = from 90 to 120 nm) while keeping semi-major axis fixed (*i.e.*, R_0 = 120 nm) to find the fabrication tolerance limit, as shown in Figure 7.7(b). The dashed lines represent the optimized parameters for our design.

As expected, with a decrease in R_0, we observe an increase in the co-polarized reflectance component. This is due to the fact that as R_0 approaches the value of r_0, the elliptical shape changes to circular which breaks the birefringence-like effect and hence, results in equal amplitudes of co-polarized and cross-polarized components of the reflected light. On the other hand, with increase in R_0, we can see a slight red-shift and broadband resonance dip in the co-polarized reflectance spectra. Thus, the device can operate as a polarization rotator with R_0 as (120 + 15) nm or (120 – 5) nm. Similarly, the polarization rotation can be achieved with semi-minor axis as well, when r_0 is (105 + 5) nm or (105 – 15) nm.

7.2.4. Summary

We presented a novel design of an electro-tunable metasurface for dynamic polarization switching. We leverage electro-tunable optical response of ITO combined with gap-plasmon resonance of metal–insulator–metal configuration to realize dynamic control of polarization states of reflected waves. The proposed device comprises a 2D array of elliptical-shaped Ag-nanopillars deposited on cascaded layers of ITO, Al_2O_3, and an optically-thick Ag-ground plane. The proposed polarization rotating device is designed in such a way that the normally-incident *x*-polarized beam can be decomposed into its two orthogonal components upon reflection, *viz.* co-polarized (R_{xx}) and cross-polarized (R_{yx}) components.

Without applying any bias-voltage, the excitation of gap-plasmon resonance mode at 1.55 μm wavelength leads to a negligible co-polarized component, which results in a y-polarized reflected wave while maintaining reflectance over 0.7. On the other hand, we have shown the **modulation of amplitude and phase of co-polarized and cross-polarized components of the reflected wave** by accumulating free-electrons of ITO at the ITO–Al_2O_3 interface upon applying electrical biasing. At 2 V bias, we have achieved a linearly polarized light with – 45° polarization angle. With further increase in the bias-voltage, the ENZ-wavelength of ITO can be tuned to the operating wavelength regime of 1.55 μm, which leads to a negligible cross-polarization component, *i.e.*, producing an *x*-polarized reflected light. The calculated Stokes parameters, $s_1 = -1$ (+1) for 0 V (5 V) bias and $s_2 = -1$ for 2 V bias, represent *y*-polarized

(*x*-polarized) and –45° linear polarized light, respectively. **This illustrates a tri-state dynamic control over three different states of linear polarization of light.** Thus, the proposed metasurface could find potential applications for realization of active polarization-controlling elements in the nanophotonic systems.

8

Conclusion and Future Scope

Contents

This Chapter summarizes the thesis work, highlighting significant findings and contributions concerning designing and realization of nanophotonic meta-devices based on ENZ effect for electro-optic and all-optical modulation. Section 8.1 discusses a summary of the contributions. Section 8.2 concludes the Chapter by jotting down the potential directions for future research.

8.1. Summary of Contributions

Over several decades, the development of photonic technologies has led us to achieve active control of electromagnetic properties of light (such as amplitude, phase, and polarization). The active manipulation of reflected or transmitted light can be done under the influence of external stimuli such as electrical biasing or optical pumping. The electro-optic and all-optical modulators are such kind of active photonic devices to manipulate the electromagnetic properties of incoming light. This thesis work has presented the prospects and challenges towards realizing electro-optic and all-optical modulation for various nanophotonic applications by leveraging the epsilon-near-zero (ENZ) phenomenon of transparent conducting oxide (TCOs).

Chapter 1 presented the outline of the thesis work, research motivation, research gaps and problem statements, methodology, the major contribution and organization of this thesis. This chapter also introduced the emerging ENZ materials and their capability in active control of light–matter interactions. Chapter 2 presented relevant theoretical background and numerical techniques adopted during the research work, followed by a literature review on the ENZ-material based nanophotonic meta-devices for modulation of optical intensity, phase, and polarization. Chapter 3 discussed the first research objective of this thesis work, *i.e.*, to achieve *dual-band* free-space electro-optic intensity modulation for both the primary telecommunication wavelength bands (C-band and O-band) by integrating the ENZ-materials into various resonating metasurfaces. Two innovative approaches have been adopted for enabling dual-band free-space electro-optic intensity modulation. By leveraging the ENZ phenomenon of TCOs combined with gap-plasmon resonance (GPR) of metal–insulator–metal structure, a novel plasmonic electro-tunable metasurface has been designed that can be used to simultaneously modulate the intensity of reflected light at both C-band and O-band. Then, by harnessing the ENZ phenomenon of TCOs combined with guided-mode resonance (GMR) of grating waveguide, a dual-band electro-tunable metasurface has been presented.

Although these metasurfaces could be useful for attaining dual-band intensity modulation, the stringent dependency on polarization state of incident light imposes several limitations on reducing the footprint of a nanophotonic system. Hence, to mitigate the limitation, Chapter 4 presented the second objective, *i.e.*, to design *polarization-insensitive* metasurfaces for free-space electro-optic intensity modulation while leveraging the ENZ phenomenon. Here also two unique design strategies have been adopted for enabling polarization-insensitive intensity modulation. To begin with, a GMR based all-dielectric polarization-insensitive modulator has been presented that can be operated with normally incident light. Then, a GPR based polarization-insensitive plasmonic metasurface has been introduced that can be operated with a wide variation of incidence angle.

Chapter 5 discussed the third objective, *i.e.*, design and investigation of an *all-optical intensity modulator* based on nonlinear phenomena in ENZ-materials. To enable ultra-fast all-optical modulation, a novel magnetic plasmon resonance based energy-efficient metasurface has been presented which can operate with ultra-fast response time in sub-picosecond scale with high modulation depth.

Chapter 6 addressed the fourth objective, *i.e.*, to design a polarization-insensitive *integrated electro-optic intensity modulator* based on the ENZ-effects. A novel design of parallel directional coupler based dual-polarization electro-absorption modulator has been presented for use in integrated photonic systems by leveraging hybrid integration of ENZ-material in a silicon waveguide. Finally, Chapter 7 presented the last objective, *i.e.*, to design an ENZ-material based free-space *electro-optic polarization modulator*. The presented GPR based plasmonic metasurface can dynamically switch among the three linear polarization states of the reflected wave upon applying external electrical biasing, allowing a tri-state polarization modulation.

This PhD thesis explores various nanophotonic active devices for modulation of the two key electromagnetic properties of light *viz*. intensity and polarization by leveraging the ENZ phenomenon. Various design strategies have been explored by integrating ENZ-materials to enable dynamic light–matter interactions. The major contributions of this thesis have been published in many prestigious peer-reviewed international journals and also were presented in renowned international conferences in the emerging field of nanophotonics, plasmonics, and metamaterials.

The summary of contributions towards the fulfilling the research objectives of this thesis ***by harnessing the ENZ phenomenon of TCOs*** is briefly given below

- **Guided Mode Resonance based Metasurface for *Dual-band* Free-Space Electro-Optic Intensity Modulation**

In the first Section of Chapter 3, we presented a unique design strategy of dual-band electro-optic intensity modulation by leveraging the ENZ phenomenon combined with guided-mode resonance (GMR) effect. The presented tunable metasurface could exhibit a dual-band intensity modulation with modulation depth covering both C-band and O-band wavelengths, which are the primary telecommunication wavelength bands (). Effective medium approximation combined with modal analysis was utilized to study the multiple resonance responses originating from excitation of waveguide modes *via* coupling with the incident light. When the ENZ-wavelength of ITO was electrically-tuned to the operating wavelength-band, a rise in the modal loss had been observed, which resulted in the disappearance of GMR-effect. Thus, we could achieve a modulation depth as high as ~22.3 dB (~19.5 dB) at 1.55 µm (1.31 µm) with a modulation speed estimated to be ~168 Mbps. The designed metasurface could find potential applications towards realization of active dual-band flat optical components in nanophotonic systems. The findings were reported in '**Optics Letters**'[180].

- **Gap Plasmon Resonance based *Incident Angle-insensitive* Metasurface for *Dual-band* Free-Space Electro-Optic Intensity Modulation**

In the second Section of Chapter 3, we introduced a gap plasmon resonance (GPR) based electro-tunable metasurface for modulation of the reflected light intensity with wide variation of incident angle, which could not be achieved in the previous design based on GMR. We exploited GPR mode in a metal–insulator–metal (MIM) structure and the ENZ phenomenon of ITO to enable dynamic control of the intensity of reflected light at both C-band and O-band wavelength regime. With a 5V external bias-voltage, the coupling of GPR-mode with ENZ-mode was observed, which resulted in a broadening and strengthening of resonance over a 370 nm spectral window ranging from 1.25 µm to 1.62 µm with more than 80% absorption.

Such dynamic control of absorption properties was then utilized for modulation of intensity of the reflected light. The metasurface exhibited a dual-band intensity modulation of reflected light with modulation depth as high as 20.5 dB and 16.6 dB at 1.55 µm and 1.31 µm of wavelength, respectively, while switching between 0 V and 5 V biasing conditions. Most importantly, this device can be operated with a wide range of incident angle (up to 60 degrees) for *x*-polarized light. This could help in realizing angle-insensitive intensity modulators operating at different wavelength bands. The findings were reported in '**Optics & Laser Technology**'[189].

- **GMR based Metasurface for *Polarization-insensitive Dual-mode* Free-Space Electro-Optic Intensity Modulation**

In the first Section of Chapter 4, we introduced a unique design strategy of a polarization-insensitive all-dielectric metasurface for electro-optic intensity modulation that could operate in both transmission and reflection modes allowing a dual-mode operation. We harnessed the GMR-effect of grating waveguide structure combined with ENZ-effect of ITO to realize dual-mode polarization-insensitive electro-optic modulation. We observed the coupling of spatial light to the waveguide mode resulting in a resonance filtering response. When the ENZ-wavelength of ITO was tuned to the operating wavelength by applying external biasing, the resonance feature disappeared due to the high modal loss, resulting in a high modulation depth.

We achieved modulation depths as high as 0.96 and 0.85 for reflection and transmission mode, respectively, at the operating wavelength of 1.55 µm with random polarization angle of incident plane waves. Our electrostatic simulations estimated the device to support up to a bit-rate of ~774 Mbps for binary modulation schemes. Moreover, the operating wavelength could be blueshifted or redshifted by utilizing the frequency-scaling property of the proposed design. As a proof of the concept, we have shown possibility of electro-optic modulation at L-band of wavelength (operating at 1.61 µm) by simply scaling up the dimensions of unit cell structure. The findings were reported in '**IEEE Journal of Quantum Electronics**'[35].

- **GPR based Metasurface for *Polarization-and Angle-insensitive* Free-Space Electro-Optic Intensity Modulation**

In the second Section of Chapter 4, we presented a GPR based polarization-insensitive electro-tunable metasurface that can modulate the intensity of reflected light by leveraging the electro-optic properties of ITO for a wide variation of incident angle, which could not be achieved in our previous designs. The numerical simulations revealed that due to the excitation of gap plasmon resonance mode, a dip at 1.72 μm in the reflectance spectra was observed at the unbiased state, which was verified by an equivalent RLC-circuit model. With 2 V applied bias, we have shown the tuning of the resonance wavelength to 1.55 μm wavelength leading to a modulation depth as high as ~25 dB for random polarization angle of the incident

Table 8.1: Comparison among Different Designs for Free-Space Electro-Optic Intensity Modulation

Presented Designs	**MD**	**f_{3dB} (MHz)**	**Polarization Insensitive?**	**Angle Insensitive?**	**Publication**
Design I (Chapter 3)	22.3 dB at 1.55 μm 20 dB at 1.31 μm	83.5	No	No (Works for normal incidence)	Optics Letters [180]
Design II (Chapter 3)	20.5 dB at 1.55 μm 16.8 dB at 1.31 μm	162	No	Yes (Up to 60° of oblique incidence)	Optics & Laser Technology[189]
Design III (Chapter 4)	20 dB at 1.55 μm	387	Yes	No (Works for normal incidence)	IEEE Journal of Quantum Electronics [35]
Design IV (Chapter 4)	25 dB at 1.55 μm	450	**Yes**	**Yes** (Up to 50° of oblique incidence)	IEEE Photonics Technology Letters [207]

*MD: Modulation Depth, f_{3dB}: 3-dB modulation bandwidth light. The proposed device can be operated with a wide range of incident angle (up to 50 degrees) for both *x*- and *y*-polarized light. Moreover, the modulator exhibited a bit-rate of 900 Mbps for binary modulation schemes while maintaining a low energy-consumption of 303 fJ/bit. The findings were reported in '**IEEE Photonics Technology Letters**'[207].

A comparison of performance metrics among these free-space electro-optic intensity modulators based on ENZ materials (presented in Chapter 3 and Chapter 4) is shown in Table 8.1.

- **ENZ-material based Nonlinear Metasurface for Free-Space Ultra-Fast *All-Optical Intensity Modulation***

In Chapter 5, we presented an ultra-fast all-optical switching scheme based on magnetic plasmon resonance phenomena of the metasurface combined with the intraband transition induced optical nonlinearities of an ENZ-material, cadmium-oxide (CdO). Due to excitation of magnetic plasmon resonance, strong light–matter interactions could be assured at the resonance wavelength leading to an enhancement of the nonlinear phenomenon of the presented CdO-coupled structure. We have theoretically achieved a high modulation depth of 0.83 at 1.55 µm wavelength under the influence of a pump-fluence of 75 µJ/cm^2. The transient study revealed that the device could exhibit ultrafast switching speed of 776 fs while maintaining a very low pump-fluence of 75 µJ/cm^2. The presented all-optical switching scheme could pave the way toward the realization of next-generation optical and quantum computation systems. The findings were reported in '**Optics Letters**'.

- **ENZ-material based *Dual-Polarization On-Chip* Electro-Optic Intensity Modulation for Integrated Photonics**

In the Chapter 6, we presented a novel design of directional coupler based dual-polarization electro-optic intensity modulator using ENZ-material. By applying independent external electrical bias at the corresponding coupling region consisting of ITO-based hybrid plasmonic waveguides (HPWs), enhancement of light–matter interactions yielding from ENZ-effect could be seen. This phenomenon was then utilized for enabling independent and synchronized modulation of both fundamental modes (TE and TM modes) of a standard silicon rib waveguide. The extinction ratio of TM (TE) polarization was achieved as 10.11 dB (9.66 dB) at 1550 nm wavelength, resulting in a 0.45 dB polarization dependent loss. With a 27 µm active length, the modulation bandwidth and power-consumption could be achieved as 122.75 GHz (107.91 GHz) and 773 fJ/bit (759 fJ/bit) for TM (TE)-modulation, respectively. To the best of our knowledge, such a compact dual-polarization electro-optic intensity modulator has been presented for the first time, which is capable of independent and parallel modulation of both polarizations by leveraging the feature of electrically-tunable ENZ effect of ITO. The findings were reported in '**Journal of Physics D: Applied Physics'** [40].

- **ENZ-material based Metasurface for Electro-Optic *Tri-State Polarization Modulation***

In Chapter 7, we presented a novel design of an electro-tunable metasurface to enable dynamic control of polarization states of the reflected light. In unbiased condition, excitation of gap-plasmon resonance in the metasurface resulted in the rotation of *x*-polarized incident light to an orthogonally polarized (*i.e.* *y*-polarized) reflected light at 1.55 µm. On the other hand, by applying 2V applied bias, we achieved a linearly polarized reflected light with a polarization angle of –45°. Furthermore, when we tuned the ENZ wavelength of ITO at the vicinity of 1.55 μm wavelength by increasing the bias to 5 V, we could achieve an *x*-polarized reflected light. Thus, with an *x*-polarized incident wave, we have shown a tri-state polarization switching (*viz*. *y*-polarization at 0 V, –45° linear-polarization at 2 V, and *x*-polarization at 5 V). The findings were reported in '**Journal of Physics: Condensed Matter**' [208].

8.2. Recommendations for Future Research

This section suggests a few directions for future research that can be extended from the work presented in this thesis.

☞ *Electro-tunable metasurface for phase modulation*

This thesis work presents different designs of nanophotonic meta-devices for attaining active control of intensity and polarization by harnessing the ENZ effect. The active manipulation of reflected or transmitted light may be extended to achieve modulation of another key electromagnetic property of light, *i.e.*, phase. The modulation of the phase of an incoming light through the metasurface could be useful in different applications such as beam-steering, holography, navigations, *etc*.

☞ *Realization of low-voltage driven electro-tunable quarter waveplate*

In Chapter 7, we introduced a tri-state polarization modulation technique, which could be useful for switching among three different states of linear polarization of the reflected light. In many applications, it is necessary to convert the linear polarized light to circularly polarized light, which can be achieved by a quarter waveplate. The previously reported metasurface based tunable quarter waveplates suffer from either high bias-voltage requirements or low intensity of light output. The ENZ-effect of TCOs can be harnessed to realize a low-voltage driven electrically-tunable quarter waveplate with minimal loss in light intensity.

☞ *Facilitating the design of metasurfaces by exploiting machine learning techniques*

The conventional procedure of metasurface design primarily involves manual optimization of the design parameters using a full wave simulation tool (such as finite-difference time-domain method or finite element method). However, such procedure is not only time consuming but also difficult in finalizing a design of meta-atoms for the desired optical response. To overcome this, we can exploit the machine learning approaches to optimize the design parameters of a meta-atom to attain a desired spectral response. This procedure is popularly known as "inverse designing of the metasurfaces", where we may use pattern recognition techniques such as machine learning, neural networks, and deep learning approaches. In the inverse designing process, the presence of sufficient amount of data (here, intensity and phase of reflected or transmitted light for various metasurface samples) can help in training the algorithms to grasp all of the possible patterns in the data. This can help one to obtain an optimal design of metasurface to produce a desired optical response, by eliminating the need to solve the Maxwell's equations numerous times, and go through the time-consuming optimisation procedure.

A

Appendix

A.1 Leveraging Magnetic Plasmon Resonance to Boost Nonlinear effects in CdO

It should be noted that the pump spot will illuminate a much larger area than just the CdO regime and the intensity-dependent refractive index change in the CdO will be different for our metasurface (introduced in Chapter 5, section 5.2) than that of bulk CdO. Due to the excitation of the magnetic plasmon resonance, we can see an enhancement of electric field inside the nanogrooves, which is filled with CdO. In other words, strong light–CdO interactions can be achieved when we have embedded the CdO-layer into the metasurface structure.

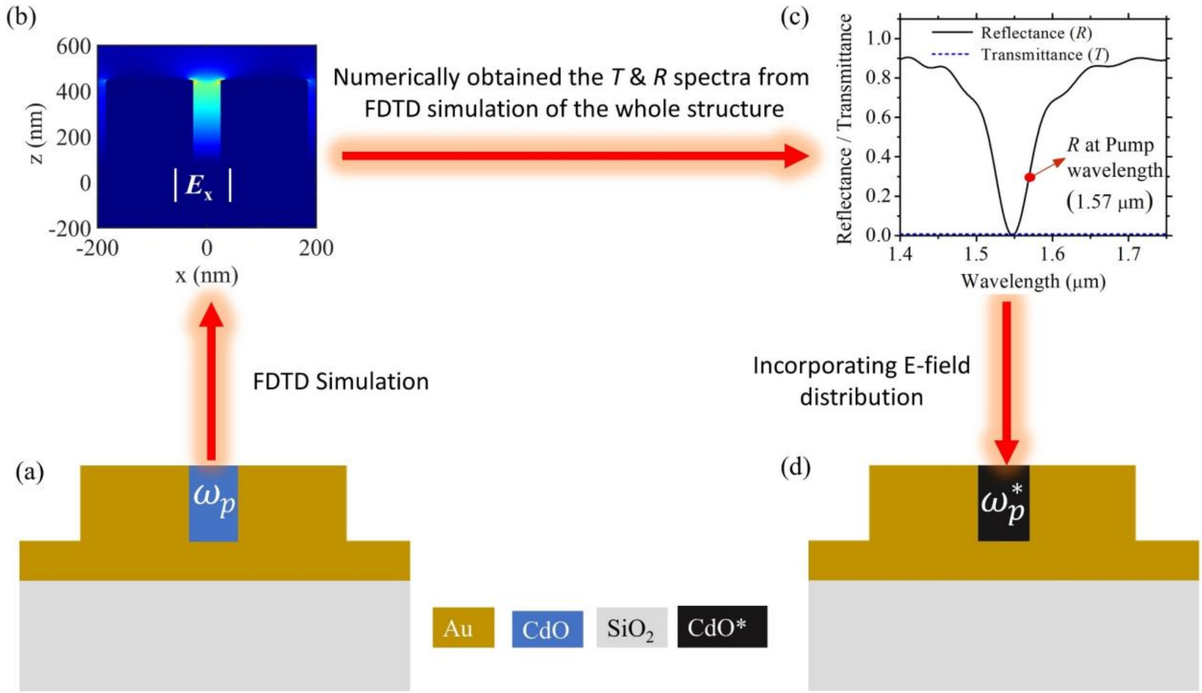

Figure A.1: Pictorial representation of a unit-cell structure of our metamaterial, where the CdO layer (with plasma frequency ω_p) embedded in the nanogroove can be replaced by the effective CdO-material (CdO* with modified plasma frequency ω_p*) after incorporating the non-uniform electric field distribution. [210]

The enhancement of electric field distributions inside the ENZ-material have been incorporated into our two-temperature modelling by calculating the effective absorbed power density P(t) of the metasurface at the pump-wavelength (1.57 μm) [47] as defined in Eq. (5.13), where the transmittance (T) and reflectance (R) for our proposed structure are obtained numerically from FDTD simulations.

Finally, the effective absorption coefficient is calculated to have a value of 3.15×10^7 m^{-1} at the pump wavelength of 1.57 μm. Thus, the redistributions of the electric field have been incorporated into our two-temperature modelling. Moreover, due to illumination of the pump-beam with a central wavelength close to that of the magnetic plasmon resonance, a high absorption of the pump-power by the metasurface can be ensured.

Then, the CdO layer embedding in the nanogrooves can be replaced with an effective CdO-layer as shown in Figure A.1. This leads to a different intensity-dependent plasma frequency variation of CdO for our metasurface as compared to that of the bulk CdO-layer of same thickness. The effective CdO-layer has a pump-intensity dependent plasma frequency (ω_p^*) variation as shown in Figure 5.5 of Chapter 5.

In other words, the plasma frequency variation as a function of pump-fluence shown in Figure 5.5 is an effective variation for our proposed structure after incorporating the field-redistribution due to the magnetic plasmon resonance. To highlight this fact, we have represented the plasma frequency and electron temperature of CdO-layer embedded in the nanogrooves of the proposed metasurface as $\omega_{\mathrm{p}}{}^*$ and $T_{\mathrm{e}}{}^*$, respectively.

A.2 Investigating the Nonlinearity of Gold in the CdO coupled Structure

We also check whether the pump induced optical nonlinearity of gold (Au) would affect the performance of our proposed structure discussed in Chapter 5 (section 5.2). It should be noted that gold also has the nonlinear optical response at picosecond-to-nanosecond time scale. However, the intrinsic nonlinearity of gold can be ignored for our study due to the negligible change in the electron-temperature of gold as compared to the ENZ-material CdO for our metasurface structure, similar to the ref. [56], [59]. Here, we would like to emphasize on the fact that the free-electron density in CdO is quite smaller than that of gold [56], [59], leading to a much smaller electron heat-capacity and larger variation in the electron temperature when all other parameters are kept constant.

To support our belief, we have shown the transient response of the electron and the lattice temperature of gold in Figure A.2. Using the extended two-temperature model first introduced by Carpene [209], we calculate the variation in the electron ($T_{e,\mathrm{Au}}{}^*$) and

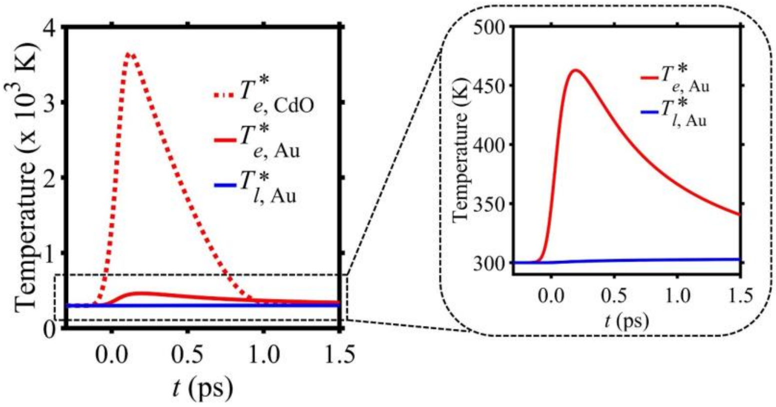

Figure A.2: Transient response of the electron ($T_{\mathrm{e,Au}}$*) and lattice ($T_{\mathrm{l,Au}}$*) temperature in Au sample of thickness 350 nm for our structure (comparing with the variation in the electron temperature of CdO-layer, $T_{\mathrm{e,CdO}}$*) calculated using the extended two-temperature model for 100 fs Gaussian pump beam excitation with fluence, F_0 = 75 µJ/cm^2 and pump wavelength of 1.57 µm. [210]

lattice ($T_{l,\mathrm{Au}}$*) temperatures of Au film of thickness 350 nm for our structure under optical pumping (fluence, F_0 = 75 µJ/cm^2). We observe that $T_{l,\mathrm{Au}}$* ≈ 300 K, thereby showing no significant change. Furthermore, we calculate the change in $T_{e,\mathrm{Au}}$* to be ~160 K at t = 0.2 ps, thus indicating that the pump induced optical nonlinearity of Au would have no such effect on the overall performance of our proposed metasurface. The variation in the $T_{e,\mathrm{Au}}$* is ~20 times smaller than the variation of T_e* of CdO for our proposed structure. Thus, the nonlinear response of the metasurface mainly comes from the intraband transition induced nonlinearity of the ENZ-material CdO.

For our metasurface structure, we have considered 350 nm thick gold-nanograting on top of a 100 nm thick gold back-reflector. With a maximum of 75 µJ/ cm^2 fluence of the pump-excitation with 100 fs pulse-width, the peak intensity will be around 750 MW/cm^2, which is much lower than that of the previously reported works [61], [110]. This assures us that the peak intensity will remain lower than the damage threshold of the gold-layer for the given thickness.

Bibliography

[1] I. Staude and J. Schilling, "Metamaterial-inspired silicon nanophotonics," *Nat. Photonics 2017 115*, vol. 11, no. 5, pp. 274–284, Apr. 2017, doi: 10.1038/nphoton.2017.39.

[2] R. Zia, J. A. Schuller, A. Chandran, and M. L. Brongersma, "Plasmonics: the next chip-scale technology," *Mater. Today*, vol. 9, no. 7–8, pp. 20–27, Jul. 2006, doi: 10.1016/S1369-7021(06)71572-3.

[3] W. Cai and V. Shalaev, *Optical Metamaterials*. New York, NY: Springer New York, 2010.

[4] N. I. Zheludev and Y. S. Kivshar, "From metamaterials to metadevices," *Nat. Mater.*, vol. 11, no. 11, pp. 917–924, Nov. 2012, doi: 10.1038/nmat3431.

[5] S. J. Kim and M. L. Brongersma, "Active flat optics using a guided mode resonance," *Opt. Lett.*, vol. 42, no. 1, p. 5, Jan. 2017, doi: 10.1364/OL.42.000005.

[6] A. K. Chowdhary, T. Bhowmik, and D. Sikdar, "Infrared-blocking plasmonic meta-glass for energy-saving passive windows," *Opt. Lett.*, vol. 47, no. 9, p. 2242, May 2022, doi: 10.1364/OL.456134.

[7] M. Khorasaninejad *et al.*, "Multispectral Chiral Imaging with a Metalens," *Nano Lett.*, vol. 16, no. 7, pp. 4595–4600, Jul. 2016, doi: 10.1021/acs.nanolett.6b01897.

[8] M. Faraji-Dana *et al.*, "Hyperspectral Imager with Folded Metasurface Optics," *ACS Photonics*, vol. 6, no. 8, pp. 2161–2167, Aug. 2019.

[9] Q. Chen, S. Song, H. Wang, L. Liang, Y. Dong, and L. Wen, “Ultra-broadband spatial light modulation with dual-resonance coupled epsilon-near-zero materials,” *Nano Res.*, vol. 14, no. 8, pp. 2673–2680, Aug. 2021, doi: 10.1007/s12274-020-3271-1.

[10] J. Zhang *et al.*, “Gate-tunable optical filter based on conducting oxide metasurface heterostructure,” *Opt. Lett.*, vol. 44, no. 15, p. 3653, Aug. 2019, doi: 10.1364/OL.44.003653.

[11] D. Marpaung, J. Yao, and J. Capmany, “Integrated microwave photonics,” *Nature Photonics*, vol. 13, no. 2. Nature Publishing Group, pp. 80–90, Feb. 01, 2019, doi: 10.1038/s41566-018-0310-5.

[12] G. Sinatkas, T. Christopoulos, O. Tsilipakos, and E. E. Kriezis, “Electro-optic modulation in integrated photonics,” *J. Appl. Phys.*, vol. 130, no. 1, p. 010901, Jul. 2021, doi: 10.1063/5.0048712.

[13] B. Zhou, E. Li, Y. Bo, and A. X. Wang, “High-Speed Plasmonic-Silicon Modulator Driven by Epsilon-Near-zero Conductive Oxide,” *J. Light. Technol.*, vol. 38, no. 13, pp. 3338–3345, Jul. 2020, doi: 10.1109/JLT.2020.2979192.

[14] yahoo! finance news, “Electro-Optic Modulator Market to Hit US$ 39.42 Billion By 2031 | Updated Research,” *finance.yahoo.com/news*, 2023. .

[15] J. Chi, H. Liu, N. Huang, and Z. Wang, “A broadband enhanced plasmonic modulator based on double-layer graphene at mid-infrared wavelength,” *J. Phys. D. Appl. Phys.*, vol. 52, no. 44, p. 445101, Aug. 2019, doi: 10.1088/1361-6463/AB36DC.

[16] M. He *et al.*, “High-performance hybrid silicon and lithium niobate Mach–Zehnder modulators for 100 Gbit s−1 and beyond,” *Nat. Photonics*, vol. 13, no. 5, May 2019, doi: 10.1038/s41566-019-0378-6.

[17] W. Zou, S. Xu, J. Wang, and J. Chen, "Silicon-based lithium niobate film electro-optic modulator array and integration method thereof," United States Patent No. US11204535B2, Dec. 21, 2021.

[18] C.-W. Hsu, C.-F. Huang, W.-S. Tsai, and W.-S. Wang, "Lithium Niobate Polarization-Independent Modulator Using Integrated Polarization Splitters and Mode Converters," *J. Light. Technol.*, vol. 35, no. 9, May 2017, doi: 10.1109/JLT.2016.2642203.

[19] Y. Xu *et al.*, "Quasi-BIC Based Low-Voltage Phase Modulation on Lithium Niobite Metasurface," *IEEE Photonics Technol. Lett.*, vol. 34, no. 20, pp. 1077–1080, Oct. 2022, doi: 10.1109/LPT.2022.3201268.

[20] T. Baba *et al.*, "50-Gb/s ring-resonator-based silicon modulator," *Opt. Express*, vol. 21, no. 10, p. 11869, May 2013, doi: 10.1364/oe.21.011869.

[21] J. Ding *et al.*, "Ultra-low-power carrier-depletion Mach-Zehnder silicon optical modulator," *Opt. Express*, vol. 20, no. 7, p. 7081, Mar. 2012, doi: 10.1364/oe.20.007081.

[22] C. Haffner *et al.*, "All-plasmonic Mach–Zehnder modulator enabling optical high-speed communication at the microscale," *Nat. Photonics*, vol. 9, no. 8, Aug. 2015, doi: 10.1038/nphoton.2015.127.

[23] J. Parra, I. Olivares, F. Ramos, and P. Sanchis, "Ultra-compact non-volatile Mach–Zehnder switch enabled by a high-mobility transparent conducting oxide," *Opt. Lett.*, vol. 45, no. 6, p. 1503, Mar. 2020, doi: 10.1364/OL.388363.

[24] G. T. Reed, G. Mashanovich, F. Y. Gardes, and D. J. Thomson, "Silicon optical modulators," *Nat. Photonics*, vol. 4, no. 8, pp. 518–526, Aug. 2010, doi: 10.1038/nphoton.2010.179.

[25] R. A. Soref and B. R. Bennett, "Electrooptical effects in silicon," *IEEE Journal of Quantum Electronics*, vol. 23, no. 1. pp. 123–129, 1987.

[26] S. Grillanda *et al.*, "107 Gb/s Ultra-High Speed, Surface-Normal Electroabsorption Modulator Devices," *J. Light. Technol.*, vol. 38, no. 4, pp. 804–810, Feb. 2020, doi: 10.1109/JLT.2019.2951290.

[27] Y. C. Shuai, D. Zhao, Y. Liu, C. Stambaugh, J. Lawall, and W. Zhou, "Coupled bilayer photonic crystal slab electro-optic spatial light modulators," *IEEE Photonics J.*, vol. 9, no. 2, Apr. 2017, doi: 10.1109/JPHOT.2017.2675619.

[28] X. Qiu, X. Ruan, Y. Li, and F. Zhang, "Indium Tin Oxide Based Dual-Polarization Electro-Optic Intensity Modulator on a Single Silicon Waveguide," *J. Light. Technol.*, vol. 36, no. 13, pp. 2563–2571, Jul. 2018, doi: 10.1109/JLT.2018.2810244.

[29] G. Kafaie Shirmanesh, R. Sokhoyan, R. A. Pala, and H. A. Atwater, "Dual-Gated Active Metasurface at 1550 nm with Wide (>300°) Phase Tunability," *Nano Lett.*, vol. 18, no. 5, pp. 2957–2963, May 2018, doi: 10.1021/acs.nanolett.8b00351.

[30] A. Forouzmand and H. Mosallaei, "Electro-optical Amplitude and Phase Modulators Based on Tunable Guided-Mode Resonance Effect," *ACS Photonics*, vol. 6, no. 11, Nov. 2019, doi: 10.1021/acsphotonics.9b00950.

[31] X. Hu, Q. Chen, L. Wen, L. Jin, H. Wang, and W. Liu, "Modulating spatial light by grating slot waveguides with transparent conducting oxides," *IEEE Photonics Technol. Lett.*, vol. 28, no. 15, pp. 1665–1668, Aug. 2016, doi: 10.1109/LPT.2016.2565507.

[32] Y. Li *et al.*, "Design of an electric-driven nonvolatile low-energy-consumption phase change optical switch," *Nanotechnology*, vol. 32, no. 40, p. 405201, Jul. 2021, doi: 10.1088/1361-6528/AC0EAD.

[33] O. Reshef, I. De Leon, M. Z. Alam, and R. W. Boyd, "Nonlinear optical effects in epsilon-near-zero media," *Nat. Rev. Mater.*, vol. 4, no. 8, pp. 535–551, Aug.

2019, doi: 10.1038/s41578-019-0120-5.

[34] A. P. Vasudev, J.-H. Kang, J. Park, X. Liu, and M. L. Brongersma, "Electro-optical modulation of a silicon waveguide with an 'epsilon-near-zero' material," *Opt. Express*, vol. 21, no. 22, p. 26387, Nov. 2013, doi: 10.1364/OE.21.026387.

[35] T. Bhowmik, A. K. A. K. Chowdhary, and D. Sikdar, "Grating-Assisted Polarization-Insensitive Dual-Mode Spatial Light Modulator Design Using Epsilon-Near-Zero Material," *IEEE J. Quantum Electron.*, vol. 58, no. 4, pp. 1–8, Aug. 2022, doi: 10.1109/JQE.2022.3166653.

[36] H. Q. Chiang, J. F. Wager, R. L. Hoffman, J. Jeong, and D. A. Keszler, "High mobility transparent thin-film transistors with amorphous zinc tin oxide channel layer," *Appl. Phys. Lett.*, vol. 86, no. 1, p. 013503, Jan. 2005, doi: 10.1063/1.1843286.

[37] A. K. Chowdhary and D. Sikdar, "Design of electrotunable all-weather smart windows," *Sol. Energy Mater. Sol. Cells*, vol. 222, p. 110921, Apr. 2021, doi: 10.1016/j.solmat.2020.110921.

[38] A. K. A. K. Chowdhary, T. Bhowmik, J. Gupta, and D. Sikdar, "Energy-saving all-weather window based on selective filtering of solar spectral radiation," *Appl. Opt.*, vol. 60, no. 5, p. 1315, Feb. 2021, doi: ao-60-5-1315.

[39] E. Feigenbaum, K. Diest, and H. A. Atwater, "Unity-order index change in transparent conducting oxides at visible frequencies," *Nano Lett.*, vol. 10, no. 6, pp. 2111–2116, Jun. 2010, doi: 10.1021/nl1006307.

[40] T. Bhowmik and D. Sikdar, "Parallel directional coupler based dual-polarization electro-absorption modulator using epsilon near-zero material," *J. Phys. D. Appl. Phys.*, vol. 55, no. 13, p. 135107, Mar. 2022, doi: 10.1088/1361-6463/ac4455.

[41] Y. Xu, X. Hu, Y. Dong, B. Zhang, and Y. Ni, “Highly-Efficient, Ultra-Compact and Polarization-Insensitive Electro-Absorption Modulator Driven by Hybrid Silicon-Indium Tin Oxide-Based MOS Capacitors,” *IEEE J. Quantum Electron.*, vol. 56, no. 1, Feb. 2020, doi: 10.1109/JQE.2019.2957131.

[42] G. Sinatkas and E. E. Kriezis, “Silicon-Photonic Electro-Optic Phase Modulators Integrating Transparent Conducting Oxides,” *IEEE J. Quantum Electron.*, vol. 54, no. 4, Aug. 2018, doi: 10.1109/JQE.2018.2852144.

[43] V. J. Sorger, N. D. Lanzillotti-Kimura, R.-M. Ma, and X. Zhang, “Ultra-compact silicon nanophotonic modulator with broadband response,” *Nanophotonics*, vol. 1, no. 1, pp. 17–22, Jul. 2012, doi: 10.1515/nanoph-2012-0009.

[44] A. Howes, W. Wang, I. Kravchenko, and J. Valentine, “Dynamic transmission control based on all-dielectric Huygens metasurfaces,” *Optica*, vol. 5, no. 7, p. 787, Jul. 2018, doi: 10.1364/OPTICA.5.000787.

[45] S. Vatani, H. Taleb, and M. K. Moravvej-Farshi, “Optical Modulation via Guided-Mode Resonance in an ITO-Loaded Distributed Bragg Reflector Topped with a Two-Dimensional Grating,” *IEEE J. Sel. Top. Quantum Electron.*, vol. 27, no. 3, May 2021, doi: 10.1109/JSTQE.2021.3055736.

[46] J. Navarro-Arenas, J. Parra, and P. Sanchis, “Ultrafast all-optical phase switching enabled by epsilon-near-zero materials in silicon,” *Opt. Express*, vol. 30, no. 9, p. 14518, Apr. 2022, doi: 10.1364/OE.454181.

[47] Y. Sha, Z. T. Xie, J. Wu, H. Y. Fu, and Q. Li, “All-optical switching in epsilon-near-zero asymmetric directional coupler,” *Sci. Rep.*, vol. 12, no. 1, p. 17958, Oct. 2022, doi: 10.1038/s41598-022-22573-7.

[48] D. A. B. Miller, “Are optical transistors the logical next step?,” *Nat. Photonics 2010 41*, vol. 4, no. 1, pp. 3–5, Jan. 2010, doi: 10.1038/nphoton.2009.240.

[49] A. Demircan, S. Amiranashvili, and G. Steinmeyer, "Controlling light by light with an optical event horizon," *Phys. Rev. Lett.*, vol. 106, no. 16, Apr. 2011, doi: 10.1103/PHYSREVLETT.106.163901/FIGURES/4/THUMBNAIL.

[50] Q. Guo *et al.*, "Femtojoule femtosecond all-optical switching in lithium niobate nanophotonics," *Nat. Photonics*, vol. 16, no. 9, pp. 625–631, Sep. 2022, doi: 10.1038/s41566-022-01044-5.

[51] H. Lambertus, F. Jack, and R. Gerald, "Controlling light with light," *J. Phys. D. Appl. Phys.*, vol. 41, no. 22, p. 220301, Nov. 2008, doi: 10.1088/0022-3727/41/22/220301.

[52] X. Fang, K. F. MacDonald, and N. I. Zheludev, "Controlling light with light using coherent metadevices: all-optical transistor, summator and invertor," *Light Sci. Appl. 2015 45*, vol. 4, no. 5, pp. e292–e292, May 2015, doi: 10.1038/lsa.2015.65.

[53] J. Zhang, K. F. MacDonald, and N. I. Zheludev, "Controlling light-with-light without nonlinearity," *Light Sci. Appl. 2012 17*, vol. 1, no. 7, pp. e18–e18, Jul. 2012, doi: 10.1038/lsa.2012.18.

[54] Z. Chai, X. Hu, F. Wang, X. Niu, J. Xie, and Q. Gong, "Ultrafast All-Optical Switching," *Adv. Opt. Mater.*, vol. 5, no. 7, Apr. 2017, doi: 10.1002/adom.201600665.

[55] N. Kinsey, C. DeVault, A. Boltasseva, and V. M. Shalaev, "Near-zero-index materials for photonics," *Nat. Rev. Mater.*, vol. 4, no. 12, pp. 742–760, Dec. 2019, doi: 10.1038/s41578-019-0133-0.

[56] M. Z. Alam, S. A. Schulz, J. Upham, I. De Leon, and R. W. Boyd, "Large optical nonlinearity of nanoantennas coupled to an epsilon-near-zero material," *Nat. Photonics*, vol. 12, no. 2, pp. 79–83, Feb. 2018, doi: 10.1038/s41566-017-0089-9.

[57] Y. Yang *et al.*, "Femtosecond optical polarization switching using a cadmium oxide-based perfect absorber," *Nat. Photonics*, vol. 11, no. 6, pp. 390–395, Jun. 2017, doi: 10.1038/nphoton.2017.64.

[58] M. Z. Alam, I. De Leon, and R. W. Boyd, "Large optical nonlinearity of indium tin oxide in its epsilon-near-zero region," *Science (80-.).*, vol. 352, no. 6287, pp. 795–797, May 2016, doi: 10.1126/science.aae0330.

[59] P. Guo, R. D. Schaller, J. B. Ketterson, and R. P. H. Chang, "Ultrafast switching of tunable infrared plasmons in indium tin oxide nanorod arrays with large absolute amplitude," *Nat. Photonics*, vol. 10, no. 4, pp. 267–273, Apr. 2016, doi: 10.1038/nphoton.2016.14.

[60] Z. T. Xie, J. Wu, H. Y. Fu, and Q. Li, "Tunable Electro- and All-Optical Switch Based on Epsilon-Near-Zero Metasurface," *IEEE Photonics J.*, vol. 12, no. 4, pp. 1–10, Aug. 2020, doi: 10.1109/JPHOT.2020.3010284.

[61] X. Niu, X. Hu, Y. Xu, H. Yang, and Q. Gong, "Ultrafast All-Optical Polarization Switching Based on Composite Metasurfaces with Gratings and an Epsilon-Near-Zero Film," *Adv. Photonics Res.*, vol. 2, no. 4, p. 2000167, Apr. 2021, doi: 10.1002/adpr.202000167.

[62] F. Zhang, X. Xiao, Y. Lu, J. Dong, and Y. Chen, "Broadband Enhancement of Optical Nonlinearity in a Plasmonic Nanocavity Coupled with an Epsilon-Near-Zero Film," *J. Phys. Chem. C*, vol. 127, no. 7, pp. 3726–3732, Feb. 2023, doi: 10.1021/acs.jpcc.2c07796.

[63] S. Vatani, B. Barahimi, and M. K. Moravvej-Farshi, "All-optical AZO-based modulator topped with Si metasurfaces," *Sci. Rep.*, vol. 12, no. 1, p. 21490, Dec. 2022, doi: 10.1038/s41598-022-25991-9.

[64] B. E. A. Saleh and M. C. Teich, *Fundamentals of Photonics*. New York, USA: Wiley, 1991.

[65] W. H. McMaster, "Polarization and the Stokes Parameters," *Am. J. Phys.*, vol. 22, no. 6, pp. 351–362, Sep. 1954, doi: 10.1119/1.1933744.

[66] E. Arbabi, S. M. Kamali, A. Arbabi, and A. Faraon, "Full-Stokes Imaging Polarimetry Using Dielectric Metasurfaces," *ACS Photonics*, vol. 5, no. 8, pp. 3132–3140, Aug. 2018, doi: 10.1021/acsphotonics.8b00362.

[67] Y. Bai *et al.*, "Asymmetric transmission of a planar metamaterial induced by symmetry breaking," *J. Phys. Condens. Matter*, vol. 30, no. 11, p. 114001, Mar. 2018, doi: 10.1088/1361-648X/aaacf5.

[68] S. Vandendriessche *et al.*, "Giant Faraday Rotation in Mesogenic Organic Molecules," *Chem. Mater.*, vol. 25, no. 7, pp. 1139–1143, Apr. 2013, doi: 10.1021/cm4004118.

[69] Y. Chen, Y. Huang, Z. Lin, and Y. Huang, "Polarization switching realized in the continuous-wave and acousto-optic Q-switched pulse Er:Yb:LaMgB 5 O 10 lasers at 1556 and 1568 nm," *Opt. Express*, vol. 26, no. 15, p. 19037, Jul. 2018, doi: 10.1364/OE.26.019037.

[70] P. Yu *et al.*, "Controllable optical activity with non-chiral plasmonic metasurfaces," *Light Sci. Appl.*, vol. 5, no. 7, pp. e16096–e16096, Feb. 2016, doi: 10.1038/lsa.2016.96.

[71] Z. Shi *et al.*, "Continuous angle-tunable birefringence with freeform metasurfaces for arbitrary polarization conversion," *Sci. Adv.*, vol. 6, no. 23, Jun. 2020, doi: 10.1126/sciadv.aba3367.

[72] X. Cai, Z. Li, Y. Kong, D. Lu, Y. Wei, and L. Huang, "Tunable polarization rotation using non-chiral all-dielectric metasurfaces," *Optik (Stuttg).*, vol. 207, p. 163769, Apr. 2020, doi: 10.1016/j.ijleo.2019.163769.

[73] Z. Li, X. Cai, L. Huang, H. Xu, Y. Wei, and N. Dai, "Controllable Polarization Rotator with Broadband High Transmission Using All-Dielectric

Metasurfaces," *Adv. Theory Simulations*, vol. 2, no. 9, p. 1900086, Sep. 2019, doi: 10.1002/adts.201900086.

[74] A. Shaltout, J. Liu, V. M. Shalaev, and A. V. Kildishev, "Optically Active Metasurface with Non-Chiral Plasmonic Nanoantennas," *Nano Lett.*, vol. 14, no. 8, pp. 4426–4431, Aug. 2014, doi: 10.1021/nl501396d.

[75] L. Jin *et al.*, "Noninterleaved Metasurface for (2 6 -1) Spin- and Wavelength-Encoded Holograms," *Nano Lett.*, vol. 18, no. 12, pp. 8016–8024, Dec. 2018, doi: 10.1021/acs.nanolett.8b04246.

[76] P. C. Wu *et al.*, "Visible Metasurfaces for On-Chip Polarimetry," *ACS Photonics*, vol. 5, no. 7, pp. 2568–2573, Jul. 2018, doi: 10.1021/acsphotonics.7b01527.

[77] Y. Cui, H. Jiang, L. Wang, B. Liu, J. Song, and Y. Jiang, "All-dielectric bifunctional polarization converter with high transmission efficiency in near-infrared region," *Appl. Opt.*, vol. 59, no. 13, p. 3825, May 2020, doi: 10.1364/AO.388097.

[78] Z. Yao, M. Lu, C. Zhang, and Y. Wang, "Dynamically tunable and transmissive linear to circular polarizer based on graphene metasurfaces," *J. Opt. Soc. Am. B*, vol. 36, no. 12, p. 3302, Dec. 2019, doi: 10.1364/JOSAB.36.003302.

[79] R.-H. Fan *et al.*, "Freely Tunable Broadband Polarization Rotator for Terahertz Waves," *Adv. Mater.*, vol. 27, no. 7, pp. 1201–1206, Feb. 2015, doi: 10.1002/adma.201404981.

[80] J. Li *et al.*, "Optical Polarization Encoding Using Graphene-Loaded Plasmonic Metasurfaces," *Adv. Opt. Mater.*, vol. 4, no. 1, pp. 91–98, Jan. 2016, doi: 10.1002/adom.201500398.

[81] P. C. Wu, R. Sokhoyan, G. K. Shirmanesh, W. Cheng, and H. A. Atwater, "Near-Infrared Active Metasurface for Dynamic Polarization Conversion,"

Adv. Opt. Mater., vol. 9, no. 16, p. 2100230, Aug. 2021, doi: 10.1002/adom.202100230.

[82] D. Sikdar, Y. Ma, A. R. Kucernak, J. B. Edel, and A. A. Kornyshev, "Nanoplasmonic Metamaterial Devices as Electrically Switchable Perfect Mirrors and Perfect Absorbers," in *Conference on Lasers and Electro-Optics*, May 2019, p. FM3C.5, doi: 10.1364/CLEO_QELS.2019.FM3C.5.

[83] Y. Chen, K. J. Si, D. Sikdar, Y. Tang, M. Premaratne, and W. Cheng, "Ultrathin Plasmene Nanosheets as Soft and Surface-Attachable SERS Substrates with High Signal Uniformity," *Adv. Opt. Mater.*, vol. 3, no. 7, pp. 919–924, Jul. 2015, doi: 10.1002/adom.201400635.

[84] Y. Chen *et al.*, "Multiscale Patterned Plasmonic Arrays for Highly Sensitive and Uniform SERS Detection," *Adv. Mater. Interfaces*, vol. 7, no. 17, p. 2000248, Sep. 2020, doi: 10.1002/admi.202000248.

[85] K. J. Si *et al.*, "Giant plasmene nanosheets, nanoribbons, and origami," *ACS Nano*, vol. 8, no. 11, pp. 11086–11093, Nov. 2014, doi: 10.1021/NN504615A/SUPPL_FILE/NN504615A_SI_002.ZIP.

[86] Y. Montelongo *et al.*, "Electrotunable nanoplasmonic liquid mirror," *Nat. Mater.*, vol. 16, no. 11, pp. 1127–1135, Nov. 2017, doi: 10.1038/nmat4969.

[87] A. Melikyan *et al.*, "High-speed plasmonic phase modulators," *Nat. Photonics*, vol. 8, no. 3, Mar. 2014, doi: 10.1038/nphoton.2014.9.

[88] L. Escoubas *et al.*, "Design and realization of light absorbers using plasmonic nanoparticles," *Prog. Quantum Electron.*, vol. 63, pp. 1–22, 2019, doi: https://doi.org/10.1016/j.pquantelec.2018.12.001.

[89] D. R. Smith, W. J. Padilla, D. C. Vier, S. C. Nemat-Nasser, and S. Schultz, "Composite Medium with Simultaneously Negative Permeability and Permittivity," *Phys. Rev. Lett.*, vol. 84, no. 18, pp. 4184–4187, May 2000, doi:

10.1103/PhysRevLett.84.4184.

[90] Y. Cheng and J. Wang, “Tunable terahertz circular polarization convertor based on graphene metamaterial,” *Diam. Relat. Mater.*, vol. 119, p. 108559, Nov. 2021, doi: 10.1016/j.diamond.2021.108559.

[91] H. Feng *et al.*, “Tunable polarization-independent and angle-insensitive broadband terahertz absorber with graphene metamaterials,” *Opt. Express*, vol. 29, no. 5, p. 7158, Mar. 2021, doi: 10.1364/OE.418865.

[92] W. Cui *et al.*, “Excellent sensing based on dual-plasmon induced transparency in graphene metasurface,” *Phys. E Low-dimensional Syst. Nanostructures*, vol. 134, p. 114850, Oct. 2021, doi: 10.1016/J.PHYSE.2021.114850.

[93] D. Yang, Y. Cheng, F. Chen, H. Luo, and L. Wu, “Efficiency tunable broadband terahertz graphene metasurface for circular polarization anomalous reflection and plane focusing effect,” *Diam. Relat. Mater.*, vol. 131, p. 109605, Jan. 2023, doi: 10.1016/j.diamond.2022.109605.

[94] L. Cong *et al.*, “A perfect metamaterial polarization rotator,” *Appl. Phys. Lett.*, vol. 103, no. 17, p. 171107, Oct. 2013, doi: 10.1063/1.4826536.

[95] Y. Ye and S. He, “90° polarization rotator using a bilayered chiral metamaterial with giant optical activity,” *Appl. Phys. Lett.*, vol. 96, no. 20, p. 203501, May 2010, doi: 10.1063/1.3429683.

[96] M. R. Tavakol, B. Rahmani, and A. Khavasi, “Terahertz Quarter Wave-Plate Metasurface Polarizer Based on Arrays of Graphene Ribbons,” *IEEE Photonics Technol. Lett.*, vol. 31, no. 12, pp. 931–934, Jun. 2019, doi: 10.1109/LPT.2019.2913503.

[97] Y. Hu *et al.*, “All-dielectric metasurfaces for polarization manipulation: principles and emerging applications,” *Nanophotonics*, vol. 9, no. 12, pp. 3755–3780, Sep. 2020, doi: 10.1515/nanoph-2020-0220.

[98] Y. Li, Z. Li, Y. Liu, Y. Kong, and L. Huang, “Broadband and highly efficient polarization conversion in infrared region using plasmonic metasurfaces,” *Opt. Mater.*, vol. 98, p. 109420, Dec. 2019, doi: 10.1016/j.optmat.2019.109420.

[99] Y. Kim *et al.*, “Phase Modulation with Electrically Tunable Vanadium Dioxide Phase-Change Metasurfaces,” *Nano Lett.*, vol. 19, no. 6, pp. 3961–3968, Jun. 2019, doi: 10.1021/acs.nanolett.9b01246.

[100] M. Amin, O. Siddiqui, and M. Farhat, “Polarization-State Modulation in Fano Resonant Graphene Metasurface Reflector,” *J. Light. Technol.*, pp. 1–1, 2021, doi: 10.1109/JLT.2021.3071246.

[101] M. M. Salary and H. Mosallaei, “Tunable All-Dielectric Metasurfaces for Phase-Only Modulation of Transmitted Light Based on Quasi-bound States in the Continuum,” *ACS Photonics*, vol. 7, no. 7, pp. 1813–1829, Jul. 2020, doi: 10.1021/acsphotonics.0c00554.

[102] A. H. Dorrah, N. A. Rubin, A. Zaidi, M. Tamagnone, and F. Capasso, “Metasurface optics for on-demand polarization transformations along the optical path,” *Nat. Photonics*, vol. 15, no. 4, pp. 287–296, Apr. 2021, doi: 10.1038/s41566-020-00750-2.

[103] M. Peng, F. Qin, L. Zhou, H. Wei, Z. Zhu, and X. Shen, “Material–structure integrated design for ultra-broadband all-dielectric metamaterial absorber,” *J. Phys. Condens. Matter*, vol. 34, no. 11, p. 115701, Mar. 2022, doi: 10.1088/1361-648X/ac431e.

[104] Y. Guo *et al.*, “Functional metasurfaces based on metallic and dielectric subwavelength slits and stripes array,” *J. Phys. Condens. Matter*, vol. 30, no. 14, p. 144003, Apr. 2018, doi: 10.1088/1361-648X/aaa84a.

[105] S. J. M. Rao, D. Kumar, G. Kumar, and D. R. Chowdhury, “Probing the Near-Field Inductive Coupling in Broadside Coupled Terahertz Metamaterials,”

IEEE J. Sel. Top. Quantum Electron., vol. 23, no. 4, pp. 1–7, Jul. 2017, doi: 10.1109/JSTQE.2016.2635020.

[106] C. U. Hail, A. U. Michel, D. Poulikakos, and H. Eghlidi, "Optical Metasurfaces: Evolving from Passive to Adaptive," *Adv. Opt. Mater.*, vol. 7, no. 14, p. 1801786, Jul. 2019, doi: 10.1002/adom.201801786.

[107] Z. Zhang *et al.*, "All-optical multi-channel switching at telecommunication wavelengths based on tunable plasmon-induced transparency," *Opt. Commun.*, vol. 425, pp. 196–203, Oct. 2018, doi: 10.1016/j.optcom.2018.04.061.

[108] S. Saha *et al.*, "Broadband, High-Speed, and Large-Amplitude Dynamic Optical Switching with Yttrium-Doped Cadmium Oxide," *Adv. Funct. Mater.*, vol. 30, no. 7, p. 1908377, Feb. 2020, doi: 10.1002/adfm.201908377.

[109] J. Chen *et al.*, "Strong Magnetic Plasmon Resonance in a Simple Metasurface for High-Quality Sensing," *J. Light. Technol.*, vol. 39, no. 13, pp. 4525–4528, Jul. 2021, doi: 10.1109/JLT.2021.3074334.

[110] K. Wang *et al.*, "High Contrast, Femtosecond Light Polarization Manipulation in Epsilon-near-Zero Material Coupled to a Plasmonic Nanoantenna Array," *ACS Photonics*, vol. 8, no. 9, pp. 2791–2799, Sep. 2021, doi: 10.1021/acsphotonics.1c00971.

[111] T. Cui, B. Bai, and H.-B. Sun, "Tunable Metasurfaces Based on Active Materials," *Adv. Funct. Mater.*, vol. 29, no. 10, p. 1806692, Mar. 2019, doi: 10.1002/ADFM.201806692.

[112] P. Genevet, F. Capasso, F. Aieta, M. Khorasaninejad, and R. Devlin, "Recent advances in planar optics: from plasmonic to dielectric metasurfaces," *Optica*, vol. 4, no. 1, p. 139, Jan. 2017, doi: 10.1364/OPTICA.4.000139.

[113] Y. Liu, X. Ling, X. Yi, X. Zhou, H. Luo, and S. Wen, "Realization of polarization evolution on higher-order Poincaré sphere with metasurface,"

Appl. Phys. Lett., vol. 104, no. 19, p. 191110, May 2014, doi: 10.1063/1.4878409.

[114] S. Saha *et al.*, “Engineering the temporal dynamics of all-optical switching with fast and slow materials,” *Nat. Commun.*, vol. 14, no. 1, p. 5877, Sep. 2023, doi: 10.1038/s41467-023-41377-5.

[115] A. K. Chowdhary and D. Sikdar, “Ultra-broadband Wide-Angle Metallo-Dielectric Metamaterial Absorber for Solar Energy Harvesting,” in *2019 Workshop on Recent Advances in Photonics (WRAP)*, Dec. 2019, pp. 1–3, doi: 10.1109/WRAP47485.2019.9013656.

[116] T. Bhowmik, A. K. A. K. Chowdhary, A. Kumar, and D. Sikdar, “Guided-Mode Resonance based All-dielectric Optical Intensity Modulator,” in *2021 IEEE Photonics Conference (IPC)*, Oct. 2021, pp. 1–2, doi: 10.1109/IPC48725.2021.9592867.

[117] J. Yang, S. Gurung, S. Bej, P. Ni, and H. W. Howard Lee, “Active optical metasurfaces: comprehensive review on physics, mechanisms, and prospective applications,” *Reports Prog. Phys.*, vol. 85, no. 3, p. 036101, Mar. 2022, doi: 10.1088/1361-6633/AC2AAF.

[118] C. Quan, J. Zou, C. Guo, W. Xu, Z. Zhu, and J. Zhang, “High-temperature resistant broadband infrared stealth metamaterial absorber,” *Opt. Laser Technol.*, vol. 156, p. 108579, Dec. 2022, doi: 10.1016/J.OPTLASTEC.2022.108579.

[119] T. Lian *et al.*, “Polarization-independent electro-absorption optical modulator based on trapezoid polymer-graphene waveguide,” *Opt. Laser Technol.*, vol. 149, p. 107815, May 2022, doi: 10.1016/J.OPTLASTEC.2021.107815.

[120] A. K. Chowdhary, A. Kumar, and D. Sikdar, “Cross–Ring Based Broadband Plasmonic Metamaterial Absorbers for Boosting Silicon Solar Cell

Efficiency," in *2021 Fifteenth International Congress on Artificial Materials for Novel Wave Phenomena (Metamaterials)*, Sep. 2021, pp. 102–104, doi: 10.1109/Metamaterials52332.2021.9577188.

[121] J. B. Edel *et al.*, "Electrochemical plasmonics: A path to electrotunable self-assembling optical metamaterials," in *7th International Topical Meeting on Nanophotonics and Metamaterials*, 2019, pp. 1–2.

[122] T. Bhowmik, A. K. Chowdhary, and D. Sikdar, "Energy-efficient Polarization-insensitive Electro-tunable Metasurface for Optical Intensity Modulation," in *The 2022 International Conference on Optical MEMS and Nanophotonics (IEEE OMN)*, 2022, pp. 1–2.

[123] R. S. Kshetrimayum, *Electromagnetic Field Theory*. Cengage Learning India, 2012.

[124] S. A. Maier, *Plasmonics: Fundamentals and applications*. Springer US, 2007.

[125] P. B. Johnson and R. W. Christy, "Optical Constants of the Noble Metals," *Phys. Rev. B*, vol. 6, no. 12, p. 4370, Dec. 1972, doi: 10.1103/PhysRevB.6.4370.

[126] S. Xiao, T. Wang, T. Liu, C. Zhou, X. Jiang, and J. Zhang, "Active metamaterials and metadevices: a review," *J. Phys. D. Appl. Phys.*, vol. 53, no. 50, p. 503002, Sep. 2020, doi: 10.1088/1361-6463/ABACED.

[127] A. Forouzmand, M. M. Salary, G. Kafaie Shirmanesh, R. Sokhoyan, H. A. Atwater, and H. Mosallaei, "Tunable all-dielectric metasurface for phase modulation of the reflected and transmitted light via permittivity tuning of indium tin oxide," *Nanophotonics*, vol. 8, no. 3, Jan. 2019, doi: 10.1515/nanoph-2018-0176.

[128] Y.-W. Huang *et al.*, "Gate-Tunable Conducting Oxide Metasurfaces," *Nano Lett.*, vol. 16, no. 9, Sep. 2016, doi: 10.1021/acs.nanolett.6b00555.

[129] S. Han *et al.*, "Optical modulating device having gate structure," United States Patent No. US9632216B2, Apr. 25, 2017.

[130] G. K. Shirmanesh, R. Sokhoyan, and H. Atwater, "Continuous Beam Steering with Multiple-Gated Reconfigurable Metasurfaces," United States Patent No. US 2019 / 0033682 A1, Jan. 31, 2019.

[131] H. W. Lee *et al.*, "Nanoscale Conducting Oxide PlasMOStor," *Nano Lett.*, vol. 14, no. 11, pp. 6463–6468, Nov. 2014, doi: 10.1021/nl502998z.

[132] G. V. Naik, V. M. Shalaev, and A. Boltasseva, "Alternative Plasmonic Materials: Beyond Gold and Silver," *Adv. Mater.*, vol. 25, no. 24, pp. 3264–3294, Jun. 2013, doi: 10.1002/adma.201205076.

[133] X. Liu *et al.*, "Tuning of Plasmons in Transparent Conductive Oxides by Carrier Accumulation," *ACS Photonics*, vol. 5, no. 4, pp. 1493–1498, Apr. 2018, doi: 10.1021/acsphotonics.7b01517.

[134] M. H. Tahersima *et al.*, "Coupling-enhanced dual ITO layer electro-absorption modulator in silicon photonics," *Nanophotonics*, vol. 8, no. 9, pp. 1559–1566, Aug. 2019, doi: 10.1515/nanoph-2019-0153.

[135] H. Wang *et al.*, "Tuning epsilon-near-zero wavelength of indium tin oxide film via annealing," *J. Phys. D. Appl. Phys.*, vol. 53, no. 22, p. 225108, May 2020, doi: 10.1088/1361-6463/ab78d8.

[136] E. Li, B. Zhou, Y. Bo, and A. X. Wang, "High-Speed Femto-Joule per Bit Silicon-Conductive Oxide Nanocavity Modulator," *J. Light. Technol.*, vol. 39, no. 1, pp. 178–185, Jan. 2021, doi: 10.1109/JLT.2020.3023644.

[137] A. Nemati, Q. Wang, N. S. S. Ang, W. Wang, M. Hong, and J. Teng, "Ultra-high extinction-ratio light modulation by electrically tunable metasurface using dual epsilon-near-zero resonances," *Opto-Electronic Adv.*, vol. 4, no. 7, pp. 200088–200088, 2021, doi: 10.29026/oea.2021.200088.

[138] J. Baek, J.-B. You, and K. Yu, “Free-carrier electro-refraction modulation based on a silicon slot waveguide with ITO,” *Opt. Express*, vol. 23, no. 12, Jun. 2015, doi: 10.1364/OE.23.015863.

[139] S. S. Mirshafieyan and D. A. Gregory, “Electrically tunable perfect light absorbers as color filters and modulators,” *Sci. Rep.*, vol. 8, no. 1, p. 2635, Dec. 2018, doi: 10.1038/s41598-018-20879-z.

[140] Z. Wang, P. Zhou, and G. Zheng, “Electrically switchable highly efficient epsilon-near-zero metasurfaces absorber with broadband response,” *Results Phys.*, vol. 14, p. 102376, Sep. 2019, doi: 10.1016/j.rinp.2019.102376.

[141] X. Qiu, J. Shi, Y. Li, and F. Zhang, “All-dielectric multifunctional transmittance-tunable metasurfaces based on guided-mode resonance and ENZ effect,” *Nanotechnology*, vol. 32, no. 6, p. 065202, Nov. 2020, doi: 10.1088/1361-6528/abc3e5.

[142] Z. Ma, Z. Li, K. Liu, C. Ye, and V. J. Sorger, “Indium-Tin-Oxide for High-performance Electro-optic Modulation,” *Nanophotonics*, vol. 4, no. 1. Walter de Gruyter GmbH, pp. 198–213, Jun. 30, 2015, doi: 10.1515/nanoph-2015-0006.

[143] F. Hu, W. Jia, Y. Meng, M. Gong, and Y. Yang, “High-contrast optical switching using an epsilon-near-zero material coupled to a Bragg microcavity,” *Opt. Express*, vol. 27, no. 19, p. 26405, Sep. 2019, doi: 10.1364/OE.27.026405.

[144] A. Forouzmand and H. Mosallaei, “All-Dielectric C-Shaped Nanoantennas for Light Manipulation: Tailoring Both Magnetic and Electric Resonances to the Desire,” *Adv. Opt. Mater.*, vol. 5, no. 14, p. 1700147, Jul. 2017, doi: 10.1002/ADOM.201700147.

[145] A. Forouzmand and H. Mosallaei, “Tunable dual-band amplitude modulation with a double epsilon-near-zero metasurface,” *J. Opt.*, vol. 22, no. 9, p. 094001,

Jul. 2020, doi: 10.1088/2040-8986/ABA03E.

[146] F. Ding, Y. Yang, R. A. Deshpande, and S. I. Bozhevolnyi, “A review of gap-surface plasmon metasurfaces: Fundamentals and applications,” *Nanophotonics*, vol. 7, no. 6, pp. 1129–1156, Jun. 2018, doi: 10.1515/NANOPH-2017-0125/ASSET/GRAPHIC/J_NANOPH-2017-0125_FIG_005.JPG.

[147] J. R. Hendrickson *et al.*, “Coupling of Epsilon-Near-Zero Mode to Gap Plasmon Mode for Flat-Top Wideband Perfect Light Absorption,” *ACS Photonics*, vol. 5, no. 3, pp. 776–781, Mar. 2018, doi: 10.1021/acsphotonics.7b01491.

[148] A. K. Osgouei, A. Ghobadi, B. Khalichi, and E. Ozbay, “A spectrally selective gap surface-plasmon-based nanoantenna emitter compatible with multiple thermal infrared applications,” *J. Opt.*, vol. 23, no. 8, p. 085001, Aug. 2021, doi: 10.1088/2040-8986/AC16B7.

[149] J. Park, J. H. Kang, X. Liu, and M. L. Brongersma, “Electrically Tunable Epsilon-Near-Zero (ENZ) Metafilm Absorbers,” *Sci. Rep.*, vol. 5, no. 1, pp. 1–9, Nov. 2015, doi: 10.1038/srep15754.

[150] D. A. B. Miller, “Attojoule Optoelectronics for Low-Energy Information Processing and Communications,” *J. Light. Technol.*, vol. 35, no. 3, pp. 346–396, Feb. 2017, doi: 10.1109/JLT.2017.2647779.

[151] R. Sabella, “Silicon Photonics for 5G and Future Networks,” *IEEE J. Sel. Top. Quantum Electron.*, vol. 26, no. 2, pp. 1–11, Mar. 2020, doi: 10.1109/JSTQE.2019.2948501.

[152] R. Amin, J. B. Khurgin, and V. J. Sorger, “Waveguide-based electro-absorption modulator performance: comparative analysis,” *Opt. Express*, vol. 26, no. 12, Jun. 2018, doi: 10.1364/OE.26.015445.

[153] P. Dong *et al.*, "Wavelength-tunable silicon microring modulator," *Opt. Express*, vol. 18, no. 11, p. 10941, May 2010, doi: 10.1364/oe.18.010941.

[154] Y. Ooka, T. Tetsumoto, A. Fushimi, W. Yoshiki, and T. Tanabe, "CMOS compatible high-Q photonic crystal nanocavity fabricated with photolithography on silicon photonic platform," *Sci. Rep.*, vol. 5, no. 1, pp. 1–9, Jun. 2015, doi: 10.1038/srep11312.

[155] Q. Gao, E. Li, and A. X. Wang, "Comparative analysis of transparent conductive oxide electro-absorption modulators [Invited]," *Opt. Mater. Express*, vol. 8, no. 9, Sep. 2018, doi: 10.1364/OME.8.002850.

[156] J. Ye, Y. Li, and S. Qu, "On-Chip Orbital Angular Momentum Sorting With a Surface Plasmon Polariton Lens," *J. Light. Technol.*, vol. 39, no. 5, pp. 1423–1428, Mar. 2021, doi: 10.1109/JLT.2020.3039270.

[157] X. Liu *et al.*, "Epsilon-Near-Zero Si Slot-Waveguide Modulator," *ACS Photonics*, vol. 5, no. 11, pp. 4484–4490, Nov. 2018, doi: 10.1021/acsphotonics.8b00945.

[158] M. Wood *et al.*, "Methods of epsilon-near-zero optical modulation," United States Patent No. US10908440B1, Feb. 02, 2021.

[159] H. W. Lee, S. Burgos, G. Papadakis, and H. A. Atwater, "Nanoscale plasmonic field-effect modulator," United States Patent No. US9864109B2, Jan. 09, 2018.

[160] M. Wood *et al.*, "Electroabsorption optical modulator," United States Patent No. US10908438B1, Feb. 02, 2021.

[161] X. Qiu, X. Ruan, Y. Li, and F. Zhang, "Multi-layer MOS capacitor based polarization insensitive electro-optic intensity modulator," *Opt. Express*, vol. 26, no. 11, p. 13902, May 2018, doi: 10.1364/OE.26.013902.

[162] M. Y. Abdelatty, M. M. Badr, and M. A. Swillam, "Compact Silicon Electro-Optical Modulator Using Hybrid ITO Tri-Coupled Waveguides," *J. Light.*

Technol., vol. 36, no. 18, pp. 4198–4204, Sep. 2018, doi: 10.1109/JLT.2018.2863571.

[163] M. G. Wood *et al.*, "Gigahertz speed operation of epsilon-near-zero silicon photonic modulators," *Optica*, vol. 5, no. 3, p. 233, Mar. 2018, doi: 10.1364/OPTICA.5.000233.

[164] D. Dai, "Silicon Nanophotonic Integrated Devices for On-Chip Multiplexing and Switching," *Journal of Lightwave Technology*, vol. 35, no. 4. Institute of Electrical and Electronics Engineers Inc., pp. 572–587, Feb. 15, 2017, doi: 10.1109/JLT.2016.2587727.

[165] J. T. Kim, "Silicon optical modulators based on tunable plasmonic directional couplers," *IEEE J. Sel. Top. Quantum Electron.*, vol. 21, no. 4, pp. 184–191, Jul. 2015, doi: 10.1109/JSTQE.2014.2346623.

[166] L. Jin, L. Wen, L. Liang, Q. Chen, and Y. Sun, "Polarization-Insensitive Surface Plasmon Polarization Electro-Absorption Modulator Based on Epsilon-Near-Zero Indium Tin Oxide," *Nanoscale Res. Lett.*, vol. 13, no. 1, 2018, doi: 10.1186/s11671-018-2446-0.

[167] E. Li, Q. Gao, R. T. Chen, and A. X. Wang, "Ultracompact Silicon-Conductive Oxide Nanocavity Modulator with 0.02 Lambda-Cubic Active Volume," *Nano Lett.*, vol. 18, no. 2, Feb. 2018, doi: 10.1021/acs.nanolett.7b04588.

[168] J.-S. Kim and J. T. Kim, "Silicon electro-optic modulator based on an ITO-integrated tunable directional coupler," *J. Phys. D. Appl. Phys.*, vol. 49, no. 7, p. 075101, Jan. 2016, doi: 10.1088/0022-3727/49/7/075101.

[169] P. Chang, C. Lin, and A. S. Helmy, "Polarization Engineering in Nanoscale Waveguides Using Lossless Media," *J. Light. Technol.*, vol. 34, no. 3, pp. 952–960, Feb. 2016, doi: 10.1109/JLT.2015.2505648.

[170] K. Wang, A.-Y. Liu, H.-H. Hsiao, C. Genet, and T. Ebbesen, "Large Optical

Nonlinearity of Dielectric Nanocavity-Assisted Mie Resonances Strongly Coupled to an Epsilon-near-Zero Mode," *Nano Lett.*, vol. 22, no. 2, pp. 702–709, Jan. 2022, doi: 10.1021/acs.nanolett.1c03876.

[171] S. T. Thurman and G. M. Morris, "Controlling the spectral response in guided-mode resonance filter design," *Appl. Opt.*, vol. 42, no. 16, p. 3225, Jun. 2003, doi: 10.1364/AO.42.003225.

[172] D. Wang, Q. Wang, and J. Gao, "Spectral Correlation between 2D and 1D Guided Mode Resonant Filters," *IEEE Photonics Technol. Lett.*, vol. 31, no. 15, pp. 1289–1292, Aug. 2019, doi: 10.1109/LPT.2019.2925770.

[173] Z. Wang, T. Sang, L. Wang, J. Zhu, Y. Wu, and L. Chen, "Guided-mode resonance Brewster filters with multiple channels," *Appl. Phys. Lett.*, vol. 88, no. 25, p. 251115, Jun. 2006, doi: 10.1063/1.2215610.

[174] Y. Zhou *et al.*, "High-Q guided mode resonance sensors based on shallow sub-wavelength grating structures," *Nanotechnology*, vol. 31, no. 32, p. 325501, May 2020, doi: 10.1088/1361-6528/AB8CF0.

[175] F. Gambino, M. Giaquinto, A. Ricciardi, and A. Cusano, "(INVITED)A review on dielectric resonant gratings: Mitigation of finite size and Gaussian beam size effects," *Results Opt.*, vol. 6, p. 100210, Jan. 2022, doi: 10.1016/J.RIO.2021.100210.

[176] A. K. Chowdhary, T. Bhowmik, and D. Sikdar, "Polarization- and angle-insensitive ultrabroadband perfect metamaterial absorber for thermophotovoltaics," *J. Opt. Soc. Am. B*, vol. 38, no. 2, p. 327, Feb. 2021, doi: 10.1364/JOSAB.411643.

[177] X. Xu, Y. Li, B. Wang, and Z. Zhou, "Prediction of multiple resonance characteristics by an extended resistor–inductor–capacitor circuit model for plasmonic metamaterials absorbers in infrared," *Opt. Lett.*, vol. 40, no. 19, p.

4432, Oct. 2015, doi: 10.1364/OL.40.004432.

[178] J. Zhu, L. Zhang, S. Jiang, J.-Y. Ou, and Q. H. Liu, "Selective light trapping of plasmonic stack metamaterials by circuit design," *Nanoscale*, vol. 12, no. 3, pp. 2057–2062, 2020, doi: 10.1039/C9NR07937H.

[179] J. Zhou, E. N. Economon, T. Koschny, and C. M. Soukoulis, "Unifying approach to left-handed material design," *Opt. Lett.*, vol. 31, no. 24, p. 3620, Dec. 2006, doi: 10.1364/OL.31.003620.

[180] T. Bhowmik and D. Sikdar, "Electrically tunable metasurface for dual-band spatial light modulation using the epsilon-near-zero effect," *Opt. Lett.*, vol. 47, no. 19, p. 4993, Oct. 2022, doi: 10.1364/OL.471974.

[181] C. Baudot *et al.*, "Low voltage 25Gbps silicon Mach-Zehnder modulator in the O-band," *Opt. Express, Vol. 25, Issue 10, pp. 11217-11222*, vol. 25, no. 10, pp. 11217–11222, May 2017, doi: 10.1364/OE.25.011217.

[182] A. L. Gaeta, K. Luke, M. R. E. Lamont, M. Lipson, and Y. Okawachi, "Broadband mid-infrared frequency comb generation in a Si_3N_4 microresonator," *Opt. Lett. Vol. 40, Issue 21, pp. 4823-4826*, vol. 40, no. 21, pp. 4823–4826, Nov. 2015, doi: 10.1364/OL.40.004823.

[183] E. D. Palik, *Handbook of Optical Constants of Solids*, vol. 2. Academic Press, 2012.

[184] S. Menon, K. M. Jyothsna, R. Biswas, A. Prosad, A. S. Lal Krishna, and V. Raghunathan, "Third harmonic generation enhancement from silicon-based multilayer guided mode resonance structures under a conical mounting condition," *Opt. Contin.*, vol. 1, no. 5, p. 1015, May 2022.

[185] L. K. A. S., L. K. A. S., V. Mere, V. Mere, S. K. Selvaraja, and V. Raghunathan, "Polarization-independent angle-tolerant mid-infrared spectral resonance using amorphous germanium high contrast gratings for notch filtering application,"

OSA Contin. Vol. 3, Issue 5, pp. 1194-1203, vol. 3, no. 5, pp. 1194–1203, May 2020, doi: 10.1364/OSAC.390644.

[186] D. R. Lide, *CRC Handbook of Chemistry and Physics*, 75th ed. New York: CRC Press, 1997.

[187] Z. Zhou, Y. Chen, Y. Tian, J. Liang, and W. Yang, "Ultra-broadband metamaterial perfect solar absorber with polarization-independent and large incident angle-insensitive," *Opt. Laser Technol.*, vol. 156, p. 108591, Dec. 2022, doi: 10.1016/J.OPTLASTEC.2022.108591.

[188] Y. Zheng *et al.*, "High efficiency Titanium oxides and nitrides ultra-broadband solar energy absorber and thermal emitter from 200 nm to 2600 nm," *Opt. Laser Technol.*, vol. 150, p. 108002, Jun. 2022, doi: 10.1016/J.OPTLASTEC.2022.108002.

[189] T. Bhowmik, B. Kr. Bhowmik, P. Kr. Pandey, G. Kumar, and D. Sikdar, "Dual-band electro-optic modulator based on tunable broadband metamaterial absorber," *Opt. Laser Technol.*, vol. 161, p. 109129, Jun. 2023, doi: 10.1016/j.optlastec.2023.109129.

[190] N. Kinsey and J. Khurgin, "Nonlinear epsilon-near-zero materials explained: opinion," *Opt. Mater. Express*, vol. 9, no. 7, p. 2793, Jul. 2019, doi: 10.1364/OME.9.002793.

[191] S. K. Vasheghani Farahani, T. D. Veal, P. D. C. King, J. Zúñiga-Pérez, V. Muñoz-Sanjosé, and C. F. McConville, "Electron mobility in CdO films," *J. Appl. Phys.*, vol. 109, no. 7, p. 73712, 2011, doi: 10.1063/1.3562141.

[192] H. Wang *et al.*, "Extended Drude Model for Intraband-Transition-Induced Optical Nonlinearity," *Phys. Rev. Appl.*, vol. 11, no. 6, p. 064062, Jun. 2019, doi: 10.1103/PhysRevApplied.11.064062.

[193] J. Baxter, A. Pérez-Casanova, L. Cortes-Herrera, A. Calà Lesina, I. De Leon, and

L. Ramunno, "Dynamic Nanophotonics in Epsilon-Near-Zero Conductive Oxide Films and Metasurfaces: A Quantitative, Nonlinear, Computational Model," *Adv. Photonics Res.*, vol. 4, no. 6, p. 2300141, 2023, doi: https://doi.org/10.1002/adpr.202300141.

[194] N. W. Ashcroft and N. D. Mermin, *Solid State Physics*. Holt-Saunders, 1976.

[195] Y. Zhu, R. J. Mendelsberg, J. Zhu, J. Han, and A. Anders, "Transparent and conductive indium doped cadmium oxide thin films prepared by pulsed filtered cathodic arc deposition," *Appl. Surf. Sci.*, vol. 265, pp. 738–744, Jan. 2013, doi: 10.1016/j.apsusc.2012.11.096.

[196] B. Zhao and Z. M. Zhang, "Study of magnetic polaritons in deep gratings for thermal emission control," *J. Quant. Spectrosc. Radiat. Transf.*, vol. 135, pp. 81–89, Mar. 2014, doi: 10.1016/j.jqsrt.2013.11.016.

[197] K. M. Yu *et al.*, "Defects and properties of cadmium oxide based transparent conductors," *J. Appl. Phys.*, vol. 119, no. 18, p. 181501, 2016.

[198] T. Munawar *et al.*, "Synthesis of novel heterostructured ZnO-CdO-CuO nanocomposite: Characterization and enhanced sunlight driven photocatalytic activity," *Mater. Chem. Phys.*, vol. 249, p. 122983, 2020.

[199] D. de Ceglia *et al.*, "Viscoelastic optical nonlocality of low-loss epsilon-near-zero nanofilms," *Sci. Rep.*, vol. 8, no. 1, p. 9335, 2018, doi: 10.1038/s41598-018-27655-z.

[200] M. Alam, I. De Leon, and R. Boyd, "Large optical nonlinearity of indium tin oxide in its epsilon-near-zero region," *Science*, vol. 352, 2016.

[201] M. Wang *et al.*, "Tunable and Robust Mid-Infrared Saturable Absorber Employing Tungsten Doping Cadmium Oxide," *Adv. Funct. Mater.*, vol. 34, no. 1, p. 2307234, Jan. 2024, doi: 10.1002/ADFM.202307234.

[202] D. R. Smith, D. C. Vier, T. Koschny, and C. M. Soukoulis, "Electromagnetic

parameter retrieval from inhomogeneous metamaterials," *Phys. Rev. E*, vol. 71, no. 3, p. 36617, Mar. 2005, doi: 10.1103/PhysRevE.71.036617.

[203] E. Sachet *et al.*, "Dysprosium-doped cadmium oxide as a gateway material for mid-infrared plasmonics," *Nat. Mater.*, vol. 14, no. 4, pp. 414–420, Apr. 2015.

[204] E. M. Jackson *et al.*, "Two-dimensional plasmonic grating for increased quantum efficiency in midwave infrared nBn detectors with thin absorbers," *Opt. Express*, vol. 26, no. 11, p. 13850, May 2018, doi: 10.1364/OE.26.013850.

[205] D. Dai, Z. Wang, and J. E. Bowers, "Ultrashort broadband polarization beam splitter based on an asymmetrical directional coupler," *Opt. Lett.*, vol. 36, no. 13, Jul. 2011, doi: 10.1364/OL.36.002590.

[206] Y. Tian, J. Qiu, C. Liu, S. Tian, Z. Huang, and J. Wu, "Compact polarization beam splitter with a high extinction ratio over S + C + L band," *Opt. Express*, vol. 27, no. 2, p. 999, Jan. 2019, doi: 10.1364/OE.27.000999.

[207] T. Bhowmik, A. K. Chowdhary, and D. Sikdar, "Polarization- and Angle-Insensitive Tunable Metasurface for Electro-Optic Modulation," *IEEE Photonics Technol. Lett.*, vol. 35, no. 16, pp. 879–882, Aug. 2023, doi: 10.1109/LPT.2023.3256584.

[208] T. Bhowmik, J. Gupta, and D. Sikdar, "Electro-tunable metasurface for tri-state dynamic polarization switching at near-infrared wavelengths," *J. Phys. Condens. Matter*, vol. 35, no. 39, p. 395701, Oct. 2023, doi: 10.1088/1361-648X/ace01b.

[209] E. Carpene, "Ultrafast laser irradiation of metals: Beyond the two-temperature model," *Phys. Rev. B*, vol. 74, 2006, doi: 10.1103/PhysRevB.74.024301.

[210] T. Bhowmik, B. Chakraborty, and D. Sikdar, "All-optical high-contrast femtosecond switching using nonlinearity from an epsilon-near-zero effect in plasmonic metamaterials," *Opt. Lett.*, vol. 49, no. 9, p. 2397, May 2024, doi: 10.1364/OL.521075.

[211] M. Kelley, A. Lee, M. Mozumdar, K. Dajani, and A. Ahmed, "Design and modeling of subpicosecond all-optical modulator using the nonlinear response of indium tin oxide," *J. Opt. Soc. Am. B*, vol. 36, no. 8, p. F149, Aug. 2019, doi: 10.1364/JOSAB.36.00F149.

[212] T. Bhowmik, A. K. Chowdhary, J. Gupta, and D. Sikdar, "Coupling-assisted Epsilon-Near-Zero Material based Energy-efficient Electro-Absorption Modulator," in *2022 Workshop on Recent Advances in Photonics (WRAP)*, Mar. 2022, pp. 1–2, doi: 10.1109/WRAP54064.2022.9758316.

[213] X. Xiao *et al.*, "High-speed, low-loss silicon Mach–Zehnder modulators with doping optimization," *Opt. Express*, vol. 21, no. 4, p. 4116, Feb. 2013, doi: 10.1364/OE.21.004116.

[214] K. Debnath *et al.*, "All-silicon carrier accumulation modulator based on a lateral metal-oxide-semiconductor capacitor," *Photonics Res.*, vol. 6, no. 5, p. 373, May 2018, doi: 10.1364/PRJ.6.000373.

[215] Z. Yong *et al.*, "U-shaped PN junctions for efficient silicon Mach-Zehnder and microring modulators in the O-band," *Opt. Express*, vol. 26, no. 25, p. 32757, Dec. 2018, doi: 10.1364/OE.26.032757.

[216] H. Mahrous *et al.*, "Design of compact, high-speed and low-loss silicon-on-silica electro-optic modulators," *Semicond. Sci. Technol.*, vol. 35, no. 9, p. 095017, Sep. 2020, doi: 10.1088/1361-6641/ab9d09.